博 士 学 位 論 文

Doctoral Dissertation

Interplay of Fluid Infiltration, Reaction and Fracturing

in the Oceanic Lithosphere

（海洋リソスフェアにおける流体浸透、反応、破壊の相互作用）

東北大学大学院環境科学研究科

Graduate School of Environmental Studies, Tohoku University

専攻 major／コース course	先進社会環境学専攻
学籍番号 Student ID No.	C1GD1007
氏　名 Name	吉田 一貴

指　導　教　員 Supervisor at Tohoku Univ.	岡本　敦　教授		
研究指導教員 Research Advisor at Tohoku Univ.			
審　査　委　員 （○印は主査） Dissertation Committee Members Name marked with "○" is the Chief Examiner	○　岡本　敦　教授		
	1　土屋　範芳　客員教授	2	中村　美千彦　教授 （理学研究科）
	3　宇野　正起　准教授	4	Oliver Plümper 准教授 （ユトレヒト大学）
	5　Christoph Hilgers 教授 （カールスルーエ工科大学）	6	上高原　理暢　教授

Abstract

Serpentinization is one of the most important water-rock reactions in oceanic lithospheres and plays an important role in a variety of geochemical processes across the hydrosphere, lithosphere, and biosphere. These processes include the global water cycle, deep biosphere maintained on the seafloor, seismic and volcanic activity in subduction zones, and ore deposit formation. Serpentinization is the reaction of olivine and pyroxenes with H_2O. Hydrous minerals such as serpentine group minerals and brucite and magnetite are the main products. In this reaction, the ferrous iron (Fe^{2+}) in the reaction minerals, such as olivine and pyroxene, is converted to ferrous iron (Fe^{3+}) in the product minerals, such as magnetite and serpentine minerals, resulting a production of the significant amount of hydrogen by the reduction of H_2O. The hydrogen produced by the serpentinization reaction is an important energy source for the energy-poor deep underground microbial biosphere due to the lack of energy from sunlight. The hydrogen production during serpentinization is a key to understanding the scale of biomass of the deep biosphere and the early life before photosynthesis. The amount of hydrogen produced depends on the progression of serpentinization and the amount of hydrogen that can be produced by a unit mass of primary rock. However, because the serpentinization process involves complex interactions of reaction-fracturing-fluid flow, it is difficult to analyze the history of the serpentinization reaction from observations of natural samples. In addition, the factors controlling the conditions for magnetite formation and the amount of Fe^{3+} in serpentine, which are important for hydrogen production, are not well understood.

The objective of this study is to determine the evolution of the hydrogen production process in the serpentinization reaction of rocks in oceanic lithospheres, which proceeds with a reaction-fracture-fluid transfer interaction. Observations and analyses were made on rock samples from the lower crust to the upper mantle of the Oman ophiolite as an analogue of oceanic lithosphere. Petrological observations, chemical analyses including iron redox state analysis, thermodynamic calculations, and numerical simulations were used to understand the serpentinization process and hydrogen production.

I observed and analyzed drill core samples from the lower crust to the upper mantle recovered during the Oman drilling project. The rocks from the lower crust to the upper mantle were extensively homogenized serpentinized over a drilling range of 300m-400m. The lower crust is mainly composed of gabbroic rock, and olivine is serpentinized with a mesh-like structure. The crustal mantle boundary is composed mainly of dunite and is almost completely serpentinized. The upper mantle is composed of harzburgite, which is serpentinized with a mesh texture. The dunite and harzburgite host rocks are cut by serpentine and magnetite veins composed of antigorite and chrysotile, which are often visible at thin section scales. Serpentinization around these mineral veins is limited, suggesting that the main serpentinization stage occurred prior to the subduction stage. The antigorite + chrysotile veins show higher As and Sb concentrations than the host rock mesh texture, suggesting that they were formed by fluids that interacted with the subducting sediments. This suggests fluid inflow from depth in the subduction zone setting. These suggest that the Oman ophiolite records rock-water reactions at the seafloor and in subduction zone settings, and that the main stage of serpentinization with mesh texture

formation occurred primarily at the seafloor.

To understand the process of serpentinization reaction, which is a coupled process of reaction-fracturing-fluid flow, I observed microstructures of natural rock samples and performed numerical simulations. In the numerical model, a simple volume-increasing hydration reaction is assumed and the reaction rate is considered to be a linear function of fluid pressure. While there have been relatively many studies on numerical simulations of serpentinization of dunite (composed only of olivine), few studies have focused on serpentinization of gabbroic rock with heterogeneous microstructure. Therefore, we focused on the serpentinization of olivine in gabbroic rocks. The olivine in gabbroic rocks is serpentinized to various degrees, forming a mesh-like structure. Radial cracks were observed around the serpentinized olivine grains. Two stages of serpentinization were recorded in the mesh texture. The early-stage microstructure consisted of serpentine, magnetite, and small amounts of brucite. In contrast, the later stage microstructure consisted of relatively Al-rich serpentine and magnetite, with no brucite present. This microstructure represents a change from a relatively closed reaction to an open reaction. Numerical simulations showed that radial cracks formed around the olivine due to the volume increase associated with the reaction. Simulations simulating thermal stresses show that cracks preferentially form inside olivine due to the difference in thermal expansion coefficients between olivine and plagioclase. Comparison of the numerical simulation results with natural samples indicates that the stress induced by the volume change due to the reaction may play an important role in the crack formation as a crack formation mechanism. This suggests that the high crack density in the olivine interior in the early serpentinization stage leads to the olivine-dominated reaction, whereas in the later stage, cracks are formed in the plagioclase and orthopyroxene as the olivine reacts, and Si and Al are supplied by the increase in the reaction area of these minerals. These results suggest that Si and Al are supplied by the increase in the reaction area of these minerals. These results indicate that the reaction-associated crack formation causes an increase in W/R and Si activity, as well as promotes the reaction.

To determine the amount of hydrogen produced during serpentinization and factors control the amount of hydrogen, bulk-rock analysis and mapping of the redox state of iron were performed using synchrotron X-ray absorption fine structure spectroscopy. The result from the bulk-rock analysis shows differences in hydrogen production by primary rock composition. The mapping of the redox state of iron in rock microstructures was used to reveal the history of hydrogen production recorded in the rock microstructures. The iron redox state in serpentine were found to be high ($Fe^{3+}/\Sigma Fe$=~0.6-1.0) around the mineral veins, which are thought to have been primary fluid pathways. On the other hand, the Fe^{3+} content of mesh texture serpentine, which main component of the serpentinite, is found to be about 30-40%. Thermodynamic calculations were performed to determine the factors controlling hydrogen production. Comparison of the results of thermodynamic calculations with those of in-situ and bulk-rock analyses revealed differences in mineral composition and the influence of fluid supply on hydrogen production. These results reveal the evolution of the reaction progress and hydrogen production with the interaction of reaction, fracturing, and fluid flow in the serpentinization in oceanic lithosphere.

These results indicate that the formation of microcracks due to the volume increase associated

with the reaction forms the fluid pathways and also increases the silica activity by forming cracks in the silica-rich minerals (orthopyroxene and plagioclase) around the olivine, increasing the reaction surface of these minerals. It is suggested that hydrogen produced by the serpentinization reaction is dynamically controlled by reaction-fracturing-fluid flow interaction during serpentinization in the oceanic lithosphere. Such changes in hydrogen production in oceanic lithospheres may lead to temporal and spatial variations in deep biosphere.

Contents

Chapter 1: Introduction and Review of Previous Studies

1.1. Significance of serpentinization

The long-term availability of water is an important factor in the origin and evolution of life and dynamics on solid Earth. Therefore, the hydration of the oceanic lithosphere plays an important role in the global water cycle. The hydrated oceanic lithosphere at the seafloor moves into the Earth's interior at subduction zones (Fig. 1.1). This process controls the budget of the H_2O and other elements between the Earth's surface and interior (Hacker, 2008; Rüpke *et al.*, 2004; Schmidt and Poli, 1998; Van Keken *et al.*, 2011). Serpentine minerals, which are formed by the hydration reaction of mantle rocks, are important as the main carrier of water into the Earth's interior. The serpentinization reaction is a reaction in which water reacts with minerals such as olivine [$(Mg,Fe)_2SiO_4$] and orthopyroxene [$(Mg,Fe)_2Si_2O_6$], which are abundant in mantle rocks, to form hydrous minerals such as serpentine [$(Mg,Fe)_3Si_2O_5(OH)_4$] and brucite [$(Mg,Fe)(OH)_2$]. The simplified serpentinization reaction is written as follow:

$$\underset{\text{Olivine}}{2Mg_2SiO_4} + \underset{\text{Water}}{3H_2O} = \underset{\text{Serpentine}}{Mg_3Si_2O_5(OH)_4} + \underset{\text{Brucite}}{Mg(OH)_2} \quad \text{(R1.1)}$$

The serpentine minerals contain ~12-13 wt. % H_2O in its crystal structure. The oceanic lithospheres, which react with seawater to form serpentine, are carried into the Earth's interior at subduction zones (*e.g.*, Japan and Chilie). The serpentine decomposes at a depth of about 100 km and a temperature of 650-700 °C, releasing water. The released water reduces the strength of the rock and is thought to be associated with the occurrence of earthquakes at shallow subduction zones (Sibson, 1992; Tauzin *et al.*, 2017). Furthermore, the water content of subducting oceanic plates is thought to be one of the factors controlling plate shape and mantle flow pattern in the subduction systems (Nakao *et al.*, 2018).

The hydrated oceanic mantle has greater potential as a water carrier than the oceanic crust (Schmidt and Poli, 1998). However, the nature of serpentinization in the lower crust-upper mantle of the oceanic lithosphere are still poorly understand due to technical problems (e.g., the difficulty of drilling deep into the oceanic lithosphere and the limited resolution of geophysical observations). As a result, the estimates of the amount of water transported into the deep Earth at subduction zones have a large uncertainty (Hacker, 2008; Hatakeyama *et al.*, 2017; Hyndman *et al.*, 2015; Rüpke *et al.*, 2004; Van Keken *et al.*, 2011).

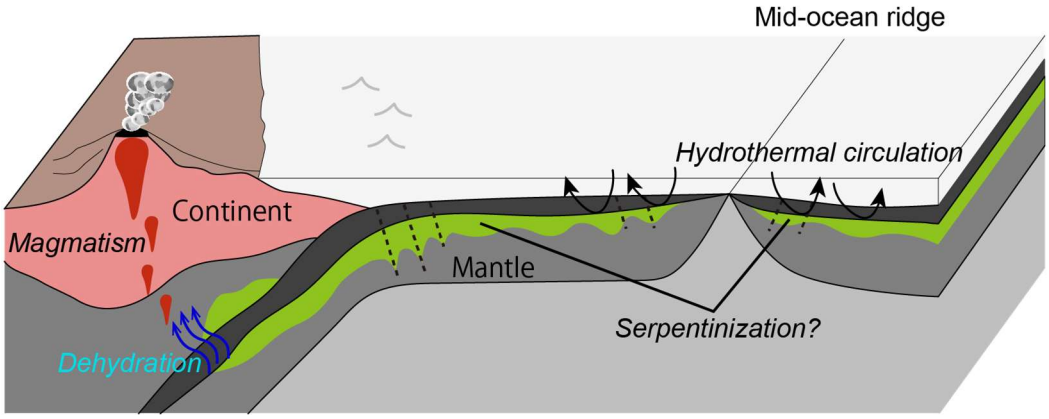

Fig. 1.1. Illustration of the oceanic lithosphere from the mid-ocean ridge to the subduction zone.

The other aspect of serpentinization has received particular attention since the discovery of a unique microbial community (methanogens) in the extreme environments associated with serpentinite host hydrothermal vents (Kelley *et al.*, 2005). This unique microbial community on the seafloor, where sunlight is not available as an energy source, provides insight into primitive life in the earliest period of the Earth, from about > 4 billion years ago (Hedges, 2002) to the emergence of photosynthetic microbial communities about 3.7 billion years ago (Nutman *et al.*, 2016).

The energy source for life on the seafloor is hydrogen generated by serpentinization reactions and mantle-derived inorganic carbon ($\Sigma CO_2 = CO_{2,\,aq} + H_2CO_3 + HCO^{3-} + CO_3^{2-}$) (Proskurowski *et al.*, 2008). Carbon is supplied by degassing of magma at the Central Ridge or from graphite and amorphous carbon. Methanogens obtain energy from methanogenic reactions based on hydrogen and carbon dioxide. Such deep subsurface life is thought to account for about 15% of life on Earth (Bar-On *et al.*, 2018).

In the serpentinization reaction, hydrogen is produced by the reduction of water as ferrous iron (Fe^{2+}) in primary mantle minerals such as olivine and pyroxene are transformed into serpentine and magnetite containing ferric iron (Fe^{3+}). The reaction is expressed as follows (McCollom *et al.*, 2022):

$$\underset{\text{Olivine}}{(\mathrm{Mg,Fe^{2+}})_2\mathrm{SiO_4}} + \underset{\text{Water}}{v\mathrm{H_2O}} \rightarrow \underset{\text{Serpentine}}{w(\mathrm{Mg,Fe^{2+},Fe^{3+}})_3(\mathrm{Si,Fe^{3+}})_2\mathrm{O_5(OH)_4}} \pm \underset{\text{Brucite}}{x(\mathrm{Mg,Fe^{2+}})(\mathrm{OH})_2} \pm \underset{\text{Magnetite}}{y\mathrm{Fe^{2+}Fe^{3+}{}_2O_4}} \pm \underset{\text{Hydrogen}}{z\mathrm{H_2}} \quad \text{(R1.2)}$$

The coefficients *v*-*z* can be highly variable depending on starting minerals, pressure-temperature conditions, and solution chemistry (McCollom *et al.*, 2016, 2020, 2022; McCollom and Bach, 2009; Ogasawara *et al.*, 2013; Okamoto *et al.*, 2011; Oyanagi *et al.*, 2018, 2020). A comprehensive analysis of the results of many laboratory experiments indicates that the amount of hydrogen produced appears to be controlled by the temperature and pressure conditions in particular (Huang *et al.*, 2021). As a result of hydrogen generation from the serpentinization reaction, cation consumption and free OH- increase and solution becomes alkaline and reduced condition (Holm *et al.*, 2015). As the result, hydrothermal

fluids from seafloor hydrothermal vents (Kelley *et al.*, 2005) and onshore spring waters (Miller *et al.*, 2016; Suda *et al.*, 2014; Suzuki *et al.*, 2017; Yoshiya *et al.*, 2019) , where serpentinization reactions are thought to occur, have a high pH. The reductive nature of the serpentinization reaction is also supported by the presence of Ni-Fe alloys in serpentinite (Frost, 1985) and the absence of epidote(Nozaka and Tateishi, 2023). The high concentrations of molecular hydrogen during serpentinization under hydrothermal conditions are reproduced in many laboratory experiments *e.g.,* (Marcaillou *et al.*, 2011; McCollom *et al.*, 2016; Seyfried *et al.*, 2007).

Life activities driven by serpentinization reactions are not limited to the seafloor but are also ubiquitous in terrestrial ultramafic bodies. Serpentinization reactions on continents are often accompanied by high pH springs, including the Cedars, USA (Suzuki *et al.*, 2017); Oman Ophiolite, Oman (Miller *et al.*, 2016), Hakuba-Happo hot spring, Japan (Suda *et al.*, 2014; Yoshiya *et al.*, 2019). In addition, unlike serpentinization on the seafloor, continental serpentinization reactions using meteoric water are poor in sodium and potassium. This makes it difficult to generate adenosine triphosphate (ATP) using the concentration gradient of sodium ions in and out of the body, which together with the strongly alkaline environment is an extreme environment for organisms (Suzuki *et al.*, 2017). However, despite such a severe environment, microorganisms have been discovered that use hydrogen produced by serpentinization as an energy source (Miller *et al.*, 2016; Suzuki *et al.*, 2017).

Trace minerals such as chromium spinel, magnetite, and Ni-Fe alloys in serpentinite act as catalysts to convert hydrogen produced by serpentinization and externally supplied carbon to generate hydrocarbon compounds (Berndt *et al.*, 1996; Horita and Berndt, 1999; Preiner *et al.*, 2020; Sleep *et al.*, 2004). Such abiotic organic matter production may have played an important role in the process of origin of life. Most of the hydrocarbon compounds produced during serpentinization have simple structures (Konn *et al.*, 2015; Ménez *et al.*, 2018), but several studies have suggested that amino acids are produced by the Fredel-Crafts reaction catalyzed by clay minerals such as saponite (Ménez *et al.*, 2018). Such organic matter synthesis processes related to serpentinization that support the hydrothermal origin of life in hydrothermal environments (Martin *et al.*, 2008; Ménez *et al.*, 2018; Russell, 2007; Sleep *et al.*, 2004). In addition, serpentine minerals can be found in meteorites and asteroidal rocks (Steele *et al.*, 2022; Yokoyama *et al.*, 2023). Thus, the biosphere in extreme environments and organic synthesis driven by serpentinization are interest for the origin of life, and for constraining of the possibility of life beyond Earth (Colman *et al.*, 2017).

1.2. Structure of oceanic lithospheres

1.2.1. Structure of the oceanic lithosphere based on geophysical observations

As mentioned in the previous section, serpentinization of the oceanic lithosphere plays an important role in the deep life, the global water cycle, and seismic activity and volcanism at subduction zones. The structure of the oceanic lithosphere and the spatial distribution of serpentinized rocks were interpreted from velocity structures observed using seismic tomography. Seismic tomography is a method of determining the spatial distribution of seismic velocities in the subsurface by examining the arrival times of a large number of seismic waves. By comparing the seismic tomography velocity structure with the p-wave velocity (V_p) and s-wave velocity (V_s) of rocks measured in laboratory experiments. The type of rock and the structure of the oceanic lithosphere can be estimated by seismic tomography.

The seismic velocity structure of the oceanic lithosphere can be divided into three distinct structures. The uppermost "first layer" is composed of sediments. The underlying "second layer" has ~1.5-2.0 km thickness, which is thought to correspond to the upper crust, has a V_p of 4.1-6.5 km/s and is thought to be composed of pillow lava and basalt (Hyndman and Drury, 1976; Whitmarsh, 1978; Wilson *et al.*, 2006). The seismic wave velocities in the upper part of the second layer are about one-third to one-half of the laboratory measured values for intact basalt rock due to high porosity (Hyndman and Drury, 1976). Seismic wave velocities in the second layer increase with depth, which is explained by a decrease in porosity (Hyndman and Drury, 1976; Whitmarsh, 1978). The "third layer" located below the second layer, is considered to correspond to the lower crust. It has a faster V_p of 6.5-7.1 km/s than the upper crust (Christensen, 1972). The higher seismic velocities than in crustal rocks (V_p = 4.1 - 7.1 km/s) may represent rock structures associated with the Crust-Mantle transition zone, where gabbroic rock and dunite alternate (Tamura *et al.*, 2022), or serpentinized mantle (Christensen, 2004). Below layer 3, the mantle is thought to consist of a mantle with a V_p of ~8.2 km/s (Christensen, 1996).

The thicknesses of the second and third layers, which are thought to comprise the oceanic crust, are known to vary with the spreading rate of the ridge (Fig. 1.2). Ridges are classified according to their spreading rates as fast-spreading ridges (~80-180 mm/yr), intermediate-spreading ridges (~55-70 mm/yr), slow-spreading ridges (20-55 mm/yr), and very slow-spreading ridges (< ~12 mm/yr) (Dick *et al.*, 2003). The crust of the slow-spreading ridges is thinner and more discontinuous than that of the fast-spreading ridges because mantle melting to form oceanic crust is limited by cooling caused by thermal conduction (Cannat, 1993).

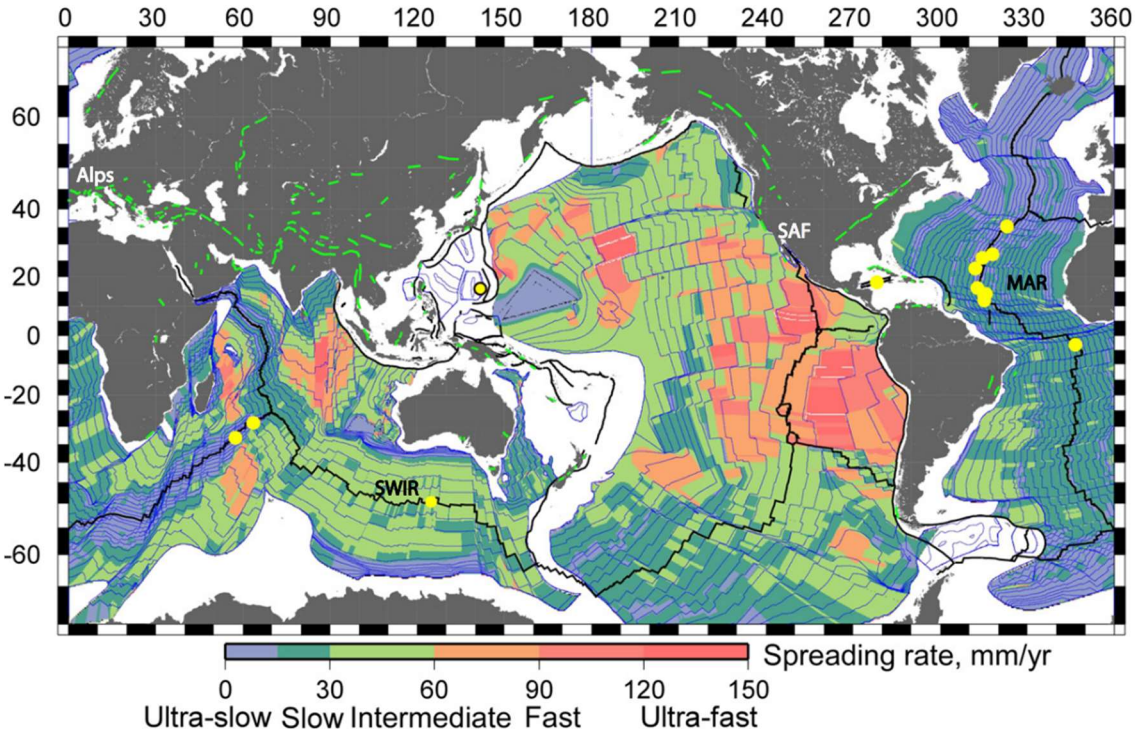

Fig. 1.2. Global map of the spreading rate of the oceanic lithosphere (Guillot et al., 2015a).

Interpretation of seismic tomography is largely based on comparisons with rock samples obtained by ocean drilling. However, no ocean drilling has penetrated more than 2 km through the ocean crust (Dick *et al.*, 2006; Michibayashi *et al.*, 2019). An ocean drilling project aimed at drilling the crust-mantle boundary, penetrating the 5-6 km thick crust was proposed more than 60 years ago to drill directly into the Moho, but has not yet been accomplished due to technical difficulties (Michibayashi *et al.*, 2019; Tamura *et al.*, 2022). Due to these limitations of observation techniques, the nature of the oceanic lithosphere, especially the lower crust to the upper mantle has not been fully understood. On the other hand, characteristics of serpentinization reaction is controlled by temperature pressure and mineral combinations. Thus, it is required that unravel the nature of the crust-mantle of the oceanic lithosphere for better understand of the serpentinization process.

1.2.2. Oman Ophiolite: the paleo-oceanic lithosphere

Ophiolite studies have been conducted to investigate rocks deep in the oceanic lithosphere, where ocean drilling is associated with technical difficulties. Ophiolites are geological bodies that have been exposed on continents from the rocks that comprised the ocean floor, providing direct access to rocks from the oceanic lithosphere from the crust to the mantle. The Oman Ophiolite is located at the southeastern tip of the Arabian Peninsula and is exposed over an area of more than ~20,000 km^2. The Oman Ophiolite has a typical stratigraphic sequence of the oceanic lithosphere from pillow lava to the upper mantle and has been well studied by researchers around the world. The Oman ophiolite consists of a crust composed of pillow lava, sheeted dikes, and gabbroic rock, and a mantle peridotite (Boudier *et al.*, 1996; Boudier and Coleman, 1981a, 1981b; Boudier and Nicolas, 1995; Garbe-Schönberg *et al.*, 2022; Hopson *et al.*, 1981; Koepke *et al.*, 2022; Nicolas *et al.*, 1988, 1996, 2000; Nicolas and Boudier, 2015). Based on U-Pb dating of zircons in crustal rocks, the Oman ophiolite is thought to be formed at a moderate to fast expanding ridge (Nicolas *et al.*, 2000; Rioux *et al.*, 2012). It is generally accepted that the Oman ophiolite is a oceanic lithospheric sequence that formed at an oceanic fast-expanding ridge, similar to the stratigraphic structure of the Pacific crust, and has been widely accepted by ocean drilling and seismic velocity structure observations (Christensen, 1978; Nicolas *et al.*, 1996).

The Oman ophiolite formed at the ridge, and with the closure of the Tethys Sea, it was uplifted above the other ocean plate and experienced a tectonic setting in the upper plate of subduction zone (Fig. 1.3). It then over thrusted the top of the subducting oceanic lithosphere and was lifted onto the continental crust of the Arabian Peninsula. The formation process of ophiolites, not just the Oman ophiolites, requires subduction process, first as subduction within the ocean, followed by short-time continental subduction beneath the ophiolite (Ninkabou *et al.*, 2021). Contact metamorphic rocks found in the lowermost part of the mantle section, known as "metamorphic sole", are thought to be traces of subduction processes during the formation of the Oman ophiolite. Metamorphic soles are thought to have formed at the onset of subduction in the ocean (Cowan *et al.*, 2014; Hacker, 1991, 1994; Hacker *et al.*, 1996), and their metamorphic ages range from 96.16-94.82 Ma, which is close to the crustal crystallization age of 96.12-95.50 Ma (Rioux *et al.*, 2016). This suggests that the overthrust of the Oman ophiolite onto the oceanic plate began shortly after the formation of the crustal section (Rioux *et al.*, 2012, 2013). Peak metamorphic temperature and pressures of the metamorphic sole reached 900 °C, 1.1-1.3 GPa (Cowan *et al.*, 2014), followed by cooling and evolution to steady-state thermal evolution of subduction process (Agard *et al.*, 2016). Subduction of continental crust occurred at ~81-77 Ma (Garber *et al.*, 2020), and after that the Oman ophiolite settled onto the Arabian Peninsula. In these formation histories, the Oman ophiolite records water-rock reactions not only on the seafloor, but also in subduction zones and on land alterations. Therefore, in order to understand the seafloor water-rock reactions of ophiolite rocks, it is necessary to separate them into individual stages.

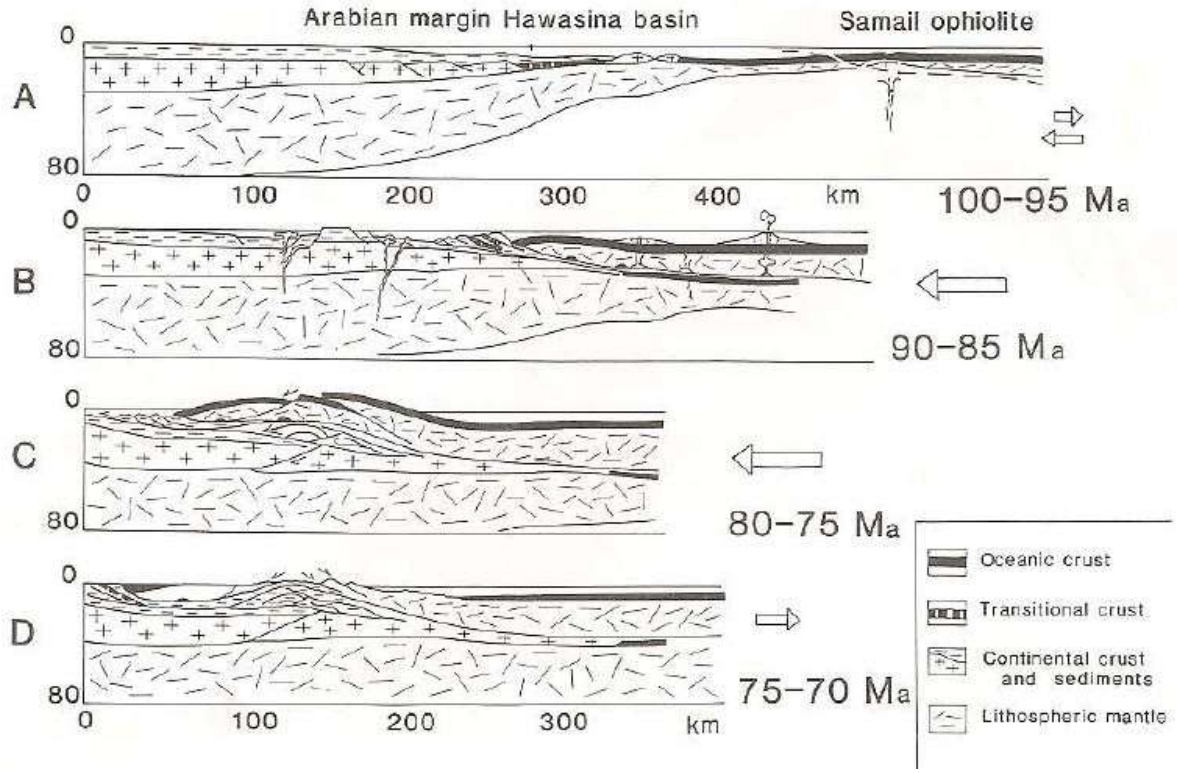

Fig. 1.3. Formation history of the Oman Ophiolite (Michard *et al.*, 1991).

1.3. Geophysical evidence for serpentinization

1.3.1. Seismic velocity of serpentinite

Insufficient constraints on the water content of the mantle of the oceanic lithospheric mantle due to technical limitations in ocean drilling and physical observations (Hyndman et al., 2015) lead to a wide range in estimates of the amount of water transported into the Earth's interior at subduction zones (Hacker, 2008; Hatakeyama *et al.*, 2017; Parai and Mukhopadhyay, 2012; Rüpke *et al.*, 2004; Schmidt and Poli, 1998; Van Keken *et al.*, 2011). Serpentine plays an important role as a water carrier because it contains a lot of H_2O (~13 wt. %) in the crystal structure (Schmidt and Poli, 1998). Estimating the amount of water transported into the Earth's interior requires accurate an estimate of the extent of serpentinization in the oceanic lithosphere. However, it is difficult to accurately estimate the degree of serpentinization of the oceanic lithosphere from the seismic velocity structure alone, except in cases of low serpentinization (~30% maximum). The V_p of 0-30% serpentinized peridotite is 7.4-8.2 km/s, which can be distinguished from the V_p of the oceanic crust (4.1-7.1 km/s). A slightly lower V_p than that of the mantle is interpreted to result in a low degree of serpentinization of ~10-20% (Fujie *et al.*, 2013; Grevemeyer *et al.*, 2018b; Ranero *et al.*, 2003; Van Avendonk *et al.*, 2011). However, the V_p of ~30-100% serpentinized peridotite is 4.5-7.0 km/s, which overlaps with the V_p of oceanic crust (4.1-7.1 km/s), making it difficult to distinguish between crust and serpentinized mantle (Horen *et al.*, 1996).

When the degree of serpentinization is high, it is difficult to constrain the degree of serpentinization from Vp alone. Therefore, the ratio of P-wave velocity to S-wave velocity (Vp/Vs) is sometimes used as an indicator to distinguish between mantle serpentinites and crustal rocks (Christensen, 2004; Grevemeyer *et al.*, 2018b; Horen *et al.*, 1996; Wang *et al.*, 2022b). Highly serpentinized peridotites (~30-40% or more) have Vp/Vs greater than 1.9, and Vp/Vs = 1.8-2.2 serpentinites can be distinguished from crustal rocks (Vp/Vs = 1.75-1.85) (Christensen, 2004; Horen *et al.*, 1996). For these reasons, Vp/Vs is sometimes used as an indicator to assess the degree of serpentinization (Grevemeyer *et al.*, 2018b). However, for technical reasons, it is not suitable for recording S-waves. Therefore, observations of Vp/Vs are not common.

1.3.2. Locations and degree of serpentinization of oceanic lithosphere

Seismic tomography observations suggest that serpentinization reactions occur mainly at: (1) near the central ridge of the seafloor (Mark *et al.*, 2023), (2) bending faults of the outer rise region of the trench (Fujie *et al.*, 2013; Grevemeyer *et al.*, 2018b; Ranero *et al.*, 2003; Van Avendonk *et al.*, 2011), (3) ultra-slow to slow spreading ridge axes (Grevemeyer *et al.*, 2018a), (4) transform faults (Rüpke and Hasenclever, 2017; Wang *et al.*, 2022b), (5) detachment faults (Tao *et al.*, 2020), and (6) subducting oceanic plate (Merdith *et al.*, 2023). Numerical simulations (Hasenclever *et al.*, 2014) and petrological observations of ophiolites (Bosch *et al.*, 2004; Boudier *et al.*, 2005) suggest that hydrothermal fluid flow is also present at some distance from the ridge axis in the fast-spreading oceanic lithosphere. Geochemical signatures of hydrothermal vent fluids and a numerical simulation of hydrothermal circulation suggest that hydrothermal fluids may circulate along faults to depths of ~10 km near the slow spreading ridge axis (Tao *et al.*, 2020). Therefore, serpentinization may be occurring at greater depths than observed, but the actual nature of this process is not known.

The degree of serpentinization of oceanic lithosphere is controlled by tectonic factors (e.g., formation of detachment faults at the seafloor and bending faults near subduction zones), age, temperature, spreading rate, and sedimentation (Grevemeyer *et al.*, 2007; Lefeldt and Grevemeyer, 2008; Ranero *et al.*, 2005; Ranero and Sallarès, 2004). The Pacific Plate, an example of an oceanic lithosphere formed on a fast-spreading axis, is thought to be serpentinized by 10-20% of the mantle in the case of the coolest and oldest Mariana Trench (150 Ma) and Kuril Trench (130 Ma) (Cai *et al.*, 2018; Fujie *et al.*, 2013; Mark *et al.*, 2023). In the Chilean Trench, plates of different ages are subducted at different locations (0 Ma at 46 °S and 50 Ma at 18 °S; Contreras-Reyes and Osses, 2010). At 45-46 °S in the Chilean Trench where the young age (~6 Ma) of plates are subducting (Scherwath et al. 2009), the subducting oceanic plates do not show serpentinization trends. At ~46.5 °S of the Chile Trench, where the slightly older 18.5 - 10 Ma oceanic plate is subducting, the oceanic mantle is estimated to be 0-9% serpentinized (Contreras-Reyes *et al.*, 2008). In the Nicaragua Rift, where the ~24 Ma Cocos Plate is subducting, 3-4 km of the upper mantle is serpentinized up to 24% (Ivandic *et al.*, 2010). In the coolest and oldest Mariana Trench (150 Ma) and Kuril Trench (130 Ma), the mantle is serpentinized up to 10-20% (Mark et al., 2023; Cai et al., 2018; Fujie et al., 2013). The serpentinization reactions are can occur along subducting plate bending faults (Mark et al., 2023; Cai et al., 2018; Fujie et al., 2013; Contreras-Reyes et al., 2007).

In the case of slow-spreading axes, the crust is discontinuous and thin, resulting in mantle rock exposure and a high degree of serpentinization at depths of 2-4 km (Grevemeyer *et al.*, 2018b). Schlindwein & Schmid (2016) show that seismic observations from the Mid-Cayman Spreading Center in the Caribbean, a slow spreading ridge axis, indicate that mantle rocks are serpentinized as far as 30 km below the seafloor (Schlindwein and Schmid, 2016). However, reanalysis suggests that the serpentinization reaction did not proceed to that depth (Grevemeyer *et al.*, 2019). If serpentinization is a continuous process on the seafloor, then the thickness of layer 3 in the seismic velocity structure should

increase with plate age. However, no reliable observations have been reported showing that the thickness of the third layer increases with age due to the progress of serpentinization reactions. Several studies in the 1970s reported that the thickness of the oceanic crust increases with age (Christensen and Salisbury, 1975; Goslin *et al.*, 1972; Lewis and Snydsman, 1979). However, subsequent re-analysis showed that the increase in the layer 3 thickness was an artifact of the data processing (McClain and Atallah, 1986). In addition, crustal thickness is also thought to be related not only to age but also to other factors such as mantle temperature (Grevemeyer et al., 2018). Thus, the analysis of the seismic velocity structure can lead to different conclusions depending on the data processing. In addition, the resolution of seafloor seismic tomography is a few hundred meters, which does not provide detailed geological structures (Cannat *et al.*, 2010). P-waves also vary with factors such as porosity, structure and temperature, making their interpretation even more complex.

1.4. Temperature-Pressure condition and kinetics of serpentinization

A combination of natural sample observations, experimental studies, and theoretical modeling is important to understand the rate and spatial extent of the serpentinization. The type of products and extent of serpentinization controlled by the availability of water and the chemistry of the starting mineral and solution. Factors controlling the serpentinization are temperature and pressure conditions, availability of water, and chemistry of starting minerals and solution. The temperature and pressure conditions of naturally occurring serpentinization reactions have been estimated based on the results of laboratory experiments and analyses using oxygen isotopes. In addition, water supply is necessary for the serpentinization reaction to proceed, and the formation of cracks is important to make fluid pathways. The following sections review previous studies focusing on the temperature-pressure state and kinetics of serpentinization based on natural sample observations, laboratory experiments, and theoretical modeling.

1.4.1. Variety of serpentine minerals in natural samples

Several types of serpentine minerals are observed in natural serpentinites. The type of serpentine mineral is basically thought to reflect the formation temperature, pressure, chemical composition of the solution, and other factors. Therefore, a classification of serpentine mineral types is sometimes useful for a rough estimate of the formation conditions. Three main types of serpentines occur naturally: lizardite, chrysotile, and antigorite (Fig. 1.4). In addition, polygonal serpentine and polyhedral serpentine can be distinguished (Andreani *et al.*, 2008). However, polygonal serpentine and polyhedral serpentine contain structures similar to both lizardite and chrysotile, making them difficult to distinguish them from lizardite and chrysotile (Andreani *et al.*, 2008; Enju *et al.*, 2023). Serpentine is composed of a variety of crystal structures, depending on the way of the assemble of the base polyhedra. Lizardite is characterized by flat layers, chrysotile by curled layers, antigorite by alternating wavy layers, and polygonal serpentine by flat kinked layers. The curling of chrysotile is caused by elastic strain due to a mismatch in the lattice constants of the T and O sheets (Demichelis *et al.*, 2016). Antigorite is slightly richer in silica than lizardite and chrysotile, because they have slightly different chemical compositions. Thus, antigorite is classified as a serpentine mineral group, but it is not a polymorph of lizardite and chrysotile (Wunder *et al.*, 2001). This difference in chemical composition is due to the wavy crystal structure characteristic of antigorite.

Antigorite is commonly observed in metamorphic bodies that experienced a subducting slab or mantle wedge environment at subduction zones with maximum metamorphic temperatures and temperatures between 300-640 °C, 0.6-2.2 GPa (Auzende *et al.*, 2002; Hermann *et al.*, 2000; Hirauchi *et al.*, 2021; MORI *et al.*, 2019; Okamoto *et al.*, 2021; Padrón-Navarta *et al.*, 2012; Schwartz *et al.*, 2013; Tulley *et al.*, 2022). Antigorite has also been found in dredging and drilling samples from the seafloor, although it is relatively rare compared to the occurrence of lizardite/chrysotile (Murata *et al.*,

2009; Rouméjon *et al.*, 2019). The conditions for antigorite formation on the seafloor are controversial. Serpentinized peridotite with antigorite crystals growing to cut lizardite/chrysotile veins has been found in samples from the Mariana Forearc, and the complex process of serpentinized peridotite in shallow mantle wedges moving to depth and precipitating antigorite with increasing temperature and then returning to the surface is thought to record a complex process of crustal deformation (Murata *et al.*, 2009). Such a complex formation path may be caused by the transport of subducted serpentinite to the surface by ascending serpentinite diapirs in the Mariana Forearc (Maekawa *et al.*, 2004). On the other hand, antigorite veins associated with talc in drilling samples from Hess Deep (East Pacific Rise) and Atlantis Massif (Mid-Atlantic Ridge, 30 °N) and dredge samples from the Southwest Indian Ridge (62 °-65 °E) are thought to have been formed by the addition of silica and as a result of recrystallization from lizardite/chrysotile due to the influx of Si-rich fluids, rather than by temperature and pressure increases (Rouméjon *et al.*, 2019).

Chrysotile is a nanotube-shaped serpentine with an outer diameter of 22-27 nm and an inner diameter of 7-10 nm (Belluso *et al.*, 2017; Whittaker, 1957). It is often produced mainly in veins in the last stage of serpentinization reactions (Andreani *et al.*, 2007; Rouméjon *et al.*, 2019) and is poor in Al and Fe^{3+} (Andreani et al., 2007; Guillot et al., 2015b; O'Hanley and Dyar, 1998). It also often occurs with lizardite (Capitani *et al.*, 2021; Viti and Mellini, 1998), antigorite (Auzende *et al.*, 2002; Viti and Mellini, 1998), and polygonal serpentine (Andreani *et al.*, 2007; Tarling *et al.*, 2018, 2021).

Lizardite predominantly comprise serpentine in seafloor dredge and ocean drilling samples and ophiolites, often occurring with chrysotile and polygonal serpentine (Andreani *et al.*, 2013; Aupart *et al.*, 2021; Bach *et al.*, 2006; Hopkinson *et al.*, 2004; Klein *et al.*, 2014; Oufi *et al.*, 2002; Schwartz *et al.*, 2013). Based on oxygen isotope ratios, formation temperature of lizardite are estimated to be around 120-270 °C (Klein *et al.*, 2014). The formation pressure is not well constrained but is thought to be less than 400 MPa (Schwartz *et al.*, 2013).

Polygonal serpentine has a crystal structure of a tubular shape with polygonal cross section, it can be larger than chrysotile with an outer diameter of >100 nm. It forms in relatively low temperature environments (T < 200-300 °C) and is thought to require open space and trivalent cations such as Al^{3+} for its formation (Andreani *et al.*, 2008). They may also occur with chrysotile veins in the later stages of serpentinization reactions (Andreani *et al.*, 2007; Tarling *et al.*, 2018, 2021).

As introduced so far, a diversity of serpentine minerals is observed in the natural samples. As described next, experimental studies have been conducted under various starting materials, solution compositions, and pressure-temperature conditions to investigate the factors controlling the serpentinization reaction.

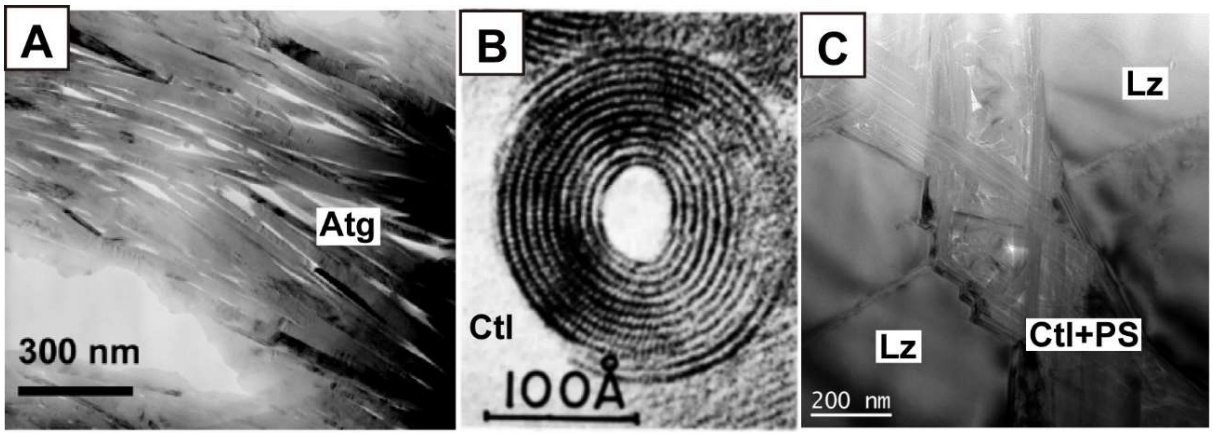

Fig. 1.4. TEM images of serpentine minerals. (A) Blade shape antigorite crystals (Ribeiro Da Costa *et al.*, 2008), (B) Chrysotile (Yada, 1971), (C) Lizardite with chrysotile and polygonal serpentine (Capitani *et al.*, 2021).

1.4.2. Experimental studies on serpentinization

Serpentine minerals are stable under a wide range of temperature and pressure conditions. Laboratory experiments at various temperature and pressure conditions have shown that different types of serpentine form under different temperature and pressure conditions (Lafay *et al.*, 2012; Malvoisin *et al.*, 2012a; Marcaillou *et al.*, 2011; McCollom *et al.*, 2020; Nakatani and Nakamura, 2016, 2019; Normand *et al.*, 2002; Ogasawara *et al.*, 2013; Okamoto *et al.*, 2011; Oyanagi *et al.*, 2018, 2020; Seyfried *et al.*, 2007; Seyfried and Dibble, 1980; Wunder *et al.*, 2001; Wunder and Schreyer, 1997; Yada and Iishi, 1977). Fig. 1.5. shows compile plot of the types of serpentines produced by the laboratory experiments under various pressure-temperature conditions. Antigorite is formed at temperature of 350-650 °C and pressure of 0.5 - 5.0 GPa. Lizardite is formed at temperature of 230-400 °C and pressure of 2.8 MPa - 1.3 GPa. Al-rich serpentine forms when starting material contains Al-rich minerals (Oyanagi *et al.*, 2018). At high-temperature and high-pressure conditions (500-580 °C, 1.3 GPa), orthopyroxene predominantly replaces Al-rich lizardite (Al_2O_3 = ~10 wt. %) rather than olivine (Nakatani and Nakamura, 2019). Chrysotile is formed at pressure-temperature condition covering the antigorite and lizardite forming condition (temperature pressure: 150-600 °C, 0.5 MPa - 5.0 GPa). Chrysotile occurs over the antigorite and lizardite temperature-pressure ranges and is can found with these minerals (formation temperature and pressure: 150-600 °C, 0.5 MPa - 5.0 GPa). In low-temperature condition, chrysotile predominantly precipitates than lizardite when solutions with high pH are used (Lafay *et al.*, 2018; Yada and Iishi, 1977) or when the small particle size (~5 um) (Malvoisin *et al.*, 2012a). High pH alkaline solutions decrease the rate of olivine dissolution (Oelkers *et al.*, 2018), but also decrease the solubility of serpentine, so that the solution approaches serpentine saturation (Wimpenny *et al.*, 2010). In the case of smaller grain sizes, the solution becomes supersaturated due to the higher rate of olivine dissolution (Malvoisin *et al.*, 2012a). Based on these facts, chrysotile is considered to precipitate predominantly at higher supersaturation than lizardite (Malvoisin *et al.*, 2012a; Normand *et al.*, 2002).

Taken together, these experimental results indicate that lizardite forms at lower temperatures than antigorite. Chrysotile can form together with antigorite and lizardite. These results support the

hypothesis of Evans (2004) that chrysotile may be a metastable phase. The tendency for antigorite to form at higher temperatures and pressures than lizardite is consistent with laboratory experiments and natural samples. Integrating the results of laboratory experiments and natural samples, lizardite forms predominantly at temperatures and pressures of 120-400 °C, <0.4 GPa; increasing Al content may extend the stability region of lizardite (Caruso and Chernosky, 1979). Antigorite forms at temperature and pressure conditions of 300-640 °C, 0.6 - 2.2 GPa. Chrysotile is a possible metastable phase and may form over the temperature and pressure conditions of lizardite and antigorite.

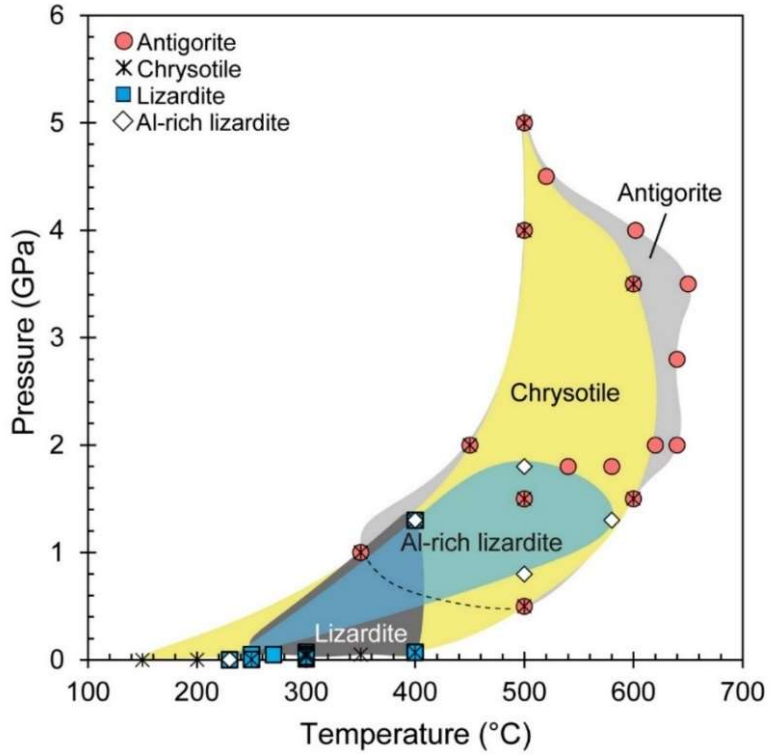

Fig. 1.5. Serpentine minerals produced in experimental studies under various pressure-temperature (PT) conditions (Lafay *et al.*, 2012; Malvoisin *et al.*, 2012a; Marcaillou *et al.*, 2011; Nakatani and Nakamura, 2016, 2019; Normand *et al.*, 2002; Ogasawara *et al.*, 2013; Okamoto *et al.*, 2011; Oyanagi *et al.*, 2018, 2020; Seyfried *et al.*, 2007; Seyfried and Dibble, 1980; Wunder *et al.*, 2001; Wunder and Schreyer, 1997; Yada and Iishi, 1977). The plots show antigorite (red circle), chrysotile (asterisk), lizardite (blue box), and Al-rich lizardite (diamond). The regions colored in light gray, yellow, dark gray, and blue show antigorite, chrysotile, lizardite, and Al-rich lizardite, respectively. Chrysotile is widely produced across wide PT conditions of lizardite and antigorite. Al-rich lizardite is produced with Al-rich mineral (e.g. plagioclase) or by replacing orthopyroxene at high PT conditions (Nakatani and Nakamura, 2016, 2019).

1.4.3. Reaction kinetics of serpentinization

Previous studies on reaction rates and rate-limiting processes of serpentinization reactions are reviewed. The reaction rate of serpentinization has been studied in detain by hydrothermal experiments using powdered olivine ± pyroxene at temperatures of ~200-300 °C. Olivine has a faster reaction rate than pyroxene at temperatures of ~200-300 °C (Andreani *et al.*, 2007; Coleman and Keith, 1971; Klein *et al.*, 2013; Martin and Fyfe, 1970; Mével, 2003), but at higher temperatures > ~400 °C, pyroxene is predominantly serpentinized than olivine (Nakatani and Nakamura, 2016, 2019). Serpentinization reactions exhibit a bell-shaped temperature dependence with maximum reaction rates around 250-300 °C (Fig. 1.6) (Malvoisin *et al.*, 2012a; Martin and Fyfe, 1970; Wegner and Ernst, 1983). The reaction rate of antigorite, which is thought to form at higher temperatures, has not been well studied due to experimental difficulties.

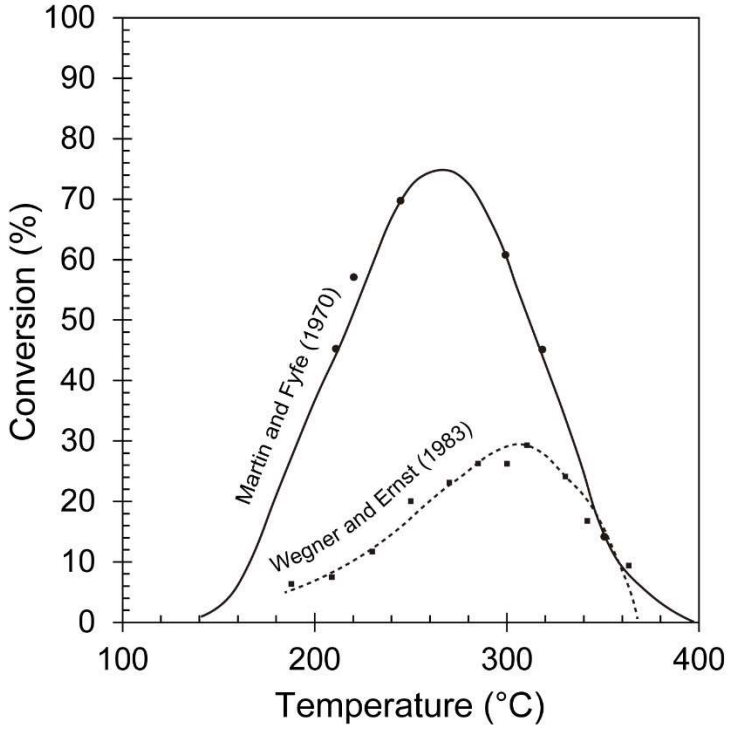

Fig. 1.6. Experimental conversion (%) versus temperature for the olivine-H_2O hydration reaction (After Martin and Fyfe., 1970; Wegner and Ernst., 1983).

The rate-limiting step of the serpentinization reaction and the type of serpentine mienral produced in hydrothermal experiments using olivine powder depend on the grain size of the starting material (Malvoisin *et al.*, 2012a). When the grain size is relatively large (5-150 μm), the rate-limiting step is the dissolution of olivine, and lizardite is mainly produced. On the other hand, if the grain size is small (< 5 μm) and the reaction surface area is large, the rate-limiting step is the precipitation reaction of serpentine. In addition, chrysotile is formed instead of lizardite.

Serpentinization is a water consuming reaction. Therefore, the reaction requires continuous

water supply. The results of several hydrothermal experiments show that the rate of serpentinization is limited more by the water supply than by the rate of olivine dissolution or the rate of serpentine precipitation. Hydrothermal experiments (300°C, 8.6 MPa) using powdered olivine with a grain size of 50-63 um showed ~80% reaction in ~2000-12000 hours (Malvoisin *et al.*, 2012a). On the other hand, hydrothermal experiments using solid samples, which are more realistic to the natural conditions, show that the reaction rate is ~30-100 times slower than the experiment using powdered olivine. Hydrothermal experiments using fresh olivine (dunite, harzburgite) core samples ~7 mm in diameter and ~4 mm in height (300 °C, 35 MPa) showed reactions of 1.8-5.5% in 7680-13176 hours (Klein and Le Roux, 2020). Hydrothermal experiments with sintered olivine aggregate with porosity of 1-10% (300°C, 0.5 MPa) showed that for ~1% porosity, 1.6% reaction required 1652 hours and for ~10% porosity, 2.7% reaction required 6956 hours (Malvoisin and Brunet, 2014). The lower reaction rate compared to experiments with powder samples is due to limited water availability and smaller reaction surface area (Klein and Le Roux, 2020; Malvoisin and Brunet, 2014). In addition, Silica activity during the reaction is also an important factor in the serpentinization reaction. Results of hydrothermal experiments using olivine and silica-rich minerals suggest that silica supply promotes serpentinization of olivine (Ogasawara *et al.*, 2013). In summary, serpentinization reaction mainly controlled by (1) temperature, (2) water supply, and (3) silica activity.

1.4.4. Volume change and formation of the fluid pathways

Faults, which are large-scale fluid flow pathways on the kilometer scale, are formed by tectonic processes (Buck *et al.*, 2005; Tauzin *et al.*, 2017; Tucholke and Lin, 1994). Normal faults near the ridge axis (de Martin *et al.*, 2007; Zihlmann *et al.*, 2018), transform faults (Früh-Green *et al.*, 2003), and bending faults in the outer ridge region (Faccenda *et al.*, 2009; Hatakeyama *et al.*, 2017; Ranero *et al.*, 2003) allow fluid supply to the deeper parts of the oceanic lithosphere. On the other hand, it has been suggested that micrometer-scale crack (microcrack) networks may be important for pervasive and homogeneous serpentinization (Boudier *et al.*, 2005; Jamtveit *et al.*, 2008; Malvoisin *et al.*, 2017; Plümper *et al.*, 2012; Rouméjon *et al.*, 2014). These microcracks are thought to be formed by the following factors: (1) thermal stresses associated with slow cooling (Boudier *et al.*, 2005; Cooper and Simmons, 1977; Nicolas, 2003), (2) tectonic stress (Kranz, 1983), and (3) reaction-induced stress (Jamtveit *et al.*, 2008; Kelemen and Hirth, 2012), or a combination of these processes (Roumejion and Cannat., 2014). However, it is not obvious which of these crack formation mechanisms is most predominant.

Serpentinization is a dynamic process resulting from a complex interaction of fracturing, fluid flow, and chemical reactions. Mass balance calculations indicate that serpentinization is not accompanied by mass transport of major elements, suggesting that the increase in solid phase volume occurs before and after the reaction (Mével, 2003). Volume changes in serpentinization reactions can cause topographic changes and fault activation (de Martin *et al.*, 2007; Germanovich *et al.*, 2012). Evidence of volumetric change can be observed in the rock microstructures at various scales. Micrometer- to centimeter-scale mesh textures are commonly observed in partially serpentinized peridotites (Fig. 1.7) (Jamtveit and Austrheim, 2010; Plümper *et al.*, 2012). Hierarchical fracture patterns (Iyer *et al.*, 2008) and "Frankenstein" cracks (Evans *et al.*, 2020) are also be observed in the outcrops. Such geometric patterns are thought to be caused by local stresses resulting from volume changes in the solid phase during mineral hydration reactions (Jamtveit *et al.*, 2000, 2009; Malthe-Sørenssen *et al.*, 2006; Malvoisin *et al.*, 2017; Okamoto and Shimizu, 2015; Uno *et al.*, 2022; Zheng *et al.*, 2018). Reaction Gibbs energy of the reaction is the driving force for the crack formation associated with the volume change of the reaction. The pressure maximum due to crystallization can be written using the reaction Gibbs energy (ΔG_r) and solid phase volume change (ΔV_s) as (Kelemen and Hirth, 2012).

$$P' = -\frac{\Delta G_r}{\Delta V_s} \tag{1.1}$$

The theoretical estimate of the maximum reaction-induced stresses from olivine serpentinization reaches a few hundred MPa to a few GPa, which sufficient to produce cracks in rocks under several kilometers to tens of kilometers underground (Kelemen and Hirth, 2012; Malvoisin *et al.*, 2017). Recently, it is reported that gigapascal level local stress induced by hydration reactions with increasing volume have

been found in natural samples (Plümper *et al.*, 2022). Crack formation promotes reaction progress because it increases the reaction surface area and provides new fluid flow pathways (Kelemen and Hirth, 2012; Okamoto and Shimizu, 2015; Plümper *et al.*, 2012). Such reaction-driven fracturing is likely to occur when reaction rates are fast relative to mass transfer (Shimizu and Okamoto, 2016) and stress relaxation (Falk and Kelemen, 2015). On the other hand, for volume-increasing reactions, including serpentinization reactions, the reaction may cause fracture closure due to volume increase. Thus, it is generally difficult to predict whether these opposing effects will accelerate or inhibit the progress of the reaction.

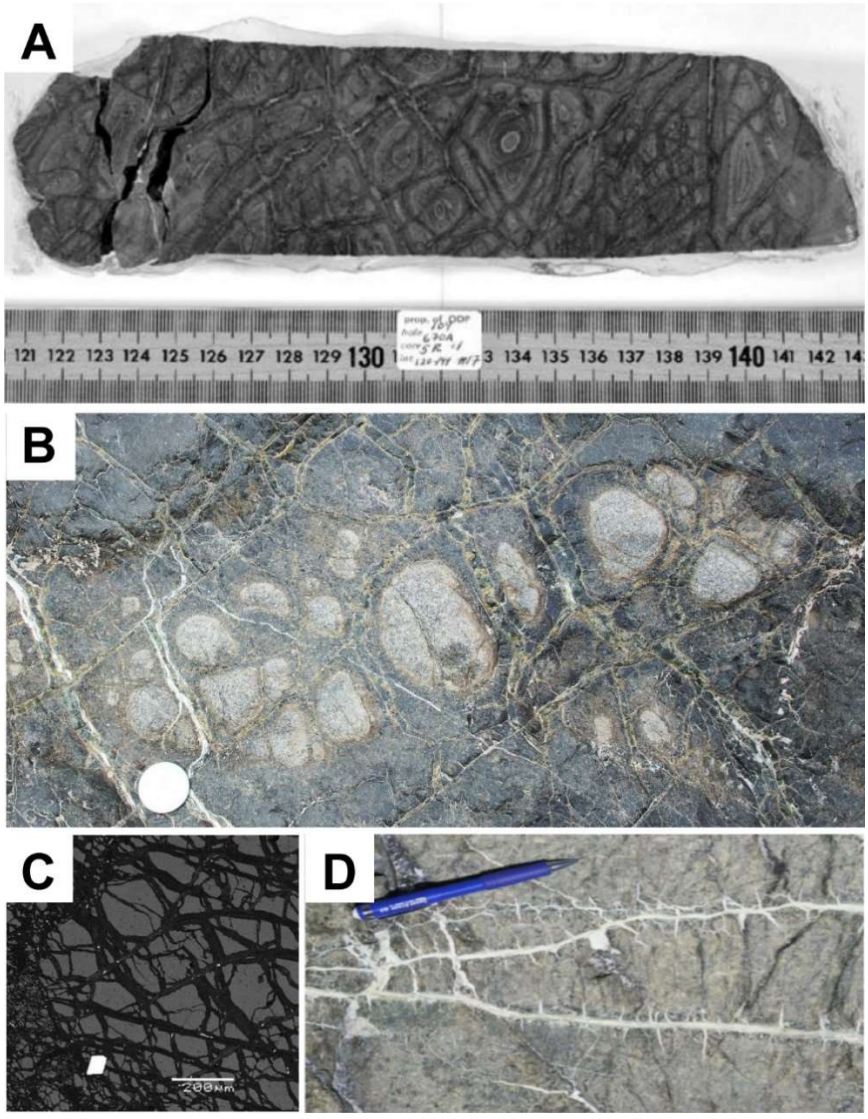

Fig. 1.7. Geometric patterns in serpentinites. Centimeter scale of mesh like texture in serpentinized peridotite from the Mid-Atlantic Ridge (Jamtveit & Austrheim, 2010) (A) and Oman ophiolite (Photo taken January 2023) (B). (C) Micrometer scale mesh texture in partly serpentinized peridotite from the Leka ophiolite complex (Jamtvein & Austrheim, 2010; Iyer et al., 2008). (C) ”Frankenstein” texture developed in partly serpentinized peridotite from the Oman ophiolite (Evans *et al.*, 2020).

1.4.5. Numerical modeling

Several studies (Evans *et al.*, 2020; Jamtveit *et al.*, 2008; Kuleci *et al.*, 2017; Okamoto and Shimizu, 2015; Røyne *et al.*, 2008; Ulven *et al.*, 2014) have used mechanochemical modeling to investigate the complex behavior caused by hydrous reactions. Numerical simulations can reproduce the mesh-like texture found in natural serpentinites (Fig. 1.8A). Jamtveit et al. (2008) and Kuleci et al., (2017) show reactive mineral generate radial cracks in the surrounding non-reactive mineral (Fig. 1.8B), which similar to the natural sample observations (Jamtveit *et al.*, 2008) and laboratory experiment (Zheng *et al.*, 2018). However, the effect of crack closure due to stress is not considered in these numerical simulations. In these numerical simulations, fluid flow is treated as diffusion reduction or assumed to be a function of porosity in these numerical simulations. In order to consider the effect of crack closure by local stress change, Okamoto and Shimizu developed a 2-D DEM model that considers advection. This code is also used in this study.

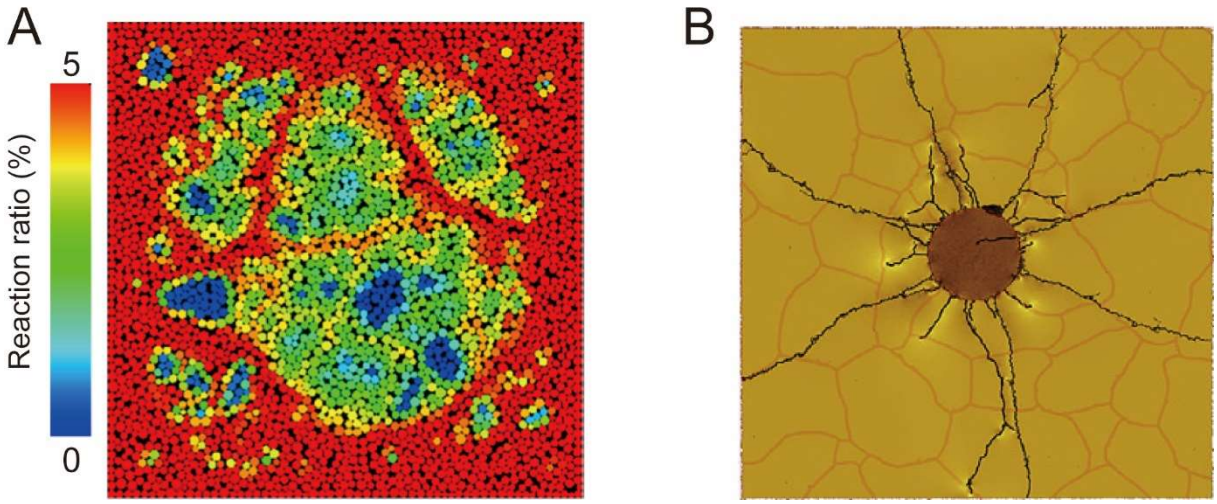

Fig. 1.8. Numerical simulations conduced in previous studies. (a)Mesh-like texture developed during volume increasing reaction (Okamoto and Shimizu, 2015). (b)Radial cracks produced in surrounding non-reactive materials (Kuleci *et al.*, 2017).

1.4.6. Hydrogen production during serpentinization

As mentioned at the beginning (1.1. Significance of serpentinization), hydrogen production during serpentinization reaction plays an essential role in the deep biosphere and in early life on Earth. In the serpentinization reaction, hydrogen is produced by the reduction of water when Fe^{2+} released into solution by the dissolution of primary minerals is oxidized to Fe^{3+}. The reduction of water by the oxidation of Fe^{2+} can be written as follows:

$$2Fe^{2+} + 2H_2O = 2Fe^{3+} + 2OH^- + H_2 \qquad (R1.3)$$

Since the Fe^{3+} produced during this process is incorporated into secondary minerals such as serpentine and magnetite, the amount of hydrogen produced can be estimated by examining the amount of Fe^{3+} contained in these minerals. The partitioning of iron determines the amount of hydrogen produced by serpentinization reactions into the product minerals and the redox states. Serpentinization reactions produce mainly serpentine, brucite, magnetite, and talc; in the absence of addition or removal of elements except H_2O and $SiO_{2,aq}$, the serpentinization reaction in the Mg-Fe-H_2O-SiO_2 system can be written as follows:

$$\begin{aligned}(\mathrm{Mg,Fe^{2+}})_2\mathrm{SiO_4}\ [\mathrm{Olivine}] + t\mathrm{H_2O}\ [\mathrm{water}] \pm u\mathrm{SiO_{2,aq}} \\ = v(\mathrm{Mg,Fe^{2+},Fe^{3+}})_3(\mathrm{Si,Fe^{3+}})_2\mathrm{O_5(OH)_4}\ [\mathrm{serpentine}] \\ + w(\mathrm{Mg,Fe^{2+}})(\mathrm{OH})_2\ [\mathrm{brucite}] + x\mathrm{Fe^{2+}Fe^{3+}}_2\mathrm{O_4}\ [\mathrm{magnetite}] \\ + y(\mathrm{Mg,Fe^{2+}})_3\mathrm{Si_4O_{10}(OH)_2}\ [\mathrm{talc}] + z\mathrm{H_2}\ [\mathrm{hydrogen}]\ (\mathrm{R1.4})\end{aligned}$$

The amount ratio and composition of each mineral varies depending on numerous factors such as temperature, pressure, silica concentration, and water-rock ratio (Fig. 1.9) (Klein *et al.*, 2009).

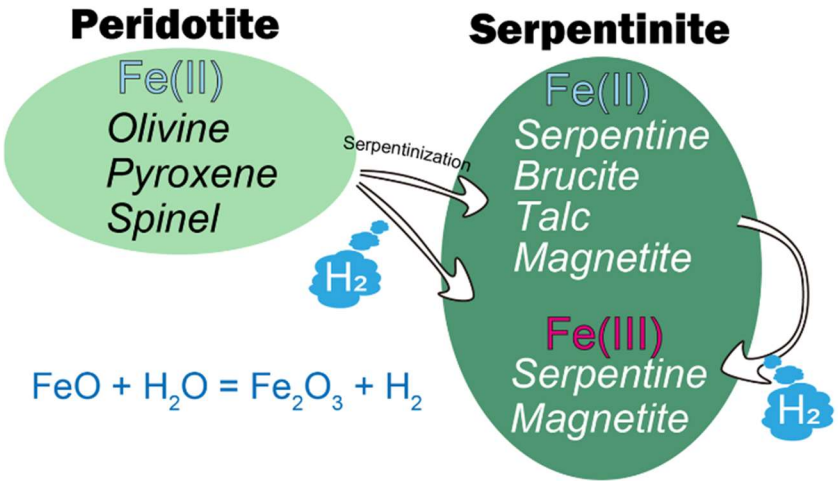

Fig. 1.9. Partitioning of iron in serpentinization reaction.

Serpentine and magnetite are key mineral for the hydrogen production. Serpentine and magnetite are the major Fe^{3+}-bearing minerals, and the amount of these minerals determines the amount of hydrogen produced. Several studies have emphasized the importance of magnetite in hydrogen production during serpentinization (Bach *et al.*, 2006; Beard *et al.*, 2009; Katayama *et al.*, 2010; Malvoisin *et al.*, 2012b). On the other hand, it has been focused that serpentine also contains Fe^{3+} (Andreani *et al.*, 2013; Klein *et al.*, 2009). The Fe^{3+} in serpentine is important for hydrogen production under conditions where magnetite does not form (Klein *et al.*, 2014). However, it is not completely known redox state of iron in serpentine minerals. The formation of magnetite and serpentine is controlled by temperature and silica activity (Klein *et al.*, 2009). Based on a natural sample observation, Katayama et al. (2010) suggest that magnetite is formed under low silica activity (Katayama *et al.*, 2010). This is consistent with the absence of magnetite around orthopyroxene in experiments at 250 °C, 3.98 MPa in

the olivine±orthopyroxene-H_2O system (Ogasawara *et al.*, 2013; Okamoto *et al.*, 2011; Oyanagi *et al.*, 2018). The fact that the presence of several Fe^{3+}-bearing minerals, such as serpentine and magnetite, and their mass ratios vary depending on a variety of factors makes it difficult to understand hydrogen production during serpentinization. Thus, despite the many vigorous works of laboratory experiments (McCollom *et al.*, 2016, 2020, 2022) and thermodynamic modeling (Klein *et al.*, 2009; McCollom *et al.*, 2022; McCollom and Bach, 2009), hydrogen production and Fe^{3+} partitioning into serpentine and magnetite are not fully understood. Hydrogen production during serpentinization is often discussed in terms of the redox state of iron and magnetite as determined by bulk rock analysis (Albers *et al.*, 2021; Evans, 2008; Oufi *et al.*, 2002). This is because it is generally difficult to measure the local redox state of iron. The problem with bulk rock analysis is that it is difficult to know where (which mineral) Fe^{3+} iron is contained. It is also difficult to avoid the influence of weathered minerals, which can lead to overestimation of hydrogen production. The Fe^{3+} content in magnetite is determined stoichiometrically, serpentine has several end members and can have a variety of iron redox states. Because bulk analysis cannot examine the redox state of each mineral separately, it is not well understood how much Fe^{3+} serpentinite contains and what factors control the $Fe^{3+}/\Sigma Fe$ of serpentine.

The main factors controlling magnetite formation are (1) serpentinization temperature and (2) silica activity. With respect to magnetite formation processes, Klein et al. (2014) found that serpentinites formed above ~200 °C are enriched in magnetite based on temperatures derived from oxygen isotopic compositions of oceanic serpentinite samples collected at different locations(Klein *et al.*, 2014). In contrast, serpentinites formed below ~200 °C are enriched in Fe-rich brucite rather than magnetite. This result is consistent with low temperature (200 °C, 0.5 MPa) hydrothermal experiments on peridotite that produced Fe-rich serpentine (X_{Mg}=0.93, $X_{Mg}=Mg^{2+}/(Mg^{2+}+Fe^{2+})$, where Mg^{2+} and Fe^{2+} are in atoms per formula unit (a.p.f.u.)) and Fe-rich brucite (X_{Mg}=0.68) with only trace amounts of magnetite (Seyfried *et al.*, 2007). Ferrous iron in Fe-rich brucite does not contribute to hydrogen production in the serpentinization reaction. Therefore, the formation of iron-rich brucite consumes available iron for water reduction and reduces the amount of hydrogen production (McCollom and Bach, 2009). On the other hand, Fe-rich brucite may be important for the formation of magnetite in the late stages of the serpentinization reaction. Several petrographic and experimental studies on natural serpentinites proposed a two-step reaction in which metastable Fe-rich brucite formed in the early stages of serpentinization is destabilized by increased silica activity associated with progressive serpentinization to form magnetite (Bach *et al.*, 2006; Frost *et al.*, 2013; Miyoshi *et al.*, 2014; Schwarzenbach *et al.*, 2016; Seyfried *et al.*, 2007). Such magnetite formation by brucite decomposition may be sufficient to maintain a microbial community (Templeton and Ellison, 2020).

At low temperatures or high silica activity conditions, where magnetite is less to form, Fe^{3+}-bearing serpentine may play an important role in hydrogen production (Andreani *et al.*, 2013). However, it is not well understood what factors control the partitioning of Fe^{3+} into serpentine minerals. Fe^{3+} is known to enter both tetrahedral ($R^{3+}_2 \leftrightarrow R^{2+}Si^{4+}$) and octahedral ($R^{2+}_3 \leftrightarrow \square R^{3+}_2$, where "□" is vacancy) sites in serpentine (Evans, 2008; O'Hanley and Dyar, 1993, 1998). There are two Fe-endmembers of

serpentine are hisingerite ($\square Fe^{3+}_2Si_2O_5(OH)_4$) and cronstedite ($Fe^{2+}_2Fe^{3+}_2SiO_5(OH)_4$). hisingerite contains Fe^{3+} in the octahedral site (Eggleton, 1998; Tutolo and Tosca, 2023), and Cronsitedite contains Fe^{2+} and Fe^{3+} in the octahedral site and Fe^{3+} in the tetrahedral site (Hybler *et al.*, 2002). Mössbauer spectroscopic studies of lizardite, chrysotile, and antigorite from different locations have shown that the ferric iron to total iron ratio ($Fe^{3+}/\Sigma Fe$) and the ferric iron in tetrahedral site to total ferric iron ratio ($^{[4]}Fe^{3+}/\Sigma Fe^{3+}$) in serpentine varies with serpentine type (O'Hanley and Dyar, 1993; Reynard *et al.*, 2022). Lizardite has a wide range of $Fe^{3+}/\Sigma Fe$ molar ratio of 0.67 ± 0.17, which is higher than the $Fe^{3+}/\Sigma Fe$ of antigorite (0.23 ± 0.10) and chrysotile (0.34 ± 0.12). The silica and alumina potentials may control the large variations of $Fe^{3+}/\Sigma Fe$ in lizardite (Reynard *et al.*, 2022). The amount of Fe^{3+} in the tetrahedral site ($^{[4]}Fe^{3+}/\Sigma Fe^{3+}$) in lizardite has a wide range of values from 25-63% (Klein *et al.*, 2009; O'Hanley and Dyar, 1993), compared to chrysotile ($^{[4]}Fe^{3+}/\Sigma Fe^{3+}$=38-44%). Antigorite does not contain Fe^{3+} in the tetrahedral site (Mellini *et al.*, 2002). This may be due to the smaller size of the tetrahedral structure in antigorite compared to lizardite (Mellini *et al.*, 2002). Hydrothermal experiments have also shown that Fe^{3+} at the tetrahedral sites in lizardite is negligible in the early stages of serpentinization, but as the reaction progresses, Fe^{3+} is distributed to the tetrahedral sites and eventually ~15% of the total Fe^{3+} in lizardite is contained in the tetrahedral site (Marcaillou *et al.*, 2011). These results suggest that $Fe^{3+}/\Sigma Fe$ may be controlled by the crystal structure and chemistry of serpentine minerals.

Thermodynamic modeling is a powerful tool for estimating mineral compositions and abundance ratios in the water-rock reactions over a wide range of temperature and pressure conditions (Klein *et al.*, 2009, 2013; McCollom and Bach, 2009). Current thermodynamic calculations assume a solid solution model of chrysotile ($Mg_3Si_2O_5(OH)_4$) – greenalite ($Fe_3Si_2O_5(OH)_4$) - cronstedite ($Fe^{2+}_2Fe^{3+}_2SiO_5(OH)_4$) or hisingerite ($Fe^{3+}_2Si_2O_5(OH)_4$) for serpentine. However, the thermodynamic properties of the of cronstedtite and hisingerite (Fe^{3+} endmembers of serpentine), and Fe-endmember of brucite have not been experimentally measured and various values have been estimated by different models (Blanc *et al.*, 2015; Klein *et al.*, 2009, 2013; Tutolo *et al.*, 2019; Zolotov, 2014). Therefore, analysis of natural samples and laboratory experiments is necessary to confirm the reliability of the thermodynamic models. In natural serpentinization reactions, the temperature and pressure conditions, water to rock (W/R) ratios are vary with time. In addition, effect of spatial distribution of primary minerals is almost unknown. The amount of hydrogen production is expected to vary because of the associated changes in the minerals produced in the serpentinization reaction (Andreani *et al.*, 2013; Klein *et al.*, 2009).

1.5. Purpose and structure of the dissertation

Understanding the nature of serpentinization reactions in oceanic lithospheres is limited by the difficulty of direct drilling of deep part of the oceanic lithosphere. In addition, dredge samples of the seafloor and field observation of ophiolite provide a valuable information for unraveling the serpentinization process of the oceanic lithosphere, but the serpentinization image that can be obtained is fragmentary. In addition, the complexity arising from the coupled mechanical, mass transport, and chemical reactions in serpentinization reactions complicates our understanding of the process (Fig. 1.10). No studies have linked hydrogen production to the reaction-fracturing-fluid flow interactions in serpentinization reactions.

This study aims to reveal the effect of interaction of the fluid flow, reaction, and fracturing on the serpentinization in oceanic lithosphere on reaction progress and hydrogen production. This study will provide bulk-rock and local analyses and detailed descriptions of the Oman ophiolite, including the redox state of iron, using continuous drilling samples from the lower crust - upper mantle. These comprehensive analyses will provide new data on the spatial distribution and nature of serpentinization reactions over hundreds of meters in the lower crust - upper mantle. In addition, numerical simulations and thermodynamic calculations will be used to understand the serpentinization mechanisms and processes occurring in natural samples. This will provide a new perspective linking micro-scale processes with the macroscopic picture of serpentinization. These results will provide a new picture of the serpentinization reaction, in which hydrogen evolution proceeds in a dynamically changing process through the reaction-fracture-fluid transfer interaction of the serpentinization reaction.

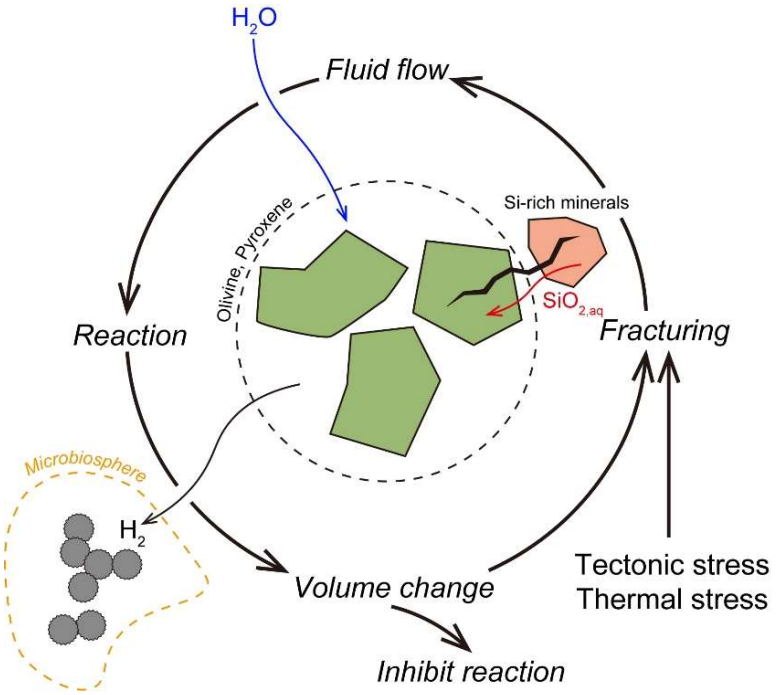

Fig. 1.10. Coupled fluid flow, reaction, fracturing during serpentinization.

This study consists of seven chapters (Fig. 1.11). In Chapter 1 provides comprehensive review of previous studies about serpentinization in the oceanic lithosphere and described the significance of serpentinization. It also explains the limitations and remaining problems of previous studies and the objectives of this study.

Chapter 2 provides new data on whole-rock analysis, rock texture observation, and mineral composition analysis for a series of drill samples from the lower crust to upper mantle of the Oman ophiolite. Comprehensive analysis focusing on serpentinization reactions will reveal the depth-dependent spatial distribution of serpentinization in the lower crust-upper mantle and its relationship to rock texture. This will contribute to our understanding of the nature of serpentinization in the lower crust-upper mantle. Following Chapters 3 through 5 focus on the processes and mechanisms of serpentinization reactions based on the observations of natural samples in Chapter 2.

Chapter 3 focuses on the mechanism of microscale crack formation based on observations of natural samples and numerical simulations. Discussion integrates observations of natural samples and numerical simulations to explore what factors contribute to crack formation and fluid flow in the oceanic lower crust.

Chapter 4 focuses on the serpentine vein network to investigate fluid activity flowing through the macroscopic fracture network. Focusing on the serpentine veins and related texture, I conducted more detailed observations from the sub-micrometer scale to the nanometer scale using scanning electron microscopy and transmission electron microscopy. The mechanism of localized water-rock reactions occurring in serpentinite is revealed from the results of these multiscale observations. Timescales of fluid flow and fluid flux through the fracture network were estimated based on the observations, thermodynamic calculations and simple mass transfer models.

Chapter 5 focuses on the hydrogen production process in the serpentinization reaction. By combining bulk analysis with in-situ analytical techniques using synchrotron radiation X-ray spectroscopy, the redox state of iron and its distribution over the scale of several hundred meters to micrometers was revealed. This provides a spatial distribution of the hydrogen production potential in the lower crust to upper mantle. Thermodynamic calculations was used to discuss the factors controlling hydrogen production during serpentinization.

In Chapter 6, I integrate the results obtained and discusses how reaction-fracture-fluid interactions affect the progression of reactions and hydrogen production during serpentinization of oceanic lithospheres. Chapter 7 is the conclusions.

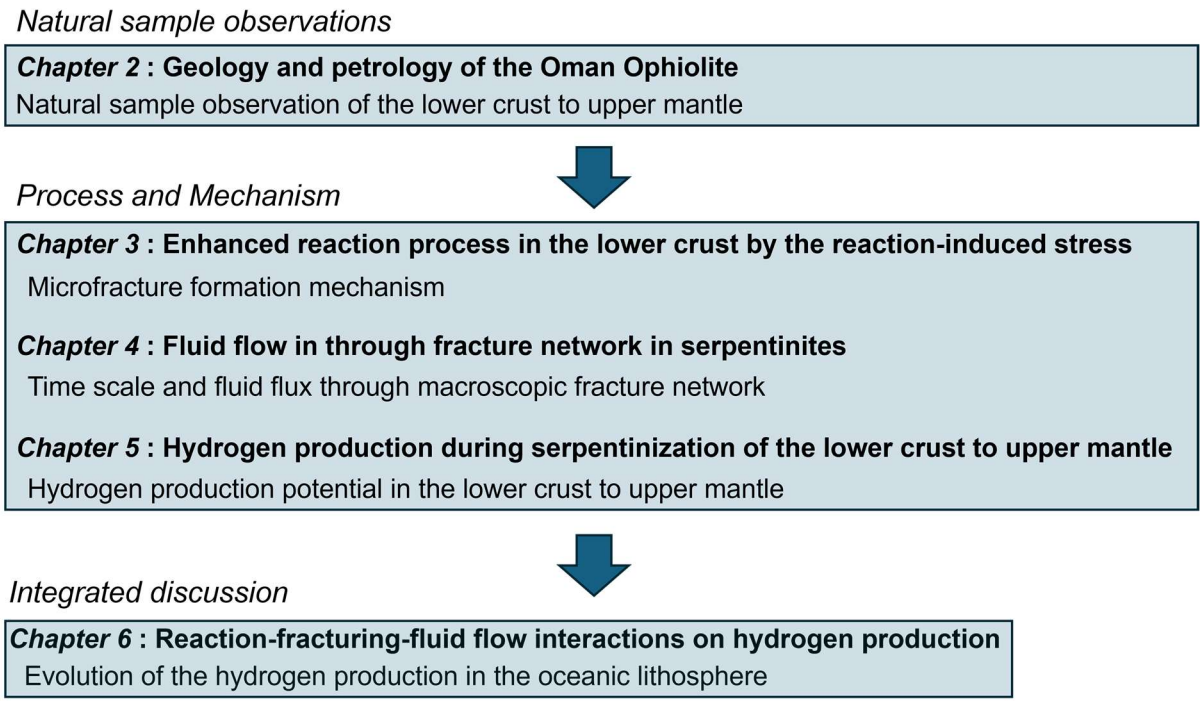

Fig. 1.11. Structure of this thesis.

Chapter 2: Geology and petrology of the Oman Ophiolite

2.1. Introduction

The Oman Ophiolite in the Middle East is the largest ophiolite in the world and is an attractive site for studying water-rock interaction in the oceanic lithosphere because of its well-preserved lithological stratigraphy. However, the ophiolite formation experiences a variety of tectonic settings as they move from the ocean floor to obduction onto the continental crust (Hacker, 1994; Michard *et al.*, 1991). Thus, the rocks in the ophiolite should be recorded several events of fluid activity at different stages. The water-rock interaction at different settings is recorded in the rocks as altered minerals. Alteration at various temperatures near the ridge axis, including very high (VHT; 900-1000 °C), high (HT; 550-900 °C), medium to low (LT; <500 °C) temperatures, has been recorded in the crustal and mantle rocks of the Oman Ophiolite (Bosch *et al.*, 2004; Nicolas, 2003; Zhang *et al.*, 2021). LT alteration, characterized by serpentinization of olivine with mesh texture formation, which is observed in the lower crust to upper mantle section (Aupart *et al.*, 2021; Bosch *et al.*, 2004; Boudier *et al.*, 2005; Hanghøj *et al.*, 2010; Zhang *et al.*, 2021). A possible stage of serpentinization in the Oman ophiolite is (1) off-axis hydrothermal alteration at the seafloor (Boudier *et al.*, 2005), (2) subduction zone setting (de Obeso *et al.*, 2022; Yoshikawa *et al.*, 2015), (3) meteoric and/or groundwater circulation after obduction (Kelemen *et al.*, 2011; Leong *et al.*, 2023). However, it is not well known the extent of serpentinization at each stage. In this chapter, I describe the overall picture of field observations and drilling cores obtained by Oman Drilling Project. In this chapter, I focus on the petrology and mineralogy, chemical composition, and spatial distribution of primary and altered minerals in the lower crust to upper mantle section of the Oman Ophiolite.

2.2. Geological setting and samples

The Oman Ophiolite has a typical stratigraphic sequence of the oceanic lithosphere from pillow lava to the upper mantle: pillow lava, sheeted dikes, and gabbroic rock, and a mantle peridotite. The Oman Ophiolite is composed of several rock bodies, which are mainly divided into northern, central, and southern bodies (Fig. 2.1) (Nicolas *et al.*, 2000). The northern body is reported to contain more volcanic rocks than the southern body and is considered to be strongly influenced by the forearc environment (Alabaster *et al.*, 1982; Ernewein *et al.*, 1988; Pearce *et al.*, 1981). In this study, I observed and analyzed rock samples from the lower crust-upper mantle of the southern Wadi Tayin body and a part of the upper mantle of the northern Hilti massif.

Field observations provide a three-dimensional view which have structural information, but the number of accessible outcrops is limited, and it is not easy to study the lithologic continuity in depth direction from outcrop. Another problem is the difficulty of collecting rocks that avoid weathering at the surface. To resolve these problems, onshore drilling of the Oman ophiolite (Oman Drilling Project)

was conducted in 2016 (Kelemen *et al.*, 2020). For the Wadi Tayin massif, I investigated samples from onshore drilling samples by the Oman Drilling Project. The Oman Drilling Project began in 2016, and one of the targets of this drilling was the crust–mantle transition zone at the drill site of hole CM1A and CM2B (Fig. 2.2A). Hole CM1A and CM2B were drilled at Wadi Zeeb, northern Sharqiyah (CM1A : 22°54.435'E, 58°20.149'N; CM2B : 22°54.660'E, 58°20.149'N; Fig. 2.2A). Fig. 2.2B and Fig. 2.2C shows cross-section of drill site. CM1A is a 404.15 m drill hole through the lower crust to the upper mantle, and CM2B is a 300.0 m drill hole through the crustal mantle boundary to the upper mantle with almost 100 % core recovery. Onboard descriptions revealed various stages of alteration reactions and veining that occurred over a range of temperatures and fluid infiltration conditions (Kelemen *et al.*, 2020).

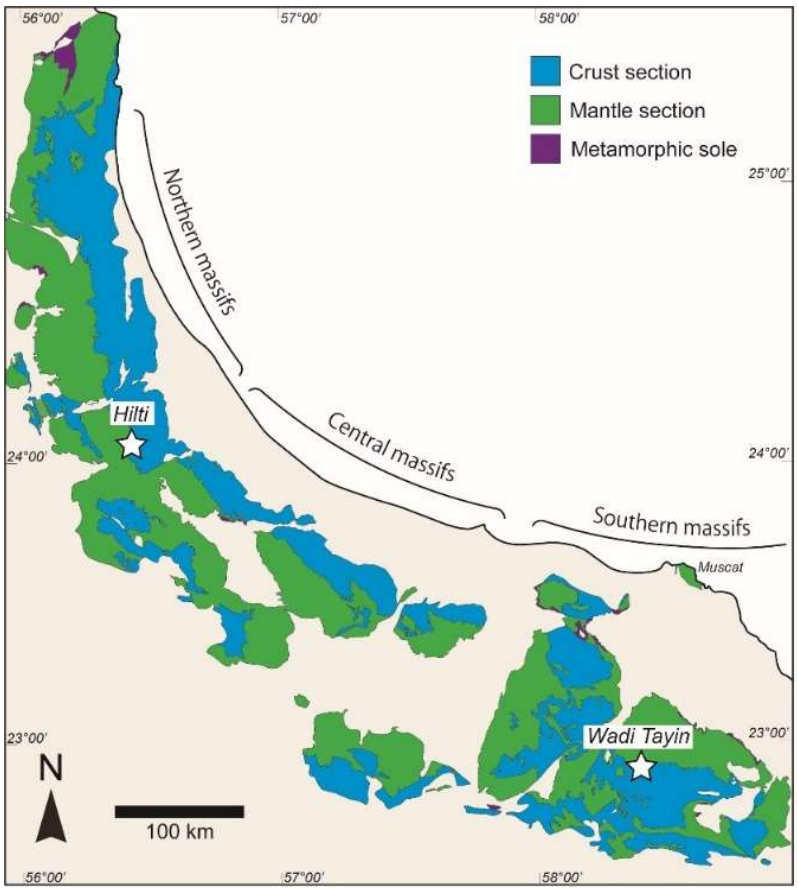

Fig. 2.1. Simplified geological map of the Oman Ophiolite (after (Nicolas *et al.*, 2000)). The stars indicate sampling locations.

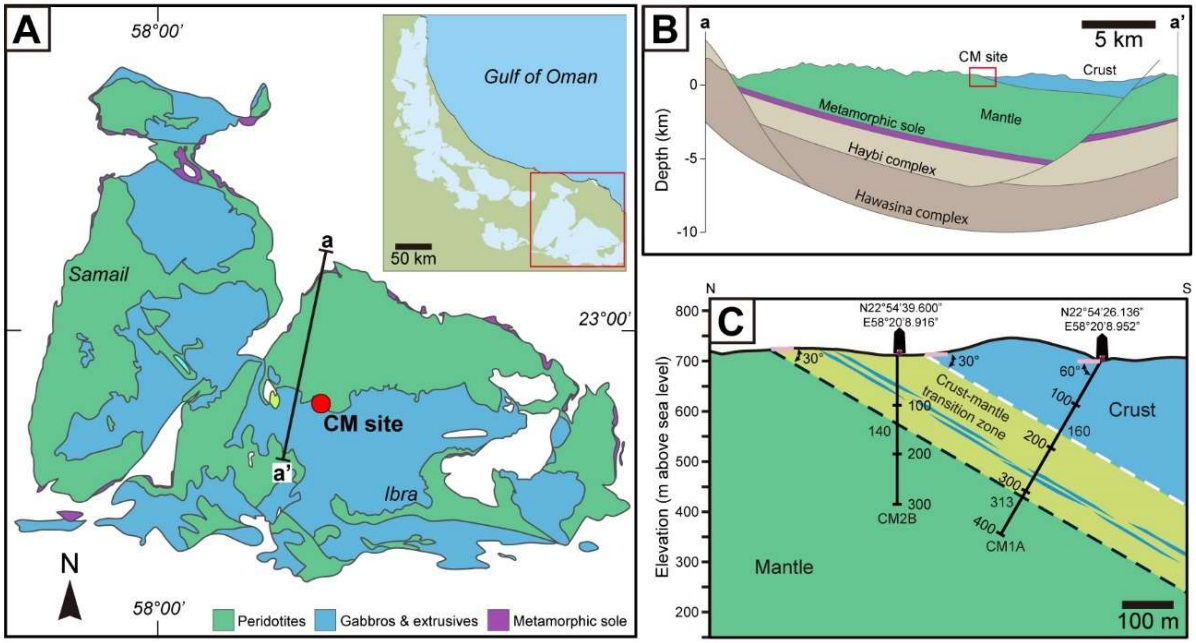

Fig. 2.2. Geological map of the OmanDP CM site (after (Kelemen *et al.*, 2020)). (A)Geological map of the Wadi Tayin massif (after Nicolas *et al*., 2000). (B)The cross-section of a-a' in (A) (after (Searle, 2007)). (C)Close up of the cross section of the drill site (after (Kelemen *et al*., 2020)). Blue thick lines in CMTZ shows gabbro sill CMTZ.

2.3. Analytical methods

Mineral identification

Electron Microprobe Analysis

Quantitative mineral chemistries were determined using an electron probe microanalyzer equipped with five wavelength dispersive X-ray (WDX) spectrometers (EPMA; JEOL JXA-8200 at Graduate School of Environmental Studies, Tohoku University, Japan). The quantitative point analysis was conducted at an accelerating voltage of 15.0 kV and a focused beam diameter of ~1–2 μm. The probe currents for quantitative point analysis and elemental mapping were 12 and 120 nA, respectively. Mineral reference standards (Wollastonite (Si, Ca), rutile (Ti), corundum (Al), hematite (Fe), manganosite (Mn), periclase (Mg), albite (Na), K-feldspar (K), and eskolaite (Cr)) were used for calibration. The total iron content was calculated as FeO (FeO^{*}).

Raman spectroscopy

Serpentine types were identified by Raman spectroscopy (Horiba XploRA PLUS; Graduate School of Environmental Studies, Tohoku University) equipped with a 532 nm green laser. The Raman spectra were collected in 5 accumulations, with the integration time set to 10 seconds and grating of 1,800 grooves/mm. I prepare thin sections for Raman spectra measurement. Thin sections were cut

parallel to the borehole direction, which is sub-perpendicular to the igneous layering. I used low fluorescence and low viscosity epoxy resin (Craft Resin®, NISSIN RESIN Co., Ltd.) for cementing rock sample and slide glass. Identification of serpentine minerals is based on previous studies (Compagnoni *et al.*, 2021; Groppo *et al.*, 2006).

Whole core X-ray CT

As a part of the Oman Drilling Project, all cores from CM1A and CM2B were scanned using an X-ray CT scanner (Discovery CT 750HD, GE Medical Systems) on board the D/V *Chikyu* to obtain information on the composition and the internal structure of the cores (Kelemen *et al.*, 2020). Three-dimensional images of 1.4 m × 0.09 m × 0.09 m with a voxel size of 0.176 mm × 0.176 mm × 0.625 mm were obtained with excitation voltage of 140 kV and a current for X-ray tube of 100 mA. The scan rate was 20 mm/s. The CT number in Hounsfield units (HU) is defined as follows:

$$CT\ number = \frac{\mu_t - \mu_w}{\mu_w} \times 1000 \tag{2.1}$$

where, μ_t and μ_w are linear attenuation coefficient the measured material and water, respectively.

Bulk rock composition and estimation of the protolith mineral mode

Bulk-rock compositions were measured by glass bead method using X-ray fluorescence analyzer equipped with wavelength dispersive X-ray spectroscopy (WDX-XRF, Rigaku ZSX Primus IV at Graduate School of Environmental Studies, Tohoku University, Japan). The rock samples were sliced using diamond cutter (a few cm size) and roughly crashed using tungsten mortar (~ 1 mm). The rock samples were powdered using Multi Beads Shocker® (Yasui Kikai Corporation, PM3000) with 2500 rpm in 120 seconds × 2 (Total 240 sec). Before making glass bead, the powdered rock heated at 950 ℃, 3 hours for measuring loss on ignition (LOI). The ignited powder sample (0.6 g) mixied with flux (5.4 g) for making glass disk. The mass fraction of the total iron contents was calculated as Fe_2O_3 ($Fe_2O_3^*$). The protolith mineral mode was estimated using the least squares method, assuming that the rock does not contain spinel and no mass transfer during alteration (Kourim *et al.*, 2022).

Micro x-ray fluorescence microscope

Thin section scale elemental maps of gabbroic rocks were obtained by micro x-ray fluorescence (XRF) microscope (Horiba Scientific XGT-7000V at Graduate School of Environmental Studies, Tohoku University, Japan) equipped with an energy dispersive spectrometer (EDS) for bulk rock classification, modal abundances of mineral. The micro-XRF analysis were conducted at an

accelerating voltage of 50 kV and tube diameter of 10 μm. The scan time was 1,800 seconds and the number of accumulations was 20 times. The resolution of the elemental mapping is 60 μm/pixel and the measurement area size is 15 × 32 mm. The element maps of Al, Ca, Mg and Fe were used to create mineral phase map. To evaluate the primary mineral mode of protolith, serpentine and magnetite were classified as the products of olivine. Chlorite and prehnite were classified as the alteration products of plagioclase. The mineral phase maps are divided into four regions, and mineral mode by area calculated for each region.

Laser ablation inductively coupled plasma mass spectrometry

Trace elemental analysis of minerals was performed using later ablation inductively coupled plasma mass spectrometry (LA-ICP-MS, ESI NWR193UC excimer LA system and Agilent 7700x quadrupole ICP-MS, Akita University, Japan). The laser beam diameter was 140 μm during analysis and 150 μm during pre-ablation. The analysis was performed with laser repetition rate = 10 Hz, He gas flow rate 0.5 L/min, with a He cup gas flow rate 0.15 L/min. Ar carrier gas flow rate 0.68 L/min, with Ar dilution gas flow rate 0.6 L/min. Laser ablation time was 70 s, and laser energy density = 8.0 J cm^{-2}. NIST 612 glass was used as the primary standard. USGS standard glasses BIR-1G and BHVO-2G were used as secondary standards to evaluate data quality (*Appendix*, Table A1).

Thermogravimetric analysis

Bulk content of hydrous minerals of the powdered rock samples were measured by thermo gravimetry (Rigaku Thermo plus EVO II TG8120; Graduate School of Environmental Studies, Tohoku University). The temperature raised from room temperature to 1100 ℃ at a rate of 10 ℃/min under argon gas atmosphere.

2.4. Field observation of the Crust-Mantle boundary of the Oman Ophiolite

The main samples investigated in this study are drilled samples of the Oman ophiolite, but supplemental field surveys and sample collection were conducted. I observed a series of lithofacies in the Oman ophiolite from pillow lava to the upper mantle (Fig. 2.3).

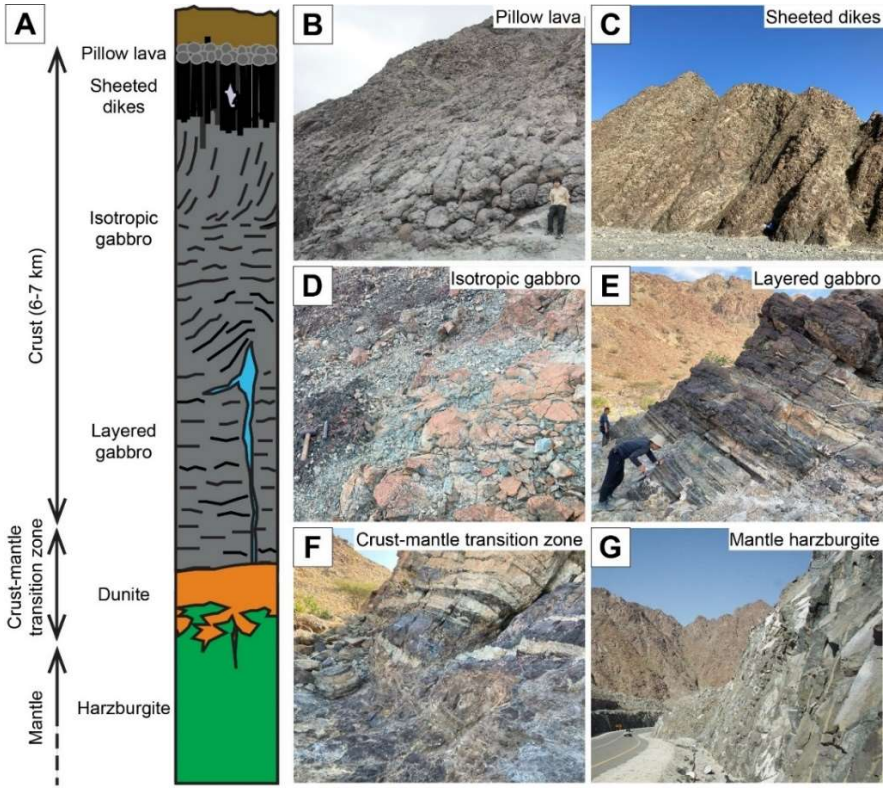

Fig. 2.3. Stratigraphy of the Oman ophiolite. (A) Illustration of the "Penrose model", a typical fast spreading oceanic lithosphere model (After Dick et al., 2006). (B-G) Outcrop photo of typical lithology in the Oman ophiolite (Photos taken on January 2023). (B) Pillow lava, (C) Sheeted dykes, (D) Isotropic gabbro, (E) Layered gabbro, (F) Crust-mantle transition zone, (G) Mantle harzburgite.

2.4.1. Wadi Tayin massif

The Wadi Tayin massif, a component of the southern part of the Oman Ophiolite, have a continuous lower crust-upper mantle stratigraphic sequence. The sampling points in field study are the lower crust-upper mantle boundary (Fig. 2.4A Point 1; N22°54'41.43, E58°20'17.84), lower crust (Fig. 2.4A Point 2; N22°54 '47.22, E58°20'13.94), and the upper mantle (Fig. 2.4A Point 3; N22°54'52.60, E58°20'06.47). A layered structure consisting of wehrlite-gabbro is characteristically observed at the lower crust and upper mantle boundary (Fig. 2.4B). The lowermost part consists of dunite with antigorite+chrysotile veins (Fig. 2.4C and D). In the wehrlite-gabbro, Distinctive serpentine veins (enriched in lizardite) develops in the gabbro layers in a direction perpendicular to the layered structure (Fig. 2.4E). The upper mantle is composed mainly of harzburgite, which has weathered to a reddish-brown surface (Fig. 2.4F). The harzburgite is cut by mafic intrusive rocks, carbonate and magnetite veins

(Fig. 2.4F and G).

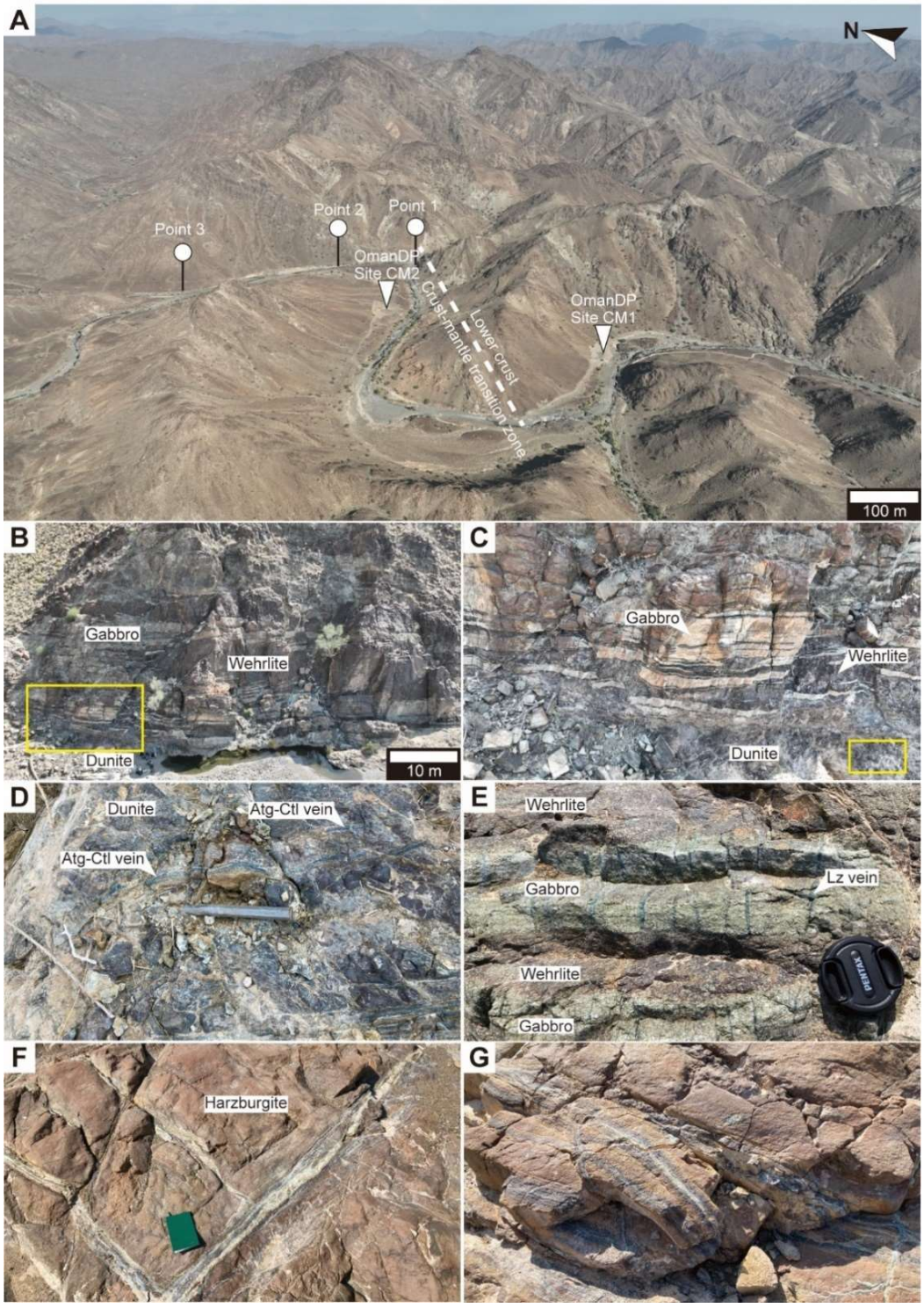

Fig. 2.4. (A) Distant view of the outcrop around the CM site. (B) Outcrop photograph of the Crust-Mantle transition zone (Point1). Alternating layered structure of wehrlite (black) and gabbro (white) observed above dunite layer. (C) Close up view of the yellow rectangle in (B). (D) Close up view of the dunite layer. Serpentinized dunite matrix cut by the antigorite-chrysotile veins. (E) Layered structure of wehrlite (black) and gabbro (white) at point 2 in (A). The gabbro layers cut by vertical lizardite (Lz) veins in the layered structures. (F) Outcrop photograph of the upper mantle section at point 3 in (A). The upper mantle section is mainly composed by harzburgite. (G) The harzburgite matrix cut by black color veins.

2.4.2. Hilti massif

The Hilti massif, which composes part of the northern Oman ophiolite, has a large outcrop of the less weathered upper mantle (Fig. 2.5A; N24°05'00.69, E56°25'29.51). The harzburgite in the upper mantle is cut by sheared vein composed of antigorite and less chrysotile (Fig. 2.5B), and the vein network are developed over the several meters scale (Fig. 2.5C and D).

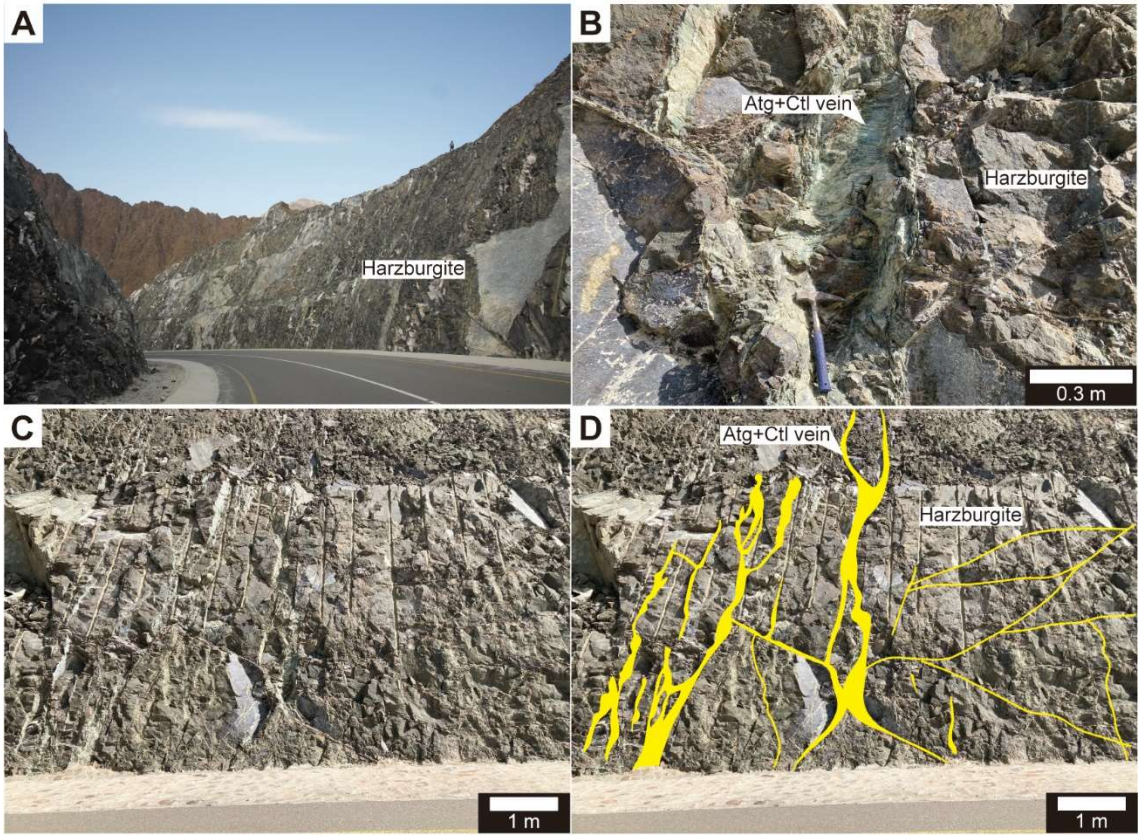

Fig. 2.5. Outcrop photograph of Hilti massif. (A) Overview of upper mantle section. (B) Antigorite (Atg) + chrysotile (Ctl) vein cut serpentinized harzburgite. (C) Overview of Atg+Ctl vein network. (D) Figure tracing the Atg+Ctl veins.

2.5. Depth profile of chemical composition and hydrous minerals

2.5.1. Overview of the lower crust to upper mantle rocks

In the following, rock samples from two boreholes (Hole CM1A and CM2B) obtained from onshore drilling of the Oman Ophiolite were analyzed in detail. Lower crust section (0–160 m depth), crust-mantle transition zone (160–310 m depth), and upper mantle section (310–404 m depth) of CM1A is mostly consist of gabbroic rocks with layered structure, dunite, and harzburgite, respectively. Crust-mantle transition zone (0-140 m depth) and upper mantle section (140-300 m depth) of CM2B mainly consist of dunite and harzburgite. The crust-mantle boundary is 313 m for CM1A, 140 m for CM2B. Volatile free bulk rock major element composition analysis using WDS-XRF and thermogravimetric analysis were performed on total 78 samples: gabbroic rocks (19 samples from CM1A and 1 sample from CM2B), dunites (10 samples from CM1A and 10 samples from CM2B), and the harzburgites (10 samples from CM1A and 28 samples from CM2B). Table 2.1 shows average bulk rock composition for each lithology. Loss on ignition (LOI) was separately measured for the powders before bulk rock composition analysis. The gabbroic rocks have high variability in bulk rock composition and LOI. Dunite has small variation (1σ <1 wt. %) except for total iron (Fe_2O_3*) and MgO. Harzburgite has small variation (1σ <1 wt. %) except for MgO and LOI. Depth profile of volatile free bulk rock major element composition shows no systematic variation with depth is observed for SiO_2, Fe_2O_3, MgO, and LOI. CaO content is high at depths in CM1A and CM2B (320-370 m and ~250 m, respectively). For CM_2B, the Na_2O, K_2O, and Al_2O_3 contents tend to increase with depth. The LOI of dunite is nearly constant at ~15 wt. %, while the LOI of harzburgite varies from 9-15 wt. % (Fig. 2.6). The gabbroic rocks show variation in LOI with respect to depth, which may be caused by variation in olivine content. Dunnite has almost homogeneous LOI with depth, indicating that it is homogeneously serpentinized. Harzburgite has greater LOI variation than dunite (Fig. 2.6).

Table 2.1. Average bulk rock composition of gabbroic rocks, duntie, and harzburgite from CM1A and CM2B.

Lithology	Gabbroic rocks		Dunite		Harzburgite	
N	20		20		38	
	Avg.	Std.	Avg.	Std.	Avg.	Std.
SiO_2	43.09	2.41	38.66	0.52	42.37	0.72
TiO_2	0.12	0.07	0.02	0.02	0.02	0.02
Al_2O_3	12.61	5.69	0.57	0.36	0.74	0.29
Fe_2O_3*	8.46	4.72	10.63	1.37	8.74	0.93
MnO	0.13	0.05	0.14	0.02	0.12	0.01
MgO	20.23	8.36	48.10	1.15	45.55	1.39
CaO	13.17	6.04	0.19	0.11	0.93	0.72
Na_2O	0.38	0.41	0.00	0.00	0.01	0.02
K_2O	0.03	0.01	0.02	0.00	0.02	0.00
Total	98.26	0.70	98.32	0.34	98.51	0.68
LOI	6.21	2.49	14.98	0.57	12.86	1.41

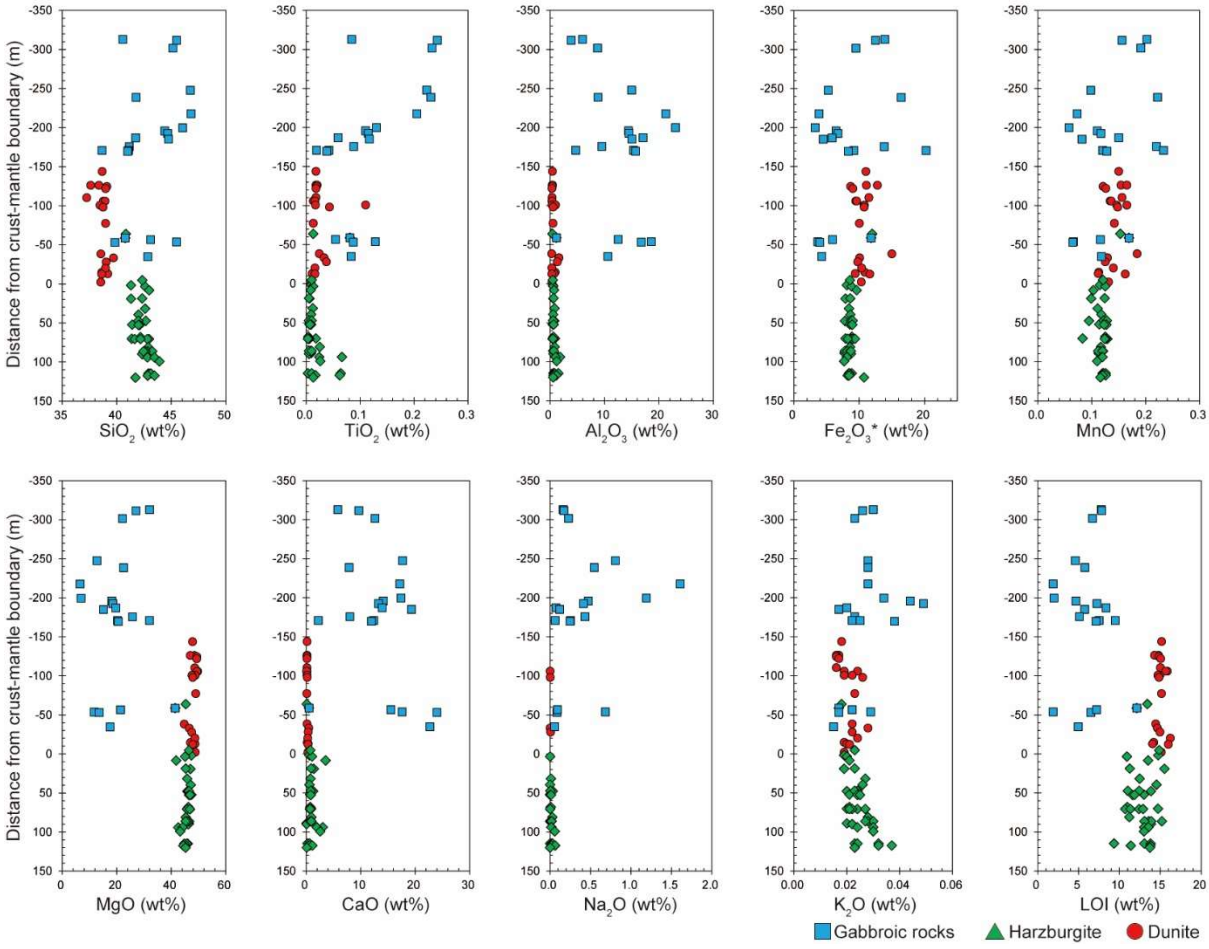

Fig. 2.6. Depth profile of bulk rock major element composition and loss on ignition (LOI). The distance from the crustal mantle boundary is calculated for each of CM1A and CM2B as follows: Depth from surface – 313 for CM1A; (Depth from the surface – 140)×cos (30°) for CM2B.

2.5.2. Thermogravimetric analysis

Gabbroic rocks

The thermogravimetric (TG) curves for the gabbroic rocks show almost no weight loss up to ~400 °C and significant weight loss of ~1-2 wt. % and ~2-3 wt. % from ~250-450 °C and ~450-800 °C, respectively (Fig. 2.7A). The weight loss above ~900 °C is almost negligible. A loss on ignition (LOI: weight loss during 200-1050 °C) of the gabbroic rocks shows 8.8-14.2 wt. %. The weight loss at 430-700 °C is caused by decomposition of chlorite (500-700 °C), lizardite/chrysotile (450-800 °C) and prehnite (100-600 °C) (Földvári, 2011; Viti, 2010). The decomposition temperatures of these minerals overlap, making it difficult to measure the amount of each mineral.

Dunite

The TG curve for dunite shows almost no mass loss up to ~250 °C, with a significant mass loss of 1.5-4.1 wt. % from 250 °C-450 °C corresponding to the decomposition of brucite and 9.8-11.3 wt. % from 450 °C-800 °C corresponding to the decomposition of serpentine (Fig. 2.7B). Above ~800 °C, there is almost no mass loss. LOI of dunite have a range of 12.5-14.8 wt. %. The peaks of the weight loss rate are observed at 366±9 °C and 626±11 °C. The amounts of brucite and serpentine calculated from the mass loss at each temperature range are 4.8-13.3 wt. % and 75.0-86.8 wt. %, respectively.

Harzburgite

The TG curve for harzburgite shows almost no mass loss up to ~250 °C, with significant mass loss of 1.2-3.0 wt. % from 250-450 °C corresponding to the decomposition of brucite and ~7.0-11.6 wt. % from 450-800 °C corresponding to the decomposition of serpentine (Fig. 2.7C). The peaks of the weight loss rate are observed at 358±8 °C and 647±21 °C. The LOI of harzburgite ranges from 8.8-14.2 wt. %. The amounts of brucite and serpentine calculated from mass loss at each temperature range are 3.7-9.7 wt. % and 53.6-89.1 wt. %, respectively.

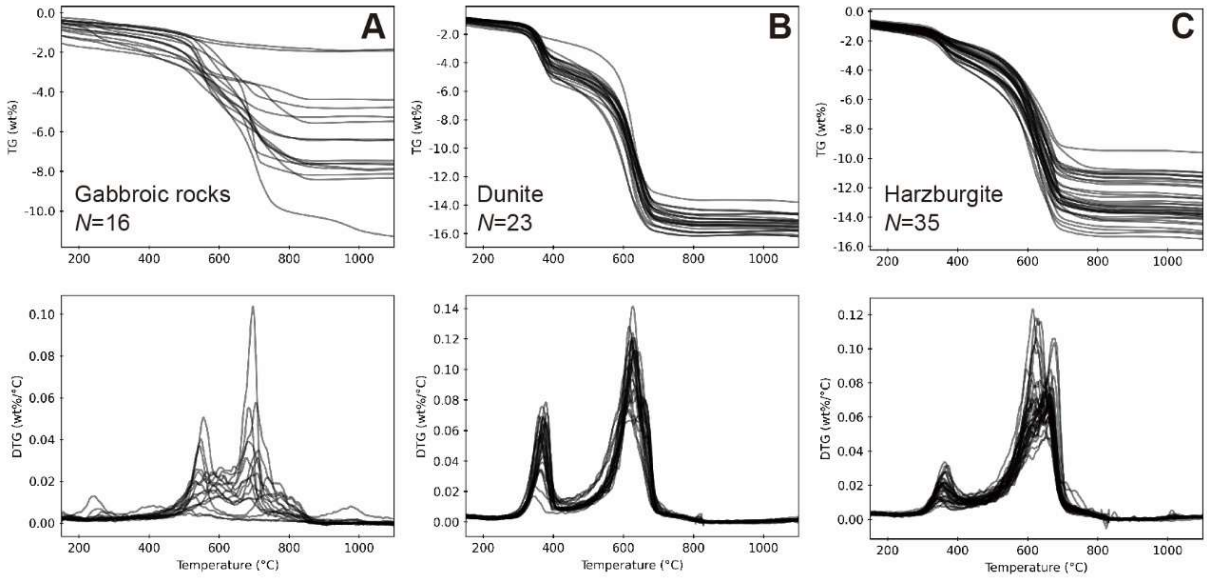

Fig. 2.7. Thermogravimetric analytic curves of gabbroic rocks (A), dunites (B), and harzburgites (C).

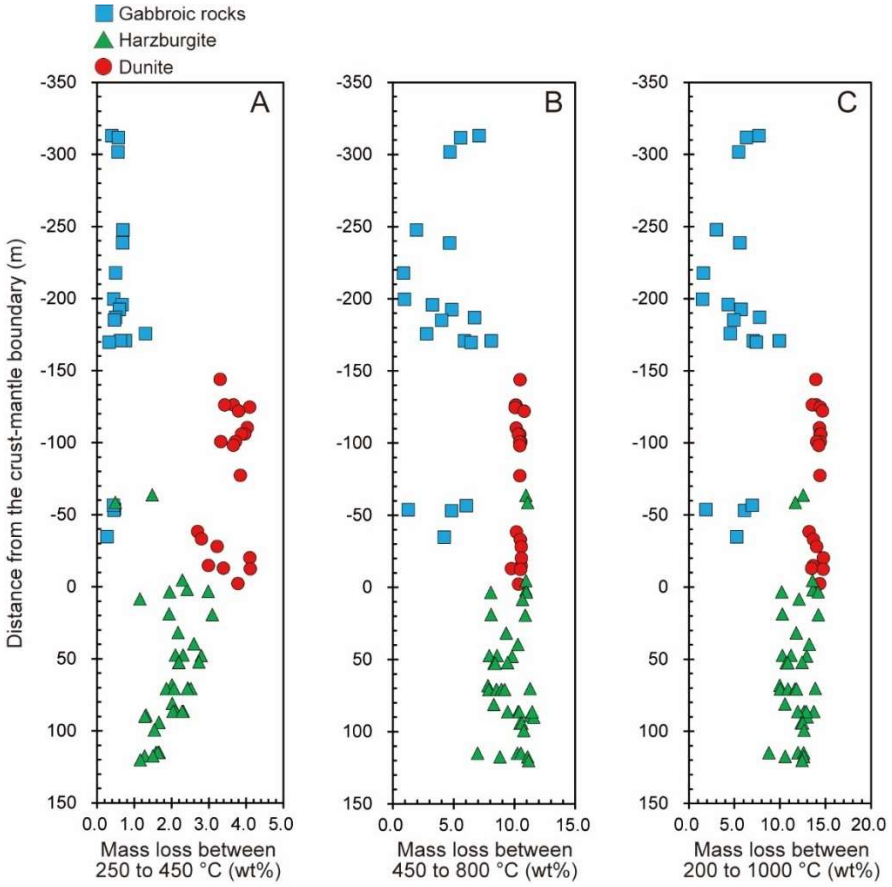

Fig. 2.8. Depth profile of the mass loss between 250 to 450 °C (A), 450 to 800 °C(B), and 200 to 1000 °C (C). The distance from the crustal mantle boundary is calculated for each of CM1A and CM2B as follows: Depth from surface – 313 for CM1A; (Depth from the surface – 140)×cos (30°) for CM2B.

2.6. Petrology and mineralogy

2.6.1. Gabbroic rocks

The gabbroic rocks show a layered structure consisting of olivine-rich dark layers and plagioclase-rich white layers every few to tens of centimeters (Fig. 2.9). The gabbroic rocks are composed of olivine, clinopyroxene, plagioclase, and spinel as primary minerals with granular texture with a grain size of 0.2-2.5 mm. Serpentine, chlorite, and prehnite veins cut the host rock (Fig. 2.10). Mineral mode determined from the bulk rock composition are olivine = 31.5 ± 20.7 wt. %, plagioclase = 38.9 ± 15.3 wt. %, and clinopyroxene = 31.3 ± 19.4 wt. % (Table 2.3). Mineral modes are also determined by micro-XRF mapping for five selected samples (Fig. 2.11; CM1A-9Z3-26-30; CM1A-47Z2-62-67; CM1A-48Z3-10-15; CM1A-55Z1-76-81; CM1A-113Z3-25-30). The mineral modes and microstructures are similar to other gabbroic rocks from the lower crustal section of the Oman ophiolite (Pallister and Hopson, 1981; Zhang *et al.*, 2021). The X_{Mg}[=Mg^{2+}/(Mg^{2+}+Fe^{2+}), where Mg and Fe^{2+} are in atoms per formula unit (a.p.f.u.)] of olivine and clinopyroxene show a wide compositional range of 0.80-0.87 and 0.85-0.90, respectively (Table. 2.2). Plagioclase in the gabbroic rocks is Ca-rich (X_{Ca} [=Ca^{2+}/(Ca^{2+}+Na^{+}), where Ca^{2+} and Na^{+} are in a.p.f.u.] of 0.82-0.95).Secondary minerals are described next.

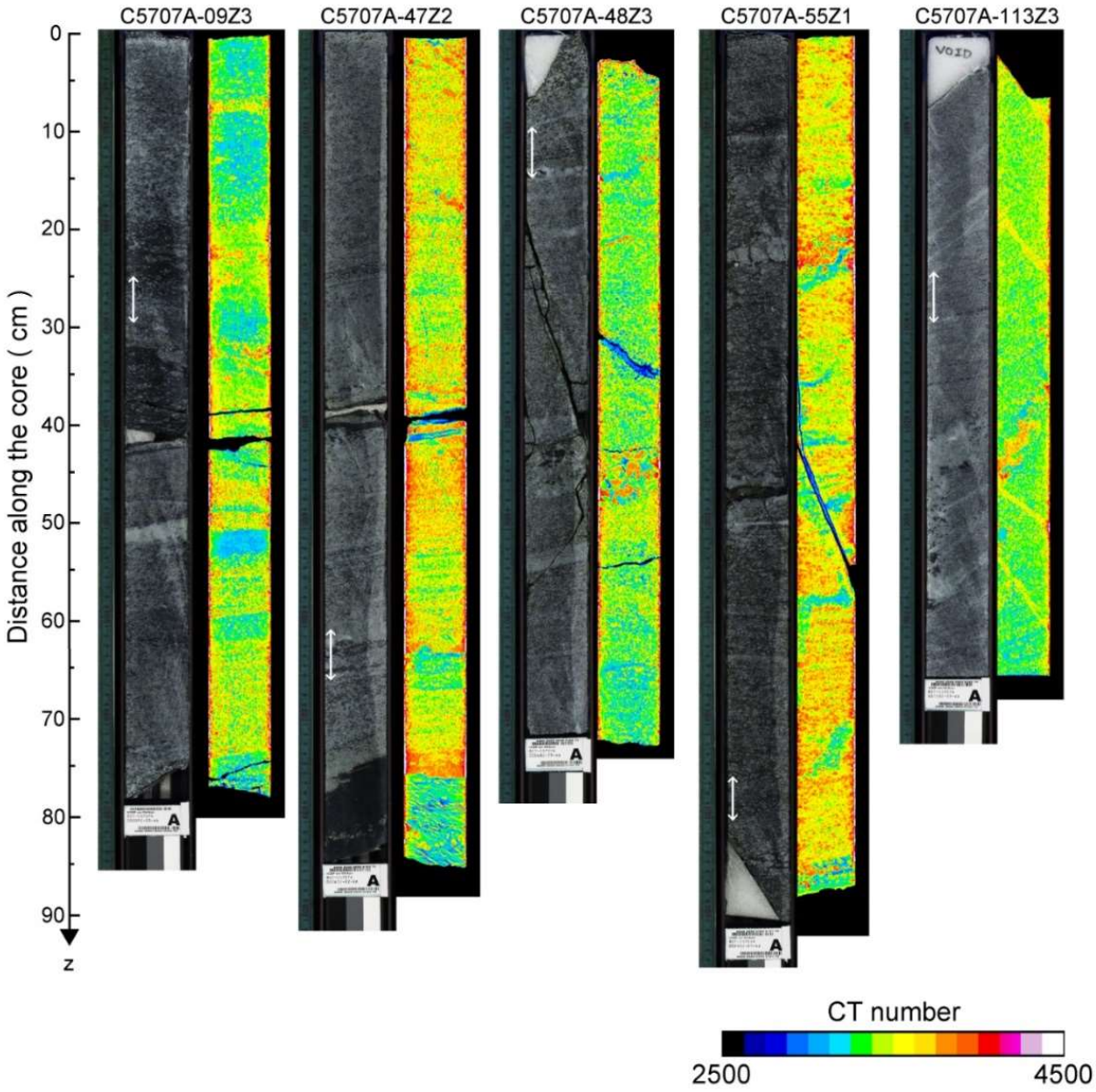

Fig. 2.9. Photograph and X-ray CT image of gabbroic rocks from OmanDP CM site. z increases with depth within the hole. The dark color parts in photographs are mainly composed of serpentinized olivine. The white color parts mainly composed of plagioclase. White color allows shows the positions of thin section.

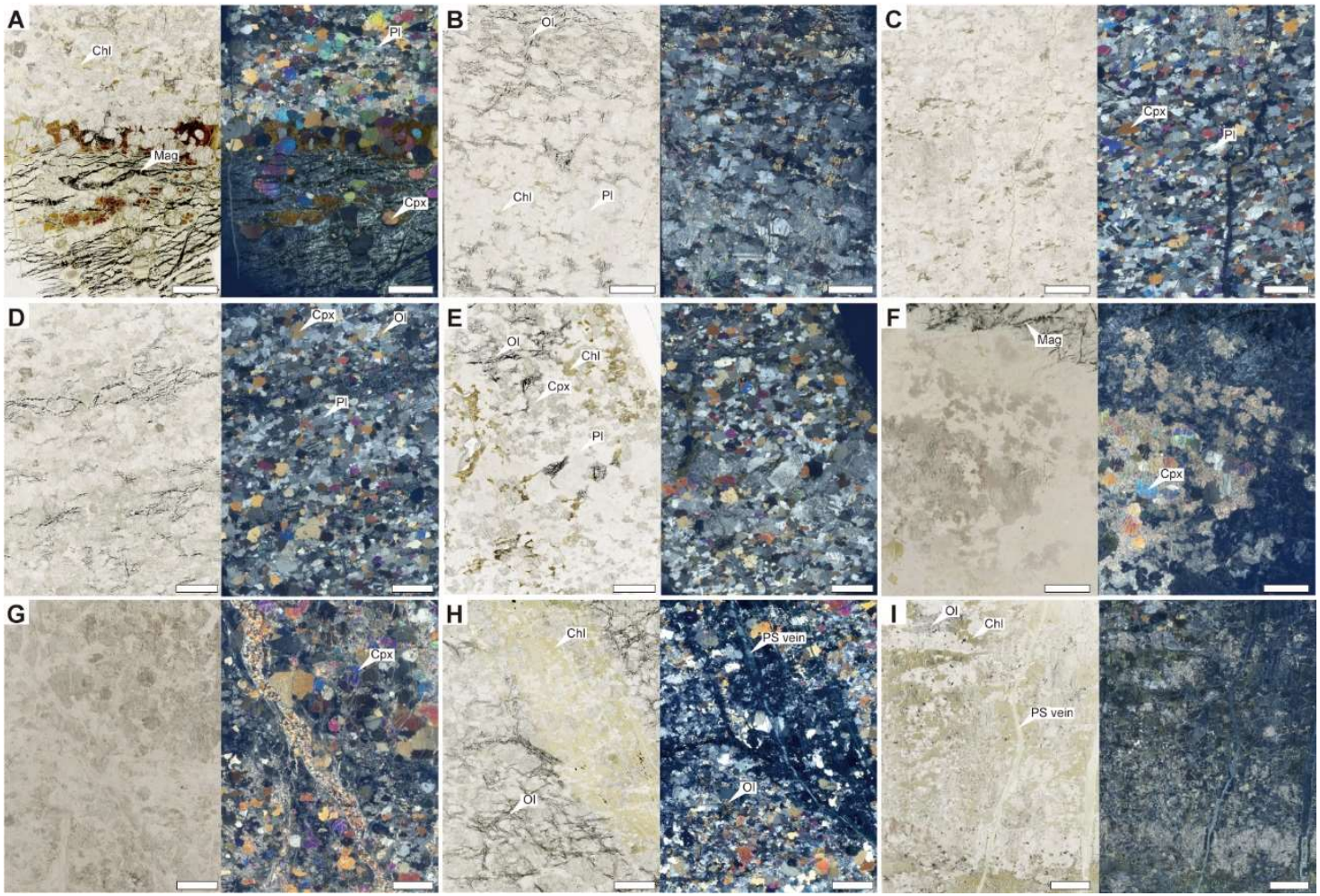

Fig. 2.10. Thin section image of the gabbroic rocks under plain polarized light and crossed polarized light. (A) CM1A-7Z2-38-42, (B) CM1A-9Z3-26-30, (C) CM1A-46Z1-34-39, (D) CM1A-47Z2-62-67, (E) CM1A-48Z3-10-15, (F) CM1A-51Z2-72-77, (G) CM1A-51Z4-72-77, (H) CM1A-55Z1-76-81, (I) CM1A-57Z3-43-48. Ol = olivine, Pl = plagioclase, Cpx = clinopyroxene, Mag = magnetite, Chl = chlorite. PS = polygonal serpentine.

Table. 2.2. Chemical composition of primary minerals in gabbroic rocks (in wt. %) with 1σ standard deviation and calculated structural formula.

Sample	CM1A-7Z1-43-45		CM1A-9Z3-26-30		CM1A-47Z2-62-67		CM1A-48Z3-10-15		CM1A-55Z1-76-81		CM1A-57Z3-12-17		CM1A-58Z1-50-54	
Lithology	Olivine gabbro		Olivine gabbro		Olivine gabbro		Olivine gabbro		Olivine gabbro		Olivine gabbro		Olivine gabbro	
Mineral	Olivine		Olivine		Olivine		Olivine		Olivine		Olivine		Olivine	
N	3		4		44		12		28		9		3	
	avg.	1σ	avg.	1σ	avg.	1σ	avg.	1σ	avg.	1σ	avg.	1σ	avg.	1σ
SiO_2	39.30	0.27	39.34	0.56	40.71	1.80	39.94	0.20	39.00	0.28	39.37	0.23	39.93	0.25
TiO_2	0.02	0.03	0.01	0.01	0.01	0.02	0.01	0.01	0.01	0.01	0.01	0.01	0.02	0.02
Al_2O_3	0.08	0.04	0.03	0.11	4.72	11.84	0.00	0.01	0.01	0.01	0.00	0.00	0.01	0.02
FeO	16.48	0.36	16.86	0.74	12.54	4.76	14.54	0.30	18.95	0.38	15.36	0.14	13.91	0.22
MnO	0.19	0.05	0.28	0.08	0.16	0.11	0.24	0.06	0.34	0.07	0.25	0.08	0.07	0.02
MgO	43.67	0.27	43.40	0.59	39.22	15.54	45.62	0.34	41.80	0.50	44.99	0.34	45.36	0.11
CaO	0.07	0.02	0.09	0.03	2.57	6.36	0.03	0.02	0.07	0.03	0.07	0.03	0.10	0.11
Na_2O	0.00	0.00	0.02	0.02	0.14	0.33	0.04	0.08	0.01	0.02	0.01	0.03	0.04	0.06
K_2O	0.00	0.01	0.01	0.01	0.00	0.01	0.00	0.01	0.00	0.01	0.00	0.00	0.00	0.00
Cr_2O_3	0.01	0.01	0.02	0.02	0.02	0.03	0.01	0.02	0.01	0.02	0.02	0.02	0.01	0.01
Total	99.83	0.61	100.05	0.66	100.09	0.76	100.44	0.63	100.20	0.56	100.09	0.46	99.54	0.56
Oxygen	4		4		4		4		4		4		4	
Si	1.00		1.00		1.01		1.00		1.00		0.99		1.00	
Ti	0.00		0.00		0.00		0.00		0.00		0.00		0.00	
Al	0.00		0.00		0.13		0.00		0.00		0.00		0.00	
Fe	0.35		0.36		0.26		0.30		0.40		0.14		0.29	
Mn	0.00		0.01		0.00		0.01		0.01		0.18		0.00	
Mg	1.65		1.64		1.46		1.70		1.59		0.75		1.70	
Ca	0.00		0.00		0.06		0.00		0.00		0.94		0.00	
Na	0.00		0.00		0.01		0.00		0.00		0.00		0.00	
K	0.00		0.00		0.00		0.00		0.00		0.00		0.00	
Cr	0.00		0.00		0.00		0.00		0.00		0.00		0.00	
Total	3.00		3.00		2.93		3.00		3.00		1.34		3.00	
X_{Mg}	0.83		0.82		0.85		0.85		0.80		0.84		0.85	

X_{Mg}=Mg^{2+}/(Mg^{2+}+Fe^{2+}), where Mg^{2+} and Fe^{2+} are in atoms per formula unit (a.p.f.u.).

Table. 2.2. Continue of chemical composition of primary minerals in gabbroic rocks (in wt. %) with 1σ standard deviation and calculated structural formula.

Sample	CM1A-113Z3-25-30		CM1A-7Z1-43-45		CM1A-9Z3-26-30		CM1A-46Z1-34-39		CM1A-47Z2-62-67		CM1A-48Z3-10-15		CM1A-51Z2-72-77	
Lithology	Gabbro		Olivine gabbro		Troctolite		Olivine gabbro		Olivine gabbro		Olivine gabbro		Olivine gabbro	
Mineral	Olivine		Clinopyroxene		Clinopyroxene		Clinopyroxene		Clinopyroxene		Clinopyroxene		Clinopyroxene	
N	19		3		9		3		12		3		7	
	avg.	1σ	avg.	1σ	avg.	1σ	avg.	1σ	avg.	1σ	avg.	1σ	avg.	1σ
SiO_2	40.11	0.47	52.36	0.33	51.75	0.27	52.48	0.06	52.00	0.33	51.87	0.59	51.20	0.29
TiO_2	0.01	0.01	0.46	0.04	0.38	0.05	0.46	0.03	0.27	0.05	0.29	0.05	0.20	0.04
Al_2O_3	0.00	0.01	2.21	0.09	2.90	0.13	2.89	0.32	2.86	0.15	2.43	0.34	3.01	0.14
FeO	12.99	0.38	4.98	0.15	4.98	0.20	5.21	0.06	4.51	0.43	4.34	0.20	3.54	0.22
MnO	0.11	0.06	0.03	0.02	0.10	0.06	0.11	0.02	0.15	0.05	0.11	0.04	0.07	0.06
MgO	47.00	0.58	16.91	0.15	16.05	0.37	16.72	0.39	17.30	0.92	16.88	0.27	16.60	0.43
CaO	0.03	0.02	21.34	0.08	22.73	0.24	21.42	0.03	21.60	0.95	22.17	0.17	21.82	0.32
Na_2O	0.02	0.03	0.28	0.09	0.26	0.05	0.24	0.04	0.21	0.08	0.28	0.03	0.30	0.08
K_2O	0.01	0.01	0.01	0.00	0.01	0.01	0.01	0.01	0.00	0.01	0.00	0.00	0.00	0.00
Cr_2O_3	0.01	0.02	0.09	0.00	0.21	0.14	0.12	0.02	0.35	0.09	0.67	0.02	0.87	0.15
Total	100.29	0.50	98.67	0.33	99.36	0.34	99.64	0.14	99.25	0.50	99.05	0.28	97.60	0.22
Oxygen	4		6		6		6		6		6		6	
Si	0.99		1.94		1.92		1.93		1.92		1.92		1.91	
Ti	0.00		0.01		0.01		0.01		0.01		0.01		0.01	
Al	0.00		0.10		0.13		0.12		0.12		0.11		0.13	
Fe	0.27		0.15		0.15		0.16		0.14		0.13		0.11	
Mn	0.00		0.00		0.00		0.00		0.00		0.00		0.00	
Mg	1.74		0.93		0.87		0.91		0.95		0.93		0.93	
Ca	0.00		0.85		0.90		0.84		0.85		0.88		0.87	
Na	0.00		0.02		0.02		0.02		0.01		0.02		0.02	
K	0.00		0.00		0.00		0.00		0.00		0.00		0.00	
Cr	0.00		0.00		0.01		0.00		0.01		0.02		0.03	
Total	3.01		4.01		4.01		4.01		4.02		4.02		4.01	
X_{Mg}	0.87		0.86		0.85		0.85		0.87		0.87		0.89	

X_{Mg}=Mg^{2+}/(Mg^{2+}+Fe^{2+}), where Mg^{2+} and Fe^{2+} are in atoms per formula unit (a.p.f.u.).

Table. 2.2. Continue of chemical composition of primary minerals in gabbroic rocks (in wt. %) with 1σ standard deviation and calculated structural formula.

Sample	CM1A-51Z4-72-77		CM1A-55Z1-76-81		CM1A-58Z1-50-54		CM1A-113Z3-25-30		CM1A-113Z4-11-16	
Lithology	Olivine gabbro		Olivine gabbro		Harzburgite		Olivine gabbro		Gabbro	
Mineral	Clinopyroxene		Clinopyroxene		Clinopyroxene		Clinopyroxene		Clinopyroxene	
N	9		5		3		11		2	
	avg.	1σ	avg.	1σ	avg.	1σ	avg.	1σ	avg.	1σ
SiO_2	52.01	0.38	50.77	0.29	51.60	0.32	52.75	0.46	53.08	0.25
TiO_2	0.17	0.08	0.52	0.05	0.26	0.04	0.34	0.03	0.31	0.01
Al_2O_3	2.46	0.22	3.52	0.11	3.12	0.09	2.55	0.51	2.94	0.11
FeO	4.38	0.92	6.28	0.28	4.65	0.16	3.77	0.24	3.79	0.06
MnO	0.20	0.08	0.17	0.01	0.07	0.05	0.15	0.06	0.08	0.03
MgO	15.93	1.69	15.91	0.47	16.33	0.22	17.37	0.24	17.55	0.08
CaO	22.41	1.18	20.78	0.88	21.78	0.10	22.37	0.44	22.05	0.04
Na_2O	0.21	0.13	0.44	0.07	0.25	0.09	0.21	0.07	0.28	0.04
K_2O	0.01	0.01	0.00	0.00	0.00	0.00	0.00	0.01	0.01	0.01
Cr_2O_3	0.26	0.17	0.69	0.05	0.68	0.03	0.07	0.08	0.26	0.02
Total	98.03	0.40	99.08	0.34	98.86	0.10	99.59	0.51	100.35	0.10
Oxygen	6		6		6		6		6	
Si	1.94		1.89		1.91		1.93		1.93	
Ti	0.00		0.01		0.01		0.01		0.01	
Al	0.11		0.15		0.14		0.11		0.13	
Fe	0.14		0.20		0.14		0.12		0.12	
Mn	0.01		0.01		0.00		0.00		0.00	
Mg	0.89		0.88		0.90		0.95		0.95	
Ca	0.90		0.83		0.87		0.88		0.86	
Na	0.02		0.03		0.02		0.01		0.02	
K	0.00		0.00		0.00		0.00		0.00	
Cr	0.01		0.02		0.02		0.00		0.01	
Total	4.00		4.02		4.01		4.01		4.01	
X_{Mg}	0.87		0.82		0.86		0.89		0.89	

X_{Mg}=Mg^{2+}/(Mg^{2+}+Fe^{2+}), where Mg^{2+} and Fe^{2+} are in atoms per formula unit (a.p.f.u.).

Table. 2.2. Continue of chemical composition of primary minerals in gabbroic rocks (in wt. %) with 1σ standard deviation and calculated structural formula.

Sample	CM1A-7Z1-43-45		CM1A-9Z3-26-30		CM1A-46Z1-34-39		CM1A-47Z2-62-67		CM1A-48Z3-10-15		CM1A-55Z1-76-81		CM1A-57Z3-12-17		CM1A-58Z1-50-54		CM1A-113Z3-25-30	
Lithology	Olivine gabbro		Olivine gabbro		Olivine gabbro		Olivine gabbro		Olivine gabbro		Olivine gabbro		Olivine gabbro		Gabbro		Harzburgite	
Mineral	Plagioclase		Plagioclase		Plagioclase		Plagioclase		Plagioclase		Plagioclase		Plagioclase		Plagioclase		Plagioclase	
N	3		4		3		8		5		12		9		6		10	
	avg.	1σ	avg.	1σ	avg.	1σ	avg.	1σ	avg.	1σ	avg.	1σ	avg.	1σ	avg.	1σ	avg.	1σ
SiO_2	46.82	0.13	46.63	0.30	46.73	0.12	45.65	0.41	45.34	0.33	45.69	1.16	46.50	0.52	45.76	0.18	46.09	0.53
TiO_2	0.01	0.02	0.01	0.01	0.00	0.01	0.02	0.02	0.01	0.02	0.02	0.04	0.04	0.04	0.01	0.01	0.01	0.01
Al_2O_3	32.99	0.07	33.00	0.29	33.03	0.16	34.09	0.26	34.29	0.13	33.73	1.05	32.84	0.27	33.65	0.27	34.07	0.45
FeO	0.49	0.03	0.51	0.06	0.45	0.04	0.46	0.13	0.30	0.01	0.45	0.14	0.46	0.07	0.45	0.09	0.30	0.08
MnO	0.00	0.00	0.03	0.05	0.01	0.01	0.03	0.02	0.02	0.02	0.02	0.03	0.01	0.03	0.03	0.03	0.02	0.03
MgO	0.06	0.02	0.06	0.02	0.05	0.02	0.02	0.02	0.03	0.03	0.07	0.07	0.05	0.04	0.02	0.02	0.04	0.04
CaO	16.84	0.03	17.35	0.05	17.39	0.09	18.01	0.26	18.03	0.30	17.64	1.01	16.81	0.35	17.80	0.09	17.76	0.54
Na_2O	1.98	0.05	1.81	0.17	1.66	0.13	1.28	0.13	1.27	0.12	1.37	0.60	1.83	0.29	1.44	0.11	1.46	0.32
K_2O	0.01	0.00	0.01	0.00	0.01	0.00	0.01	0.01	0.00	0.00	0.00	0.01	0.02	0.01	0.01	0.01	0.03	0.03
Cr_2O_3	0.01	0.01	0.01	0.01	0.00	0.00	0.01	0.02	0.00	0.01	0.00	0.01	0.01	0.02	0.01	0.01	0.01	0.01
Total	99.21	0.08	99.41	0.39	99.33	0.32	99.58	0.43	99.30	0.18	99.01	0.40	98.57	0.49	99.23	0.16	99.78	0.44
Oxygen	8		8		8		8		8		8		8		8		8	
Si	2.17		2.16		2.17		2.12		2.11		2.13		2.17		2.13		2.13	
Ti	0.00		0.00		0.00		0.00		0.00		0.00		0.00		0.00		0.00	
Al	1.80		1.80		1.80		1.86		1.88		1.85		1.81		1.85		1.85	
Fe	0.02		0.02		0.02		0.02		0.01		0.02		0.02		0.02		0.01	
Mn	0.00		0.00		0.00		0.00		0.00		0.00		0.00		0.00		0.00	
Mg	0.00		0.00		0.00		0.00		0.00		0.00		0.00		0.00		0.00	
Ca	0.84		0.86		0.86		0.89		0.90		0.88		0.84		0.89		0.88	
Na	0.18		0.16		0.15		0.11		0.11		0.12		0.17		0.13		0.13	
K	0.00		0.00		0.00		0.00		0.00		0.00		0.00		0.00		0.00	
Cr	0.00		0.00		0.00		0.00		0.00		0.00		0.00		0.00		0.00	
Total	5.01		5.02		5.01		5.01		5.01		5.01		5.01		5.01		5.01	
X_{Ca}	0.82		0.84		0.85		0.89		0.89		0.88		0.84		0.87		0.87	

$X_{Mg}=Mg^{2+}/(Mg^{2+}+Fe^{2+})$, where Mg^{2+} and Fe^{2+} are in atoms per formula unit (a.p.f.u.).

Table 2.3. Protolith mineral mode of gabbroic rocks determined by bulk-rock chemistry

	Mineral mode			
Sample	Pl (wt%)	Cpx (wt%)	Ol (wt%)	Total
C5707A-7Z1-43-45	17.0 - 18.0	10.3 - 13.8	64.1 - 72.2	91.4 - 104.1
C5707A-7Z2-38-42	11.1 - 11.7	32.2 - 37.0	44.3 - 52.0	87.6 - 100.7
C5707A-8Z2-10-14	24.9 - 26.4	33.0 - 39.9	32.3 - 39.9	90.2 - 106.2
C5707A-28Z1-85-88	42.8 - 45.4	39.3 - 49.5	8.2 - 15.2	90.3 - 110.0
C5707A-32Z1-53-55	25.1 - 26.6	12.2 - 17.1	42.1 - 48.8	79.4 - 92.6
C5707A-39Z1-84-88	60.7 - 64.3	21.4 - 32.6	1.3 - 7.2	83.4 - 104.1
C5707A-46Z1-34-39	65.8 - 69.8	17.9 - 29.5	3.3 - 9.4	87.0 - 108.7
C5707A-47Z2-62-67	41.1 - 43.6	25.4 - 34.0	26.2 - 33.6	92.7 - 111.1
C5707A-48Z3-10-15	41.3 - 43.8	21.4 - 29.7	28.6 - 35.9	91.4 - 109.4
C5707A-51Z2-72-77	48.7 - 51.7	17.9 - 26.9	32.1 - 39.9	98.7 - 118.5
C5707A-51Z4-72-77	42.9 - 45.5	46.3 - 57.2	10.4 - 18.2	99.6 - 120.9
C5707A-55Z1-76-81	27.1 - 28.7	11.1 - 16.2	49.6 - 57.1	87.8 - 102.1
C5707A-57Z3-12-17	13.5 - 14.3	0.0 - 0.0	69.7 - 77.0	83.2 - 91.3
C5707A-57Z3-43-48	43.7 - 46.4	15.4 - 23.4	34.7 - 42.1	93.8 - 112.0
C5707A-58Z1-50-54	44.8 - 47.5	12.7 - 20.7	36.5 - 44.0	94.0 - 112.1
C5707A-113Z3-25-30	53.1 - 56.3	29.9 - 40.7	9.4 - 16.4	92.4 - 113.4
C5707A-113Z4-11-16	47.8 - 50.7	62.3 - 75.4	0.0 - 8.5	110.1 - 134.6
C5707A-124Z1-40-48	30.3 - 32.1	72.1 - 83.5	5.3 - 14.2	107.7 - 129.8
C5708B-41Z4-72-77	35.8 - 37.9	36.2 - 45.0	28.8 - 37.1	100.8 - 120.0

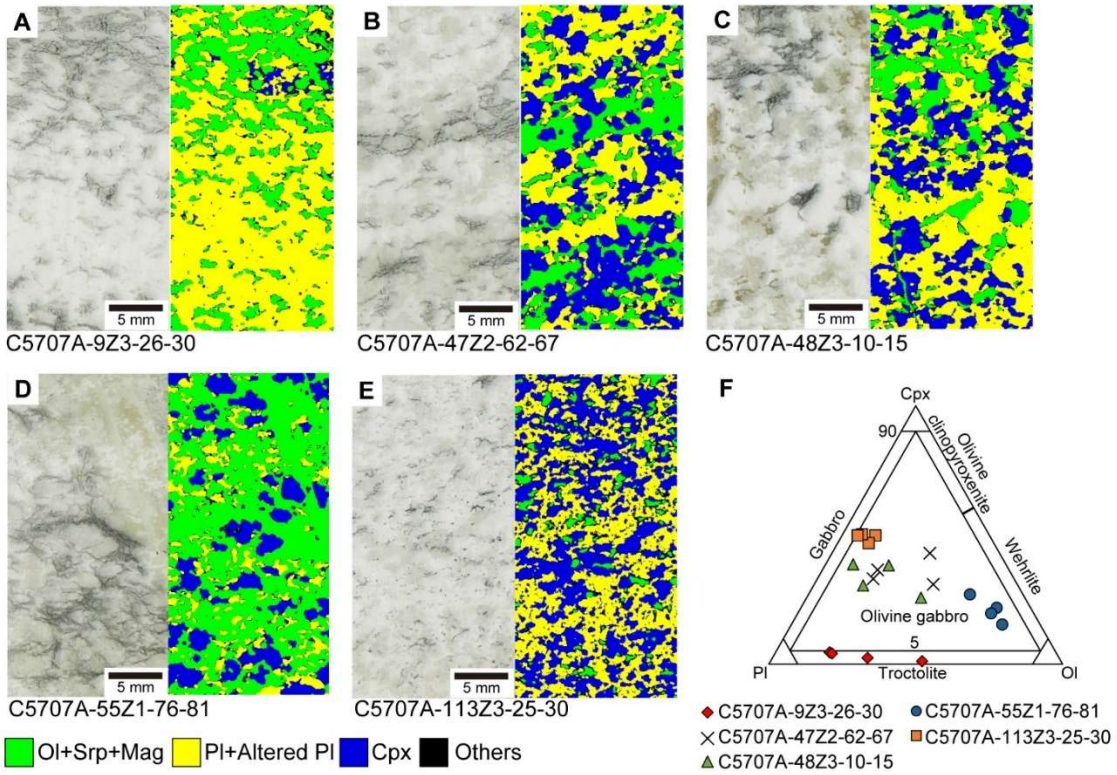

Fig. 2.11. Mineral phase map of selected gabbroic rocks. The mineral phase map based on element map of Ca, Al, Mg, and Fe obtained by micro XRF. (A)CM1A-9Z3-26-30. (B)CM1A-47Z2-62-67. (C)CM1A-48Z3-10-15. (D)CM1A-55Z1-76-81. (E)CM1A-113Z3-25-30. (F)Classification of the gabbroic rocks based on plagioclase-clinopyroxene-olivine diagram. Ol=olivine, Srp=serpentine, Mag=magnetite, Pl=plagioclase, Cpx=clinopyroxene.

Serpentinite

The olivine in the gabbroic rocks is partially serpentinized with a mesh texture. Radial cracks are observed in the pyroxene and plagioclase surrounding the serpentinized olivine (Fig. 2.12A-B). Compared to olivine, clinopyroxene is less altered (Fig. 2.12A). The alteration of olivine (serpentinization) is higher than plagioclase (Fig. 2.12B). A mesh texture is seen within the single crystal olivine. Type 1 mesh textures (~5-30 μm wide) are cut by thicker type 2 mesh textures (~50-150 μm wide) (Fig. 2.12C).

The type 2 mesh texture is connected to radial cracks in the plagioclase (Fig. 2.13A-B). The type 2 mesh texture cutting the type 1 mesh texture is enriched in Al (Fig. 2.13C-D). The serpentine around clinopyroxene is richer in Al (Al_2O_3=~2.5-3.0 wt. %; Table 2.4) and Fe (FeO^* = ~6-10 wt. %; Table 2.4), than the serpentine that replaces the olivine (Al_2O_3 = ~0 wt. %, FeO^* = ~2.5-4.0 wt. %; Table 2.4). The Si versus Mg+Fe plot based on structural chemical formula shows that the type 1 mesh texture is on a mixed line of serpentine + brucite, whereas the type 2 mesh texture is closer to a mixed line of serpentine + talc (Fig. 2.14A). On the other hand, the Si versus Mg plot shows that type 1 is not on the serpentine + brucite mixing line, indicating a high Fe content in the brucite (Fig. 2.14B). X_{Mg} of serpentine obtained from the extrapolation of the Si versus Mg+Fe and Si versus Mg plots are 0.96.

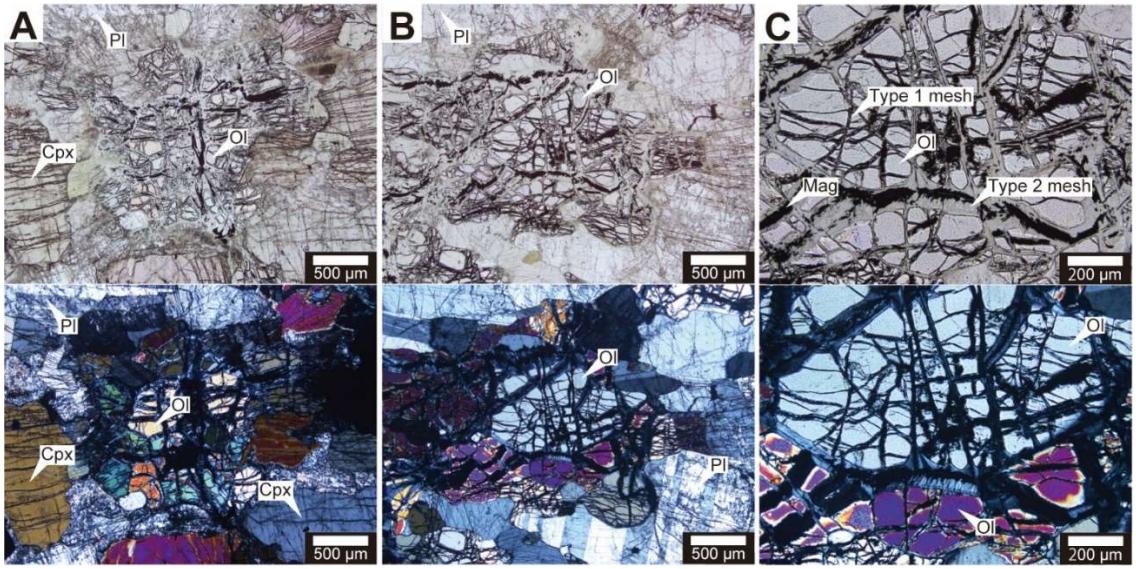

Fig. 2.12. Optical microscope photographs of gabbroic rocks under plane polarized light and crossed polarized light. (A)Partly serpentinized olivine in olivine gabbro (CM1A-47Z2-62-67). (B)Partly serpentinized olivine in troctolite (CM1A-9Z2-26-30). (C)Close up view of the mesh texture. A type 1 mesh textures with a smaller width (~5-30 μm) are cut by a type 2 mesh textures with a larger width (~50-150 μm).

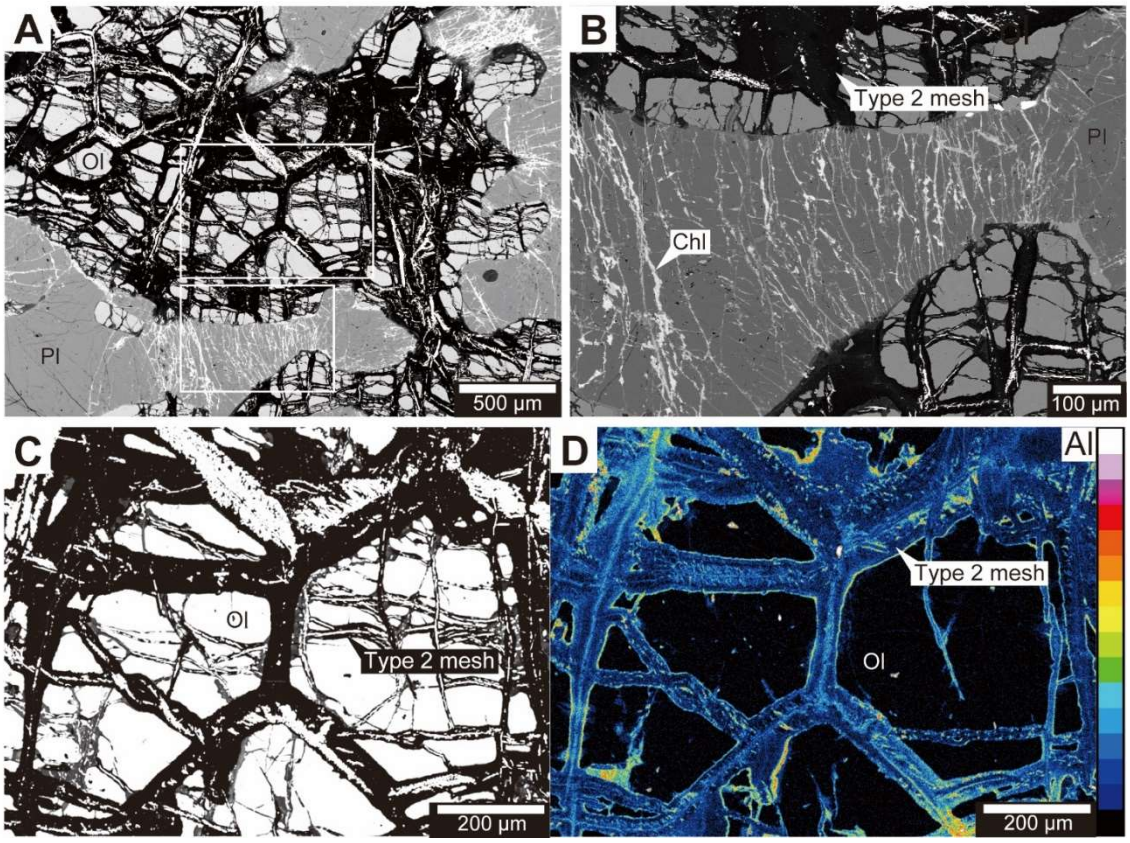

Fig. 2.13. (A) Backscattered electron image of partly serpentinized olivine in troctolite (CM1A-9Z2-26-30). (B) Close up view of the olivine-plagioclase boundary. (C)Close up view of the backscattered electron image of mesh texture and (D) element map of Al shows Al-rich type 2 mesh texture.

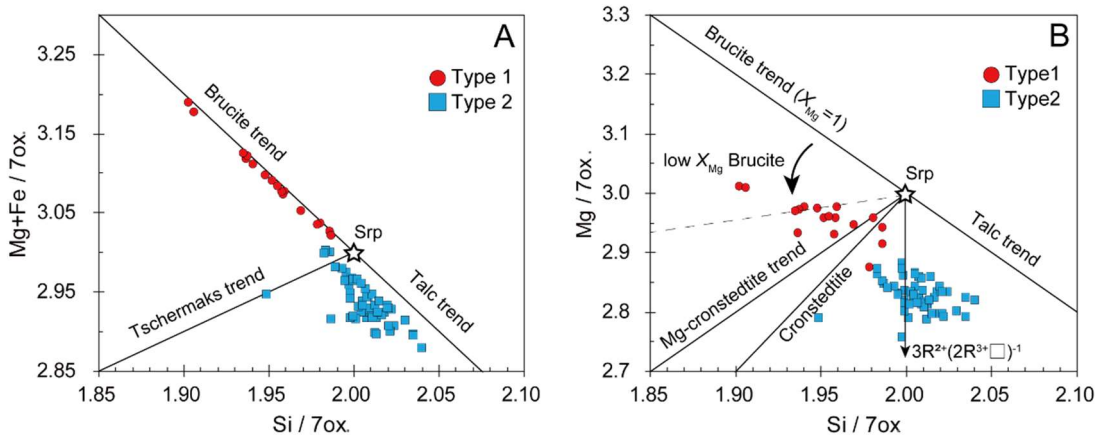

Fig. 2.14. (A) Si versus Mg+Fe plot and (B) Si versus Mg plot of type 1 mesh texture and type 2 mesh texture.

Table 2.4. Chemical composition of serpentine±brucite in gabbroic rocks (in wt. %) with 1σ standard deviation and calculated structural formula.

Sample	CM1A-7Z1-43-45		CM1A-9Z3-26-30				CM1A-47Z2-62-67				CM1A-48Z3-10-15		CM1A-51Z2-72-77			
Lithology	Olivine gabbro		Troctolite				Olivine gabbro				Olivine gabbro		Olivine gabbro			
Mineral	Srp		Srp+Brc		Srp		Srp+Brc		Srp		Srp		Srp		Srp	
Type	Mesh		Type 1 mesh		Type 2 mesh		Type 1 mesh		Type 2 mesh		Mesh		Mesh rim		Mesh core	
N	8		35		208		42		121		11		45		19	
	avg.	1σ	avg.	1σ	avg.	1σ	avg.	1σ	avg.	1σ	avg.	1σ	avg.	1σ	avg.	1σ
SiO_2	40.56	0.44	39.98	1.33	41.20	0.94	40.66	2.01	41.33	1.68	40.93	0.95	41.05	1.09	37.90	0.42
TiO_2	0.01	0.01	0.01	0.01	0.01	0.01	0.01	0.01	0.01	0.02	0.01	0.01	0.02	0.02	0.01	0.01
Al_2O_3	1.86	0.75	0.01	0.01	0.70	0.36	0.22	0.91	0.63	0.78	0.36	0.18	1.58	1.44	5.95	0.23
FeO	3.87	0.29	3.90	1.59	2.75	0.95	4.43	3.74	2.68	2.18	3.33	1.77	2.40	0.84	8.11	0.26
MnO	0.06	0.04	0.03	0.04	0.04	0.04	0.02	0.04	0.02	0.03	0.01	0.01	0.03	0.03	0.04	0.04
MgO	37.59	0.55	40.45	0.96	39.00	1.61	38.60	3.42	39.95	1.60	39.41	0.98	38.68	1.34	30.61	0.44
CaO	0.04	0.01	0.02	0.02	0.04	0.02	0.02	0.02	0.01	0.01	0.05	0.03	0.15	0.04	0.43	0.03
Na_2O	0.01	0.01	0.02	0.02	0.01	0.02	0.01	0.02	0.02	0.03	0.04	0.03	0.02	0.04	0.04	0.05
K_2O	0.01	0.01	0.01	0.01	0.01	0.02	0.01	0.01	0.00	0.01	0.01	0.01	0.01	0.01	0.03	0.01
Cr_2O_3	0.01	0.01	0.01	0.01	0.01	0.02	0.01	0.01	0.01	0.02	0.01	0.01	0.01	0.02	0.02	0.02
Total	83.99	0.96	84.44	1.12	83.76	1.98	84.00	1.59	84.66	1.59	84.16	0.55	83.94	0.71	83.14	0.63
Oxygen	7		7		7		7		7		7		7		7	
Si	1.97		1.95		2.00		1.99		1.99		1.99		1.98		1.90	
Ti	0.00		0.00		0.00		0.00		0.00		0.00		0.00		0.00	
Al	0.11		0.00		0.04		0.01		0.04		0.02		0.09		0.35	
Fe	0.16		0.16		0.11		0.19		0.11		0.14		0.10		0.34	
Mn	0.00		0.00		0.00		0.00		0.00		0.00		0.00		0.00	
Mg	2.73		2.94		2.82		2.81		2.86		2.85		2.79		2.29	
Ca	0.00		0.00		0.00		0.00		0.00		0.00		0.01		0.02	
Na	0.00		0.00		0.00		0.00		0.00		0.00		0.00		0.00	
K	0.00		0.00		0.00		0.00		0.00		0.00		0.00		0.00	
Cr	0.00		0.00		0.00		0.00		0.00		0.00		0.00		0.00	
Total	4.97		5.05		4.98		5.00		5.00		5.00		4.97		4.92	
X_{Srp}			0.97				0.99									
X_{Mg} of Srp	0.95		0.98		0.96		0.94		0.96		0.95		0.97		0.87	
X_{Mg} of Brc			0.50				0.73									

$X_{Mg}=Mg^{2+}/(Mg^{2+}+Fe^{2+})$, where Mg^{2+} and Fe^{2+} are in atoms per formula unit (a.p.f.u.).

Table 2.4. Continue of chemical composition of serpentine±brucite in gabbroic rocks (in wt. %) with 1σ standard deviation and calculated structural formula.

Sample	CM1A-55Z1-76-81				CM1A-57Z3-12-17				CM1A-58Z1-50-54		CM1A-113Z3-25-30		OM230111P4-1			
Lithology	Olivine gabbro				Olivine gabbro				Olivine gabbro		Olivine gabbro		Olivine gabbro			
Mineral	Srp+Brc		Srp		Srp		Srp		Srp		Srp+Brc		Srp		Srp	
Type	Type 1 mesh		Type 2 mesh		Mesh rim		Mesh core		Mesh		Mesh		Mesh rim		Mesh core	
N	22		20		30		20		3		51		10		10	
	avg.	1σ	avg.	1σ	avg.	1σ	avg.	1σ	avg.	1σ	avg.	1σ	avg.	1σ	avg.	1σ
SiO_2	38.57	1.35	40.81	0.55	42.48	1.08	36.86	0.47	41.91	0.20	37.48	3.90	41.68	0.52	39.77	0.41
TiO_2	0.01	0.01	0.02	0.02	0.02	0.03	0.02	0.03	0.00	0.01	0.01	0.01	0.01	0.02	0.01	0.02
Al_2O_3	0.03	0.03	0.02	0.04	0.39	0.44	6.82	0.35	0.74	0.03	0.14	0.18	0.53	0.19	1.93	0.09
FeO	8.87	1.95	3.84	1.00	3.66	0.92	16.02	0.33	5.23	0.10	6.01	5.96	2.87	0.55	6.94	0.32
MnO	0.05	0.05	0.06	0.04	0.05	0.04	0.08	0.05	0.11	0.03	0.02	0.03	0.04	0.04	0.13	0.06
MgO	36.33	1.50	39.81	0.54	38.30	0.98	20.85	0.84	34.47	0.59	41.06	2.40	38.87	0.82	30.46	0.69
CaO	0.12	0.06	0.09	0.02	0.11	0.11	1.48	0.37	0.68	0.04	0.05	0.03	0.04	0.02	0.11	0.01
Na_2O	0.02	0.04	0.02	0.04	0.03	0.05	0.08	0.06	0.11	0.02	0.04	0.04	0.02	0.04	0.08	0.06
K_2O	0.01	0.01	0.00	0.00	0.01	0.01	0.09	0.02	0.01	0.01	0.01	0.01	0.01	0.01	0.01	0.01
Cr_2O_3	0.01	0.02	0.01	0.02	0.01	0.02	0.02	0.03	0.02	0.02	0.01	0.01	0.01	0.02	0.01	0.02
Total	84.02	0.78	84.70	0.82	85.06	0.97	82.31	1.56	83.34	0.61	84.83	1.88	84.08	0.64	79.47	1.14
Oxygen	7		7		7		7		7		7		7		7	
Si	1.94		1.98		2.04		1.95		2.07		1.85		2.02		2.07	
Ti	0.00		0.00		0.00		0.00		0.00		0.00		0.00		0.00	
Al	0.00		0.00		0.02		0.43		0.04		0.01		0.03		0.12	
Fe	0.37		0.16		0.15		0.71		0.22		0.26		0.12		0.30	
Mn	0.00		0.00		0.00		0.00		0.00		0.00		0.00		0.01	
Mg	2.73		2.88		2.74		1.65		2.54		3.03		2.80		2.36	
Ca	0.01		0.00		0.01		0.08		0.04		0.00		0.00		0.01	
Na	0.00		0.00		0.00		0.01		0.01		0.00		0.00		0.01	
K	0.00		0.00		0.00		0.01		0.00		0.00		0.00		0.00	
Cr	0.00		0.00		0.00		0.00		0.00		0.00		0.00		0.00	
Total	5.06		5.02		4.95		4.84		4.91		5.15		4.97		4.87	
X_{Srp}	0.97										0.92					
X_{Mg} of Srp	0.89		0.95		0.95		0.70		0.92		1.00		0.96		0.89	
X_{Mg} of Brc	0.67										0.51					

X_{Mg}=Mg^{2+}/(Mg^{2+}+Fe^{2+}), where Mg^{2+} and Fe^{2+} are in atoms per formula unit (a.p.f.u.).

The Raman spectra of the Type 1 and Type 2 mesh textures have peaks at 230.53, 283.61, 688.6, 3682.56, 3705.23 and 129.74, 230.53, 385.39, 688.60, 3682.56, 3705.23 cm^{-1}, respectively. The strong peak at 3682.56 cm^{-1} and the smaller peak at 3705.23 cm^{-1} are similar to the Raman spectrum of lizardite (Fig. 2.15). Although the EPMA analysis indicates that the Type 1 mesh texture contains brucite (Fig. 2.14A), the Raman spectrum shows no brucite peaks (3631 cm^{-1}; Fig. 2.15). This may be due to the low brucite content. Multi-stage serpentine veins, such as thinner first-generation mesh textures (type 1) associate with brucite and thicker second-generation mesh textures (type 2) without brucite, in gabbroic rocks are also found in oceanic gabbroic rocks (Beard *et al.*, 2009) and in dunite in other ophiolites (Frost *et al.*, 2013).

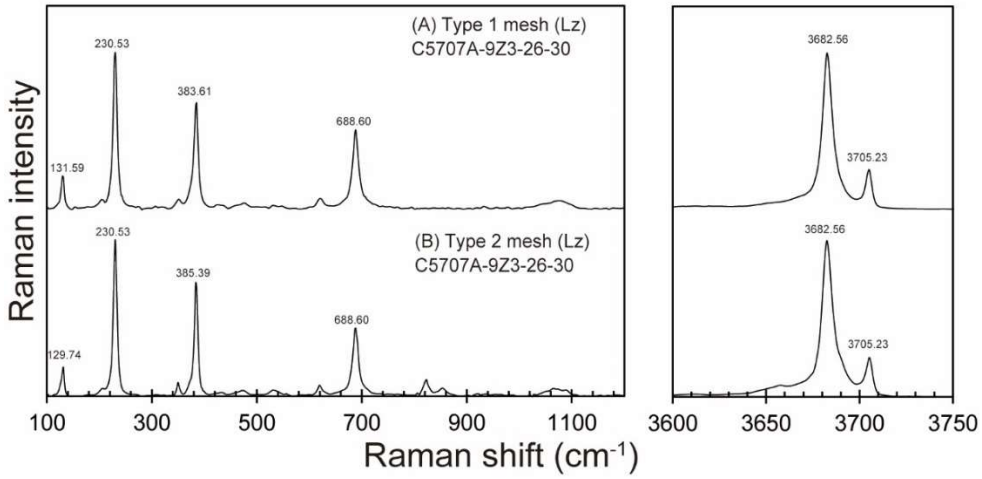

Fig. 2.15. Raman spectra of serpentine minerals in gabbroic rocks. (A)Type 1 mesh (CM1A-9Z3-26-30), (B)Type 2 mesh (CM1A-9Z3-26-30).

Chlorite, prehnite and talc

Chlorite and prehnite are found as minerals that filling in the radial cracks in plagioclase around the olivine grains (Fig. 2.13B) or replacing plagioclase (Fig. 2.16A). In the highly altered gabbroic rocks, chlorite and prehnite completely replace the plagioclase (Fig. 2.16B). Less amount of magnetite observed in serpentinized olivine adjacent to prehnite and chlorite (Fig. 2.16B). Talc is found as a mineral that replacing olivine near partly altered plagioclase (Fig. 2.16C).

Chlorite in the gabbroic rocks shows a wide range of Fe contents (FeO^* = ~ 4-30 wt. %; Table 2.5). Chlorite filling radial fractures in plagioclase is enriched in Fe (FeO^* = ~30 wt. %), and Fe-rich talc (FeO^* = ~8.5 wt. %) partially replacing olivine in contact with clinopyroxene. Such Fe-rich talc has also been reported from oceanic gabbroic rocks (Majumdar *et al.*, 2020). Prehnite contains small amounts of FeO and MgO (FeO^* = ~0.2 wt. %, MgO = ~0.1 wt. %; Table 2.5) and is similar to other prehnites found in ultramafic rocks (Zhang *et al.*, 2021). The Raman spectra of chlorite have peaks at 197.70, 547.38, 678.37, 3592.72, and 3677.39 cm^{-1} (Fig. 2.17A). The peaks near 550 and 3600 cm^{-1} are specific to chlorite (Reynard *et al.*, 2015; Wang *et al.*, 2015), and the peaks below 3600 cm^{-1} are attributed to OH groups attached to octahedral sites containing Al (Prieto, 1991). The peaks in the 3600-3700 cm^{-1} range are found in serpentine and talc and are attributed to OH bonded to octahedral sites containing Mg and Fe (Reynard *et al.*, 2015). The absence of a peak at 380 cm^{-1}, which is characteristic of Raman peak of serpentine minerals (Groppo *et al.*, 2006), suggests that the peak at 3677 cm^{-1} is a contribution of talc. The Raman spectrum of prehnite has peaks at 387.17, 521.22, 678.37, and 3479.30 cm^{-1} (Fig. 2.17B), consistent with the characteristics of prehnite reported in a previous study (Wang *et al.*, 2022a). The Raman spectra of talc have peaks at 190.38, 674.95, and 3677.39 cm^{-1} (Fig. 2.17C), consistent with the characteristics of talc reported in previous studies (Reynard *et al.*, 2015).

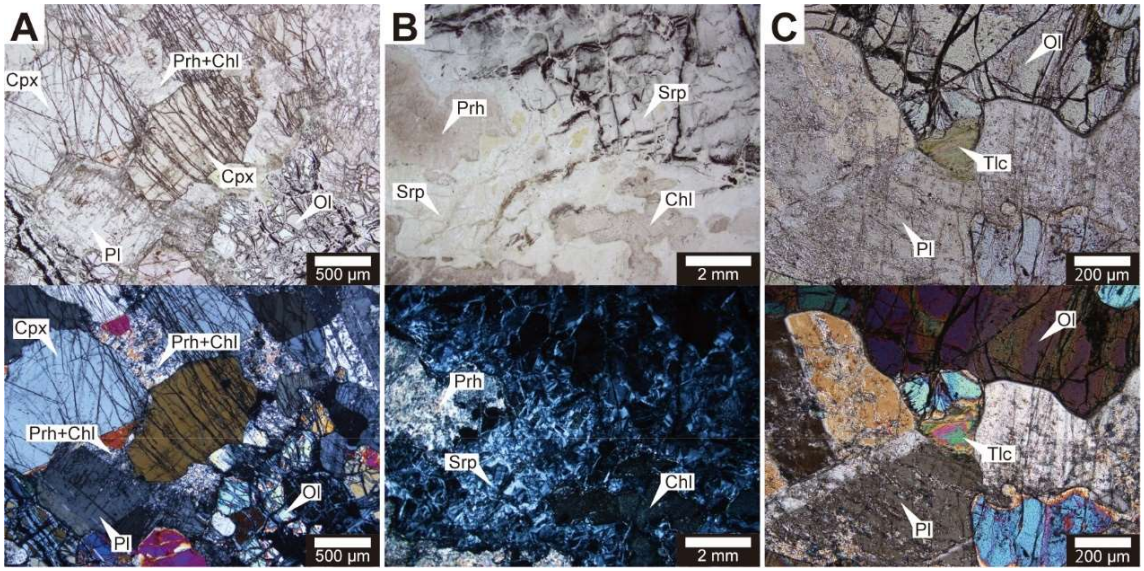

Fig. 2.16. Optical microscope photographs of gabbroic rocks under plane polarized light and crossed polarized light. (A)Partly altered plagioclase shows complex texture of prehnite and chlorite mixture (CM1A-47Z2-62-67). (B) Plagioclase completely altered to prehnite and chlorite in extensively altered gabbro (CM1A-51Z2-72-77). (C)Olivine replaced by talc (CM1A-7Z2-38-42).

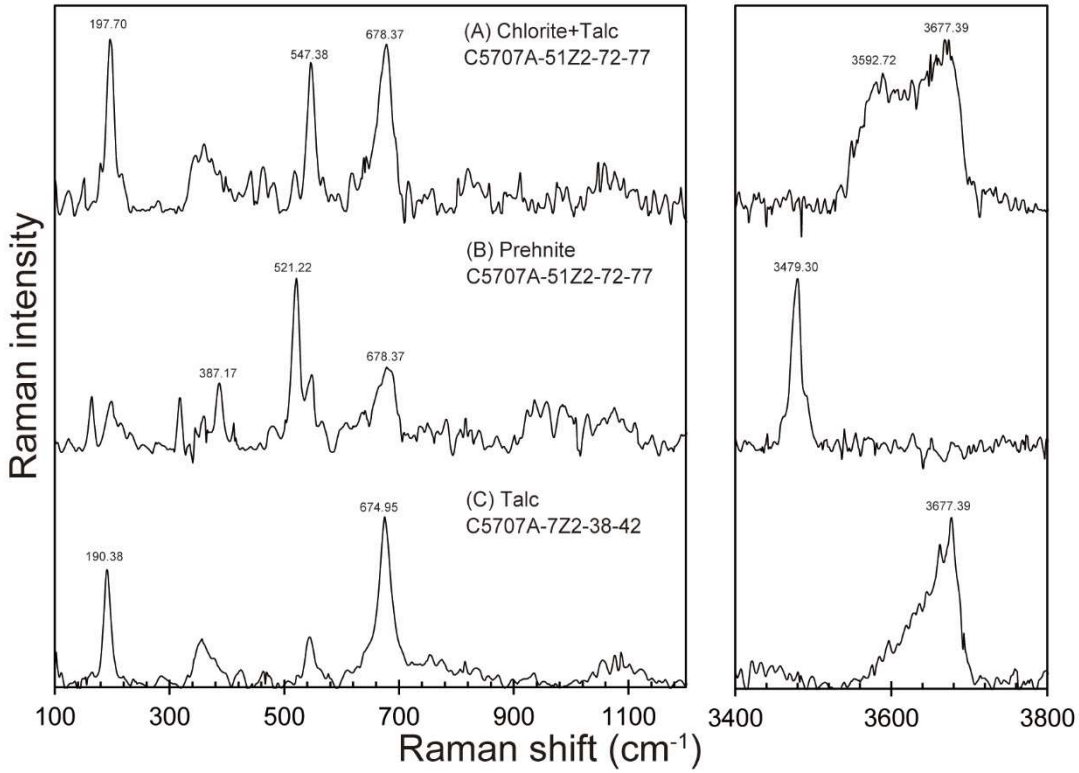

Fig. 2.17. Raman spectra of chlorite, prehnite, and talc. (A)Raman spectra of the chlorite and talc mixture after plagioclase (CM1A-51Z2-72-77). (B)Raman spectra of the prehnite after plagioclase (CM1A-51Z2-72-77). (C)Raman spectra of talc after olivine (CM1A-7Z2-38-42).

Table 2.5. Chemical composition of chlorite, prehnite, and talc in gabbroic rocks (in wt. %) with 1σ standard deviation and calculated structural formula.

Sample	CM1A-7Z1-43-45		CM1A-9Z3-26-30		CM1A-47Z2-62-67		CM1A-48Z3-10-15		CM1A-51Z2-72-77				CM1A-51Z4-72-77		CM1A-55Z1-76-81	
Lithology	Olivine gabbro		Troctolite		Olivine gabbro		Olivine gabbro		Olivine gabbro				Olivine gabbro		Olivine gabbro	
Mineral	Chlorite		Chlorite		Chlorite		Chlorite		Chlorite				Chlorite		Chlorite	
N	7		3		10		2		15		10		20		10	
	avg.	1σ	avg.	1σ	avg.	1σ	avg.	1σ	avg.	1σ	avg.	1σ	avg.	1σ	avg.	1σ
SiO_2	34.67	1.36	24.75	0.44	30.21	4.43	26.34	1.16	30.52	0.98	31.60	0.29	30.75	1.69	24.77	0.48
TiO_2	0.03	0.03	0.01	0.01	0.01	0.02	0.00	0.00	0.02	0.02	0.01	0.01	0.01	0.02	0.02	0.03
Al_2O_3	14.57	1.32	21.91	0.52	18.10	3.99	21.55	0.23	16.75	1.83	17.99	0.34	18.08	1.36	19.87	1.27
FeO	5.66	2.63	33.01	1.80	12.97	11.68	26.52	6.69	11.21	1.64	3.18	0.39	8.08	0.94	29.69	2.27
MnO	0.05	0.07	4.07	0.52	0.64	0.92	0.68	0.28	0.21	0.06	0.20	0.08	0.10	0.05	1.25	0.15
MgO	29.11	2.97	3.81	0.68	23.59	11.82	11.98	5.68	24.96	1.12	30.40	0.44	25.58	3.00	8.25	2.10
CaO	0.35	0.23	0.67	0.17	0.24	0.16	0.27	0.10	0.27	0.20	0.07	0.02	1.58	2.73	0.77	0.07
Na_2O	0.05	0.03	0.07	0.02	0.02	0.02	0.00	0.00	0.07	0.07	0.00	0.01	0.01	0.03	0.05	0.06
K_2O	0.03	0.02	0.01	0.01	0.00	0.00	0.00	0.00	0.01	0.01	0.01	0.01	0.01	0.01	0.00	0.00
Cr_2O_3	0.01	0.01	0.02	0.03	0.01	0.02	0.07	0.04	0.00	0.01	0.01	0.01	0.01	0.02	0.00	0.01
Total	84.53	0.64	88.32	0.57	85.79	0.75	87.41	0.51	84.01	0.94	83.47	0.59	84.22	2.83	84.68	1.55
Oxygen	14		14		14		14		14		14		14		14	
Si	3.38		2.75		3.02		2.80		3.10		3.09		3.07		2.80	
Ti	0.00		0.00		0.00		0.00		0.00		0.00		0.00		0.00	
Al	1.67		2.87		2.19		2.70		2.00		2.07		2.13		2.65	
Fe	0.46		3.08		1.16		2.39		0.95		0.26		0.68		2.81	
Mn	0.00		0.38		0.06		0.06		0.02		0.02		0.01		0.12	
Mg	4.22		0.63		3.43		1.86		3.78		4.43		3.82		1.39	
Ca	0.04		0.08		0.03		0.03		0.03		0.01		0.16		0.09	
Na	0.01		0.01		0.00		0.00		0.01		0.00		0.00		0.01	
K	0.00		0.00		0.00		0.00		0.00		0.00		0.00		0.00	
Cr	0.00		0.00		0.00		0.01		0.00		0.00		0.00		0.00	
Total	9.79		9.82		9.89		9.85		9.90		9.88		9.87		9.88	
X_{Mg}	0.90		0.17		0.75		0.44		0.80		0.94		0.85		0.33	

$X_{Mg}=Mg^{2+}/(Mg^{2+}+Fe^{2+})$, where Mg^{2+} and Fe^{2+} are in atoms per formula unit (a.p.f.u.).

Table 2.5. Continue of chemical composition of chlorite, prehnite, and talc in gabbroic rocks (in wt. %) with 1σ standard deviation and calculated structural formula.

Sample	CM1A-57Z3-12-17		CM1A-58Z1-50-54		CM1A-7Z1-43-45		CM1A-51Z2-72-77		CM1A-51Z4-72-77				CM1A-57Z3-12-17		CM1A-58Z1-50-54		CM1A-7Z1-43-45	
Lithology	Olivine gabbro		Gabbro		Olivine gabbro		Olivine gabbro		Olivine gabbro				Olivine gabbro		Olivine gabbro		Olivine gabbro	
Mineral	Chlorite		Chlorite		Prehnite		Prehnite		Prehnite Matrix		Prehnite Vein		Prehnite		Prehnite		Talc	
N	20		6		3		23		20		3		3		3		3	
	avg.	1σ			avg.	1σ	avg.	1σ	avg.	1σ	avg.	1σ	avg.	1σ	avg.	1σ	avg.	1σ
SiO_2	31.00	0.63	33.22	2.24	43.63	0.20	42.51	0.48	43.21	0.41	43.03	0.37	42.78	0.33	43.61	0.35	54.40	3.21
TiO_2	0.01	0.02	0.02	0.02	0.02	0.01	0.02	0.02	0.02	0.02	0.02	0.02	0.08	0.07	0.03	0.03	0.02	0.01
Al_2O_3	18.14	0.79	14.95	3.98	23.95	0.14	23.82	0.31	23.50	0.27	23.45	0.38	23.95	0.29	23.86	0.09	0.05	0.05
FeO	4.36	0.32	5.66	0.39	0.29	0.02	0.21	0.37	0.06	0.05	0.08	0.06	0.22	0.07	0.21	0.11	6.07	2.44
MnO	0.05	0.04	0.05	0.03	0.00	0.00	0.05	0.06	0.02	0.03	0.04	0.05	0.08	0.03	0.05	0.04	0.02	0.02
MgO	30.66	0.42	31.47	1.91	0.00	0.00	0.13	0.47	0.18	0.21	0.01	0.02	0.01	0.01	0.04	0.01	24.05	1.85
CaO	0.11	0.07	0.08	0.06	25.78	0.15	25.70	0.65	25.40	0.45	25.52	0.25	25.51	0.28	25.37	0.26	6.70	6.48
Na_2O	0.04	0.05	0.06	0.05	0.07	0.07	0.05	0.07	0.05	0.07	0.07	0.07	0.06	0.10	0.07	0.04	0.07	0.05
K_2O	0.01	0.01	0.01	0.01	0.01	0.01	0.01	0.01	0.01	0.01	0.01	0.01	0.01	0.01	0.01	0.01	0.02	0.01
Cr_2O_3	0.01	0.01	0.02	0.03	0.02	0.03	0.01	0.02	0.02	0.02	0.02	0.03	0.03	0.03	0.02	0.01	0.03	0.03
Total	84.40	0.53	85.64	1.52	93.76	0.42	92.51	0.48	92.47	0.67	92.26	0.77	92.71	0.65	93.35	0.68	91.43	5.44
Oxygen	14		14		11		11		11		11		11		11		11	
Si	3.02		3.21		3.05		3.01		3.05		3.05		3.02		3.05		3.81	
Ti	0.00		0.00		0.00		0.00		0.00		0.00		0.00		0.00		0.00	
Al	2.08		1.70		1.97		1.99		1.96		1.96		1.99		1.97		0.00	
Fe	0.36		0.46		0.02		0.01		0.00		0.00		0.01		0.01		0.36	
Mn	0.00		0.00		0.00		0.00		0.00		0.00		0.00		0.00		0.00	
Mg	4.45		4.54		0.00		0.01		0.02		0.00		0.00		0.00		2.53	
Ca	0.01		0.01		1.93		1.95		1.92		1.94		1.93		1.90		0.48	
Na	0.01		0.01		0.01		0.01		0.01		0.01		0.01		0.01		0.01	
K	0.00		0.00		0.00		0.00		0.00		0.00		0.00		0.00		0.00	
Cr	0.00		0.00		0.00		0.00		0.00		0.00		0.00		0.00		0.00	
Total	9.94		9.94		6.97		6.99		6.97		6.97		6.98		6.96		7.19	
X_{Mg}	0.93		0.91														0.87	

X_{Mg}=Mg^{2+}/(Mg^{2+}+Fe^{2+}), where Mg^{2+} and Fe^{2+} are in atoms per formula unit (a.p.f.u.).

Amphibole

A small amount of hornblende replaces olivine at the boundaries with plagioclase (Fig. 2.18A-B). Similar occurrence of amphibole is observed in other site of the Oman ophiolite, which may be produced during high temperature hydrothermal alteration near the mid-ocean ridge (Bosch *et al.*, 2004; Manning *et al.*, 2000). The chemical composition of amphibole minerals is shown in Table 2.6.

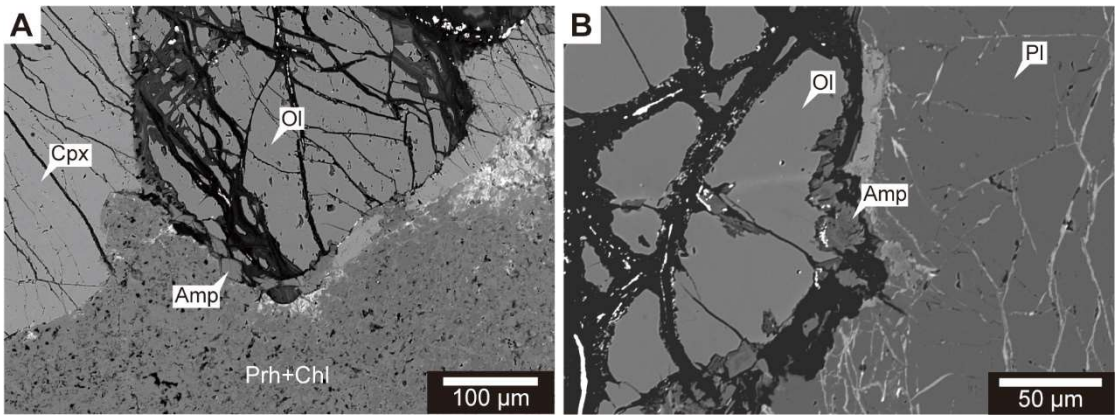

Fig. 2.18. Backscattered electron image of amphibole located along the olivine-plagioclase boundary (CM1A-47Z2-62-67).

Table 2.6. Chemical composition of amphibole in gabbroic rocks (in wt. %) with 1σ standard deviation and calculated structural formula.

Sample	CM1A-7Z1-43-45		CM1A-9Z3-26-30				CM1A-47Z2-62-67				CM1A-48Z3-10-15			
Lithology	Olivine gabbro		Troctolite				Olivine gabbro				Olivine gabbro			
Mineral	Tremolite		Hornblende		Actinorite		Hornblende		Tremolite		Hornblende		Tremolite	
N	8		8		3		14		1		2		3	
	avg.	1σ	avg.	1σ	avg.	1σ	avg.	1σ	avg.		avg.	1σ	avg.	1σ
SiO_2	54.50	3.00	48.42	1.66	51.27	0.09	44.74	1.83	55.25		43.37	4.57	50.65	0.22
TiO_2	0.02	0.02	0.22	0.10	0.46	0.05	0.05	0.03	0.00		0.01	0.01	0.01	0.02
Al_2O_3	1.03	1.34	8.44	2.33	2.59	0.13	13.51	1.95	2.56		19.97	9.14	6.89	0.42
FeO	3.49	0.39	5.76	0.50	4.68	0.16	5.62	0.44	2.70		4.68	0.31	4.00	0.28
MnO	0.05	0.05	0.09	0.04	0.14	0.01	0.05	0.02	0.04		0.08	0.01	0.06	0.02
MgO	24.34	2.06	18.20	0.79	15.69	0.08	17.26	0.86	22.13		9.70	9.63	20.67	0.96
CaO	10.87	2.29	12.58	0.13	22.95	0.26	12.69	0.20	13.08		17.58	5.42	12.78	0.47
Na_2O	0.15	0.11	1.37	0.41	0.31	0.05	2.17	0.43	0.28		0.91	0.84	1.17	0.20
K_2O	0.01	0.01	0.07	0.05	0.01	0.01	0.05	0.03	0.02		0.00	0.00	0.00	0.00
Cr_2O_3	0.01	0.02	0.12	0.07	0.26	0.02	0.02	0.02	0.03		0.01	0.01	0.03	0.01
Total	94.48	2.17	95.27	1.59	98.34	0.10	96.16	0.50	96.08		96.31	0.80	96.26	0.29
Oxygen = 23														
Si	7.74		7.00		7.35		6.44		7.72		6.22		7.17	
Ti	0.00		0.02		0.05		0.01		0.00		0.00		0.00	
Al	0.18		1.44		0.44		2.30		0.42		3.40		1.15	
Fe	0.42		0.70		0.56		0.68		0.32		0.56		0.47	
Mn	0.01		0.01		0.02		0.01		0.00		0.01		0.01	
Mg	5.17		3.92		3.35		3.71		4.61		2.04		4.36	
Ca	1.65		1.95		3.52		1.96		1.96		2.72		1.94	
Na	0.04		0.38		0.08		0.61		0.07		0.25		0.32	
K	0.00		0.01		0.00		0.01		0.00		0.00		0.00	
Cr	0.00		0.01		0.03		0.00		0.00		0.00		0.00	
Total	15.19		15.45		15.41		15.71		15.11		15.21		15.42	
X_{Mg}	0.93		0.85		0.86		0.85		0.94		0.78		0.90	

X_{Mg}=Mg^{2+}/(Mg^{2+}+Fe^{2+}), where Mg^{2+} and Fe^{2+} are in atoms per formula unit (a.p.f.u.).

Table 2.6. Continue of chemical composition of amphibole in gabbroic rocks (in wt. %) with 1σ standard deviation and calculated structural formula.

Sample	CM1A-55Z1-76-81				CM1A-57Z3-12-17		CM1A-58Z1-50-54				CM1A-113Z3-25-30	
Lithology	Olivine gabbro				Olivine gabbro		Olivine gabbro				Olivine gabbro	
Mineral	Hornblende		Tremolite		Tremolite		Hornblende		Tremolite		Tremolite	
N	6		3		10		3		3		5	
	avg.	1σ	avg.	1σ	avg.	1σ	avg.	1σ	avg.	1σ	avg.	1σ
SiO_2	45.46	1.39	56.71	0.95	52.32	4.42	45.09	0.23	58.09	0.39	55.06	1.01
TiO_2	0.05	0.03	0.01	0.02	0.01	0.01	0.02	0.03	0.01	0.01	0.02	0.03
Al_2O_3	12.55	1.66	0.29	0.15	1.97	1.73	13.44	0.45	0.10	0.01	3.59	1.05
FeO	6.83	0.48	3.00	0.07	3.03	0.73	6.09	0.26	1.58	0.16	2.94	0.49
MnO	0.16	0.19	0.10	0.01	0.10	0.05	0.05	0.02	0.02	0.01	0.09	0.04
MgO	16.82	0.58	22.12	0.72	22.00	2.52	16.53	0.26	22.97	0.04	21.89	0.46
CaO	12.13	0.49	13.83	0.34	15.57	4.94	12.61	0.09	13.37	0.17	12.71	0.23
Na_2O	2.37	0.23	0.14	0.02	0.20	0.20	1.98	0.04	0.01	0.01	0.71	0.28
K_2O	0.03	0.01	0.00	0.00	0.01	0.01	0.02	0.00	0.00	0.01	0.02	0.01
Cr_2O_3	0.00	0.01	0.01	0.01	0.02	0.02	0.00	0.00	0.01	0.01	0.01	0.01
Total	96.41	0.41	96.21	1.16	95.24	3.13	95.85	0.20	96.23	0.41	97.03	0.31
Oxygen = 23												
Si	6.56		7.93		7.49		6.51		8.03		7.63	
Ti	0.01		0.00		0.00		0.00		0.00		0.00	
Al	2.13		0.05		0.34		2.29		0.02		0.59	
Fe	0.82		0.35		0.36		0.74		0.18		0.34	
Mn	0.02		0.01		0.01		0.01		0.00		0.01	
Mg	3.62		4.61		4.72		3.56		4.74		4.52	
Ca	1.88		2.07		2.38		1.95		1.98		1.89	
Na	0.66		0.04		0.06		0.55		0.00		0.19	
K	0.00		0.00		0.00		0.00		0.00		0.00	
Cr	0.00		0.00		0.00		0.00		0.00		0.00	
Total	15.70		15.06		15.37		15.62		14.96		15.17	
X_{Mg}	0.81		0.93		0.93		0.83		0.96		0.93	

X_{Mg}=Mg^{2+}/(Mg^{2+}+Fe^{2+}), where Mg^{2+} and Fe^{2+} are in atoms per formula unit (a.p.f.u.).

Serpentine vein

Serpentine veins sometimes cut gabbroic rocks, and yellow-colored serpentine is found around the serpentine veins (Fig. 2.19A). The serpentine veins have a radial crystal texture (Fig. 2.19B). At the boundary between the yellow serpentine and the host rock, the mesh texture remains in the yellow serpentine (Fig. 2.19C). However, the yellow serpentine near the serpentine vein has no mesh texture (Fig. 2.19D). Yellow-color serpentine is also found around the serpentine veins (Fig. 2.19E), which cuts vertically through the layered structure of the gabbroic rocks (Fig. 2.4E). The serpentine vein has a microstructural zoning from the host rock boundary to the vein center: chlorite, fine-grained lizardite, core-grained lizardite, and fine-grained lizardite (Fig. 2.19F). The serpentine veins and yellow serpentine are enriched in Al and Fe (Serpentine veins: Al_2O_3 = 0.5-6.7 wt. %, FeO^* = 5-15 wt. %; Yellow serpentine: Al_2O_3=~0.6-6.8 wt. % FeO^* = ~14-16 wt. %; Table 2.7) than the mesh textured serpentine (FeO^* = ~3-4 wt. %, Al_2O_3=~ 0.02-0.03wt. %).

Raman spectra of serpentine veins show peaks at 124.21, 186.72, 226.89, 380.04, 683.48, and 3688.75 cm^{-1} (Fig. 2.20). The peaks above 3600 cm^{-1} are attributed to OH bound to octahedral sites occupied by varying proportions of Mg and Fe, which are dominant in serpentine and talc(Reynard *et al.*, 2015). The presence of a peak near 380 cm^{-1} indicates that it is a serpentine mineral (Groppo *et al.*, 2006). Lizardite and polyhedral serpentine are difficult to distinguish due to similar peaks, but the crystal texture similar to polyhedral serpentine (Fig. 2.19E, Andreani *et al.*, 2008). The yellow serpentine has Raman peaks at 118.67-126.05, 221.43-225.07, 374.69-380.04, 680.07-685.19, and 3683.59-3685.66 cm^{-1}, similar to lizardite. However, the peak at ~3683 cm^{-1} is broader than lizardite, indicating low crystallinity. The serpentine veins that vertically cut the layered structure (Figs. 2.4E, 2.19E, and 2.19F) have similar Raman peaks for the fine-grained lizardite near the boundary with the host rock, the larger-grained lizardite, and the fine-grained lizardite at the center of the vein (Fig. 2.19F), although the serpentine with larger crystals has a peak at 3690.82 cm^{-1} which caused by effect of the crystal orientation anisotropy (Compagnoni *et al.*, 2021).

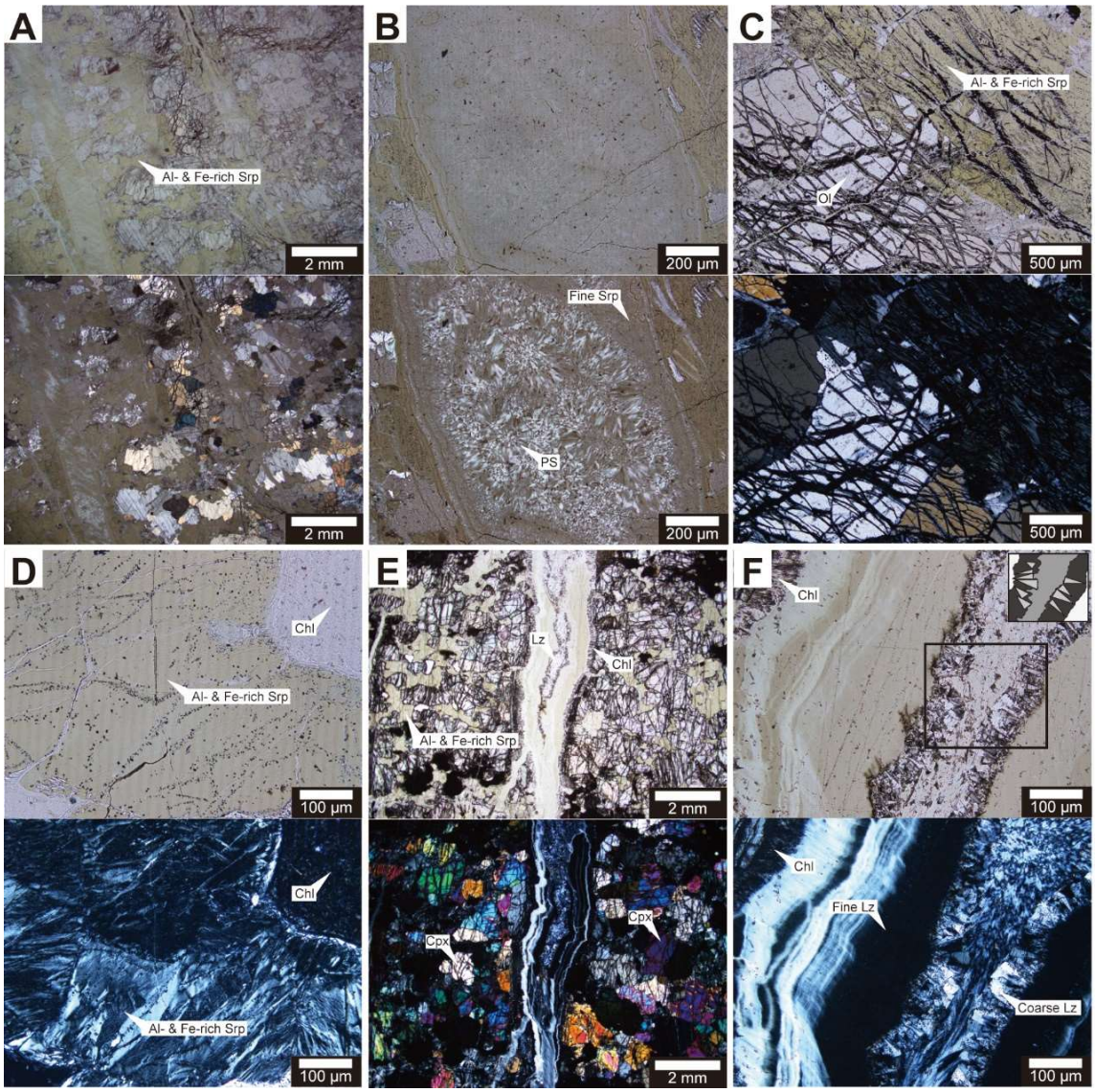

Fig. 2.19. Optical microscope photographs of serpentine veins in gabbroic rocks and Al- and Fe-rich yellow color serpentine under plane polarized light and crossed polarized light. (A)Al and Fe rich serpentine vein cut host rock (CM1A-55Z1-76-81). (B)Close up view of the serpentine vein with a radial texture. (C)Mesh texture partly overwritten by the Al- & Fe-rich serpentine. (D)Mesh texture completely overwritten by Al- & Fe-rich serpentine. (E)Serpentine vein oriented vertically relative to the layered structure of the gabbro (See Fig.2.2E; OM230111P4-1). (F)Close up view of the serpentine vein shows structural zoning texture.

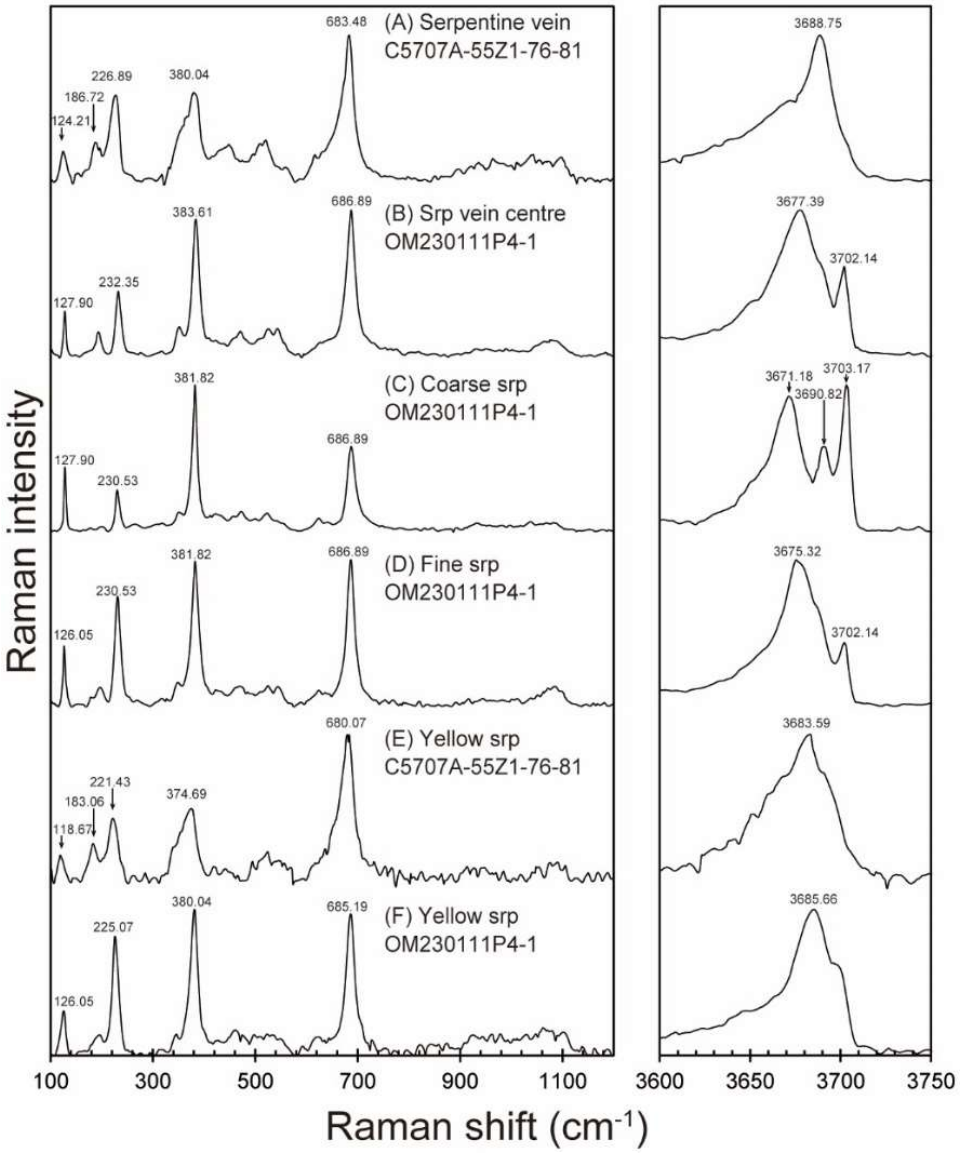

Fig. 2.20. Raman spectra of serpentine veins in gabbroic rocks and yellow color Al- and Fe-rich serpentine near the serpentine veins. (A)Serpentine vein from CM1A-55Z1-76-81. (B)Serpentine vein centre, (C)coarse serpentine crystal, (D)fine serpentine crystal from OM230111P4-1. (E)Yellow color Al- and Fe-rich serpentine from CM1A55Z1-76-81. (F)Yellow color Al- and Fe-rich serpentine from OM230111P4-1.

Table 2.7. Chemical composition of serpentine vein in gabbroic rocks (in wt. %) with 1σ standard deviation and calculated structural formula.

Sample	C5707A-55Z1-76-81						OM230111P4-1			
Lithology	Olivine gabbro						Olivine gabbro			
Mineral	Serpentine		Serpentine		Serpentine		Serpentine		Serpentine	
Type	Vein		Selvage mesh rim		Selvage mesh core		Selvage		Vein	
N	29		10		30		5		20	
	avg.	1σ	avg.	1σ	avg.	1σ	avg.	1σ	avg.	1σ
SiO_2	40.45	0.39	41.93	0.44	39.62	0.57	38.22	0.36	38.35	0.65
TiO_2	0.01	0.02	0.02	0.02	0.01	0.02	0.06	0.04	0.03	0.03
Al_2O_3	0.54	0.19	0.07	0.08	0.62	0.55	2.27	0.16	5.47	0.82
FeO	15.45	1.32	2.22	0.51	13.77	1.69	6.65	0.32	4.46	0.75
MnO	0.21	0.09	0.02	0.02	0.15	0.06	0.12	0.02	0.06	0.04
MgO	27.89	0.92	40.42	0.61	26.89	1.25	26.40	0.74	36.42	1.02
CaO	0.33	0.06	0.08	0.04	0.68	0.05	0.14	0.01	0.02	0.01
Na_2O	0.04	0.06	0.04	0.05	0.04	0.05	0.02	0.03	0.02	0.03
K_2O	0.01	0.01	0.01	0.01	0.01	0.01	0.02	0.01	0.00	0.01
Cr_2O_3	0.01	0.01	0.01	0.02	0.01	0.02	0.05	0.02	0.01	0.02
Total	84.95	0.92	84.81	0.81	81.81	0.92	73.95	1.41	84.86	1.09
Oxygen	7		7		7		7		7	
Si	2.07		2.01		2.09		2.13		1.86	
Ti	0.00		0.00		0.00		0.00		0.00	
Al	0.03		0.00		0.04		0.15		0.31	
Fe	0.66		0.09		0.61		0.31		0.18	
Mn	0.01		0.00		0.01		0.01		0.00	
Mg	2.12		2.88		2.11		2.19		2.63	
Ca	0.02		0.00		0.04		0.01		0.00	
Na	0.00		0.00		0.00		0.00		0.00	
K	0.00		0.00		0.00		0.00		0.00	
Cr	0.00		0.00		0.00		0.00		0.00	
Total	4.92		4.99		4.90		4.80		4.99	
X_{Mg}	0.76		0.97		0.78		0.88		0.94	

$X_{Mg}=Mg^{2+}/(Mg^{2+}+Fe^{2+})$, where Mg^{2+} and Fe^{2+} are in atoms per formula unit (a.p.f.u.).

Prehnite vein

Prehnite veins are observed in highly altered gabbros. In the highly altered gabbro, olivine and plagioclase are completely altered to prehnite and/or chlorite. On the other hand, the clinopyroxene is relatively fresh (Fig. 2.21A). The prehnite veins are composed of course-graine prehnite (~50-500 μm; Fig. 2.21B). The composition of the prehnite in the veins is similar to that of the plagioclase-substituted host prehnite. Prehnite veins are commonly observed in the Oman Ophiolite (Zhang *et al.*, 2021).

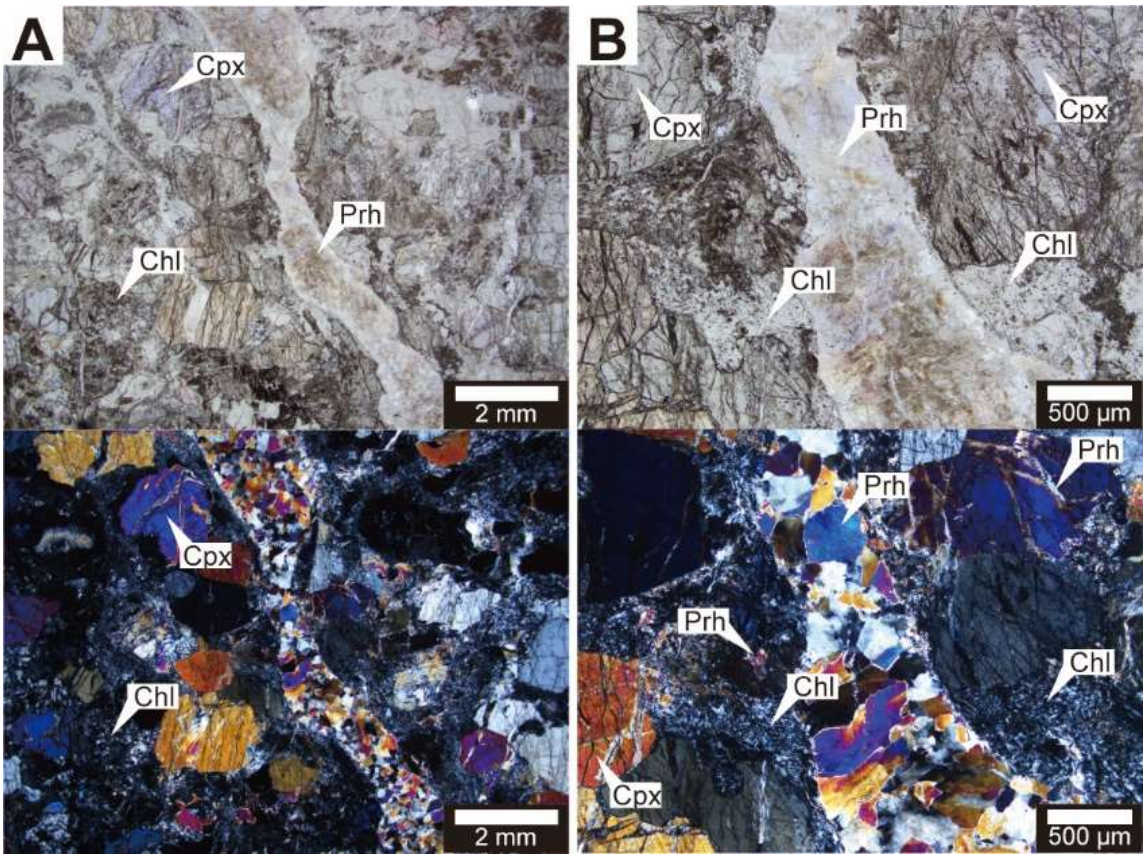

Fig. 2.21. Optical microscope photographs of prehnite vein in the gabbroic rock under plane polarized light and crossed polarized light (CM1A-51Z4-72-77). (A)Prehnite vein cut host rock. (B)Close up view of the prehnite vein. The prehnite filling the vein have large crystal size of ~50-500 μm.

2.6.2. Dunites

Although dunite is originally >90% olivine, the dunites from the CM site are almost completely serpentinized and homogeneous in structure. X-ray CT images show a vein network at a wide range of depths in the samples (Fig. 2.22). The serpentinized dunite is composed of serpentine, brucite, magnetite and Cr-spinels. Only a few samples contain olivine (CM1A-58Z1-50-54 and CM2B-56Z3-51-56), and these relict olivine have X_{Mg} of 0.91 (Table 2.8), which is generally consistent with values from previous studies (Abily and Ceuleneer, 2013). The protolith mineral mode, determined from the relict olivine composition and bulk rock composition, indicates that these dunites are composed of olivine = 94.2 ± 3.7 (wt. %).

Multi-stage mineral veins are observed in the dunite (Fig. 2.23). Antigorite ± chrysotile veins cut the host rock. The width of the antigorite ± chrysotile veins vary from ~100 um to 6.0 mm (Fig. 2.23). Second generation magnetite veins cut the antigorite ± chrysotile vein and the host rock. Third-generation chrysotile veins cut the entire texture and develop in a direction perpendicular to the antigorite and magnetite veins. Secondary minerals are described in detail below.

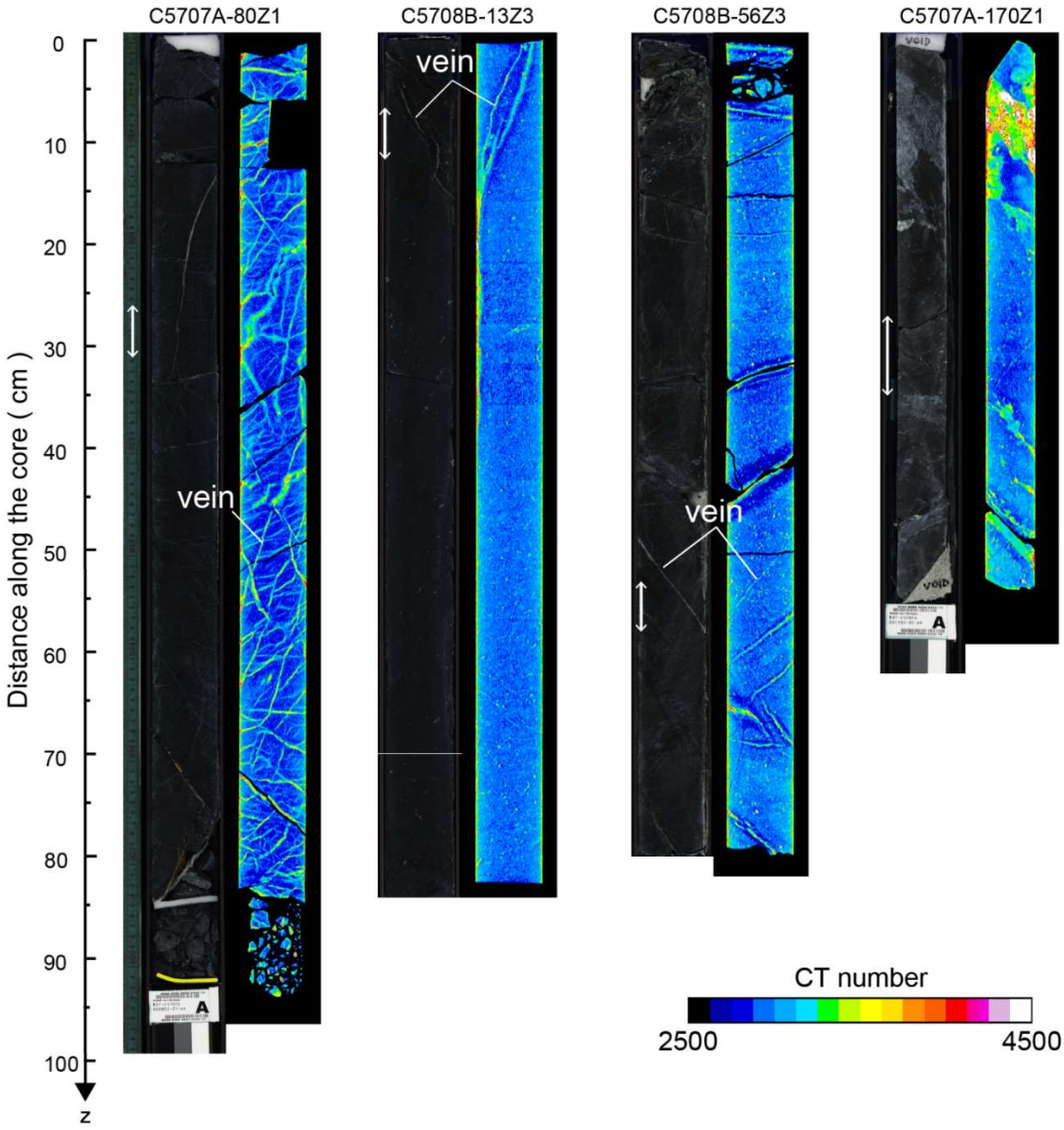

Fig. 2.22. Photograph and X-ray CT image of dunites from OmanDP CM site. z increases with depth within the hole. The dark color parts in photographs are mainly composed of serpentinized olivine. The white color parts mainly composed of plagioclase. White color allows shows the positions of thin section.

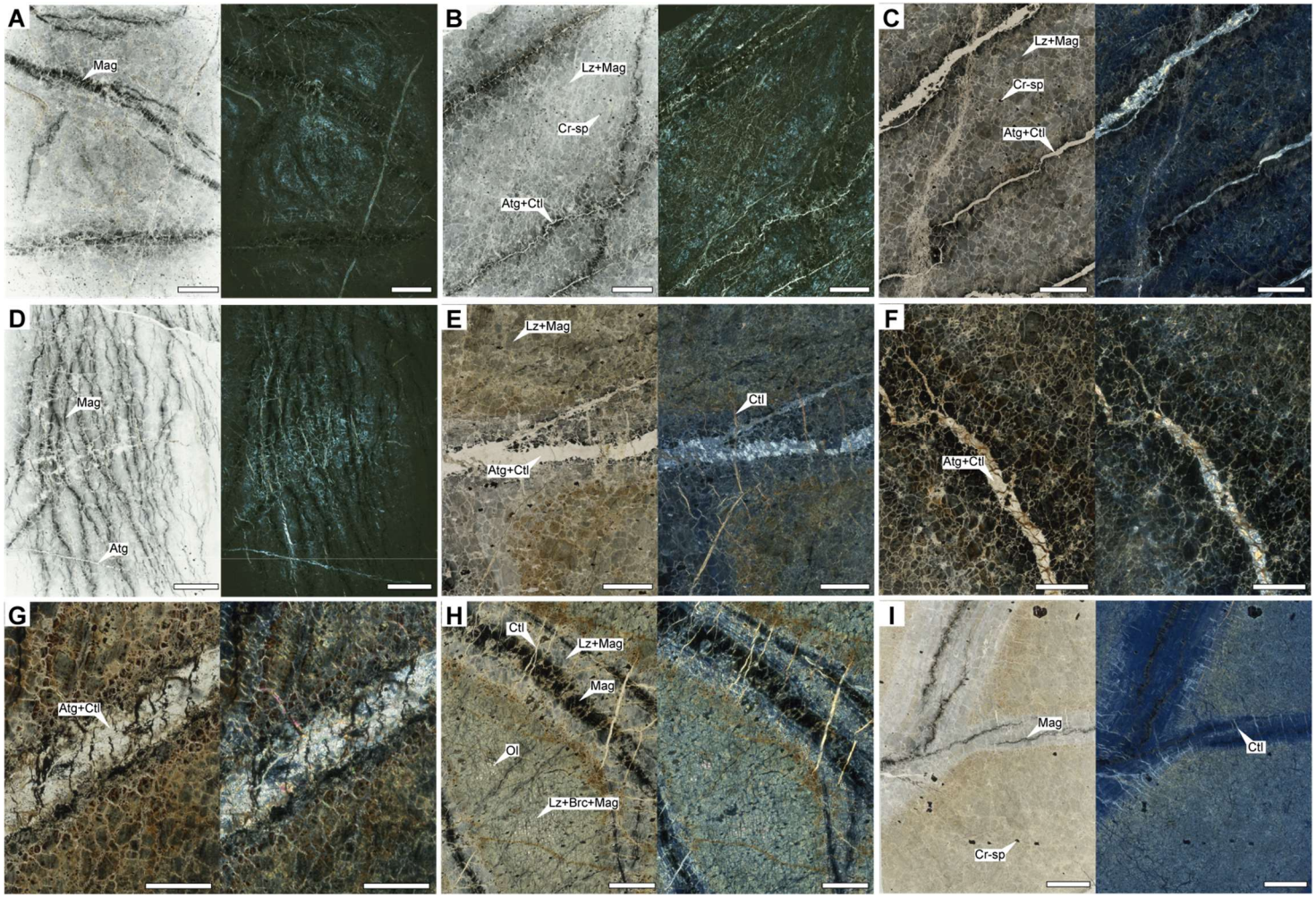

Fig. 2.23. Thin section image of the dunites under plain polarized light and crossed polarized light. (A) CM1A-70Z2-26-31, (B) CM1A-80Z1-26-31, (C) CM1A-90Z2-48-53, (D) CM1A-107Z2-5-10, (E) CM1A-137Z3-46-54, (F) CM2B-13Z3-7-12, (G) CM2B-15Z3-38-43, (H) CM2B-54Z1-29-34, (I) CM2B-59Z4-11-16. Ol = olivine, Pl = plagioclase, Cpx = clinopyroxene, Mag = magnetite, Chl = chlorite. Scale bar = 5 mm.

Table 2.8. Chemical composition of primary minerals in dunite (in wt. %) with 1σ standard deviation and calculated structural formula.

Sample	CM2B-54Z1-29-34		CM2B-56Z3-51-56		CM1A-80Z1-26-31		CM1A-90Z2-48-53		CM1A-107Z2-5-10		CM2B-13Z3-7-12		CM2B-16Z2-34-35		CM2B-54Z1-29-34		CM2B-56Z3-51-56	
Lithology	Dunite		Dunite		Dunite		Dunite		Dunite		Dunite		Dunite		Dunite		Dunite	
Mineral	Olivine		Olivine		Cr-spinel		Cr-spinel		Cr-spinel		Cr-spinel		Cr-spinel		Cr-spinel		Cr-spinel	
N	19		8		6		20		10		6		21		6		8	
	avg.	1σ	avg.	1σ	avg.	1σ	avg.	1σ	avg.	1σ	avg.	1σ	avg.	1σ	avg.	1σ	avg.	1σ
SiO_2	40.67	0.44	40.88	0.36	0.01	0.01	0.13	0.41	0.01	0.03	0.00	0.00	0.02	0.03	0.02	0.03	0.02	0.03
TiO_2	0.01	0.02	0.01	0.01	0.46	0.03	0.54	0.05	0.34	0.02	0.42	0.05	0.66	0.30	0.66	0.05	0.52	0.06
Al_2O_3	0.00	0.01	0.02	0.02	21.05	0.28	20.04	0.92	33.79	0.60	20.80	0.67	20.60	2.33	21.47	0.26	21.50	0.39
FeO	9.18	0.26	8.59	0.22	22.61	0.44	21.39	0.60	24.33	0.45	26.56	0.46	27.65	0.86	21.74	0.88	21.30	0.79
MnO	0.15	0.04	0.15	0.06	0.31	0.10	0.29	0.06	0.30	0.06	0.35	0.04	0.33	0.09	0.34	0.09	0.30	0.08
MgO	50.17	0.69	50.35	0.53	11.36	0.22	12.54	0.79	12.63	0.38	10.64	0.19	10.87	1.13	11.17	0.33	11.67	0.60
CaO	0.07	0.01	0.06	0.02	0.01	0.01	0.01	0.01	0.01	0.01	0.01	0.01	0.01	0.01	0.00	0.00	0.01	0.01
Na_2O	0.04	0.05	0.01	0.02	0.07	0.06	0.06	0.09	0.05	0.06	0.06	0.05	0.03	0.06	0.03	0.04	0.01	0.03
K_2O	0.01	0.01	0.01	0.01	0.00	0.01	0.00	0.00	0.00	0.00	0.00	0.01	0.00	0.01	0.00	0.00	0.00	0.00
Cr_2O_3	0.02	0.02	0.02	0.03	43.65	0.37	43.50	1.23	29.83	0.37	40.61	0.65	39.61	1.88	43.10	0.13	43.94	0.23
Total	100.32	1.02	100.23	0.92	99.52	0.37	98.50	0.97	101.29	0.90	99.68	0.60	99.85	0.88	98.54	0.60	99.32	0.36
Oxygen	4		4		4		4		4		4		4		4		4	
Si	0.99		1.00		0.00		0.00		0.00		0.00		0.00		0.00		0.00	
Ti	0.00		0.00		0.01		0.01		0.01		0.01		0.02		0.02		0.01	
Al	0.00		0.00		0.79		0.76		1.18		0.79		0.78		0.81		0.80	
Fe	0.19		0.17		0.60		0.57		0.60		0.72		0.75		0.58		0.56	
Mn	0.00		0.00		0.01		0.01		0.01		0.01		0.01		0.01		0.01	
Mg	1.82		1.83		0.54		0.60		0.56		0.51		0.52		0.53		0.55	
Ca	0.00		0.00		0.00		0.00		0.00		0.00		0.00		0.00		0.00	
Na	0.00		0.00		0.00		0.00		0.00		0.00		0.00		0.00		0.00	
K	0.00		0.00		0.00		0.00		0.00		0.00		0.00		0.00		0.00	
Cr	0.00		0.00		1.10		1.10		0.70		1.04		1.01		1.09		1.10	
Total	3.01		3.00		3.05		3.06		3.05		3.08		3.09		3.04		3.04	
X_{Mg}	0.91		0.91		0.47		0.51		0.48		0.42		0.41		0.48		0.49	
X_{Cr}					0.58		0.59		0.37		0.57		0.56		0.57		0.58	

X_{Mg}=Mg^{2+}/(Mg^{2+}+Fe^{2+}), where Mg^{2+} and Fe^{2+} are in atoms per formula unit (a.p.f.u.). X_{Cr}=Mg^{2+}/(Mg^{2+}+Fe^{2+}), where Mg^{2+} and Fe^{2+} are in atoms per formula unit (a.p.f.u.).

Serpentinite

Mesh textures occur in both partially and completely serpentinized dunite (Fig. 2.24A-D). The mesh rims are composed of a mixture of lizardite and brucite, often cut by transparent veins with 20-40 μm width, which composed of chrysotile, brucite, and relatively coarse-grained magnetite with size of several tens micrometers (Fig. 2.24B and D). In the partially serpentinized dunite, from the boundary between the olivine and serpentinized mesh rim to the mesh rim, regions composed of (1)lizardite, (2)lizardite and brucite, (3)chrysotile, and (4)brucite and magnetite are observed (Fig. 2.25A-D). Similar microtextures are found in other ophiolitic peridotites (Miyoshi *et al.*, 2014; Schwarzenbach *et al.*, 2016). In completely serpentinized dunite, the mesh core is composed of lizardite ± brucite, with a layered structure of brucite-rich and serpentine-rich areas toward the mesh rim (Fig. 2.26A-D). The mesh rim is composed of brucite and magnetite, with both sides composed of chrysotile (Fig. 2.26D). The Si versus Mg+Fe plot shows that the mesh rim is a mixture of serpentine and brucite (Fig. 2.27A). The X_{Mg} of serpentine and brucite in mesh rim obtained from the Si versus Mg+Fe plots are 0.96-0.97 and 0.72-0.90, respectively (Table 2.9). The mesh core serpentine and brucite shows X_{Mg} of 0.95-0.98 and 0.76-0.94, respectively.

The Raman spectra of transparent veins in the mesh rim of the completely and partly serpentinized dunites show similar peaks of 127.90-129.74, 226.69-228.71, 381.82-385.39, 686.89-690.30, 1099.46-1104.25, and 3686.69-3699.06 cm^{-1} and 3638.93-3641.02 cm^{-1} (Fig. 2.28A and B), which correspond to the peaks of chrysotile and brucite, respectively (Groppo *et al.*, 2006). The Raman spectra of the mesh rim both side of the transparent vein of the completely and partly serpentinized dunites shows peaks of liardite at 127.90-129.74, 226.89-228.71, 380.04-383.61, 683.48-686.89, 3682.56-3684.63, and 3702.14-3701.12 cm^{-1} with weak peaks of brucite at 435.09 and 3638.93-3636.84 cm^{-1}. The mesh core of the completely serpentinized dunite shows peaks of lizardite at 129.74, 226.89, 380.04, 686.89, 3684.63, and 3701.12 cm^{-1}.

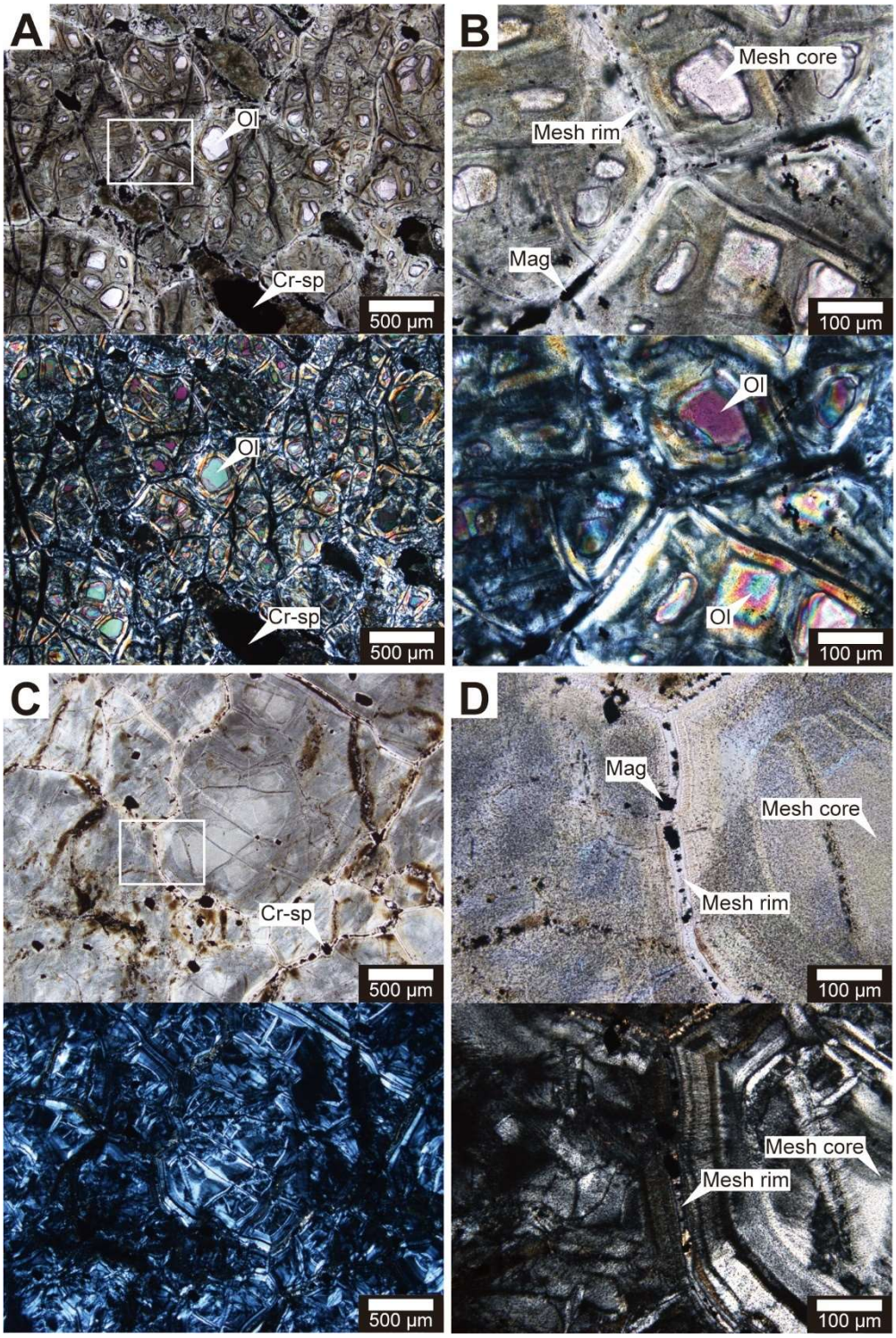

Fig. 2.24. Optical microscope photographs of partly and completely serpentinized dunite under plane polarized light and crossed polarized light. (A) Mesh texture of partly serpentinized dunite (CM2B-56Z3-51-56). (B) Close up view of the mesh texture. (C) Mesh texture of completely serpentinized dunite (CM2B-16Z2-30-35). (D) Closer up view of the mesh texture. Ol=olivine, Cr-sp=Cr spinel.

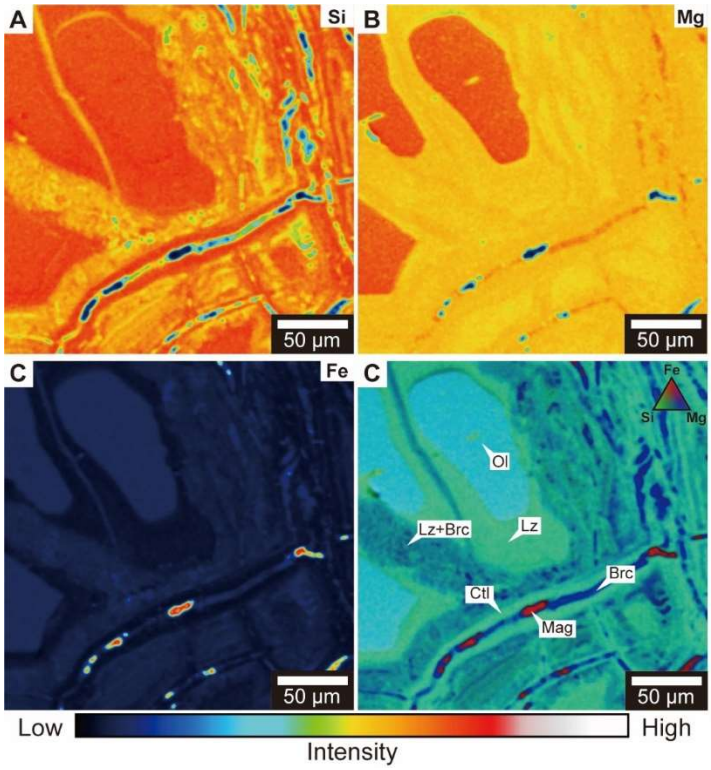

Fig. 2.25. Element mapping of the mesh texture of partly serpentinized dunite (CM2B-56Z3-51-56) for Si, Mg, and Fe (A-C). (D) Three element composite map of Si (Green), Mg (Blue), and Fe (Red). Ol=olivine, Srp = serpentine, Brc = brucite, Mag = magnetite.

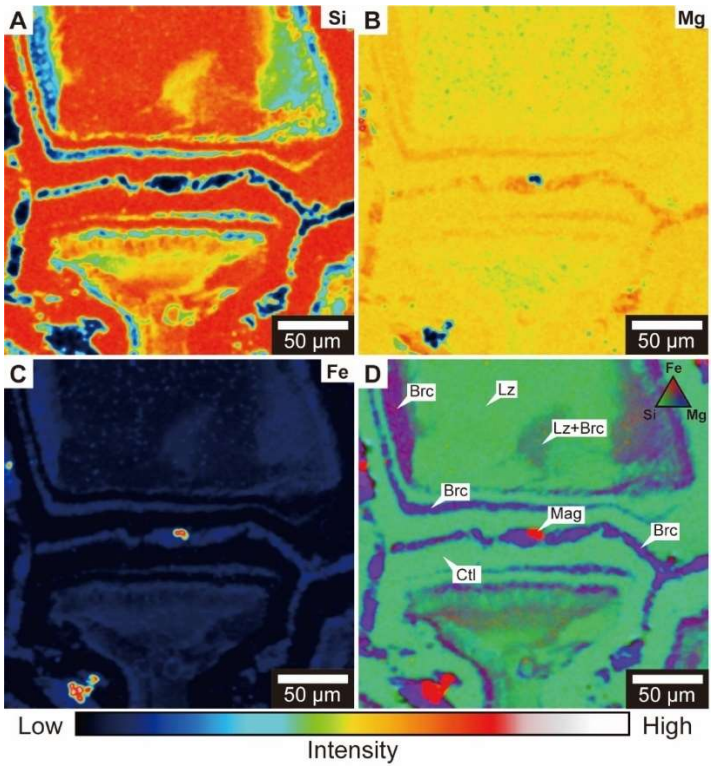

Fig. 2.26. Element mapping of the mesh texture of completely serpentinized dunite (CM2B-13Z3-7-12) for Si, Mg, and Fe (A-C). (D) Three element composite map of Si (Green), Mg (Blue), and Fe (Red). Srp = serpentine, Brc = brucite, Mag = magnetite.

Table 2.9. Chemical composition of serpentine and brucite in dunite (in wt. %) with 1σ standard deviation and calculated structural formula.

Sample	CM1A-70Z2-26-31				CM1A-80Z1-26-31				CM1A-90Z2-48-53				CM1A-107Z2-5-10		CM2B-13Z3-7-12			
Lithology	Dunite				Dunite				Dunite				Dunite		Dunite			
Mineral	Srp		Srp+Brc		Brc+Srp		Srp		Srp+Brc		Srp+Brc		Srp		Srp+Brc		Srp+Brc	
Type	Mesh rim		Mesh core		Mesh rim		Mesh core		Mesh rim		Mesh core		Matrix		Mesh rim		Mesh core	
N	10		20		20		10		35		50		20		46		11	
	avg.	1σ	avg.	1σ	avg.	1σ	avg.	1σ	avg.	1σ	avg.	1σ	avg.	1σ	avg.	1σ	avg.	1σ
SiO_2	40.36	0.53	33.53	7.13	9.61	13.85	41.50	0.38	36.06	12.15	32.11	9.13	41.52	0.42	32.13	14.32	16.97	2.81
TiO_2	0.02	0.02	0.02	0.03	0.01	0.01	0.01	0.02	0.01	0.02	0.01	0.02	0.02	0.03	0.01	0.02	0.01	0.03
Al_2O_3	0.03	0.05	0.02	0.03	0.01	0.01	0.02	0.03	0.01	0.02	0.01	0.02	0.30	0.48	0.01	0.02	0.01	0.02
FeO	2.55	0.31	6.36	3.56	10.75	3.81	2.46	0.54	3.50	3.85	6.33	3.80	2.15	0.29	5.26	4.21	14.23	1.48
MnO	0.06	0.04	0.19	0.13	0.34	0.15	0.07	0.06	0.11	0.11	0.19	0.16	0.12	0.06	0.07	0.07	0.32	0.11
MgO	39.06	0.35	42.11	3.44	60.08	9.37	40.23	0.45	42.38	7.33	43.89	4.92	40.46	0.61	45.48	9.52	49.61	1.08
CaO	0.04	0.01	0.33	0.62	0.05	0.05	0.09	0.01	0.09	0.12	0.08	0.05	0.06	0.02	0.03	0.02	0.11	0.02
Na_2O	0.03	0.03	0.02	0.03	0.02	0.03	0.01	0.02	0.02	0.03	0.02	0.03	0.03	0.04	0.01	0.03	0.04	0.05
K_2O	0.01	0.01	0.00	0.00	0.00	0.01	0.00	0.00	0.01	0.01	0.00	0.01	0.00	0.00	0.00	0.01	0.00	0.00
Cr_2O_3	0.00	0.00	0.03	0.03	0.02	0.02	0.02	0.02	0.02	0.02	0.03	0.03	0.01	0.02	0.01	0.02	0.01	0.01
Total	82.14	0.56	82.61	1.72	80.88	2.19	84.41	0.72	82.21	1.75	82.68	1.91	84.67	0.69	83.13	1.30	81.64	0.69
Oxygen	7		7		1		7		7		7		7		7		7	
Si	2.00		1.72		0.07		2.00		1.78		1.64		1.99		1.59		0.98	
Ti	0.00		0.00		0.00		0.00		0.00		0.00		0.00		0.00		0.00	
Al	0.00		0.00		0.00		0.00		0.00		0.00		0.02		0.00		0.00	
Fe	0.11		0.28		0.08		0.10		0.16		0.28		0.09		0.24		0.69	
Mn	0.00		0.01		0.00		0.00		0.01		0.01		0.00		0.00		0.02	
Mg	2.89		3.26		0.77		2.89		3.26		3.42		2.89		3.57		4.31	
Ca	0.00		0.02		0.00		0.00		0.00		0.00		0.00		0.00		0.01	
Na	0.00		0.00		0.00		0.00		0.00		0.00		0.00		0.00		0.00	
K	0.00		0.00		0.00		0.00		0.00		0.00		0.00		0.00		0.00	
Cr	0.00		0.00		0.00		0.00		0.00		0.00		0.00		0.00		0.00	
Total	5.00		5.28		0.93		5.00		5.22		5.36		5.00		5.41		6.02	
X_{Srp}			0.86		0.25				0.89		0.82				0.80		0.49	
X_{Mg} of Srp	0.96		0.96		0.97		0.95		0.97		0.96		0.97		0.96		0.98	
X_{Mg} of Brc			0.82		0.90				0.89		0.85				0.89		0.81	

Srp=serpentine, Brc = brucite. $X_{Mg}=Mg^{2+}/(Mg^{2+}+Fe^{2+})$, where Mg^{2+} and Fe^{2+} are in atoms per formula unit (a.p.f.u.).

Table 2.9. Continue of chemical composition of serpentine and brucite in dunite (in wt. %) with 1σ standard deviation and calculated structural formula.

Sample	CM2B-16Z2-34-35				CM2B-54Z1-29-34		CM2B-56Z3-51-56				CM2B-59Z4-11-16			
Lithology	Dunite				Dunite		Dunite				Dunite			
Mineral	Srp+Brc		Srp+Brc		Srp+Brc		Srp+Brc		Srp		Srp+Brc		Srp+Brc	
Type	Mesh rim		Mesh core		Mesh		Mesh rim		Mesh core		Mesh rim		Mesh core	
N	125		75		75		45		10		33		19	
	avg.	1σ	avg.	1σ	avg.	1σ	avg.	1σ	avg.	1σ	avg.	1σ	avg.	1σ
SiO_2	33.85	7.46	37.65	4.88	36.35	4.08	36.38	4.20	40.82	0.36	38.67	0.69	36.13	2.50
TiO_2	0.02	0.02	0.02	0.02	0.02	0.02	0.02	0.02	0.01	0.01	0.01	0.02	0.01	0.02
Al_2O_3	0.03	0.04	0.03	0.04	0.23	0.19	0.21	0.41	0.25	0.04	0.04	0.04	0.05	0.04
FeO	5.92	3.33	5.18	2.36	5.24	1.72	5.21	2.06	3.52	0.15	3.62	0.50	5.41	1.50
MnO	0.13	0.11	0.12	0.09	0.10	0.07	0.08	0.06	0.04	0.03	0.11	0.06	0.15	0.10
MgO	42.48	4.14	39.54	2.59	42.66	2.93	41.99	2.49	39.73	0.50	39.06	0.54	38.87	1.23
CaO	0.09	0.03	0.12	0.03	0.11	0.04	0.13	0.04	0.20	0.02	0.22	0.02	0.23	0.11
Na_2O	0.03	0.04	0.03	0.04	0.03	0.04	0.03	0.04	0.02	0.02	0.03	0.05	0.05	0.08
K_2O	0.00	0.01	0.00	0.01	0.01	0.01	0.00	0.01	0.00	0.01	0.01	0.01	0.01	0.01
Cr_2O_3	0.02	0.02	0.02	0.02	0.02	0.02	0.01	0.02	0.01	0.01	0.02	0.02	0.01	0.01
Total	82.61	2.01	82.71	1.27	84.75	2.48	84.09	1.69	84.59	0.64	81.79	0.89	80.93	1.22
Oxygen	7		7		7		7		7		7		7	
Si	1.72		1.89		1.80		1.81		1.98		1.95		1.87	
Ti	0.00		0.00		0.00		0.00		0.00		0.00		0.00	
Al	0.00		0.00		0.01		0.01		0.01		0.00		0.00	
Fe	0.26		0.22		0.22		0.22		0.14		0.15		0.24	
Mn	0.01		0.01		0.00		0.00		0.00		0.00		0.01	
Mg	3.27		2.98		3.15		3.13		2.87		2.93		3.00	
Ca	0.00		0.01		0.01		0.01		0.01		0.01		0.01	
Na	0.00		0.00		0.00		0.00		0.00		0.00		0.01	
K	0.00		0.00		0.00		0.00		0.00		0.00		0.00	
Cr	0.00		0.00		0.00		0.00		0.00		0.00		0.00	
Total	5.28		5.11		5.20		5.18		5.02		5.05		5.13	
X_{Srp}	0.86		0.95		0.90		0.91				0.97		0.93	
X_{Mg} of Srp	0.96		0.94		0.95		0.96		0.95		0.96		0.95	
X_{Mg} of Brc	0.84		0.83		0.87		0.84				0.72		0.76	

Srp=serpentine, Brc = brucite. $X_{Mg}=Mg^{2+}/(Mg^{2+}+Fe^{2+})$, where Mg^{2+} and Fe^{2+} are in atoms per formula unit (a.p.f.u.).

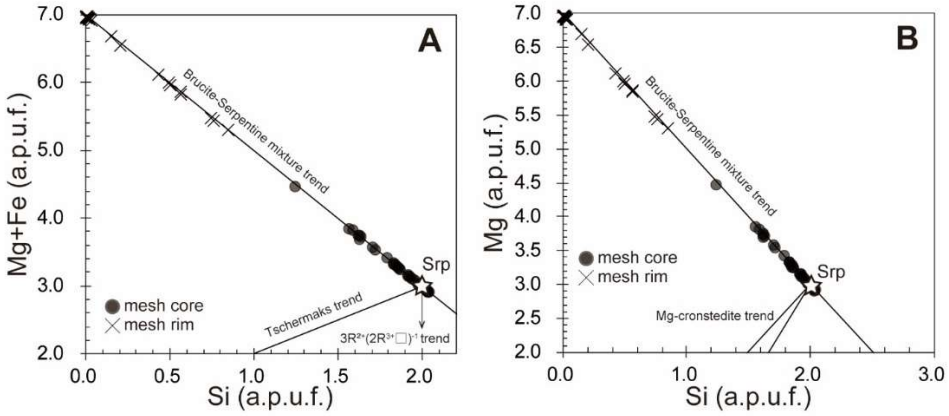

Fig. 2.27. Si versus Mg+Fe plot of serpentinized dunite.

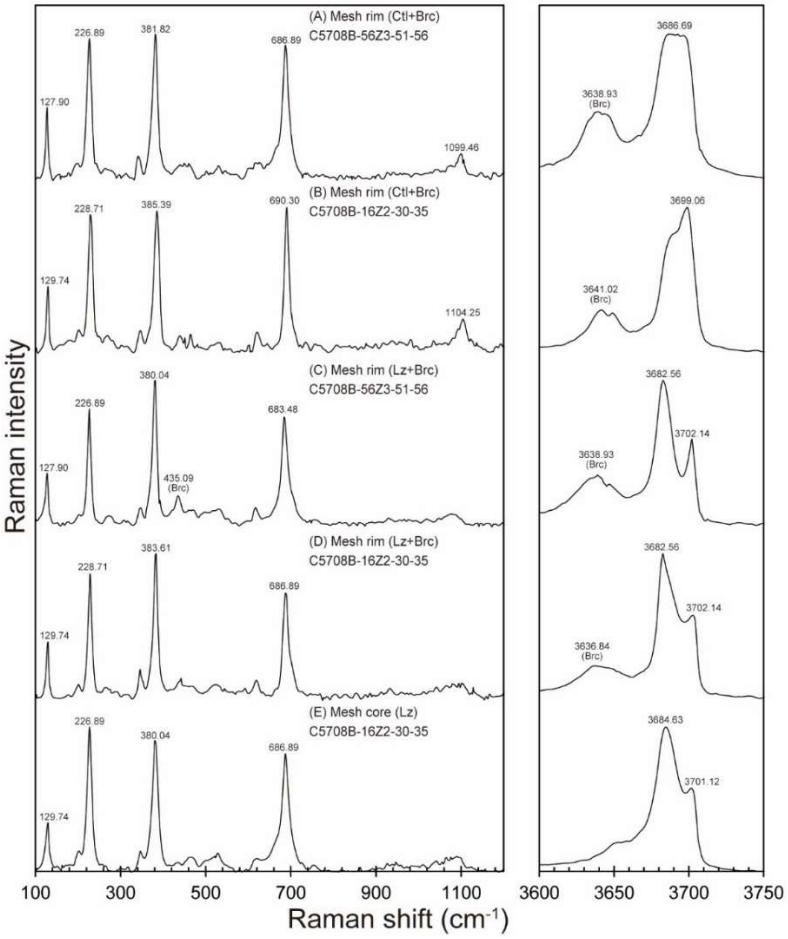

Fig. 2.28. Raman spectra of serpentine and brucite in dunite (A) Center of the mesh rim with relict olivine (CM2B-56Z3-51-56). (B) Center of the mesh rim of completely serpentinized dunite (CM2B-16Z2-30-35). (C) Mesh rim of partly serpentinized dunite (CM2B-56Z3-51-56). (D) Mesh rim of partly serpentinized dunite (CM2B-16Z2-30-35). (E) Mesh core of completely serpentinized dunite (CM2B-16Z2-30-35). Lz = lizardite, Ctl = chrysotile, Brc = brucite.

Serpentine vein

Three types of serpentine veins were identified in the dunite: antigorite ± chrysotile vein, lizardite vein, and chrysotile veins that cutting them (Fig. 2.29). The later stage chrysotile veins cut perpendicular to the antigorite ± chrysotile and lizardite veins (Fig. 2.29). Antigorite veins are cut by magnetite veins (Fig. 2.29C). Brucite-rich reaction zones are observed on both sides of some antigorite + chrysotile veins (Fig. 2.30). In the reaction zone, the matrix mesh texture is replaced by brucite over several millimeters, with preserving the mesh texture.

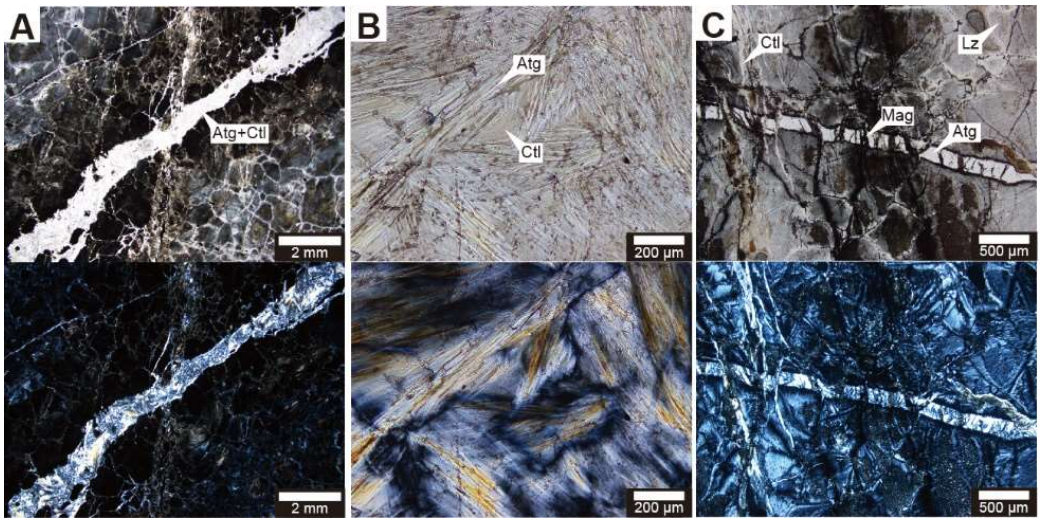

Fig. 2.29. Optical micrographs of serpentine veins in dunite. (A) Antigorite + chrysotile veins (CM1A-90Z2-48-53). (B) Close up view of antigorite + chrysotile veins. (C) Crosscut relationship between antigorite and magnetite veins (CM1A-107Z2-5-10). Atg = antigorite, Ctl = chrysotile, Mag = magnetite, Lz = lizardite.

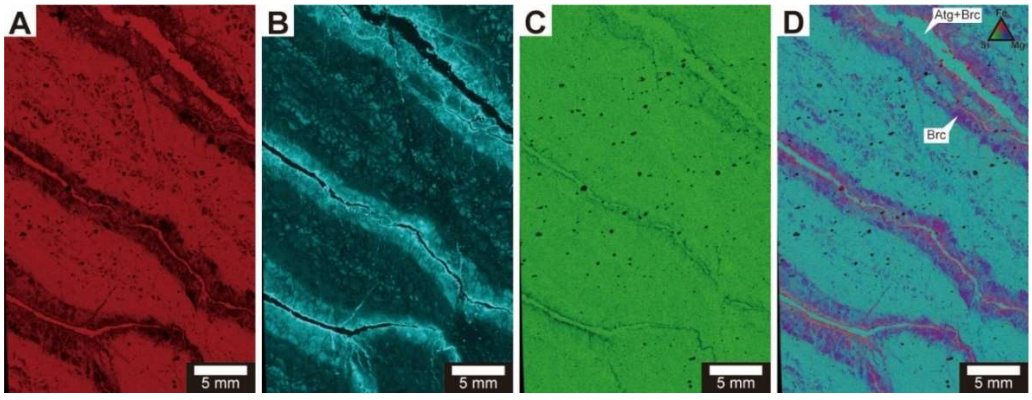

Fig. 2.30. Micro-XRF element mapping of dunite containing antigorite + chrysotile veins with brucite-rich reaction zones (CM1A-90Z2-48-53). Brc = brucite.

The antigorite ± chrysotile vein contains fragments of host rock (Fig. 2.31A). In the antigorite ± chrysotile vein, chrysotile fills the spaces between the blade shape antigorite (Fig. 2.31B). The antigorite±chrysotile vein is more Al-rich (Al_2O_3>~0.3 wt. %; Table 2.10) than the serpentine in the mesh texture. Antigorite and chrysotile in the antigorite±chrysotile veins have similar X_{Mg} of 0.97-0.98. Unlike antigorite veins found on the seafloor, it is not accompanied by talc (Rouméjon *et al.*, 2019). It also has less iron than the antigorite found in the Oman ophiolite listvenite (Falk and Kelemen, 2015).

Raman spectra of blade-shape antigorite show a peak at 1045 cm^{-1} characteristic of antigorite (Fig. 2.32A). Raman spectra of chrysotile in the antigorite+chrysotile vein and later stage chrysotile veins show a peak near 1100 cm^{-1} characteristic of chrysotile (Fig. 2.32B and D). Brucite on both sides of the antigorite+chrysotile vein show peaks similar to the Raman peaks of brucite reported in previous study (Debret *et al.*, 2019). The Raman spectrum of the mesh rim of the brucite-rich reaction zone shows a peak at ~1100cm^{-1}, similar to chrysotile (Fig. 2.32).

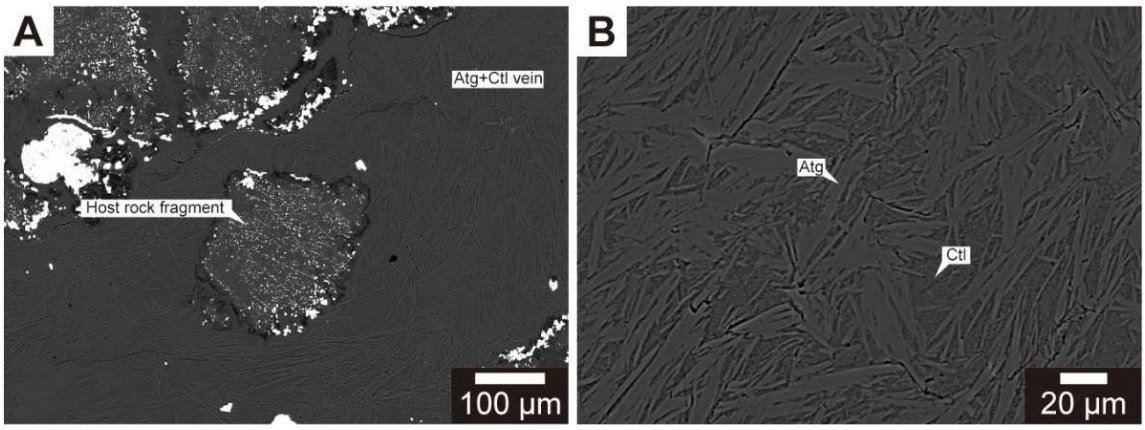

Fig. 2.31. Backscattered electron images of the antigorite+chrysotile (Atg+Ctl) vein and lizardite vein. (A) Atg+Ctl vein from CM1A-90Z2-48-53. (B) Close up view of the Atg+Ctl vein. Atg=antigorite, Ctl=chrysotile, Mag=magnetite.

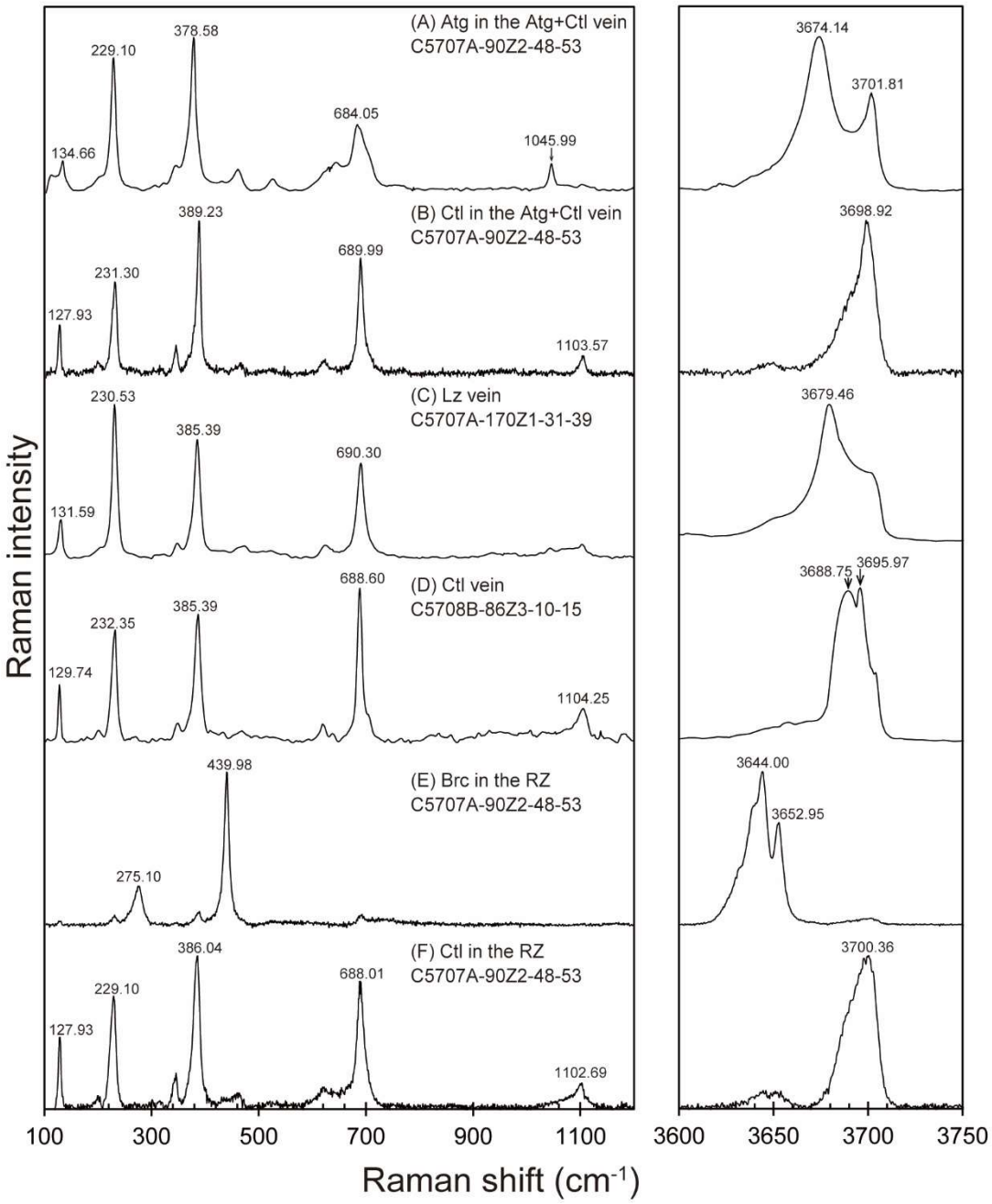

Fig. 2.32. Raman spectra of serpentine veins and a reaction zone in dunite. (A) antigorite in antigorite+chrysotile vein, (B) chrysotile in antigorite+chrysotile vein, (C) lizardite vein, (D) chrysotile vein, (E) brucite in the reaction zone, (F) chrysotile in the reaction zone.

Table 2.10. Chemical composition of serpentine veins and reaction zone in dunite (in wt. %) with 1σ standard deviation and calculated structural formula.

Sample	C5707A-70Z2-26-31								C5707A-80Z1-26-31							
Lithology	Dunite								Dunite							
Mineral	Atg		Ctl		Brc		Ctl+Brc		Atg		Ctl		Brc		Ctl	
Type	Atg+Ctl vein		Atg+Ctl vein		Reaction zone		Reaction zone		Atg+Ctl vein		Atg+Ctl vein		Reaction zone		Reaction zone	
N	13		10		17		6		29		10		21		22	
	avg.	1σ	avg.	1σ	avg.	1σ	avg.	1σ	avg.	1σ	avg.	1σ	avg.	1σ	avg.	1σ
SiO_2	42.64	0.42	39.43	2.71	4.61	3.16	30.19	6.51	43.24	0.52	42.28	0.34	0.92	1.87	41.45	1.54
TiO_2	0.03	0.03	0.02	0.03	0.02	0.02	0.02	0.02	0.02	0.02	0.01	0.02	0.01	0.01	0.01	0.02
Al_2O_3	0.66	0.14	0.07	0.09	0.02	0.03	0.02	0.03	0.25	0.11	0.09	0.08	0.03	0.03	0.00	0.01
FeO	2.79	0.14	3.22	1.15	15.09	5.35	6.34	2.32	2.34	0.17	2.32	0.16	16.47	6.15	2.89	1.03
MnO	0.04	0.04	0.12	0.07	0.49	0.09	0.23	0.12	0.06	0.04	0.08	0.05	0.42	0.09	0.07	0.05
MgO	38.78	0.37	39.84	2.24	62.37	3.05	44.49	4.60	39.87	0.44	40.68	0.57	63.26	2.77	40.79	1.09
CaO	0.01	0.01	0.03	0.01	0.02	0.02	0.57	0.48	0.03	0.02	0.03	0.02	0.02	0.02	0.07	0.03
Na_2O	0.02	0.06	0.03	0.04	0.04	0.07	0.01	0.02	0.01	0.03	0.02	0.03	0.03	0.04	0.03	0.05
K_2O	0.00	0.01	0.00	0.00	0.00	0.00	0.00	0.00	0.00	0.01	0.00	0.01	0.00	0.01	0.00	0.01
Cr_2O_3	0.18	0.08	0.01	0.02	0.01	0.02	0.00	0.00	0.04	0.04	0.00	0.01	0.00	0.00	0.02	0.02
Total	85.16	0.73	82.77	1.36	82.65	4.03	81.88	1.56	85.86	0.85	85.53	0.84	81.16	4.76	85.33	1.23
Oxygen	7		7		1		7		7		7		1		7	
Si	2.03		1.95		0.04		1.58		2.04		2.01		0.01		1.98	
Ti	0.00		0.00		0.00		0.00		0.00		0.00		0.00		0.00	
Al	0.04		0.00		0.00		0.00		0.01		0.01		0.00		0.00	
Fe	0.11		0.13		0.11		0.28		0.09		0.09		0.12		0.12	
Mn	0.00		0.00		0.00		0.01		0.00		0.00		0.00		0.00	
Mg	2.75		2.94		0.81		3.51		2.80		2.88		0.86		2.91	
Ca	0.00		0.00		0.00		0.03		0.00		0.00		0.00		0.00	
Na	0.00		0.00		0.00		0.00		0.00		0.00		0.00		0.00	
K	0.00		0.00		0.00		0.00		0.00		0.00		0.00		0.00	
Cr	0.01		0.00		0.00		0.00		0.00		0.00		0.00		0.00	
Total	4.95		5.05		0.96		5.42		4.95		4.99		0.99		5.02	
X_{Srp}							0.79									
X_{Mg} of Srp	0.96		0.96				0.95		0.95		0.95				0.95	
X_{Mg} of Brc					0.88		0.88						0.87			

Atg=antigorite, Ctl=chrysotile, Brc = brucite. $X_{Mg}=Mg^{2+}/(Mg^{2+}+Fe^{2+})$, where Mg^{2+} and Fe^{2+} are in atoms per formula unit (a.p.f.u.).

Table 2.10. Continue of chemical composition of serpentine veins and reaction zone in dunite (in wt. %) with 1σ standard deviation and calculated structural formula.

Sample	C5707A-90Z2-48-53								C5708B-13Z3-7-12								C5708B-59Z4-11-16			
Lithology	Dunite								Dunite								Dunite			
Mineral	Atg		Ctl		Brc		Ctl		Atg		Ctl		Ctl				Srp		Brc	
Type	Atg+Ctl vein		Atg+Ctl vein		Reaction zone		Reaction zone		Atg+Ctl vein		Atg+Ctl vein		Vein				Selvage		with magnetite vein	
N	32		9		52		24		17		3		6				30		14	
	avg.	1σ	avg.	1σ	avg.	1σ	avg.	1σ	avg.	1σ	avg.	1σ	avg.	1σ			avg.	1σ	avg.	1σ
SiO_2	43.73	1.32	41.76	0.78	3.88	3.25	40.57	0.67	43.78	0.69	41.79	0.20	42.32	2.72			40.90	0.43	2.39	2.46
TiO_2	0.02	0.01	0.01	0.01	0.01	0.01	0.02	0.03	0.01	0.02	0.03	0.04	0.01	0.01			0.02	0.02	0.01	0.01
Al_2O_3	0.53	0.13	0.18	0.08	0.01	0.02	0.02	0.03	0.08	0.06	0.02	0.02	0.05	0.05			0.01	0.03	0.03	0.04
FeO	1.86	0.19	1.88	0.22	13.70	3.99	2.49	0.33	2.27	0.21	2.25	0.04	3.08	0.98			2.35	0.15	14.76	1.46
MnO	0.03	0.03	0.04	0.05	0.42	0.09	0.07	0.05	0.03	0.03	0.05	0.03	0.09	0.07			0.06	0.04	0.44	0.07
MgO	40.18	1.23	39.50	1.11	62.59	3.02	38.94	0.46	39.23	0.60	38.37	0.51	37.27	2.33			39.68	0.46	61.17	3.05
CaO	0.01	0.01	0.02	0.02	0.02	0.02	0.08	0.03	0.01	0.02	0.01	0.01	0.02	0.02			0.09	0.01	0.07	0.02
Na_2O	0.02	0.03	0.01	0.02	0.03	0.04	0.02	0.04	0.02	0.03	0.02	0.03	0.01	0.02			0.02	0.04	0.03	0.05
K_2O	0.01	0.01	0.01	0.01	0.00	0.00	0.01	0.01	0.01	0.01	0.00	0.00	0.00	0.01			0.00	0.01	0.00	0.00
Cr_2O_3	0.04	0.03	0.03	0.03	0.01	0.02	0.01	0.02	0.06	0.05	0.00	0.00	0.03	0.03			0.01	0.02	0.01	0.01
Total	86.42	2.49	83.43	1.59	80.67	2.74	82.22	0.90	85.52	0.92	82.54	0.56	82.88	4.05			83.14	0.74	78.91	2.11
Oxygen	7		7		1		7		7		7		7				7		1	
Si	2.04		2.04		0.03		2.01		2.07		2.05		2.07				2.00		0.02	
Ti	0.00		0.00		0.00		0.00		0.00		0.00		0.00				0.00		0.00	
Al	0.03		0.01		0.00		0.00		0.00		0.00		0.00				0.00		0.00	
Fe	0.07		0.07		0.10		0.10		0.09		0.09		0.13				0.10		0.11	
Mn	0.00		0.00		0.00		0.00		0.00		0.00		0.00				0.00		0.00	
Mg	2.80		2.82		0.83		2.87		2.76		2.80		2.72				2.89		0.84	
Ca	0.00		0.00		0.00		0.00		0.00		0.00		0.00				0.00		0.00	
Na	0.00		0.00		0.00		0.00		0.00		0.00		0.00				0.00		0.00	
K	0.00		0.00		0.00		0.00		0.00		0.00		0.00				0.00		0.00	
Cr	0.00		0.00		0.00		0.00		0.00		0.00		0.00				0.00		0.00	
Total	4.94		4.95		0.97		4.99		4.93		4.95		4.93				5.00		0.98	
X_{Mg} of Srp	0.97		0.98				0.97		0.97		0.97		0.95				0.97			
X_{Mg} of Brc					0.89														0.88	

Atg=antigorite, Ctl=chrysotile, Brc = brucite. X_{Mg}=Mg^{2+}/(Mg^{2+}+Fe^{2+}), where Mg^{2+} and Fe^{2+} are in atoms per formula unit (a.p.f.u.).

Magnetite vein

The selvage of the magnetite veins is composed of lizardite and fine-grained magnetite (Fig. 2.33). Raman spectra show that the selvage of the magnetite veins is not containing brucite (Fig. 2.34). X_{Mg} of lizardite around the magnetite veins is 0.97, while the X_{Mg} of chrysotile veins cutting the selvage of the magnetite veins is 0.95 (Table 2.9). The loss of brucite and associated magnetite formation has also been observed in samples from the ophiolitic and oceanic peridotites (Frost *et al.*, 2013; Klein *et al.*, 2009; Schwarzenbach *et al.*, 2016).

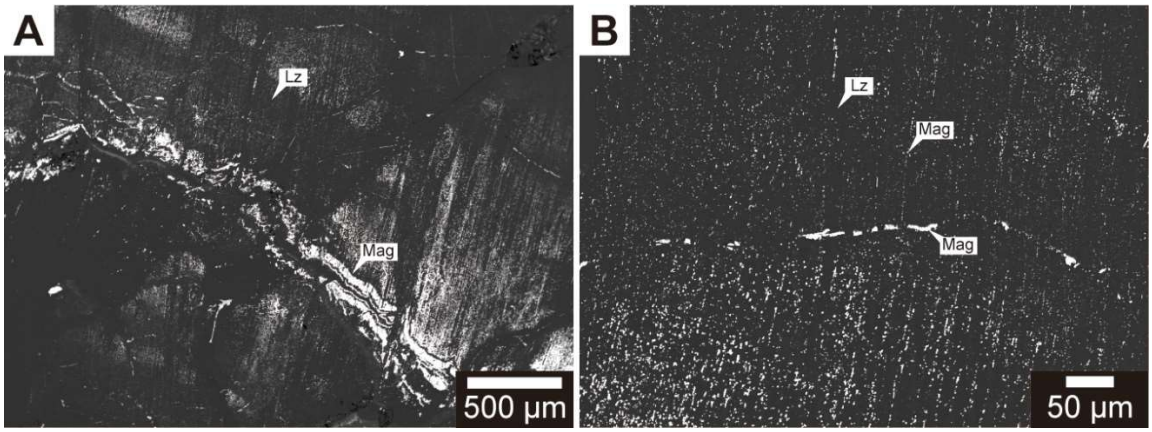

Fig. 2.33. Backscattered electron images of magnetite vein in dunite (CM2B-54Z1-29-34).

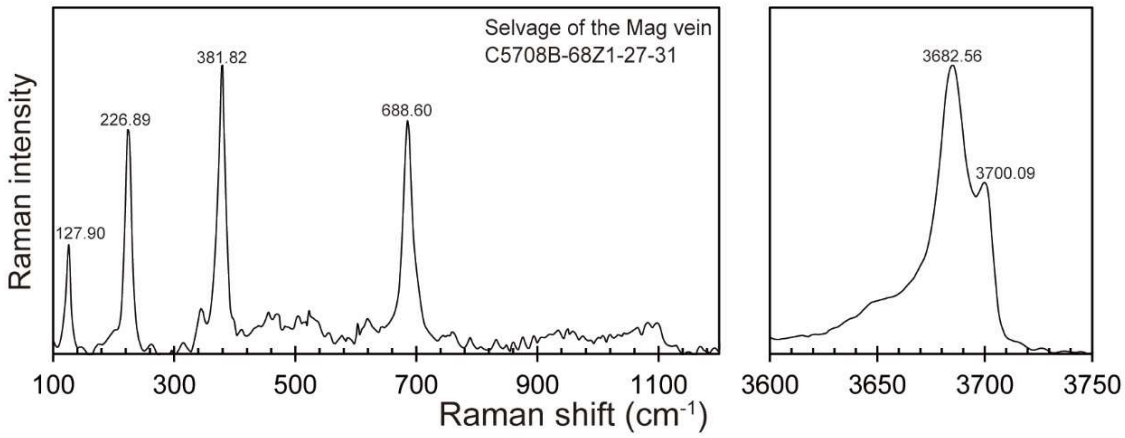

Fig. 2.34. Raman spectra of selvage of the magnetite vein (CM2B-68Z1-27-31).

2.6.3. Harzburgites

Harzburgite is 70-95% serpentinized. The orthopyroxene is less serpentinized than olivine, and orthopyroxene grains can be seen in the core photographs and X-ray CT images. Mineral vein networks are well developed in the harzburgite, and serpentinization is especially high around the veins (Fig. 2.35). The harzburgite contains olivine, orthopyroxene, and Cr-spinels as primary minerals. The olivine and pyroxene have X_{Mg} values of 0.92 and 0.91-0.92, respectively, and are nearly homogeneous in composition (Table 2.11). Mineral mode determined from chemical composition of the primary minerals and bulk rock compositions are olivine = 64.8 ± 12.1 wt. %, orthopyroxene 38.0 ± 15.3 wt. % (Table 2.12). The following three types of mineral veins were observed in harzburgite (Fig. 2.36): (a) tremolite+andradite vein, (b) antigorite vein, (c) magnetite vein, (d) chlorite vein, and (e) chrysotile vein.

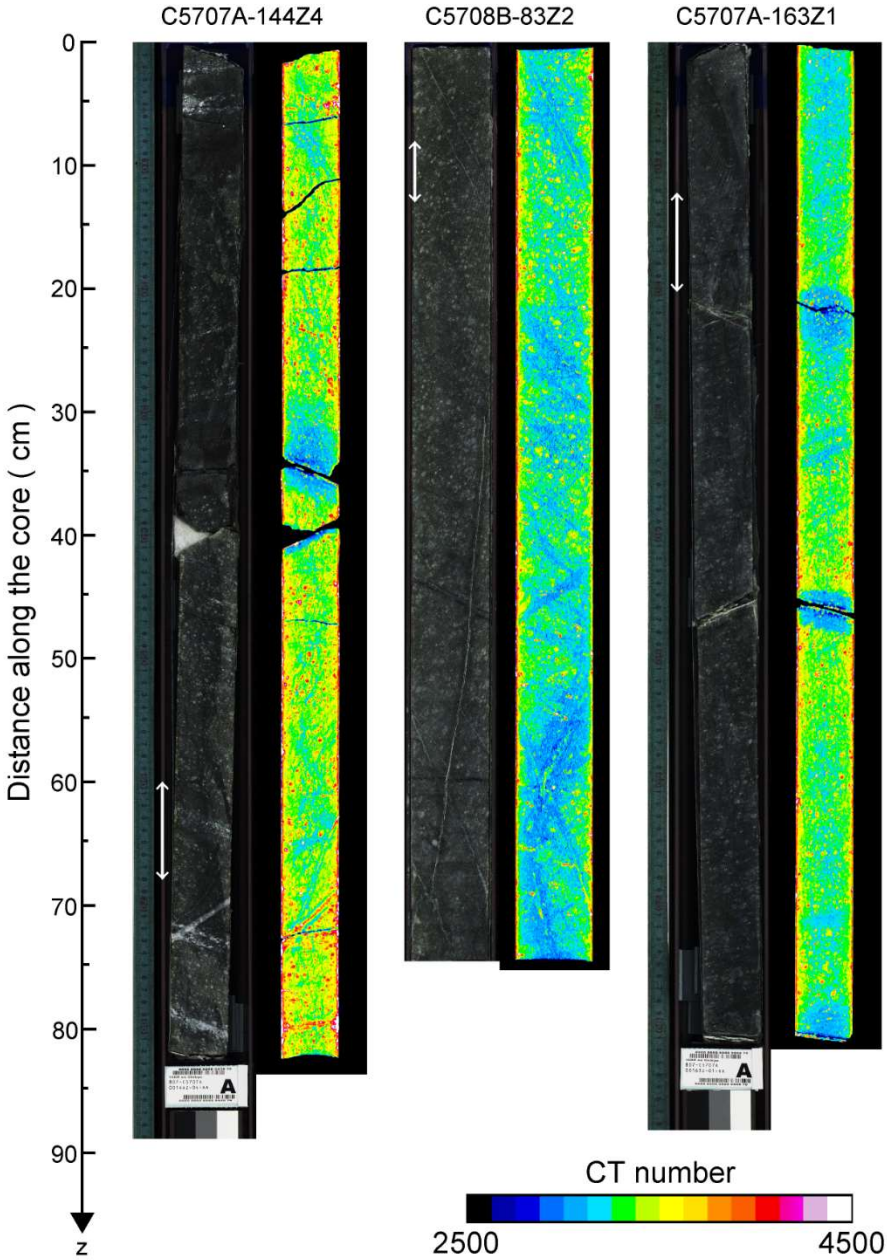

Fig. 2.35. Photograph and X-ray CT image of harzburgites from OmanDP CM site. z increases with depth within the hole. The dark color parts in photographs are mainly composed of serpentinized olivine. The white color parts mainly composed of plagioclase. White color allows shows the positions of thin section.

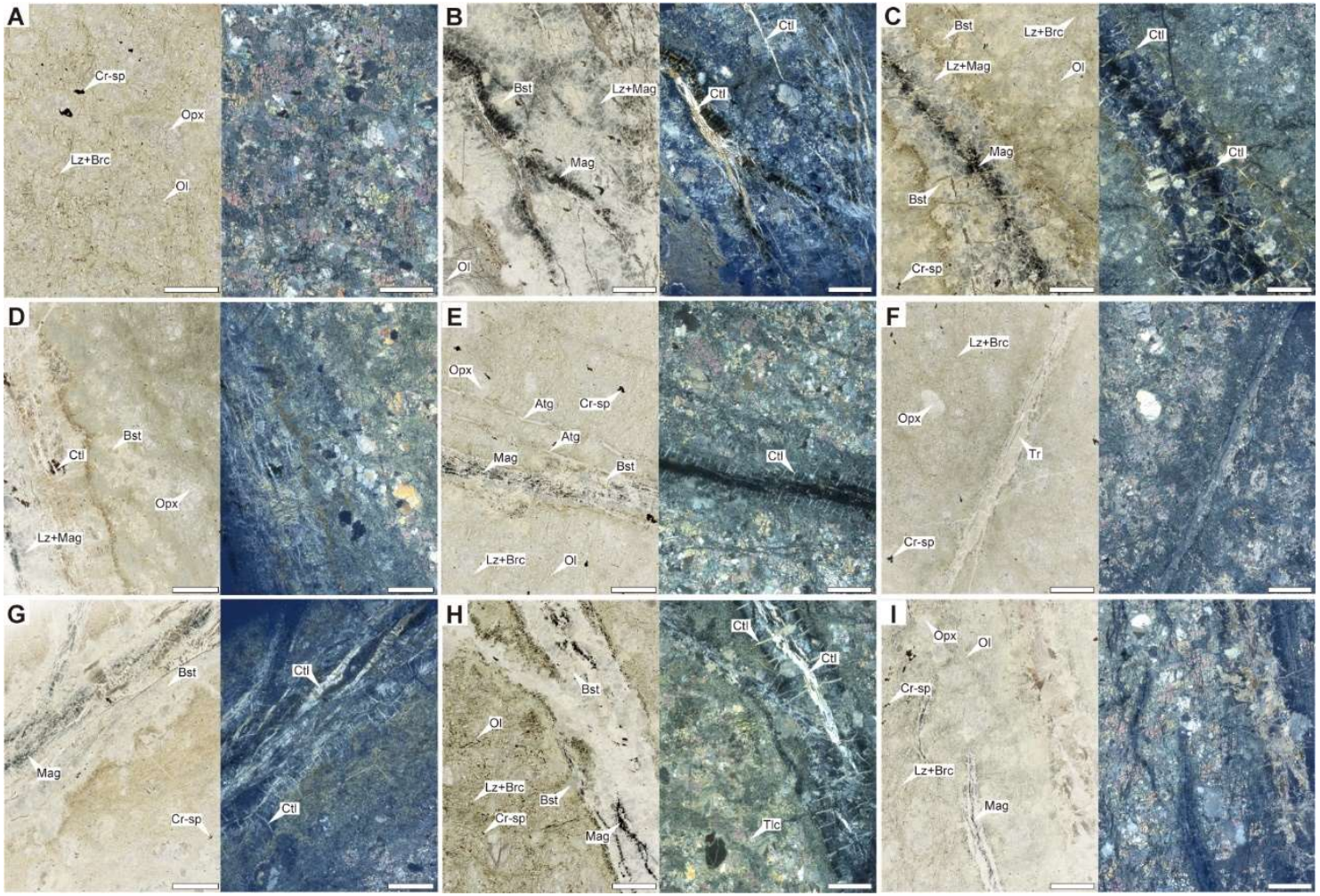

Fig. 2.36. Thin section image of the gabbroic rocks under plain polarized light and crossed polarized light. (A) CM1A-144Z4-60-68, (B) CM1A-179Z2-30-35, (C) CM2B-68Z1-27-31, (D) CM2B-73Z3-64-69, (E) CM2B-77Z4-70-75, (F) CM2B-83Z2-8-13_, (G) CM2B-106Z3-16-21, (H) CM2B-119Z2-7-12, (I) CM2B-120Z3-8-13. Ol = olivine, Pl = plagioclase, Opx = orthopyroxene, Mag = magnetite, Chl = chlorite. Bst=bastite.

Table 2.11. Chemical composition of primary minerals in harzburgite (in wt. %) with 1σ standard deviation and calculated structural formula.

Sample	CM1A-144Z4-60-68		CM1A-163Z1-12-20		CM1A-170Z1-31-39		CM2B-68Z1-27-31		CM2B-77Z4-70-75		CM2B-83Z2-8-13		CM2B-119Z2-7-12	
Lithology	Harzburgite		Harzburgite		Harzburgite		Harzburgite		Harzburgite		Harzburgite		Harzburgite	
Mineral	Olivine		Olivine		Olivine		Olivine		Olivine		Olivine		Olivine	
N	7		10		3		10		9		27		16	
	avg.	1σ	avg.	1σ	avg.	1σ	avg.	1σ	avg.	1σ	avg.	1σ	avg.	1σ
SiO_2	41.08	0.23	41.00	0.27	41.16	0.26	41.14	0.40	40.62	0.21	41.02	0.40	41.02	0.40
TiO_2	0.01	0.02	0.02	0.01	0.00	0.00	0.01	0.02	0.01	0.02	0.01	0.02	0.01	0.02
Al_2O_3	0.02	0.04	0.02	0.03	0.00	0.00	0.03	0.04	0.01	0.03	0.02	0.03	0.02	0.03
FeO	8.36	0.39	7.96	0.23	7.73	0.35	8.55	0.24	8.08	0.25	8.10	0.25	8.10	0.25
MnO	0.10	0.05	0.09	0.05	0.12	0.08	0.14	0.04	0.13	0.04	0.13	0.06	0.13	0.06
MgO	50.29	0.28	50.54	0.82	51.49	0.13	50.90	0.40	50.13	0.19	50.79	0.42	50.79	0.42
CaO	0.02	0.02	0.02	0.01	0.01	0.01	0.03	0.01	0.04	0.01	0.02	0.02	0.02	0.02
Na_2O	0.03	0.04	0.03	0.03	0.03	0.04	0.06	0.06	0.01	0.03	0.03	0.04	0.03	0.04
K_2O	0.00	0.01	0.00	0.00	0.00	0.00	0.00	0.00	0.00	0.00	0.00	0.01	0.00	0.01
Cr_2O_3	0.02	0.02	0.02	0.02	0.00	0.00	0.02	0.02	0.01	0.02	0.04	0.10	0.04	0.10
Total	99.94	0.49	99.78	1.15	100.91	0.64	100.88	0.68	99.04	0.37	100.31	0.59	100.31	0.59
Oxygen	4		4		4		4		4		4		4	
Si	1.00		1.00		1.74		0.99		1.00		1.00		1.00	
Ti	0.00		0.00		0.00		0.00		0.00		0.00		0.00	
Al	0.00		0.00		0.00		0.00		0.00		0.00		0.00	
Fe	0.17		0.16		0.27		0.17		0.17		0.16		0.16	
Mn	0.00		0.00		0.00		0.00		0.00		0.00		0.00	
Mg	1.82		1.84		3.24		1.83		1.83		1.84		1.84	
Ca	0.00		0.00		0.00		0.00		0.00		0.00		0.00	
Na	0.00		0.00		0.00		0.00		0.00		0.00		0.00	
K	0.00		0.00		0.00		0.00		0.00		0.00		0.00	
Cr	0.00		0.00		0.00		0.00		0.00		0.00		0.00	
Total	3.00		3.00		5.26		3.01		3.00		3.00		3.00	
X_{Mg}	0.91		0.92		0.92		0.91		0.92		0.92		0.92	

X_{Mg}=Mg^{2+}/(Mg^{2+}+Fe^{2+}), where Mg^{2+} and Fe^{2+} are in atoms per formula unit (a.p.f.u.).

Table 2.11. Continue of chemical composition of primary minerals in harzburgite (in wt. %) with 1σ standard deviation and calculated structural formula.

Sample	CM1A-144Z4-60-68		CM1A-163Z1-12-20		CM2B-77Z4-70-75		CM2B-83Z2-8-13		CM2B-119Z2-7-12		CM1A-58Z1-50-54		CM1A-144Z4-60-68		CM2B-56Z3-51-56	
Lithology	Harzburgite		Harzburgite		Harzburgite		Harzburgite		Harzburgite		Harzburgite		Harzburgite		Harzburgite	
Mineral	Orthopyroxene		Orthopyroxene		Orthopyroxene		Orthopyroxene		Orthopyroxene		Clinopyroxene		Clinopyroxene		Clinopyroxene	
N	3		6		17		22		16		3		8		6	
	avg.	1σ	avg.	1σ	avg.	1σ	avg.	1σ	avg.	1σ	avg.	1σ	avg.	1σ	avg.	1σ
SiO_2	56.79	0.34	56.56	0.26	55.59	1.18	56.55	0.68	56.18	0.38	51.60	0.32	53.17	0.24	53.05	1.14
TiO_2	0.01	0.02	0.02	0.00	0.02	0.02	0.02	0.02	0.02	0.02	0.26	0.04	0.05	0.03	0.16	0.11
Al_2O_3	1.89	0.02	2.06	0.06	1.94	0.21	1.49	0.64	1.88	0.18	3.12	0.09	2.42	0.28	1.51	1.14
FeO	5.69	0.15	5.11	0.12	4.76	1.07	5.44	0.19	5.23	0.35	4.65	0.16	2.52	0.14	2.13	0.46
MnO	0.11	0.07	0.13	0.03	0.15	0.07	0.15	0.04	0.14	0.06	0.07	0.05	0.06	0.03	0.08	0.03
MgO	33.99	0.25	34.30	0.26	30.84	5.78	34.61	0.80	33.95	0.32	16.33	0.22	17.89	0.39	17.80	0.34
CaO	1.43	0.02	1.44	0.11	5.35	7.86	1.08	0.79	1.90	0.38	21.78	0.10	22.16	0.34	23.41	1.45
Na_2O	0.02	0.01	0.04	0.05	0.03	0.05	0.02	0.04	0.04	0.05	0.25	0.09	0.34	0.16	0.13	0.10
K_2O	0.01	0.01	0.00	0.01	0.00	0.00	0.00	0.00	0.00	0.00	0.00	0.00	0.00	0.00	0.01	0.01
Cr_2O_3	0.67	0.03	0.68	0.02	0.69	0.14	0.50	0.27	0.76	0.06	0.68	0.03	1.04	0.10	0.73	0.46
Total	100.60	0.17	100.47	0.22	99.37	0.54	99.89	0.58	100.11	0.55	98.86	0.10	99.67	0.28	99.08	0.50
Oxygen	6		6		6		6		6		6		6		6	
Si	1.95		1.94		1.95		1.95		1.94		1.91		1.94		1.28	
Ti	0.00		0.00		0.00		0.00		0.00		0.01		0.00		0.01	
Al	0.08		0.08		0.08		0.06		0.08		0.14		0.10		0.08	
Fe	0.16		0.15		0.14		0.16		0.15		0.14		0.08		0.05	
Mn	0.00		0.00		0.00		0.00		0.00		0.00		0.00		0.00	
Mg	1.74		1.76		1.61		1.78		1.75		0.90		0.97		0.65	
Ca	0.05		0.05		0.21		0.04		0.07		0.87		0.87		0.58	
Na	0.00		0.00		0.00		0.00		0.00		0.02		0.02		0.01	
K	0.00		0.00		0.00		0.00		0.00		0.00		0.00		0.00	
Cr	0.02		0.02		0.02		0.01		0.02		0.02		0.03		0.02	
Total	4.00		4.01		4.00		4.01		4.01		4.01		4.01		2.67	
X_{Mg}	0.91		0.92		0.92		0.92		0.92		0.86		0.93		0.92	

X_{Mg}=Mg^{2+}/(Mg^{2+}+Fe^{2+}), where Mg^{2+} and Fe^{2+} are in atoms per formula unit (a.p.f.u.).

Table 2.11. Continue of chemical composition of primary minerals in harzburgite (in wt. %) with 1σ standard deviation and calculated structural formula.

Sample	CM1A-144Z4-60-68		CM1A-163Z1-12-20		CM1A-170Z1-31-39		CM1A-179Z3-18-26		CM2B-68Z1-27-31		CM2B-77Z4-70-75		CM2B-83Z2-8-13		CM2B-106Z2-16-21	
Lithology	Harzburgite		Harzburgite		Harzburgite		Harzburgite		Harzburgite		Harzburgite		Harzburgite		Harzburgite	
Mineral	Cr-spinel		Cr-spinel		Cr-spinel		Cr-spinel		Cr-spinel		Cr-spinel		Cr-spinel		Cr-spinel	
N	9		7		6		7		10		10		7		5	
	avg.	1σ	avg.	1σ	avg.	1σ	avg.	1σ	avg.	1σ	avg.	1σ	avg.	1σ	avg.	1σ
SiO_2	0.01	0.02	0.01	0.01	0.03	0.03	0.03	0.05	0.01	0.03	0.02	0.04	0.02	0.04	0.00	0.01
TiO_2	0.07	0.02	0.03	0.03	0.17	0.08	0.04	0.03	0.05	0.02	0.03	0.03	0.01	0.01	0.05	0.03
Al_2O_3	24.80	0.31	27.36	0.39	19.81	8.60	27.50	0.57	19.08	0.24	22.41	0.19	23.64	0.49	25.62	0.58
FeO	21.27	0.97	19.82	0.47	30.09	9.73	14.80	0.57	23.17	0.32	18.21	0.37	23.24	0.82	21.66	0.33
MnO	0.26	0.09	0.20	0.04	0.30	0.09	0.21	0.06	0.38	0.03	0.30	0.09	0.33	0.03	0.32	0.05
MgO	11.08	0.63	11.90	0.25	9.84	3.45	14.76	0.37	9.52	0.27	12.12	0.24	10.55	0.74	11.67	0.38
CaO	0.01	0.01	0.01	0.01	0.01	0.01	0.01	0.01	0.00	0.00	0.01	0.01	0.01	0.01	0.01	0.00
Na_2O	0.03	0.04	0.02	0.03	0.02	0.03	0.06	0.08	0.05	0.08	0.03	0.09	0.12	0.14	0.00	0.00
K_2O	0.00	0.01	0.00	0.01	0.01	0.01	0.01	0.01	0.00	0.00	0.00	0.00	0.00	0.01	0.00	0.00
Cr_2O_3	41.67	0.40	39.67	0.31	37.69	0.76	42.44	0.48	47.84	0.38	44.42	0.30	42.26	0.27	42.54	0.19
Total	99.33	0.54	99.19	0.64	98.45	1.67	99.84	0.56	100.09	0.70	97.56	0.48	100.26	0.67	101.88	0.78
Oxygen	4		4		4		4		4		4		4		4	
Si	0.00		0.00		0.00		0.00		0.00		0.00		0.00		0.00	
Ti	0.00		0.00		0.00		0.00		0.00		0.00		0.00		0.00	
Al	0.91		0.99		0.75		0.97		0.72		0.84		0.87		0.92	
Fe	0.56		0.51		0.87		0.37		0.62		0.48		0.61		0.55	
Mn	0.01		0.01		0.01		0.01		0.01		0.01		0.01		0.01	
Mg	0.52		0.55		0.48		0.66		0.46		0.57		0.49		0.53	
Ca	0.00		0.00		0.00		0.00		0.00		0.00		0.00		0.00	
Na	0.00		0.00		0.00		0.00		0.00		0.00		0.01		0.00	
K	0.00		0.00		0.00		0.00		0.00		0.00		0.00		0.00	
Cr	1.03		0.97		1.00		1.00		1.22		1.12		1.05		1.02	
Total	3.03		3.02		3.12		3.01		3.03		3.02		3.04		3.03	
X_{Mg}	0.48		0.52		0.35		0.64		0.42		0.54		0.45		0.49	
X_{Cr}	0.53		0.49		0.57		0.51		0.63		0.57		0.55		0.53	

X_{Mg}=Mg^{2+}/(Mg^{2+}+Fe^{2+}), where Mg^{2+} and Fe^{2+} are in atoms per formula unit (a.p.f.u.).

Table. 2.12. Protolith mineral mode of harzburgites determined by bulk-rock chemistry

	Mineral mode			
Sample	Ol (wt%)		Opx (wt%)	
C5707A-144Z2-24-32	75.3	77.7	25.0	26.3
C5707A-144Z4-60-68	67.3	69.7	30.0	31.6
C5707A-160Z3-47-55	62.8	65.4	38.8	40.8
C5707A-163Z1-12-20	75.8	78.2	24.5	25.7
C5707A-179Z2-30-38	62.9	65.6	40.0	42.1
C5707A-179Z3-18-26	69.2	71.7	30.7	32.3
C5708B-68Z1-27-31	73.8	76.1	24.8	26.1
C5708B-73Z3-64-69	56.1	58.5	36.8	38.7
C5708B-77Z4-70-75	65.9	68.4	32.6	34.3
C5708B-83Z2-8-13	60.7	63.4	41.6	43.7
C5708B-86Z3-10-15	72.0	74.5	29.1	30.6
C5708B-90Z3-40-45	71.0	73.4	27.7	29.2
C5708B-90Z4-65-70	71.0	73.4	28.6	30.1
C5708B-92Z4-35-40	68.0	70.5	33.0	34.7
C5708B-92Z4-80-85	68.5	71.1	33.4	35.1
C5708B-99Z2-68-73	68.5	71.0	31.6	33.2
C5708B-100Z2-15-20	68.9	71.3	29.8	31.3
C5708B-100Z2-65-70	70.9	73.2	27.1	28.5
C5708B-100Z2-80-85	76.2	78.5	22.4	23.5
C5708B-100Z2-85-90	72.9	75.3	26.8	28.2
C5708B-104Z1-33-38	58.6	61.4	43.0	45.3
C5708B-106Z2-16-21	68.2	70.7	32.8	34.5
C5708B-106Z3-16-21	66.6	69.1	32.5	34.2
C5708B-106Z3-33-38	69.7	72.1	29.0	30.5
C5708B-106Z3-45-50	64.4	66.9	34.7	36.5
C5708B-110Z1-57-62	18.5	22.2	92.5	97.3
C5708B-110Z1-62-67	50.5	53.3	51.4	54.1
C5708B-112Z4-47-52	42.1	45.1	60.8	64.0
C5708B-119Z1-34-39	68.6	71.1	30.8	32.4
C5708B-119Z2-7-12	61.2	63.8	40.4	42.5
C5708B-119Z3-78-83	34.2	37.7	76.3	80.3
C5708B-120Z3-8-13	64.3	66.8	33.3	35.0
C5708B-120Z4-82-87	45.9	48.9	58.6	61.6
C5708B-121Z4-55-60	68.7	71.1	28.5	29.9

Serpentinite

Olivine grains are serpentinized with a mesh texture, and a small amount of magnetite is found in the mesh rim. Orthopyroxene is less serpentinized than olivine (Fig. 2.37). Orthopyroxene grains near magnetite veins, tremolite veins, and antigorite veins are highly serpentinized and show a bastite texture (Fig. 2.37). The mesh texture of the harzburgite is observed to have a distinct hierarchical structure from the mesh rim to the mesh core: (1) type 1 rim composed of brucite+chrysotile+magnetite (Brc+Ctl+Mag), (2) type 2 rim composed of lizardite+chrysotile (Lz+Ctl), and (3) type 3 rim composed of lizardite+brucite (Lz+Brc). In the elemental map, areas with low Si concentration and high Fe concentration are regions containing a large amount of brucite, indicating a heterogeneous distribution of brucite (Fig. 2.38). The central part of the mesh vein where magnetite is precipitated has a higher Si concentration and lower Fe concentration than the surrounding mesh texture. Similar microstructures are found in other ophiolite peridotites (Miyoshi *et al.*, 2014; Schwarzenbach *et al.*, 2016). Serpentine after orthopyroxene is more Fe- and Al- rich (X_{Mg}=0.91-0.92, Al_2O_3 = 0.69-1.2 wt. %; Table 2.13) than the serpentine after olivine (X_{Mg} = 0.93-0.98, Al_2O_3 = 0.03-0.35 wt. %; Table 2.13).

The plot of atoms per formula unit of Si versus Mg+Fe indicates that the mesh texture replacing olivine is a mixture of serpentine and brucite (Fig. 2.39). By extrapolating the Si versus Mg+Fe line and Si versus Mg line to the end members, X_{Mg} of serpentine and brucite of the mesh texture are calculated to be 0.97 and 0.72, respectively, indicating that brucite is more Fe-rich than serpentine.

The Raman spectrum of type 1 rim is characterized by peaks at 129.74, 230.53, 383.61, 690.30, 1099.46, and 3695.97 cm^{-1} corresponding to chrystile and 274.08, 438.62, 3638.93, and 3648.32 cm^{-1} corresponding to brucite (Fig. 2.40). The Raman spectrum of type 2 rim is characterized by peaks at 129.74, 228.71, 383.61, 690.30, 3686.69, and 3703.17 cm^{-1} corresponding to lizardite and a small peak at 1097.86 cm^{-1} corresponding to chrysotile. The Raman spectrum of type 3 rim is characterized by peaks at 131.59, 228.71, 381.82, 688.60, 3681.53, and 3704.20 cm^{-1} corresponding to lizardite and small peaks of brucite at 440.39 and 3633.71 cm^{-1}. The Raman spectrum of bastite is characterized by peaks at 124.21, 223.25, 378.26, 686.89, 1094.67, and 3689.78 cm^{-1}. The peaks at 1094.67 and 3689.78 cm^{-1} are similar to those of chrysotile.

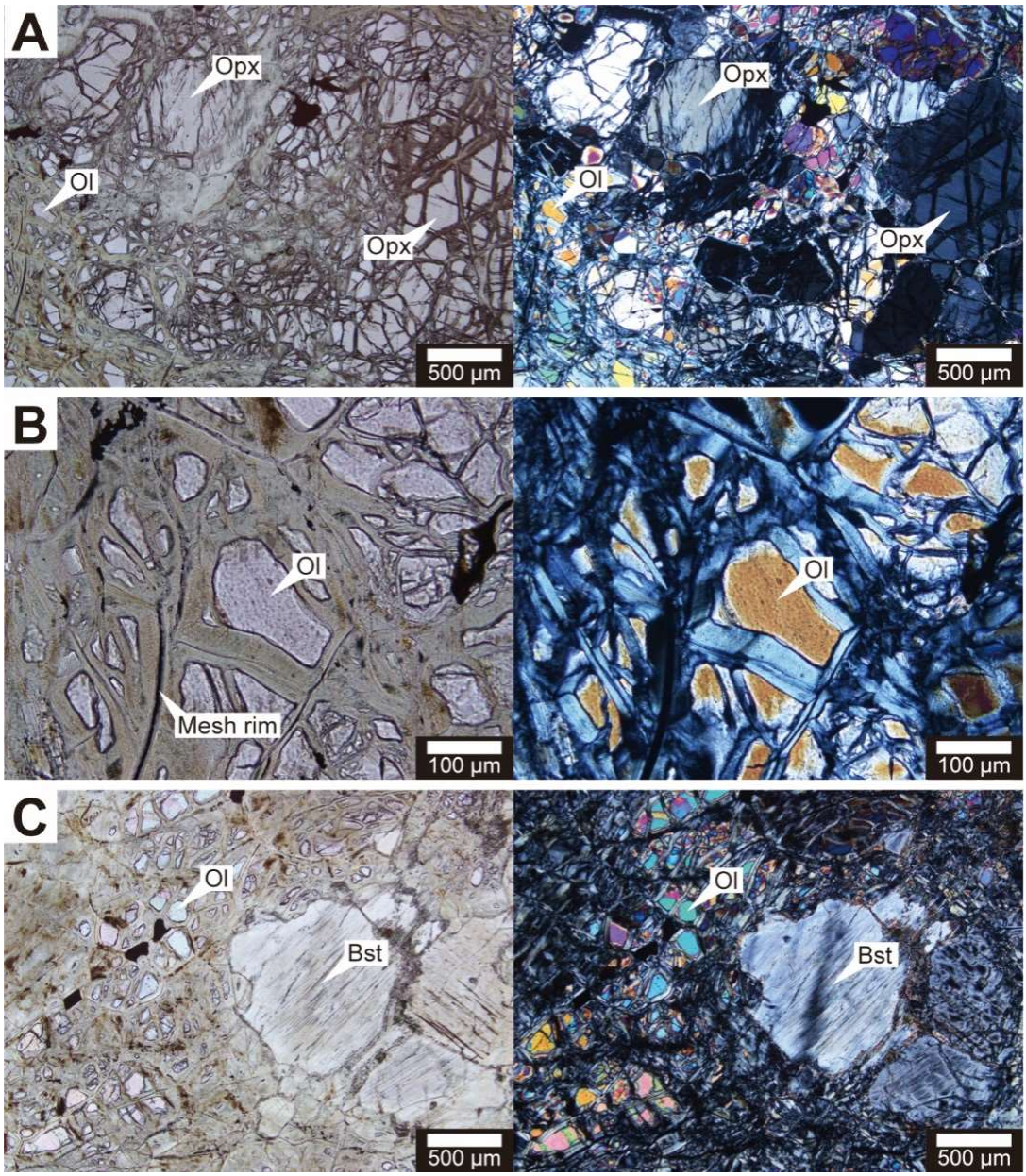

Fig. 2.37. Plain polarized light (PPL) and crossed polarized light (XPL) optical microscope photos of harzburgites. (A) Mesh texture composed of lizardite and brucite (CM1A-144Z4-60-68). (B) Close up view of the mesh texture. (C) Serpentinized orthopyroxene shows “bastite” texture (CM2B-68Z1-27-31).

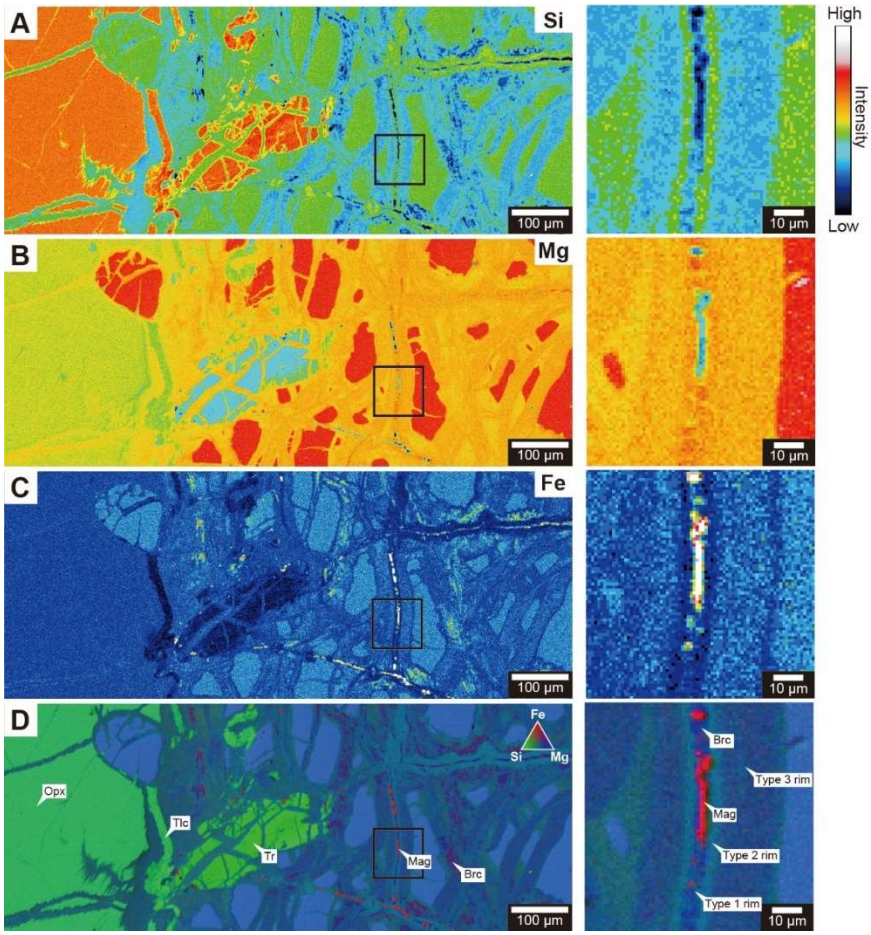

Fig. 2.38. Element mapping of the partly serpentinized harzburgite (CM1A-144Z4-60-68) for Si, Mg, and Fe with close up view in the rectangle (A-C). (D)Three element composite map of Si (Green), Mg (Blue), and Fe (Red). Ol=olivine, Srp = serpentine, Brc = brucite, Mag = magnetite.

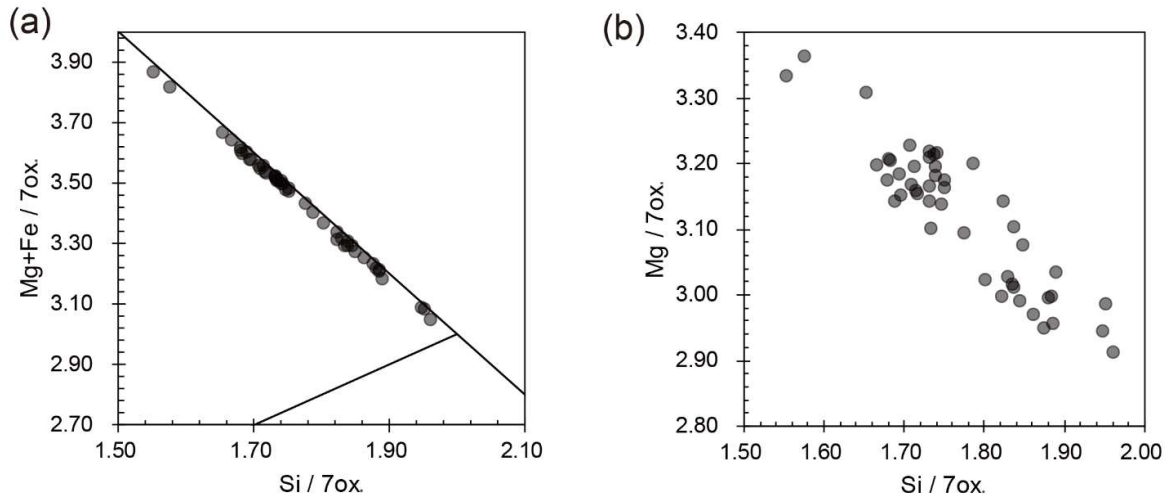

Fig. 2.39. (A) Si versus Mg+Fe plot. (B)Si versus Mg plot.

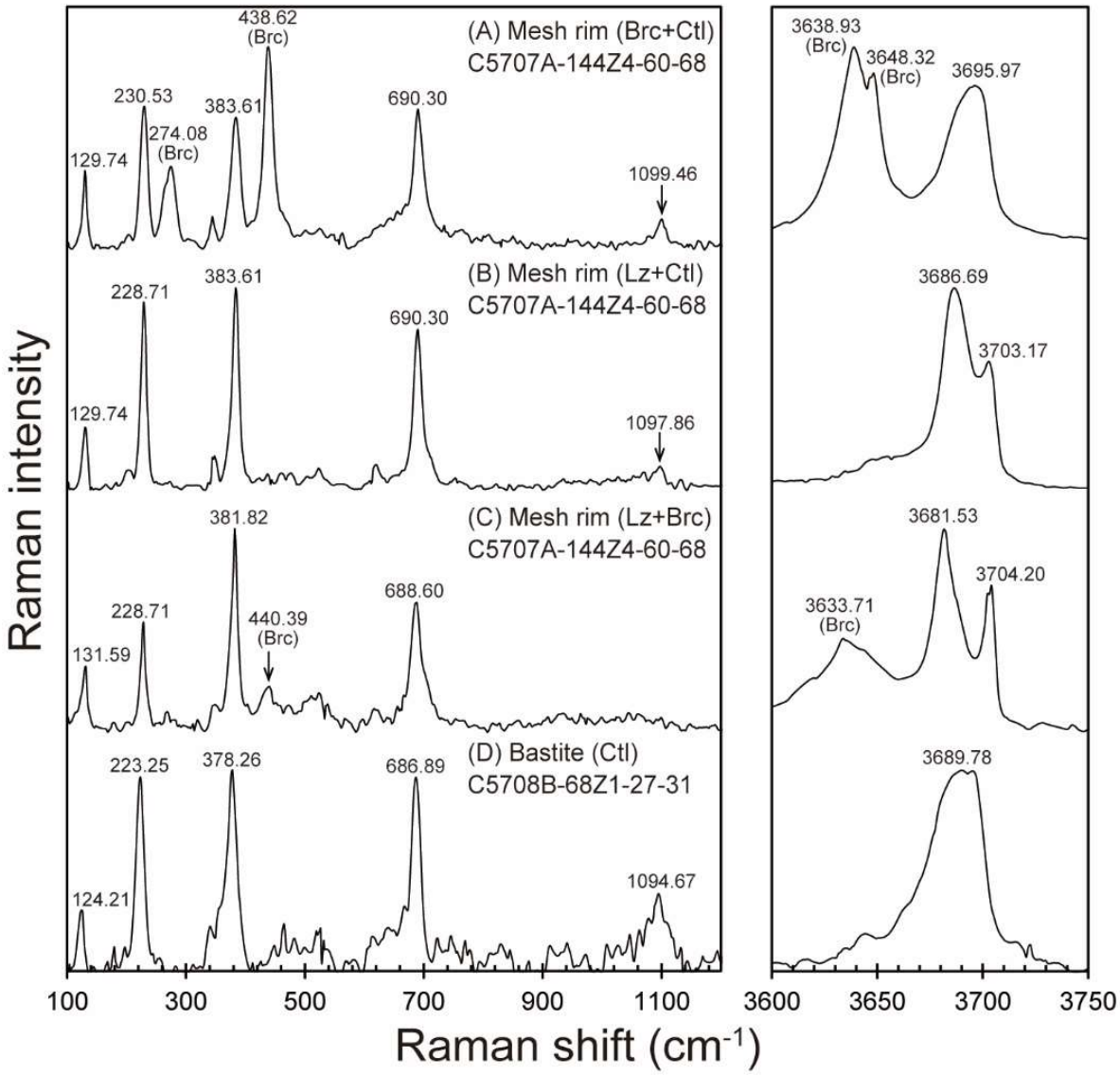

Fig. 2.40. Raman spectra of mesh texture (CM1A-144Z4-60-68) and bastite(CM2B-68Z1-27-31).

Table 2.13 Chemical composition of serpentine and brucite in harzburgite (in wt. %) with 1σ standard deviation and calculated structural formula.

Sample	CM1A-137Z3-46-54				CM1A-144Z4-60-68				CM1A-150Z1-24-32				CM1A-163Z1-12-20	
Lithology	Harzburgite				Harzburgite				Harzburgite				Harzburgite	
Mineral	Srp		Srp+Brc		Srp+Brc		Srp		Srp+Brc		Srp+Brc		Srp+Brc	
Type	Mesh rim		Mesh core		Mesh rim		After Opx		Mesh rim		Mesh core		Mesh rim	
N	15		25		95		3		15		10		70	
	avg.	1σ	avg.	1σ	avg.	1σ	avg.	1σ	avg.	1σ	avg.	1σ	avg.	1σ
SiO_2	41.45	0.40	24.62	18.30	34.15	7.50	38.82	0.89	35.41	2.12	39.40	0.97	34.59	3.85
TiO_2	0.01	0.01	0.01	0.02	0.01	0.02	0.05	0.01	0.02	0.02	0.01	0.01	0.01	0.02
Al_2O_3	0.19	0.06	0.15	0.08	0.03	0.04	1.20	0.28	0.04	0.06	0.35	0.05	0.03	0.03
FeO	1.99	0.28	4.67	2.65	7.62	4.53	6.47	0.11	5.61	1.28	3.96	0.44	7.53	3.30
MnO	0.05	0.05	0.21	0.21	0.07	0.07	0.05	0.06	0.07	0.05	0.05	0.05	0.14	0.11
MgO	40.55	0.56	53.37	14.06	42.26	4.56	36.73	0.75	41.86	1.16	39.70	0.42	41.59	2.32
CaO	0.09	0.01	0.07	0.03	0.21	0.28	0.85	0.48	0.23	0.09	0.38	0.03	0.16	0.06
Na_2O	0.03	0.04	0.03	0.03	0.02	0.03	0.02	0.02	0.02	0.04	0.03	0.04	0.02	0.03
K_2O	0.00	0.00	0.00	0.01	0.00	0.01	0.01	0.00	0.00	0.01	0.00	0.01	0.00	0.00
Cr_2O_3	0.02	0.02	0.01	0.02	0.02	0.03	0.54	0.10	0.03	0.03	0.03	0.02	0.02	0.02
Total	84.37	0.88	83.15	1.91	84.50	4.32	84.71	0.79	83.30	1.07	83.93	0.40	84.12	2.13
Oxygen	7		7		7		7		7		7		7	
Si	1.99		1.20		1.72		1.92		1.79		1.94		1.75	
Ti	0.00		0.00		0.00		0.00		0.00		0.00		0.00	
Al	0.01		0.01		0.00		0.07		0.00		0.02		0.00	
Fe	0.08		0.22		0.34		0.27		0.24		0.16		0.32	
Mn	0.00		0.01		0.00		0.00		0.00		0.00		0.01	
Mg	2.91		4.34		3.21		2.71		3.16		2.91		3.15	
Ca	0.00		0.00		0.01		0.05		0.01		0.02		0.01	
Na	0.00		0.00		0.00		0.00		0.00		0.00		0.00	
K	0.00		0.00		0.00		0.00		0.00		0.00		0.00	
Cr	0.00		0.00		0.00		0.02		0.00		0.00		0.00	
Total	5.00		5.79		5.28		5.03		5.21		5.05		5.25	
X_{Srp}			0.60		0.86				0.90		0.97		0.88	
X_{Mg} of Srp	0.97		0.97		0.95		0.91		0.97		0.96		0.96	
X_{Mg} of Brc			0.94		0.78				0.79		0.82		0.74	

X_{Mg}=Mg^{2+}/(Mg^{2+}+Fe^{2+}), where Mg^{2+} and Fe^{2+} are in atoms per formula unit (a.p.f.u.).

Table 2.13 Continue of chemical composition of serpentine and brucite in harzburgite (in wt. %) with 1σ standard deviation and calculated structural formula.

Sample	CM1A-170Z1-31-39		CM1A-179Z3-18-26		CM2B-68Z1-27-31		CM2B-77Z4-70-75				CM2B-83Z2-8-13				CM2B-119Z2-7-12	
Lithology	Harzburgite		Harzburgite		Harzburgite		Harzburgite				Harzburgite				Harzburgite	
Mineral	Srp+Brc		Srp		Srp+Brc		Srp+Brc		Srp		Srp+Brc		Srp		Srp+Brc	
Type	Mesh rim		Matrix		Mesh		Mesh		After Opx		Mesh		After Opx		Mesh	
N	17		41		52		10		72		134		36		78	
	avg.	1σ	avg.	1σ	avg.	1σ	avg.	1σ	avg.	1σ	avg.	1σ	avg.	1σ	avg.	1σ
SiO_2	34.70	3.29	42.03	0.52	36.15	2.86	36.14	2.17	37.70	3.07	35.72	3.15	38.74	0.92	38.27	3.68
TiO_2	0.01	0.02	0.02	0.02	0.01	0.02	0.01	0.02	0.02	0.02	0.01	0.01	0.02	0.03	0.01	0.02
Al_2O_3	0.09	0.08	0.27	0.11	0.03	0.04	0.16	0.13	0.69	0.46	0.04	0.06	1.02	0.24	0.08	0.09
FeO	5.35	0.84	1.64	0.21	5.30	2.00	5.43	0.90	5.75	0.87	6.62	3.72	5.59	0.30	4.61	2.51
MnO	0.05	0.04	0.06	0.04	0.06	0.05	0.10	0.08	0.12	0.07	0.11	0.07	0.14	0.07	0.07	0.06
MgO	41.90	3.43	39.89	0.98	41.06	2.67	39.55	1.21	36.48	2.84	40.71	1.83	36.37	0.68	40.10	1.36
CaO	0.07	0.04	0.02	0.01	0.20	0.14	0.17	0.06	0.71	0.74	0.18	0.06	0.78	0.51	0.03	0.02
Na_2O	0.02	0.04	0.02	0.04	0.03	0.04	0.04	0.07	0.03	0.05	0.02	0.03	0.03	0.05	0.02	0.04
K_2O	0.00	0.00	0.00	0.01	0.00	0.00	0.00	0.00	0.01	0.01	0.00	0.01	0.01	0.01	0.00	0.01
Cr_2O_3	0.02	0.02	0.03	0.03	0.01	0.02	0.02	0.03	0.41	0.34	0.02	0.02	0.64	0.17	0.02	0.03
Total	82.61	1.18	83.99	1.26	82.86	2.62	81.64	0.75	81.91	3.36	83.54	2.39	83.38	1.26	83.21	1.27
Oxygen	7		7		7		7		7		7		7		7	
Si	1.78		2.02		1.83		1.85		1.92		1.81		1.94		1.90	
Ti	0.00		0.00		0.00		0.00		0.00		0.00		0.00		0.00	
Al	0.01		0.02		0.00		0.01		0.04		0.00		0.06		0.00	
Fe	0.23		0.07		0.23		0.23		0.25		0.28		0.23		0.19	
Mn	0.00		0.00		0.00		0.00		0.01		0.00		0.01		0.00	
Mg	3.20		2.86		3.10		3.03		2.78		3.08		2.71		2.98	
Ca	0.00		0.00		0.01		0.01		0.04		0.01		0.04		0.00	
Na	0.00		0.00		0.00		0.00		0.00		0.00		0.00		0.00	
K	0.00		0.00		0.00		0.00		0.00		0.00		0.00		0.00	
Cr	0.00		0.00		0.00		0.00		0.02		0.00		0.03		0.00	
Total	5.22		4.97		5.17		5.14		5.05		5.19		5.02		5.09	
X_{Srp}	0.89				0.91		0.93				0.90				0.95	
X_{Mg} of Srp	0.93		0.98		0.96		0.94		0.92		0.98		0.92		0.96	
X_{Mg} of Brc	0.94				0.79		0.84				0.65				0.76	

$X_{Mg}=Mg^{2+}/(Mg^{2+}+Fe^{2+})$, where Mg^{2+} and Fe^{2+} are in atoms per formula unit (a.p.f.u.).

Talc and tremolite

Talc and tremolite are found at the boundary between olivine and orthopyroxene (Fig. 2.41 and Fig. 2.38D). Veins of talc and serpentine also cut the orthopyroxene (Fig. 2.41B). Compared to talc in gabbroic rocks, talc in harzburgite is enriched in Mg (X_{Mg} = 0.97-0.98). The X_{Mg} of tremolite is 0.90-0.94. The Raman spectrum of talc shows characteristic peaks of talc at 192.21, 225.07, 358.62, 673.24, 3675.32 cm^{-1} (Fig. 2.42). The small peaks at 225.07, 380.04 and 3686.69 cm^{-1} correspond to a small amount of serpentine.

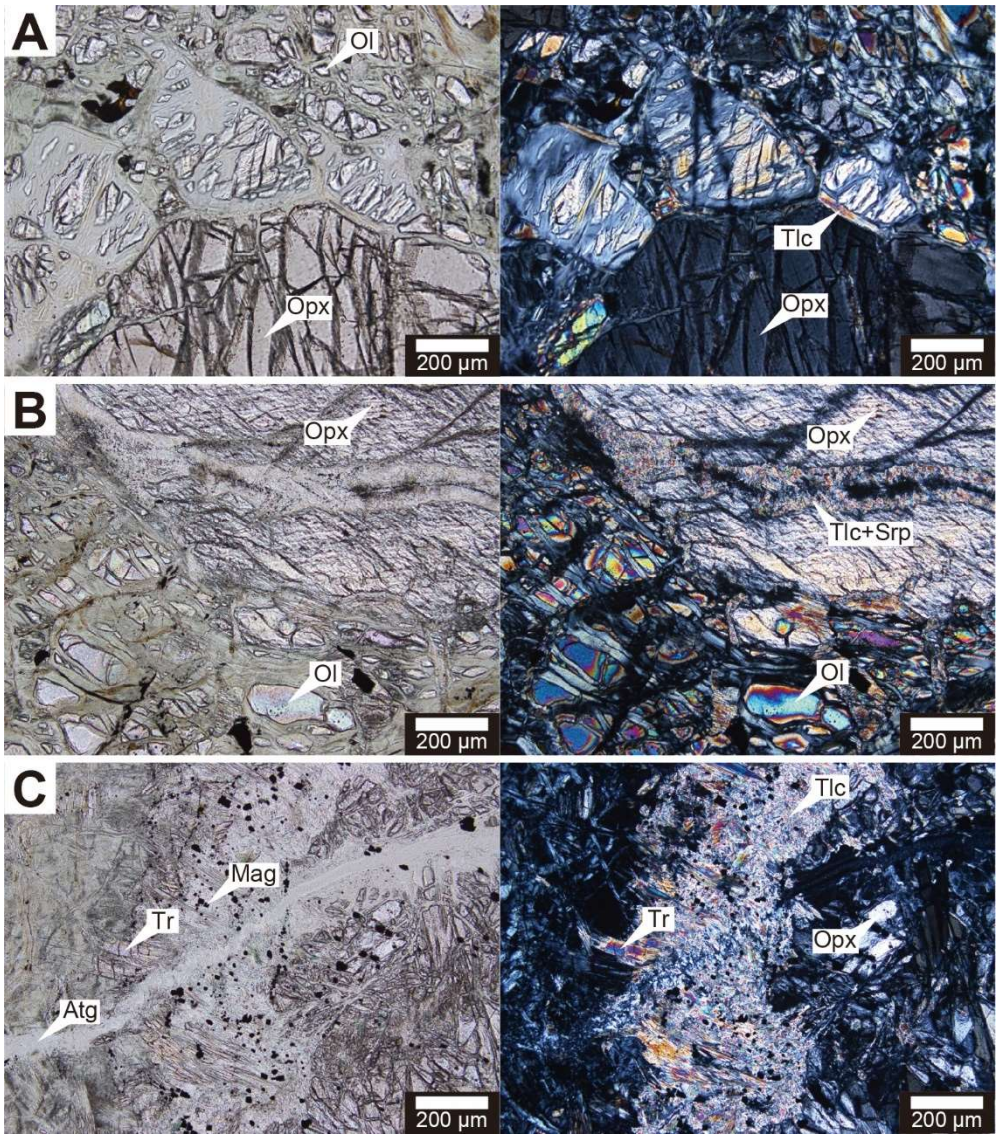

Fig. 2.41. Optical micrographs of talc and tremolite in harzburgite. (A)Talc (CM2B-120Z3-8-13). (B)Vein of talc and serpentine cut through orthopyroxene grain (CM2B-83Z2-8-13). (C)Talc and tremolite (CM2B-83Z2-8-13). Ol = olivine, Opx = orthopyroxene, Tlc = talc, Srp = serpentine, Atg = antigorite, Tr = tremolite, Mag = magnetite.

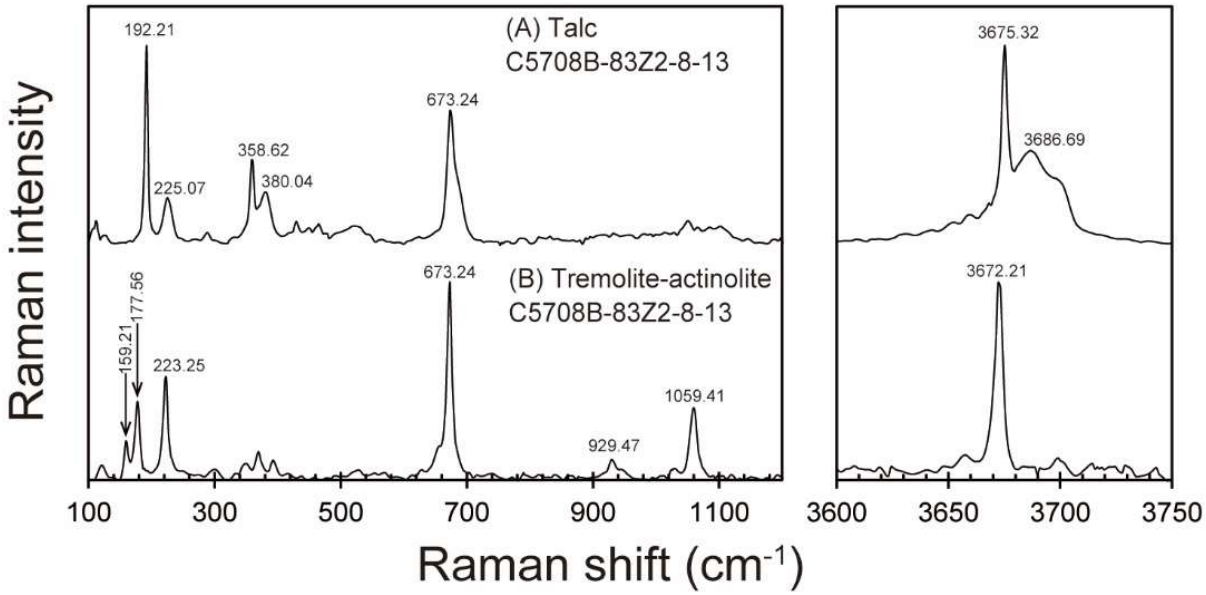

Fig. 2.42. Raman spectra of talc and tremolite in a harzburgite (CM2B-83Z2-8-13).

Table 2.14 Chemical composition of talc and amphibole in harzburgite (in wt. %) with 1σ standard deviation and calculated structural formula.

Sample	CM1A-163Z1-12-20		CM2B-83Z2-8-13		CM1A-144Z4-60-68		CM1A-144Z4-60-68				CM1A-163Z1-12-20		CM2B-83Z2-8-13			
Lithology	Harzburgite		Harzburgite		Harzburgite		Harzburgite				Harzburgute		Harzburgite			
Mineral	Talc		Talc		Tremolite		Actinolite		Tremolite		Tremolite		Tremolite		Tremolite	
	Matrix		Matrix		Matrix		Matrix		Vein		Matrix		Matrix		Vein	
N	3		16		2		2		19		7		9		31	
	avg.	1σ	avg.	1σ	avg.	1σ	avg.	1σ	avg.	1σ	avg.	1σ	avg.	1σ	avg.	1σ
SiO_2	59.77	0.82	58.43	1.85	55.80	0.18	56.79	0.16	57.17	0.72	52.30	2.12	54.34	4.22	54.95	2.68
TiO_2	0.01	0.00	0.01	0.02	0.05	0.01	0.00	0.00	0.02	0.02	0.02	0.01	0.03	0.03	0.07	0.09
Al_2O_3	1.83	0.43	1.07	0.42	2.05	0.01	1.30	0.03	0.88	0.50	5.12	1.58	3.58	3.68	2.00	2.24
FeO	1.33	0.12	1.99	0.35	1.73	0.09	6.18	0.12	1.91	0.15	2.69	0.27	2.44	0.77	1.90	0.53
MnO	0.03	0.01	0.02	0.03	0.00	0.00	0.06	0.04	0.05	0.05	0.03	0.03	0.07	0.04	0.05	0.04
MgO	30.61	0.40	30.83	0.60	22.63	0.10	26.11	0.42	23.07	0.46	21.95	1.23	22.55	1.71	23.36	1.58
CaO	0.11	0.12	0.06	0.03	12.95	0.08	5.20	0.12	13.03	0.24	11.71	0.55	12.17	0.82	12.11	1.03
Na_2O	0.51	0.10	0.11	0.09	0.24	0.02	0.31	0.06	0.20	0.14	1.33	0.38	0.86	0.89	0.48	0.50
K_2O	0.00	0.00	0.02	0.01	0.00	0.00	0.00	0.00	0.01	0.01	0.01	0.01	0.03	0.05	0.01	0.02
Cr_2O_3	0.69	0.04	0.46	0.13	1.04	0.04	0.15	0.03	0.09	0.13	1.35	0.33	0.85	0.64	0.43	0.43
Total	95.04	0.61	93.02	1.18	96.50	0.11	96.22	0.45	96.50	0.67	96.58	0.68	97.03	0.40	95.36	1.18
Oxygen	11		11		23		23		23		23		23		23	
Si	3.85		3.84		7.74		7.86		7.91		7.36		7.54		7.71	
Ti	0.00		0.00		0.00		0.00		0.00		0.00		0.00		0.01	
Al	0.14		0.08		0.34		0.21		0.14		0.81		0.60		0.33	
Fe	0.07		0.11		0.20		0.72		0.22		0.31		0.28		0.22	
Mn	0.00		0.00		0.00		0.01		0.01		0.00		0.01		0.01	
Mg	2.94		3.03		4.68		5.39		4.76		4.62		4.66		4.89	
Ca	0.01		0.00		1.92		0.77		1.93		1.75		1.81		1.82	
Na	0.06		0.01		0.06		0.08		0.05		0.35		0.24		0.13	
K	0.00		0.00		0.00		0.00		0.00		0.00		0.01		0.00	
Cr	0.03		0.02		0.11		0.02		0.01		0.14		0.09		0.05	
Total	7.10		7.11		15.06		15.06		15.04		15.34		15.24		15.16	
X_{Mg}	0.98		0.97		0.96		0.88		0.96		0.94		0.94		0.96	

X_{Mg}=Mg^{2+}/(Mg^{2+}+Fe^{2+}), where Mg^{2+} and Fe^{2+} are in atoms per formula unit (a.p.f.u.).

Serpentine vein

Antigorite veins cut the mesh texture, and both sides of the antigorite vein are highly serpentinized with mesh texture (Fig. 2.43). Part of the orthopyroxene grain in contact with the antigorite vein is highly serpentinized (Fig. 2.43). Antigorite vein also cuts tremolite-talc textures (Fig. 2.41C). Antigorite crystals extends perpendicular to the vein at the boundary with the host rock. The center of the vein composed of randomly oriented antigorite crystals (Fig. 2.43B). The chrysotile vein cuts in a direction perpendicular to the antigorite vein (Fig.2.43B). The antigorite vein is relatively rich in Al (Al_2O_3=0.08-0.59 wt. %; Table 2.15) than mesh texture serpentine and X_{Mg} is 0.92-0.97. Chrysotile veins cutting antigorite veins are relatively Fe-rich (X_{Mg} = 0.88-0.91). Raman spectra of the antigorite veins show a characteristic peak of antigorite at 1049.76 cm-1 (Fig. 2.44A). Chrysotile veins show a characteristic peak of chrysotile at 1107.44 cm-1 (Fig. 2.44B).

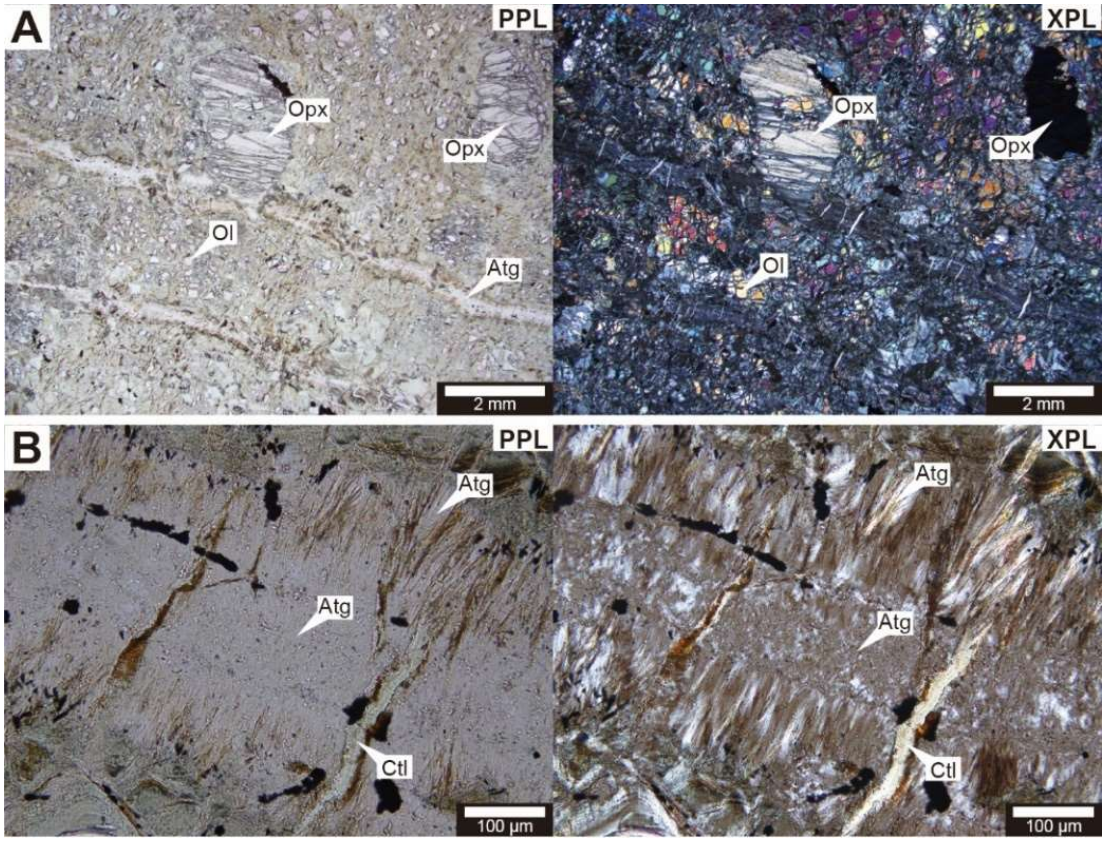

Fig. 2.43. Optical micrographs of antigorite veins in harzburgite (CM2B-77Z4-70-75). (A) Antigorite veins cut mesh texture host rock and a orthopyroxene grain. (B) Close up view of the antigorite vein. Antigorite crystals extends perpendicular to the vein at the boundary with the host rock. The center of the vein shows randomly oriented antigorite crystals. Ol = olivine, Opx = orthopyroxene, Atg = antigorite, Ctl = chrysotile.

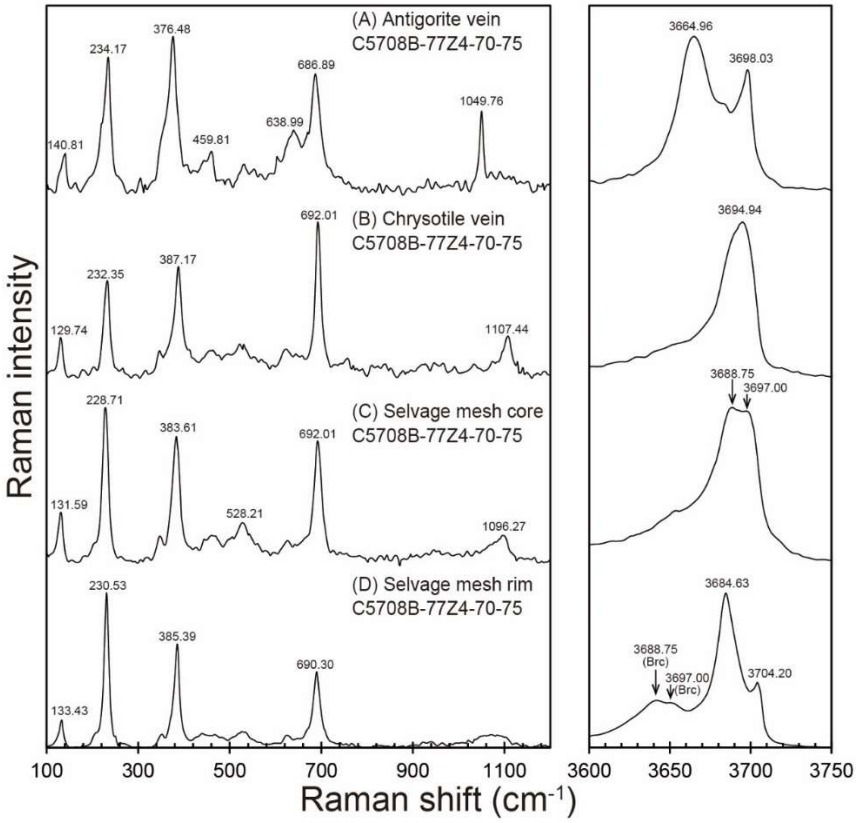

Fig. 2.44. Raman spectra of the serpentine veins and the selvage of the veins (CM2B-77Z4-70-75). (A)antigorite vein, (B)chrysotile vein, (C)selvage of the antigorite vein.

Table 2.15 Chemical composition of serpentine in harzburgite (in wt. %) with 1σ standard deviation and calculated structural formula.

Sample	CM1A-137Z3-46-54						CM1A-144Z4-60-68						CM1A-150Z1-24-32			
Lithology	Harzburgite						Harzburgite						Harzburgite			
Mineral	Atg		Ctl		Ctl		Ctl		Srp+Brc		Srp+Brc		Atg		Ctl	
Type	Atg+Ctl vein		Atg+Ctl vein		Ctl vein		with tremolite vein		Selvage mesh rim		Selvage mesh core		Atg+Ctl vein		Atg+Ctl vein	
N	15		10		10		45		28		41		10		10	
	avg.	1σ	avg.	1σ	avg.	1σ	avg.	1σ	avg.	1σ	avg.	1σ	avg.	1σ	avg.	1σ
SiO_2	43.56	0.43	41.02	0.65	40.82	0.82	40.77	0.49	39.53	0.86	38.26	1.29	43.13	0.53	41.05	0.29
TiO_2	0.02	0.02	0.02	0.02	0.01	0.02	0.01	0.02	0.01	0.02	0.02	0.02	0.02	0.02	0.02	0.02
Al_2O_3	0.59	0.15	0.52	0.21	0.24	0.11	0.38	0.05	0.09	0.06	0.32	0.16	0.45	0.17	0.96	0.07
FeO	2.80	0.16	3.14	0.32	2.62	0.72	5.61	0.31	5.32	0.56	6.82	1.42	2.52	0.22	2.76	0.14
MnO	0.06	0.05	0.07	0.05	0.06	0.05	0.07	0.06	0.06	0.06	0.08	0.05	0.02	0.03	0.04	0.04
MgO	38.60	0.93	38.82	0.45	38.05	1.61	37.41	0.45	37.99	0.70	36.77	1.19	39.48	0.43	39.40	0.57
CaO	0.02	0.01	0.13	0.15	0.04	0.01	0.26	0.03	0.18	0.09	0.41	0.23	0.07	0.02	0.11	0.01
Na_2O	0.02	0.03	0.00	0.01	0.01	0.02	0.01	0.02	0.02	0.03	0.02	0.03	0.02	0.03	0.03	0.05
K_2O	0.00	0.01	0.01	0.01	0.00	0.00	0.00	0.01	0.00	0.01	0.00	0.00	0.00	0.01	0.01	0.01
Cr_2O_3	0.02	0.02	0.01	0.02	0.01	0.02	0.02	0.02	0.01	0.02	0.03	0.04	0.01	0.02	0.02	0.02
Total	85.69	1.13	83.74	1.07	81.86	2.75	84.58	0.63	83.37	1.07	82.99	1.06	85.73	0.53	84.40	0.82
Oxygen	7		7		7		7		7		7		7		7	
Si	2.06		2.00		2.03		1.99		1.97		1.94		2.04		1.98	
Ti	0.00		0.00		0.00		0.00		0.00		0.00		0.00		0.00	
Al	0.03		0.03		0.01		0.02		0.01		0.02		0.03		0.05	
Fe	0.11		0.13		0.11		0.23		0.22		0.29		0.10		0.11	
Mn	0.00		0.00		0.00		0.00		0.00		0.00		0.00		0.00	
Mg	2.72		2.82		2.81		2.73		2.82		2.78		2.78		2.83	
Ca	0.00		0.01		0.00		0.01		0.01		0.02		0.00		0.01	
Na	0.00		0.00		0.00		0.00		0.00		0.00		0.00		0.00	
K	0.00		0.00		0.00		0.00		0.00		0.00		0.00		0.00	
Cr	0.00		0.00		0.00		0.00		0.00		0.00		0.00		0.00	
Total	4.93		4.99		4.97		4.99		5.03		5.05		4.95		4.99	
X_{Srp}									0.98		0.97					
X_{Mg} of Srp	0.96		0.96		0.96		0.92		0.94		0.94		0.97		0.96	
X_{Mg} of Brc									0.67		0.32					

X_{Mg}=Mg^{2+}/(Mg^{2+}+Fe^{2+}), where Mg^{2+} and Fe^{2+} are in atoms per formula unit (a.p.f.u.).

Table 2.15 Continue of chemical composition of serpentine in harzburgite (in wt. %) with 1σ standard deviation and calculated structural formula.

Sample	CM1A-150Z1-24-32				CM1A-170Z1-31-39				CM1A-179Z3-18-26		CM2B-77Z4-70-75					
Lithology	Harzburgite				Harzburgite				Harzburgite		Harzburgite					
Mineral	Srp+Brc		Brc+Srp		Srp+Brc		Ctl		Ctl		Atg		Srp		Ctl	
Type	Selvage mesh rim		Selvage mesh core		Selvage		Vein		Vein		Vein		Selvage		Vein	
N	5		6		3		3		13		25		35		15	
	avg.	1σ	avg.	1σ	avg.	1σ	avg.	1σ	avg.	1σ	avg.	1σ	avg.	1σ	avg.	1σ
SiO_2	34.97	0.97	7.22	1.43	38.68	1.86	40.29	0.73	43.83	0.47	43.18	0.39	37.49	2.98	39.44	0.54
TiO_2	0.01	0.02	0.01	0.01	0.01	0.01	0.01	0.01	0.01	0.02	0.01	0.02	0.01	0.02	0.01	0.02
Al_2O_3	0.29	0.05	0.03	0.03	0.24	0.16	0.38	0.01	0.36	0.08	0.08	0.06	0.15	0.10	0.14	0.15
FeO	6.41	0.43	19.88	0.78	3.27	0.65	7.75	0.34	1.57	0.15	3.11	0.40	5.11	1.34	6.42	0.84
MnO	0.10	0.01	0.54	0.05	0.07	0.07	0.08	0.01	0.10	0.07	0.05	0.05	0.09	0.08	0.13	0.07
MgO	39.38	0.81	52.10	0.83	40.36	1.81	32.17	1.13	41.15	1.27	37.91	0.59	39.05	1.48	35.18	1.08
CaO	0.56	0.11	1.39	0.05	0.20	0.05	0.05	0.01	0.01	0.01	0.02	0.02	0.26	0.09	0.20	0.03
Na_2O	0.04	0.04	0.06	0.04	0.04	0.03	0.00	0.00	0.02	0.04	0.02	0.04	0.02	0.04	0.03	0.05
K_2O	0.00	0.00	0.00	0.00	0.01	0.01	0.00	0.00	0.00	0.01	0.00	0.01	0.01	0.01	0.00	0.01
Cr_2O_3	0.01	0.02	0.01	0.01	0.01	0.02	0.01	0.01	0.01	0.01	0.01	0.01	0.01	0.02	0.01	0.01
Total	81.77	0.59	81.24	1.04	82.89	1.26	80.82	2.01	87.06	1.59	84.39	0.84	82.20	1.28	81.59	1.54
Oxygen	7		1		7		7		7		7		7		7	
Si	1.81		0.45		1.92		2.08		2.03		2.07		1.90		2.01	
Ti	0.00		0.00		0.00		0.00		0.00		0.00		0.00		0.00	
Al	0.02		0.00		0.01		0.02		0.02		0.00		0.01		0.01	
Fe	0.28		1.05		0.14		0.33		0.06		0.13		0.22		0.27	
Mn	0.00		0.03		0.00		0.00		0.00		0.00		0.00		0.01	
Mg	3.04		4.91		2.99		2.47		2.84		2.71		2.95		2.67	
Ca	0.03		0.09		0.01		0.00		0.00		0.00		0.01		0.01	
Na	0.00		0.01		0.00		0.00		0.00		0.00		0.00		0.00	
K	0.00		0.00		0.00		0.00		0.00		0.00		0.00		0.00	
Cr	0.00		0.00		0.00		0.00		0.00		0.00		0.00		0.00	
Total	5.18		6.55		5.08		4.91		4.96		4.92		5.10		4.99	
X_{Srp}	0.90		0.23													
X_{Mg} of Srp	0.93		1.00		0.96		0.88		0.98		0.96		0.93		0.91	
X_{Mg} of Brc	0.85		0.80													

X_{Mg}=Mg^{2+}/(Mg^{2+}+Fe^{2+}), where Mg^{2+} and Fe^{2+} are in atoms per formula unit (a.p.f.u.).

Table 2.15 Continue of chemical composition of serpentine in harzburgite (in wt. %) with 1σ standard deviation and calculated structural formula.

Sample	CM2B-83Z2-8-13						CM2B-106Z2-16-21		CM2B-119Z2-7-12				OM230111 P6-3			
Lithology	Harzburgite						Harzburgite		Harzburgite				Serpentine vein in harzburgite			
Mineral	Atg		Srp		Ctl		Srp		Srp		Ctl		Atg		Ctl	
Type	Vein		Selvage		with andradite		Selvage		Selvage		Vein		Vein		Vein	
N	20		10		3		14		32		20		10		10	
	avg.	1σ	avg.	1σ	avg.	1σ	avg.	1σ	avg.	1σ	avg.	1σ	avg.	1σ	avg.	1σ
SiO_2	43.12	2.00	39.33	0.55	41.37	0.15	40.57	0.48	41.65	0.28	39.71	0.54	43.13	0.21	41.62	0.65
TiO_2	0.02	0.02	0.01	0.02	0.00	0.00	0.01	0.01	0.02	0.02	0.02	0.02	0.01	0.02	0.01	0.01
Al_2O_3	0.18	0.10	0.20	0.07	0.36	0.07	0.30	0.06	0.24	0.05	0.31	0.10	0.48	0.07	0.51	0.11
FeO	5.72	0.43	5.04	0.48	5.39	0.09	3.65	0.40	1.97	0.25	8.50	0.85	3.04	0.21	1.62	0.16
MnO	0.09	0.05	0.10	0.06	0.10	0.02	0.08	0.05	0.07	0.05	0.19	0.09	0.06	0.05	0.06	0.05
MgO	35.55	0.75	37.57	0.46	37.35	0.38	38.79	0.55	40.56	0.43	35.21	0.73	38.20	0.58	38.10	0.55
CaO	0.22	0.04	0.37	0.05	0.14	0.01	0.11	0.02	0.02	0.01	0.02	0.01	0.01	0.01	0.04	0.02
Na_2O	0.06	0.05	0.05	0.05	0.00	0.00	0.03	0.04	0.02	0.04	0.01	0.04	0.02	0.03	0.03	0.05
K_2O	0.01	0.01	0.00	0.00	0.01	0.01	0.01	0.01	0.01	0.01	0.01	0.01	0.01	0.01	0.01	0.01
Cr_2O_3	0.03	0.03	0.02	0.02	0.01	0.01	0.02	0.02	0.03	0.02	0.02	0.02	0.01	0.02	0.01	0.01
Total	84.99	1.57	82.70	0.65	84.74	0.37	83.57	0.88	84.59	0.60	84.00	1.14	84.97	0.41	82.01	0.74
Oxygen	7		7		7		7		7		7		7		7	
Si	2.08		1.97		2.01		1.99		2.00		1.99		2.06		2.05	
Ti	0.00		0.00		0.00		0.00		0.00		0.00		0.00		0.00	
Al	0.01		0.01		0.02		0.02		0.01		0.02		0.03		0.03	
Fe	0.23		0.21		0.22		0.15		0.08		0.37		0.12		0.07	
Mn	0.00		0.00		0.00		0.00		0.00		0.01		0.00		0.00	
Mg	2.56		2.80		2.71		2.83		2.90		2.61		2.72		2.79	
Ca	0.01		0.02		0.01		0.01		0.00		0.00		0.00		0.00	
Na	0.01		0.00		0.00		0.00		0.00		0.00		0.00		0.00	
K	0.00		0.00		0.00		0.00		0.00		0.00		0.00		0.00	
Cr	0.00		0.00		0.00		0.00		0.00		0.00		0.00		0.00	
Total	4.91		5.03		4.98		5.00		5.00		5.00		4.93		4.94	
X_{Mg} of Srp	0.92		0.93		0.93		0.95		0.97		0.88		0.96		0.98	

X_{Mg}=Mg^{2+}/(Mg^{2+}+Fe^{2+}), where Mg^{2+} and Fe^{2+} are in atoms per formula unit (a.p.f.u.).

Magnetite vein

The magnetite veins in the harzburgites cut the host rock mesh texture (Fig. 2.45). Magnetite vein and surrounding area are cut by chrysotile veins in a direction perpendicular to the magnetite vein (Fig. 2.45). Both olivine and orthopyroxene are completely serpentinized around the magnetite veins. The area near the magnetite veins is composed of lizardite and particulate magnetite. Similar to magnetite veins in dunites, Raman spectra indicate no brucite content in the area around magnetite veins (Fig. 2.46). The X_{Mg} of lizardite around magnetite veins is 0.97 (Table 2.15).

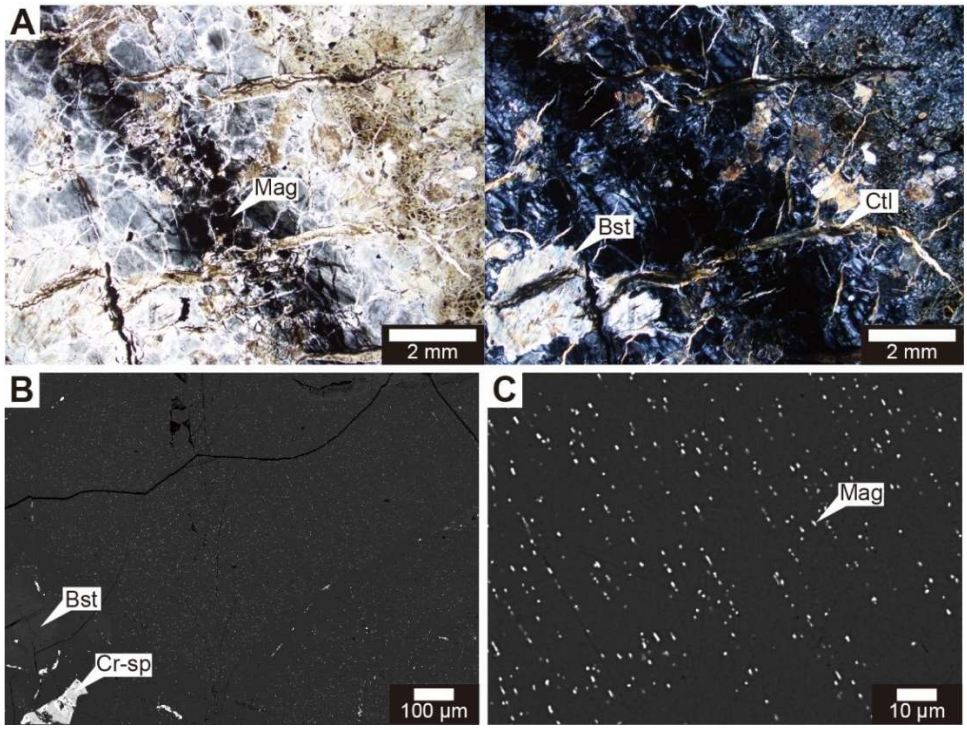

Fig. 2.45. Microtexture of the magnetite vein and the selvage in a harzburgite (CM2B-68Z1-27-31). (A) Optical microscope photograph of magnetite vein. (B, C) Backscattered electron images of selvage of the magnetite vein.

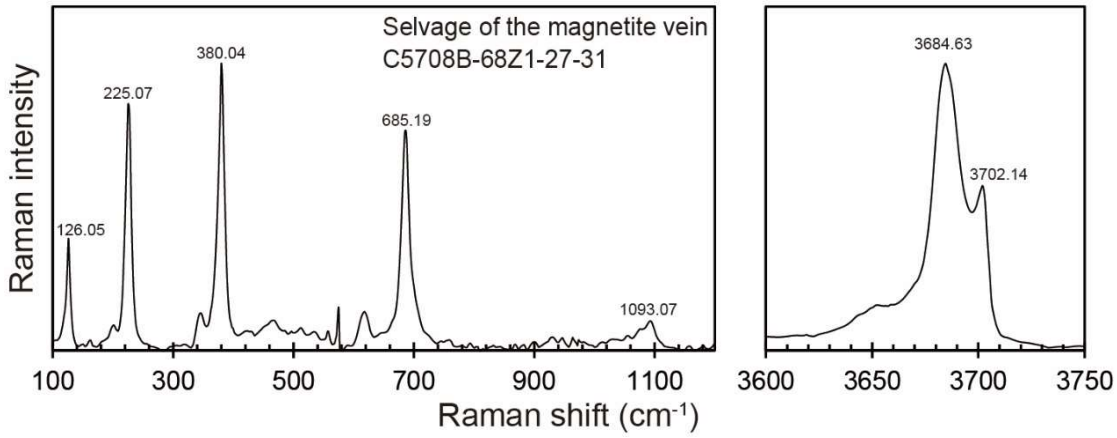

Fig. 2.46. Raman spectra of the selvage of magnetite vein (CM2B-68Z1-27-31).

Tremolite vein

Tremolite veins cut the host rock and antigorite veins (Fig. 2.47A). The tremolite vein composed of fragmented coarse-grained tremolite and fine-grained tremolite. The later stage chrysotile vein cuts in a direction perpendicular to the tremolite vein. The tremolite vein is internally sheared and the shear plane cuts a chrysotile vein perpendicular to the tremolite vein. The shear plane is filled by chrysotile with spherical andradite (Fig. 2.47B). Such spherical andradite may have formed over a short period of time (seconds to weeks) at low temperatures (<200°C) (Plümper *et al.*, 2014). The X_{Mg} of chrysotile vein cutting tremolite vein is 0.93. Chrysotile veins cutting tremolite and chrysotile on the shear plane have a peak at ~1100 cm^{-1} characteristic of chrysotile (Groppo *et al.*, 2006). The Raman spectrum of spherical andradite (Fig. 2.48) in the shear plane peaks are similar to the Raman spectrum of andradite in previous studies (Hofmeister and Chopelas, 1991). The broad peak at 3546.00 cm^{-1} is attributed to the OH group in andradite resulting from $O_4H_4 \leftrightarrow SiO_4$ substitution (Passaglia and Rinaldi, 1984; Sacerdoti and Passaglia, 1985).

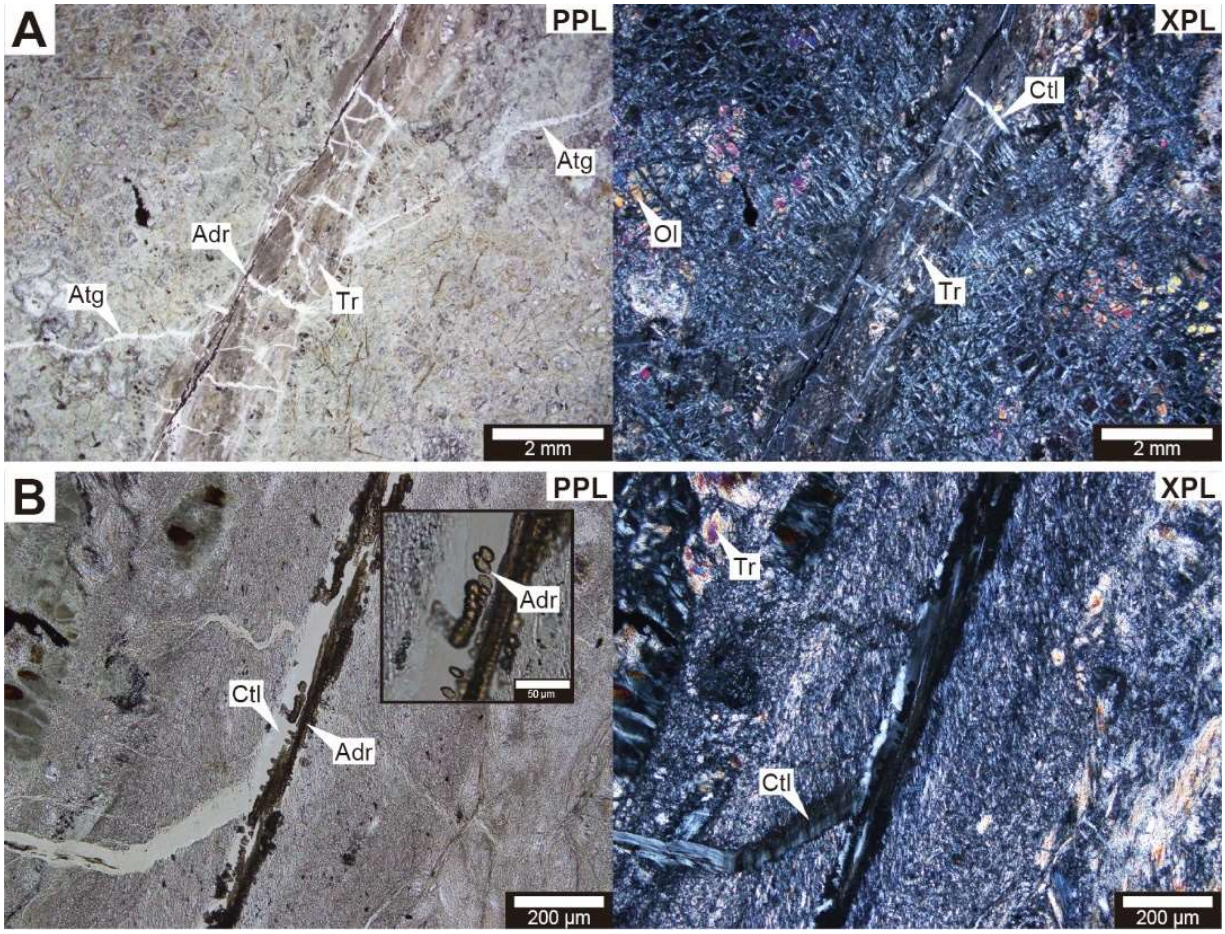

Fig. 2.47. Optical microscope photographs of tremolite vein in harzburgite (CM2B-83Z2-8-13). (A) Tremolite vein cut mesh texture and antigorite vein. (B) Close up view of the tremolite vein and spherical shape andradite in chrysotile.

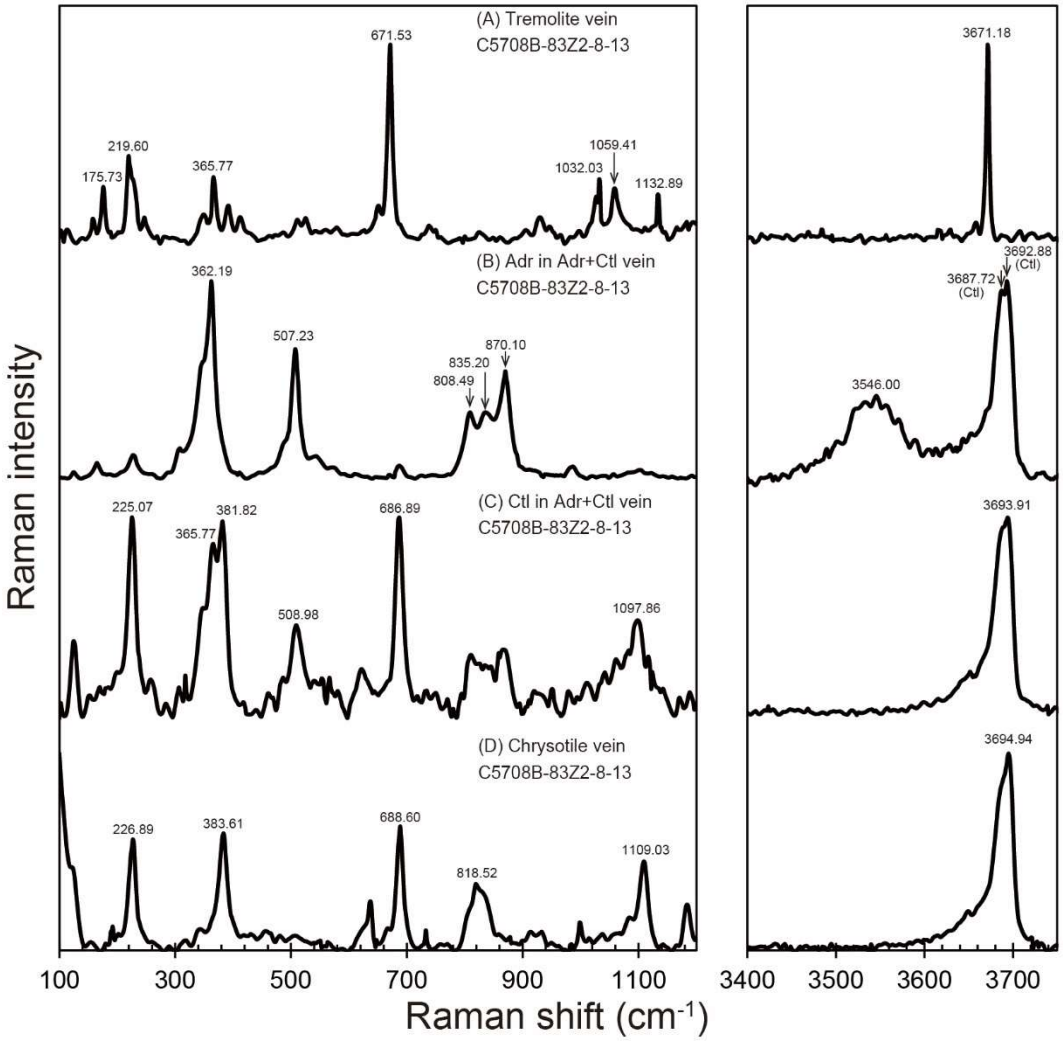

Fig. 2.48. Raman spectra of tremolite vein, andradite, chrysotile vein from CM2B-83Z2-8-13. (A) Tremolite vein. (B) Spherical andradite in the shear zone. (C) Chrysotile in the shear zone. (D) Crysotile vein cut perpendicular to the tremolite vein.

2.6.4. In-situ trace element analysis using LA-ICP-MS

In situ trace element analysis by laser ablation inductively coupled plasma mass spectrometry (LA-ICP-MS) carried for selected three samples (CM1A-80Z1-26-31, CM1A-90Z2-48-53, and CM1A-137Z3-46-54) for trace element concentrations of antigorite±chrysotile veins and host rock mesh texture lizardite. A total 43 points were analyzed, including 16 points from antigorite+chrysotile veins and 27 points form lizardite in the host rock mesh texture. The analyzed sites are shown in Fig. 2.49. Because antigorite and chrysotile occur in the vein as micron-scale aggregates (Fig. 2.31B), the trace element concentrations represent a mixture of antigorite and chrysotile. Antigorite-chrysotile veins are enriched in As and Sb and deficient in Ni and Co compared to the lizardite in the matrix (Fig. 2.50). The lizardite in the host rock mesh texture has low As and Sb concentrations, similar to the depleted mantle; in contrast, the Atg-Ctl vein is enriched in As and Sb and is on a mixed line between marine sediments and the mantle (Fig. 2.51).

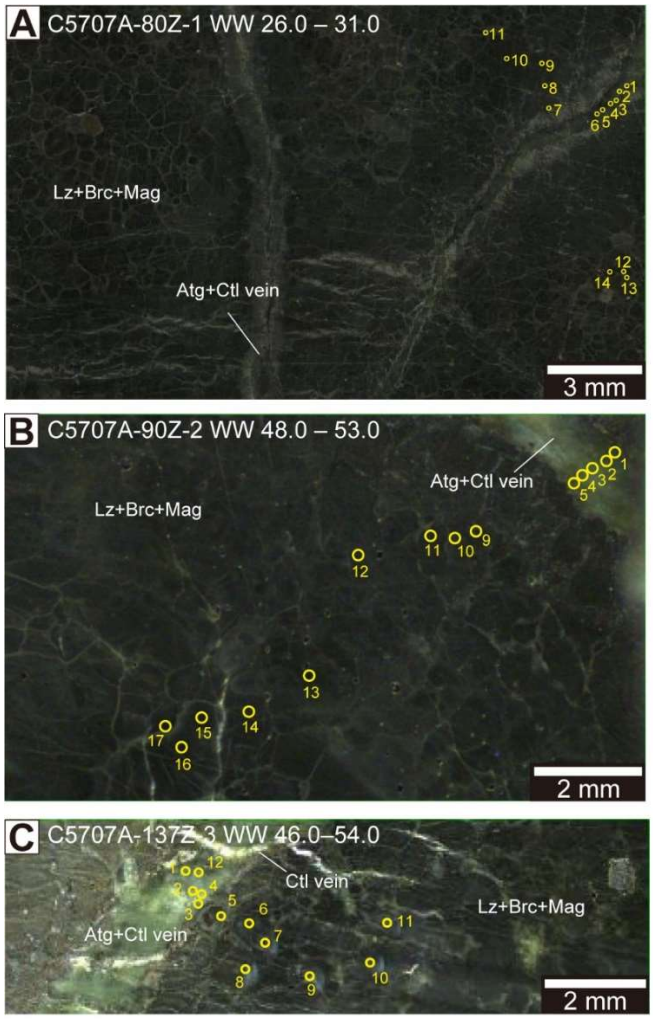

Fig. 2.49. Analyzed locations of LA-ICP-MS analysis. Three dunites were selected as representative Atg-Ctl vein bearing samples. (A)CM1A-80Z1-26–31, (B)CM1A-90Z2-48–53, (C) CM1A-137Z3-46–54. Lz = lizardite, Brc = brucite; Mag = magnetite; Atg = antigorite; Ctl = chrysotile.

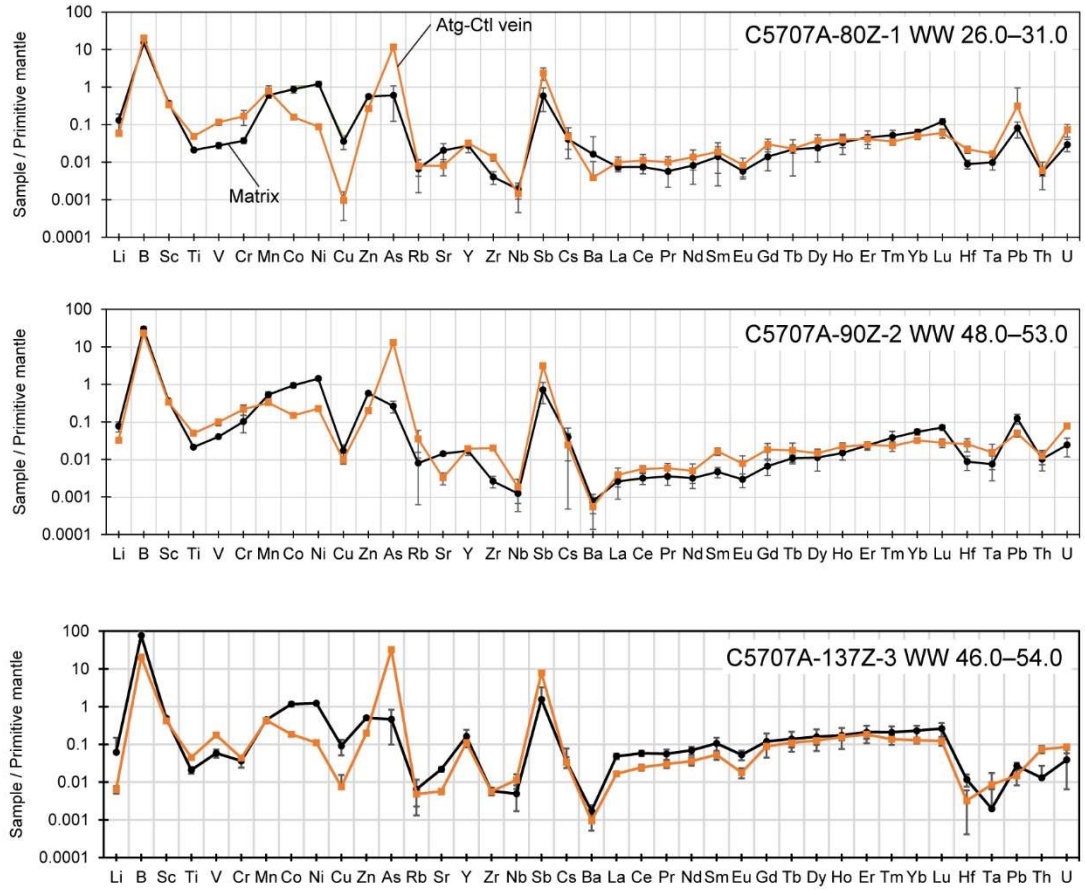

Fig. 2.50. Trace element concentrations of the three dunites. (A)CM1A-80Z1-26–31, (B)CM1A-90Z2-48–53, (C) CM1A-137Z3-46–54.

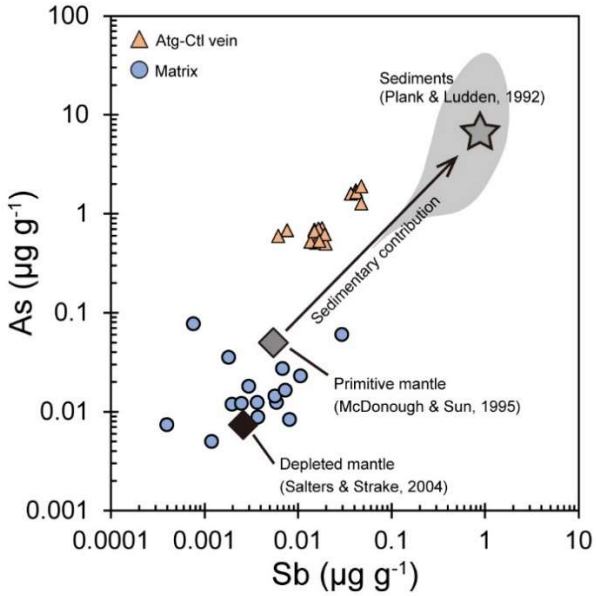

Fig. 2.51. Sb vs As plot of antigorite-chrysotile (Atg+Ctl) vein (orange triangles) and host rock mesh texture lizardite (blue circles). The gray field shows marine sediments and the gray star indicate the average value (Plank and Ludden, 1992). The gray and black diamonds indicate the composition of the primitive (McDonough and Sun, 1995) and depleted mantle composition (Salters and Stracke, 2004).

2.7. Discussions

2.7.1. Multi-stage vein formation in the lower crust to upper mantle section

Several types of serpentine veins are observed in the lower crust to upper mantle: Al-rich serpentine veins cut the matrix mesh structure in the lower crustal gabbroic rocks. Antigorite ± chrysotile vein networks have been observed in dunite at the crust-mantle transition zone, sometimes associated with brucite-rich reaction zones on both sides of the veins. Antigorite and tremolite veins were observed in the harzburgite in the upper mantle, cutting through the host rock mesh texture. Based on the microstructural observations and geochemical results, the possible order of formation is as follows. (1) Mesh texture serpentinization (Lz+Brc+Mag). (2) antigorite and tremolite veins, (3) magnetite veins, (4) chrysotile veins perpendicular to these veins. The formation of these multi-stage veins was discussed next.

Antigorite and tremolite veins cutting the mesh texture of the host rocks were observed over approximately 300 m of the OmanDP samples from the crust-mantle transition zone to the upper mantle section. The network of the antigorite veins were also observed in the outcrop. Antigorite + tremolite veins have been reported in "suprasubduction" type ophiolites, which are thought to have experienced subduction zone setting (Cluzel *et al.*, 2020), and in ocean drilling samples from the Mariana forearc (Murata *et al.*, 2009). These antigorite veins are thought to have been formed by fluid inflow associated with plate subduction (Cluzel *et al.*, 2020; Murata *et al.*, 2009). Tremolite forms at around 350-550 °C at 0.1-0.5 GPa (Chernosky, 1998), and antigorite + tremolite veins in the supra-subduction type ophiolite harzburgite reported in a previous study are thought to have formed at 350-400 °C (Cluzel *et al.*, 2020). Antigorite has only been reported in limited locations in the Oman ophiolite, where it is associated with carbonated serpentinite and is assumed to have formed at low temperature (~100 °C) with high silica activity in aqueous fluids (Falk and Kelemen, 2015). The antigorite veins from the crust-mantle transition zone to the upper mantle section shown in this chapter, the cross-sectional relationship between antigorite-chrysotile veins and host rock mesh texture indicates that vein formation occurred after serpentinization of the host rock mesh texture serpentinization. The high Ni concentration of the host rock mesh texture suggests that the first stage of serpentinization proceeded by replacement of primary olivine (i.e., the Ni concentration of olivine is as high as ~3000 ppm (Sato, 1977)). However, the low Ni concentration of the antigorite-chrysotile veins in the analyzed samples suggests that vein formation occurred after the completion of olivine serpentinization. In contrast to the low concentrations of As and Sb similar to the depleted mantle conposition in the host rock mesh texture, the enrichment of As and Sb in the antigorite-chrysotile veins (Fig. 2.51) suggests that some of the vein-forming fluids were interacted with the subducted sediment (Deschamps *et al.*, 2011, 2013; Hattori and Guillot, 2003). This is consistent with a study that revealed that serpentinite close to the basal thrust of the Oman

ophiolite is influenced by fluids derived from subducted sediments at temperatures above 400 °C (de Obeso *et al.*, 2022). These features suggest that the formation of antigorite+chrysotile veins is due to aqueous fluid infiltration in a subduction zone setting. Magnetite veins observed in dunites and harzburgites may have formed later than antigorite veins based on cross-cut relationships (Fig. 2.29C). Magnetite veins are thought to form with increasing W/R associated with hydrothermal activity (Dandar *et al.*, 2021; Gahlan *et al.*, 2006). Chrysotile veins develop perpendicular to antigorite and magnetite veins in dunite and harzburgite. This type of fracture is commonly observed in partially altered peridotite outcrops of the Oman ophiolite, the so-called "Frankensteinian" texture (Evans *et al.*, 2020). The Frankensteinian texture was observed around all antigorite veins in the upper mantle dunite samples, whereas this texture was absent around antigorite veins in some dunites at the crust-mantle transition zone. It is suggested that some of the antigorite veins at the crust-mantle boundary may have formed after the completion of host rock serpentinization, since the formation of a Frankenstein texture requires that an unreacted part remains prior to the formation of the main vein.

2.7.2. Stage of serpentinization

In the Omani ophiolite, a variety of aqueous fluid sources can be considerable for the serpentinization: A circulating seawater near the ridge (Bosch *et al.*, 2004; Nicolas, 2003; Zhang *et al.*, 2021), slab-derived fluids that entered the Omani ophiolite from the bottom at the onset of subduction (de Obeso *et al.*, 2022; Ishikawa *et al.*, 2005; Yoshikawa *et al.*, 2015), and seawater from the ocean floor at off-axis (Aupart *et al.*, 2021; Scicchitano *et al.*, 2021), and meteoric water onshore after emplacement (Scicchitano *et al.*, 2021). The involvement of these fluids has been investigated by geoscientific analysis: bulk rock chemistry of serpentinized dunite and harzburgite recovered from core samples at the CM site shows positive and negative Eu anomalies (Kourim *et al.*, 2022). Positive Eu anomalies are considered to be a signature of hydrothermal activity at the ocean floor, as they result from the interaction between seawater and Eu rich minerals (e.g., plagioclase) in crustal rocks (Bach and Irber, 1998). Positive Eu anomalies are found in hydrothermal vent solutions (Bach and Irber, 1998) and in altered minerals (Epidote) in gabbroic rocks from ocean floor drilling (Chen *et al.*, 2023). Eu release is associated with alteration (chloritization) of plagioclase in the gabbroic rocks (Yoshitake *et al.*, 2009). Negative Eu anomalies, on the other hand, are thought to be due to magmatic fluids (Bach and Irber, 1998). The finding of both of positive and negative Eu anomaly may reflect the complex fluid-rock interaction history during the formation of the Oman ophiolite from the start of subduction to its stationing on to the continental crust.

In situ oxygen isotope data for the serpentine mesh texture of the Oman ophiolite suggest that the temperature of serpentinization that formed the mesh structure was ~200-250 °C (Aupart *et al.*, 2021). This temperature range is consistent with the 120-280 °C temperature range estimated from oxygen isotope thermometers in serpentinite dredged from the ocean floor (Klein *et al.*, 2014). The upper mantle harzburgites studied in this study contain relatively iron-rich brucite (X_{Mg} = ~0.72) with less amount of

magnetite. These features are similar to harzburgites serpentinized at temperatures of T < ~200 °C (Klein *et al.*, 2014). Moreover, orthopyroxene and clinopyroxene are more resistant to serpentinization than olivine at temperature of 250 ~ 300 ℃ and 3.0 ~ 4.0 kbar (Marcaillou *et al.*, 2011; Ogasawara *et al.*, 2013). These suggest that the main serpentinization stage that formed the mesh texture likely occurred at seafloor.

2.8. Summaries

This chapter focused on rocks from the lower crust to the upper mantle of the Oman Ophiolite obtained from field studies and onshore drilling and describes mineral descriptions and rock-water reactions. The crustal-mantle boundary, dunite and harzburgite, which form the upper mantle, are found to be homogeneously serpentinized in the depth direction, independent of fault distribution. Petrological and geochemical analysis reveals two stage serpentinization (serpentinization with mesh texture in seafloor setting vs antigorite vein network in subduction zone setting) in the Oman Ophiolite.

Part of the content of the Chapter 2 has been published as the following publications:

1. Yoshida, K., Okamoto, A., Shimizu, H., Oyanagi, R., Tsuchiya, N., Oman Drilling Project Phase 2 Science Party, "Fluid Infiltration Through Oceanic Lower Crust in Response to Reaction‐Induced Fracturing: Insights From Serpentinized Troctolite and Numerical Models", *Journal of Geophysical Research: Solid Earth*, 125, 11, 2020, DOI:10.1029/2020JB020268.
2. Kazuki Yoshida, Ryosuke Oyanagi, Masao Kimura, Oliver Plümper, Mayuko Fukuyama, Atsushi Okamoto, "Geological recordsof transient fluid drainage into the shallow mantlewedge", *Science Advances*, 9, 14, 2023, DOI:10.1126/sciadv.ade6674.

Chapter 3: Enhanced reaction process in the lower crust by the reaction-induced stress

3.1. Introduction

Serpentinization require H_2O for continuous reaction, therefore microcracks are could be important for perversive serpentinization of gabbroic rocks. Two mechanisms have been proposed for the crack formation: (1) thermal fracturing during cooling of the oceanic lithosphere (Boudier *et al.*, 2005; Cooper and Simmons, 1977; Korenaga, 2007; Nicolas, 2003); (2) reaction-induced stress caused by the volume-changing reactions within rocks (Jamtveit *et al.*, 2008; Okamoto and Shimizu, 2015; Shimizu and Okamoto, 2016). In particular, volume expansion by hydration of reactive mineral grains (e.g., olivine and periclase) can cause radial fractures in the surrounding matrix (Jamtveit *et al.*, 2008; Kelemen and Hirth, 2012; Kuleci *et al.*, 2017). Such characteristic fracture networks induced by olivine serpentinization in a plagioclase matrix have been reported from several localities, including troctolites from the South Kawishiwi intrusion of the Duluth Igneous Complex, USA (Jamtveit *et al.*, 2008), troctolites from the East Pacific Rise (Gillis *et al.*, 2014), and olivine gabbro from the Mid-Atlantic Ridge (Blackman *et al.*, 2006). Based on numerical simulations (discrete element method; DEM) of olivine hydration in troctolite, Jamtveit et al. (2008) showed that positive feedback between reaction progress and fracturing result in the formation of the fracture network during this type of reaction. However, their model did not explicitly account for fluid flow. In addition, there are few descriptions of fracture networks related to the serpentinization of gabbroic rocks in the Oman ophiolite. As such, the influence of reaction-induced fracturing on fluid flow within the oceanic lower crust during LT alteration remains unclear.

As shown in Chapter 2, olivine was homogeneously serpentinized from the lower crust to the upper mantle. Seawater would have to pass through the less permeable lower crust to the upper mantle ($\sim 10^{-22}$-10^{-23} m^2) (Farough *et al.*, 2016; Katayama *et al.*, 2012), but how homogeneous serpentinization occurred is unclear. In addition, the serpentinite microtexture records a change from a closed to an open system characterized by differences in Al and Si contents. The mechanism of the change from a closed to an open system in the serpentinization reaction is unclear. In this chapter, I focus on microcracks in gabbroic rocks and discusses the process of microcrack formation in gabbroic rocks. A numerical simulation based on discrete element method was performed to understand the coupled mechanical-chemical-fluid flow process of serpentinization. By comparison with fracturing induced by thermal effects and tectonic stress, I demonstrate the importance of reaction-induced fracturing for permeability enhancement and perversive serpentinization within the oceanic lower crust.

3.2. Microcracks in the gabbroic rocks

There are distinct radial cracks in the clinopyroxene and plagioclase around the serpentinized olivine grains, and these fractures connect between olivine grains. These radial fractures are significantly observed in gabbroic rocks that have a large amount of olivine (e.g., the modal abundance of olivine ranges from 19-41 area% in CM1A-47Z2, 10-39 area% in CM1A-48Z3; see Chapter 2). Olivine grains in these samples are highly serpentinized (59-65 area%; Fig. 3.1A-C). In the case of CM1A-133Z3, which has a lower olivine mode (6-12 area%), olivine grains are less serpentinized (~5%) than those in the other olivine gabbros (Fig.3.1A-C). Discrete mesh-like fractures exist within the olivine grains, whereas there are less radial fractures in plagioclase and clinopyroxene around the less serpentinized olivine grains (~5 area%; Fig.3.1D) than in the other olivine gabbros (Fig.3.1A-C). Discrete mesh fractures are present within the olivine grains, whereas there are few fractures in the plagioclase and clinopyroxene (Fig. 3.1D).

A layered structure of olivine-rich (Fig. 3.2A and C; 0-20 mm) and plagioclase-rich (Fig. 3.2A and C; 20-32 mm) is observed in troctolite (C577A-9Z2) at the thin section scale. An intense network of cracks develops in the minerals (Fig. 3.1A). Cracks in olivine and plagioclase fractures traced by hand (Fig. 3.2B). Thin section mineral mode determined by EPMA elemental maps (Fig. 3.2C). The mineral mode of olivine varies gradually from 10 to 75 area% (Fig. 3.2C). A small amount of orthopyroxene (<~10 area%) is present in some olivine-rich layers (Fig. 3.2C). The degree of olivine serpentinization (area ratio of serpentine to original olivine grains) varies from layer to layer (Fig. 3.2D). Olivine grains in the olivine-rich layers are highly serpentinized (40-60 %; Fig. 3.2D), while olivine grains in the plagioclase-rich layers have various degrees of serpentinization, but less than in the olivine-rich layers (Fig. 3.2D). The hand-traced fractures in olivine and plagioclase show that fractures in plagioclase are preferentially oriented in the direction perpendicular to the layered structure, whereas fractures in olivine are oriented in both vertical and horizontal directions (Fig. 3.3).

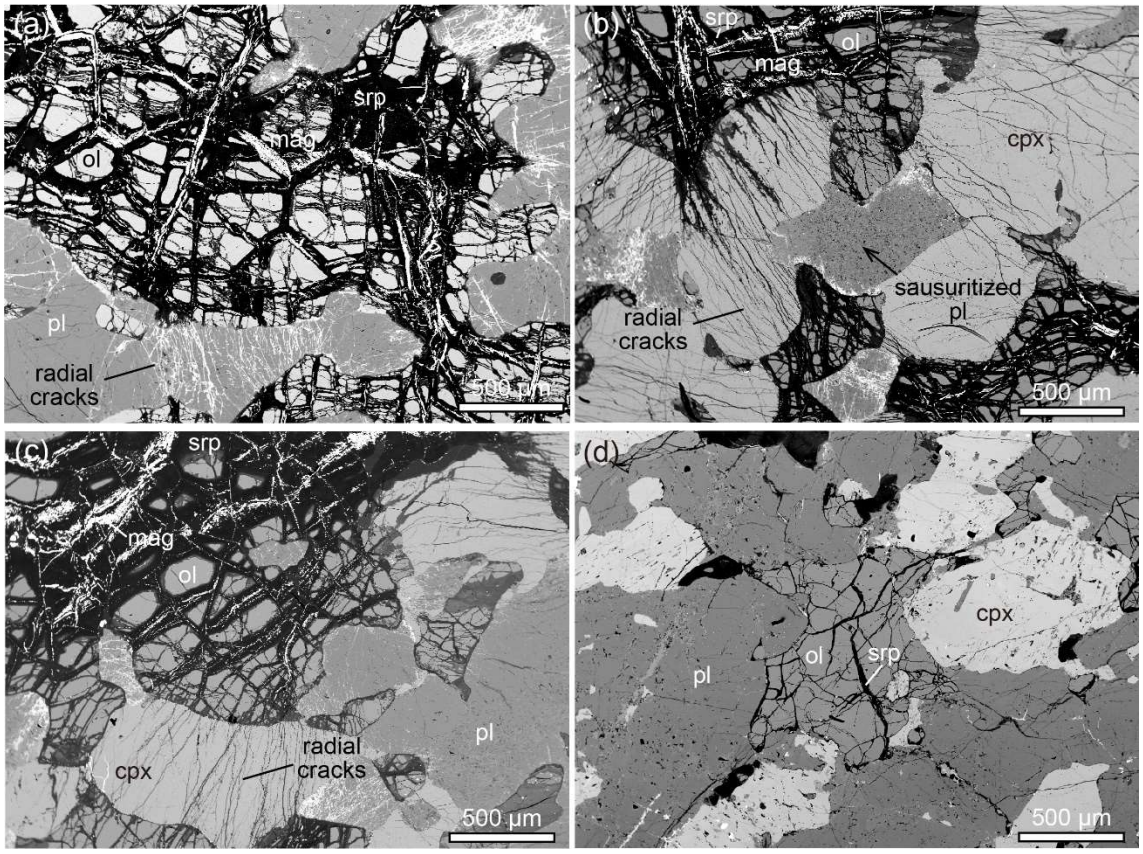

Fig. 3.1. Backscattered electron images of gabbroic rocks with different degrees of serpentinization ξ_{Srp}. (A) Troctorite from CM1A-9Z3-26-31 (CM1A-9Z3, degree of serpentinization ξ_{Srp} = 59%). (B-D) Olivine gabbro from (B) CM1A-47Z-02-62-67 (47Z02, ξSrp = 65%); (C) CM1A-48Z-03-10-15 (48Z03, ξ_{Srp} = 69%); (D) CM1A-113Z-03-25-30 (113Z03, ξ_{Srp} = 11%). Ol = olivine; Pl = plagioclase; Srp = serpentine; Cpx = clinopyroxene; Mag = magnetite. $\xi_{Srp} = A_{Srp}/(A_{Ol} + A_{Srp} + A_{Mag})$, where A_x is the area of mineral x.

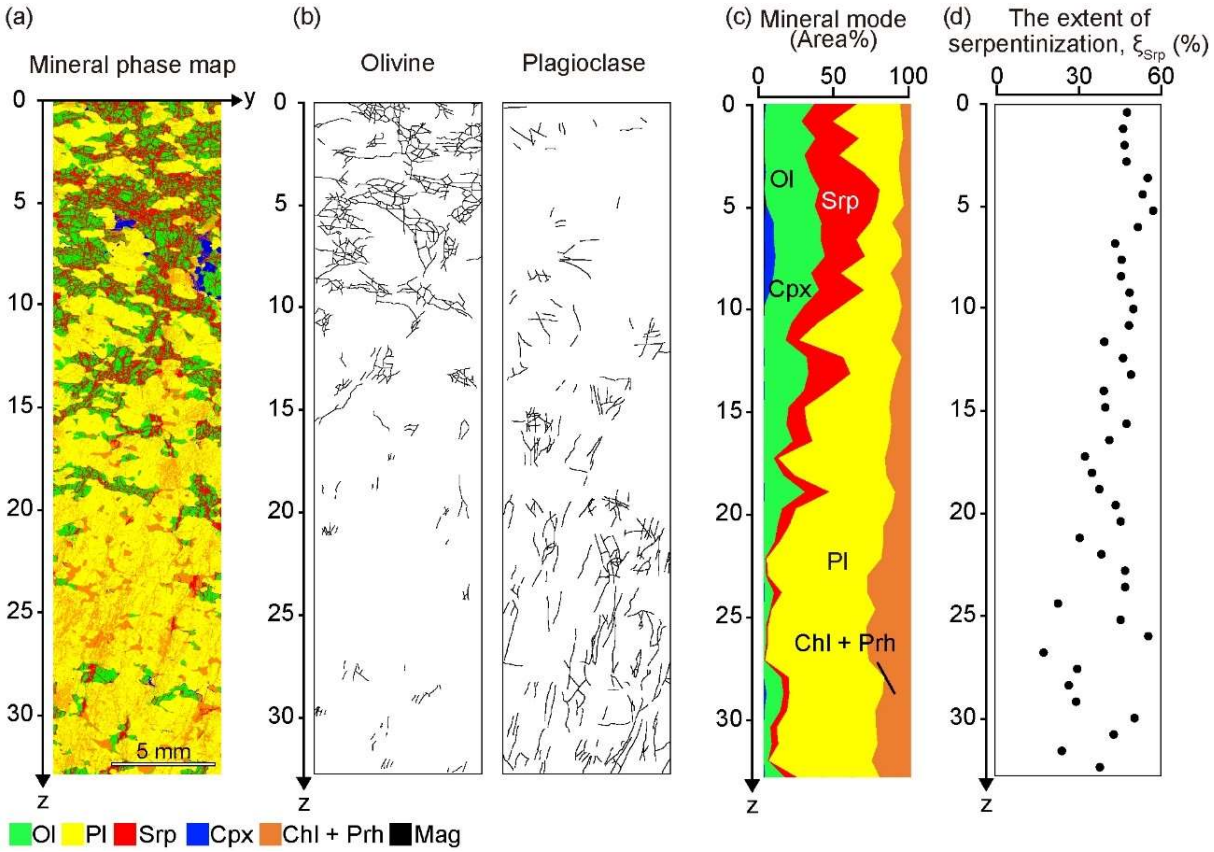

Fig. 3.2. Mineral and fracture distribution of troctolite (CM1A-09Z-03). (a) Mineral phase diagram of a troctolite thin section composed of Ol- and Pl-rich layers from EPMA elemental mapping. (b) Traces of olivine (red) and plagioclase (blue) fractures. (c) Variation in modal mineral composition (area ratio). (d) Degree of serpentinization ξSrp calculated from area ratios as ASrp/(AOl + ASrp + AMag); Ol = olivine; Pl = plagioclase; Srp = serpentine; Cpx = clinopyroxene; Chl = chlorite; Prh = prehnite; Mag = magnetite.

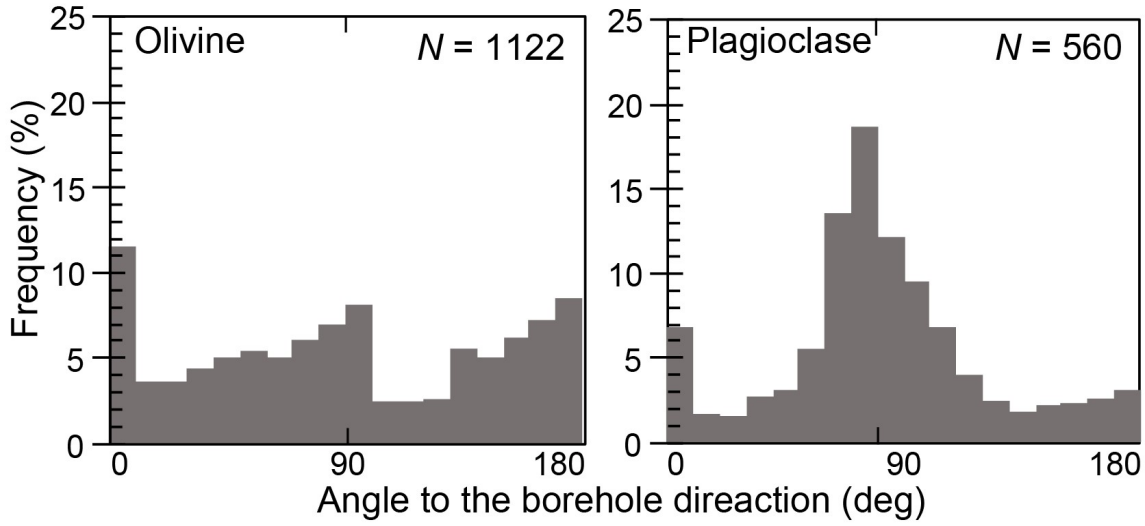

Fig. 3.3. Histogram of orientation of cracks in olivine and plagioclase shown in Fig. 3B. The angle of the crack is from the horizontal (parallel to the layered structure). N = total number of cracks.

3.3. Combined mechanical-hydraulic-chemical discrete element method

3.3.1. Numerical model

Numerical simulations of the coupled fluid flow, reaction, and fracturing were performed using the two-dimensional discrete element method (2D-DEM) developed by Okamoto and Shimizu (2015). In the DEM, the rock is modeled as an aggregate of circular elements. These elements are connected by elastic elements, which represent the bonds between the grains. The stresses and moments of the elastic elements are calculated at each step. In this study, tensile forces are assumed to be negative and compressive forces are assumed to be positive. The elastic elements consist of three springs, a slider, and a clutch (Fig. 3.4). The cross-sectional area (A), length (L), and bending moment (I) of the elastic elements are calculated from the radii of the two particles as follows:

$$A = \frac{4\mathrm{r_i} r_\mathrm{j}}{r_\mathrm{i} + r_\mathrm{j}}, \tag{3.1}$$

$$L = r_\mathrm{i} + r_\mathrm{j}, \tag{3.2}$$

$$I = \frac{A^3}{12}. \tag{3.3}$$

where r_i and r_j are the radius of particle i and j. The cross-sectional shape of the elastic element is assumed to be a rectangle with height (A) and width of unit length = 1. The spring constant of a normal spring (k_N) is determined from the elastic modulus and the cross-sectional area (A) and length of the elastic element (L). The spring constants of shear springs (k_S) and bending springs (k_B) are determined from the ratios to the spring constant of the normal spring as follows:

$$k_N = \frac{E_P A}{L}, \tag{3.4}$$

$$k_S = \alpha_\mathrm{S} \cdot k_N, \tag{3.5}$$

$$k_B = \beta_\mathrm{S} \cdot k_N. \tag{3.6}$$

where, E_p is elastic modulus of the elastic element, α_S is constant factor for the shear spring constant, β_S is constant factor for bending spring constant (In this study, β_S = 1). If the external force exceeds either the tensile or shear strength of the elastic element, the coupling will separate and no force will be transmitted between the elements (occurrence of microcrack). This corresponds to the occurrence of microcracks. The tensile and shear strength of the elastic elements are set as follows:

$$-F_{\mathrm{N}} \geq \sigma_c \cdot A, \tag{3.7}$$

$$\|F_{\mathrm{S}}\| \geq \tau_c \cdot A. \tag{3.8}$$

where, F_{N} is external force of normal direction, F_{S} is external force of shear direction, σ_{c} is tensile strength of the elastic element, τ_{c} is shear strength of the elastic element. The crack mode of the microcrack is determined as follows:

$$-F_{\mathrm{N}} \geq \|F_S\| \quad \cdots \quad Tensile\ crack \tag{3.9}$$

$$-F_{\mathrm{N}} < \|F_S\| \quad \cdots \quad Shear\ crack \tag{3.10}$$

In real rock fracturing processes, various microscopic processes such as friction and deformation dissipate kinetic energy by converting it into thermal and surface energy. Local non-viscous dashpots is used to dissipate kinetic energy in DEM (Potyondy & Cundall, 2004). The dashpot causes a force (F^{d}) to act in the direction opposite to the direction of motion of the element. The force exerted on the dashpot is obtained from the following equation:

$$F^d = -\zeta F \mathrm{sign}(V) \tag{3.11}$$

Where ζ is a damping constant between 0 and 1 (ζ = 0.5 in this study), F is the magnitude of the force on the element in each direction, V is the velocity of movement of the element in each direction, and "sign" is a sign function (positive = 1, negative = -1). This equation is applied separately to each coordinate systems.

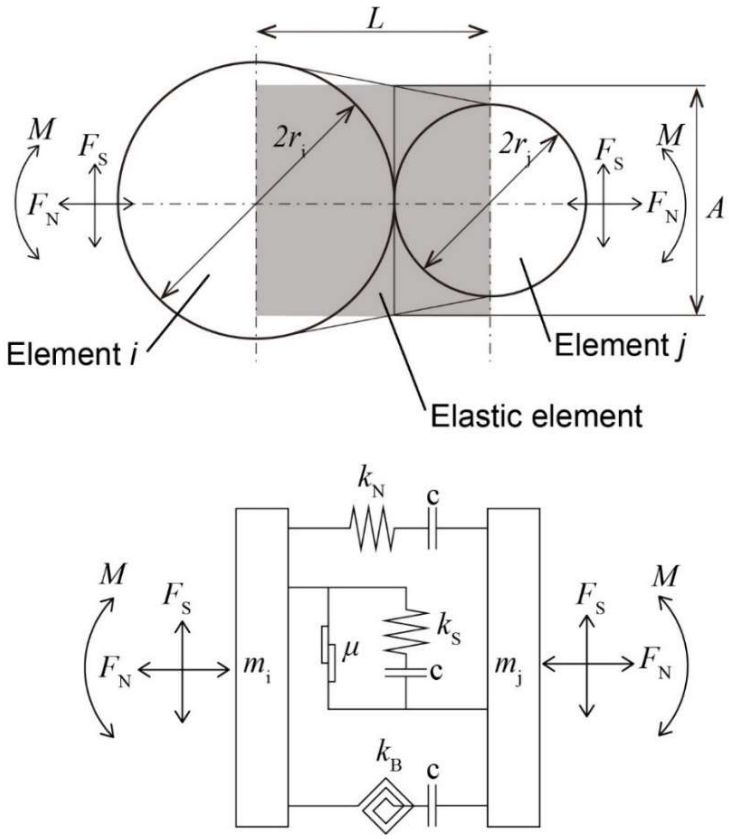

Fig. 3.4. Bonded particle model.

Fluid flow

Fluid flow in the DEM model is based on the network flow model (Al-Busaidi et al., 2005). In this model, fluid flow is modeled as fluid flow along a path connecting each domain. Domains are defined as a region surrounding neighboring elements (Fig. 3.5A). The flow rate (Q) through each channel is obtained assuming laminar flow between two flat plates (Poiseuille flow), as follows:

$$Q = \frac{w^3}{12\mu_f}\frac{\Delta P_{\mathrm{F}}}{L_p}, \tag{3.12}$$

where w is the width between the flat plates, μ_{f} is the viscosity coefficient of the fluid, L_{p} is the length of the channel, and ΔP_{F} is the difference in fluid pressure between the domains. The width between two flat plates (w) varies with the external force and formation of microcrack. The force direction of closing the width makes the width smaller. On the other hand, the width in the opening direction is constant as follows:

$$w = \begin{cases} w_{\mathrm{M}}\ (F_{\mathrm{N}} \le 0) \\ \dfrac{w_{\mathrm{M}} \cdot F_0}{F_{\mathrm{N}} + F_0}\ (F_{\mathrm{N}} > 0) \end{cases}, \tag{3.13}$$

where F_{N} is the external force of normal direction, w_{M} is the initial aperture between the elements, w_{M} is the initial width. F_0 is calculated from the spring constant of a normal spring (k_{N}) and initial width of two flat plates (w_{M}) as following:

$$F_0 = \frac{1}{2}k_N w_M, \tag{3.14}$$

As microcracks form, the initial width (w_{M}) in Equations (3.13) and (3.14) changes to a width of a crack aperture (w_{C}). The length of flow channel is calculated as follow:

$$L_{\mathrm{P}} = \frac{4\mathrm{r_i}r_{\mathrm{j}}}{r_{\mathrm{i}} + r_{\mathrm{j}}} \tag{3.15}$$

Where r_{i} and r_j are radius of element i and j, respectively. The pressure gradient between two domains is calculated as follow:

$$\Delta P_{\mathrm{F}} = \frac{K_{\mathrm{F}}}{V_{\mathrm{M}}}\left(\sum Q\mathrm{d}t - \mathrm{d}V_{\mathrm{M}}\right) \tag{3.16}$$

Where, K_{F} is elastic modulus of the fluid, dt is time step size. The volume of domains (V_{M}) is calculated as follow:

$$V_{\mathrm{M}} = \varphi_0 \cdot V_{\mathrm{D}} \tag{3.17}$$

Where, V_{M} is modified domain volume, V_{D} is actual domain volume, φ_0 is porosity.

The force act on element from fluid pressure (Fig. 3.6) is calculated as follow:

$$F_P = \int_{\theta_1}^{\theta_2} P_F \cos(\theta)\, r_{\mathrm{i}} \mathrm{d}\theta \tag{3.18}$$

where, P_{F} is fluid pressure, θ is angle between the boundaries of the domain.

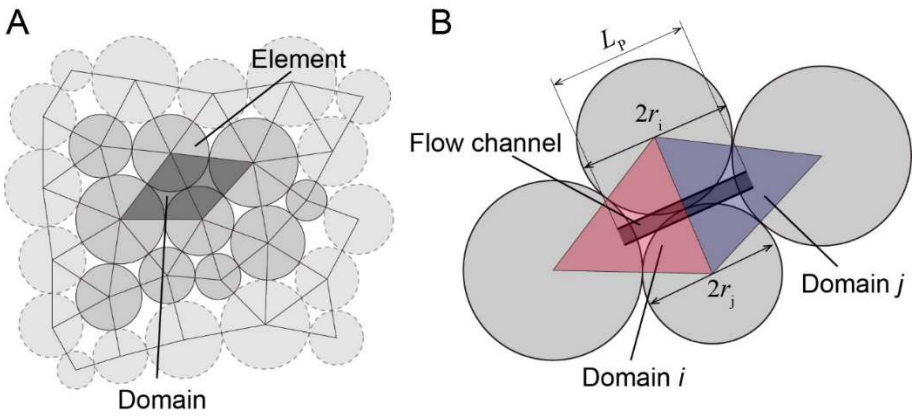

Fig. 3.5. Network flow model and hydrodynamic forces acting on each element. (A) Conceptual illustration of domains. Domain is a small area connecting adjacent elements. (B) Flow paths connecting each domain.

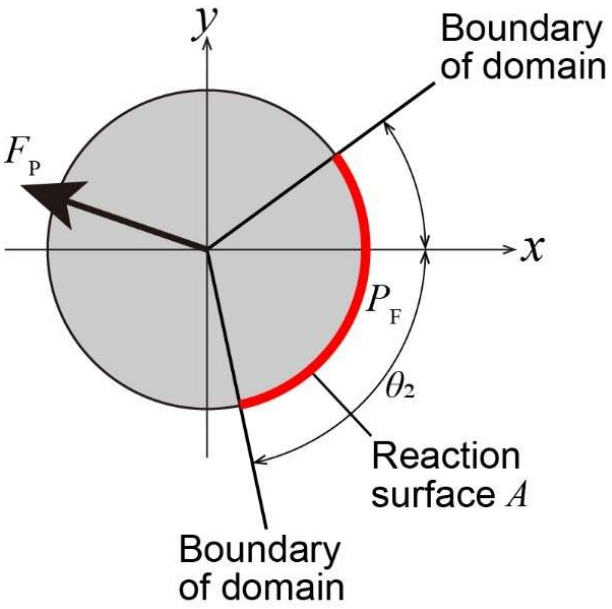

Fig. 3.6. Fluid pressure act on an element and reaction surface.

Chemical reaction

The reaction treated in the simulation is a simple hydration reaction involving an increase in solid volume (Mineral A + H_2O = Mineral B). As a serpentine reaction, I assume the following simple reaction in the MgO-SiO_2-H_2O system with no mass transfer other than water (R3.1). This reaction is accompanied by a 150% increase in volume.

$$2Mg_2SiO_4[\text{Olivine}] + 3H_2O = Mg_3Si_2O_5(OH)_4\ [\text{Serpentine}] + Mg(OH)_2\ [\text{Brucite}] \qquad \text{(R3.1)}$$

The rates of change in particle volume ($\Delta V_{\text{particle}}$) and fluid volume ($\Delta V_{\text{fluid}}$) for the hydration reaction were calculated as follows:

$$\Delta V_{\text{particle}} = Z \cdot A_{\text{p}} \cdot dt, \qquad (3.19)$$

$$\Delta V_{\text{fluid}} = \alpha \cdot \Delta V_{\text{particle}}, \qquad (3.20)$$

Where A_{p} is the reaction surface area (Fig. 3.6) and α is the reaction coefficient, which represents the ratio of fluid to element volume change. The reaction rate (Z) is expressed as a linear function of fluid pressure as follows:

$$Z = \begin{cases} Z_{max}\ (P_{\mathrm{F}} > P_{max}) \\ Z_{max} \cdot \dfrac{P_{max} - P_{\mathrm{F}}}{P_{max} - P_{min}}\ (P_{min} \le P_{\mathrm{F}} \le P_{max}), \\ 0\ (P_{\mathrm{F}} < P_{min}) \end{cases} \tag{3.21}$$

Where Z_{max} is the maximum reaction rate, P_{max} is the maximum fluid pressure, and P_{min} is the minimum fluid pressure required for the reaction progress. The reaction rate increases linearly from P_{min} to P_{max} (Fig. 3.7).

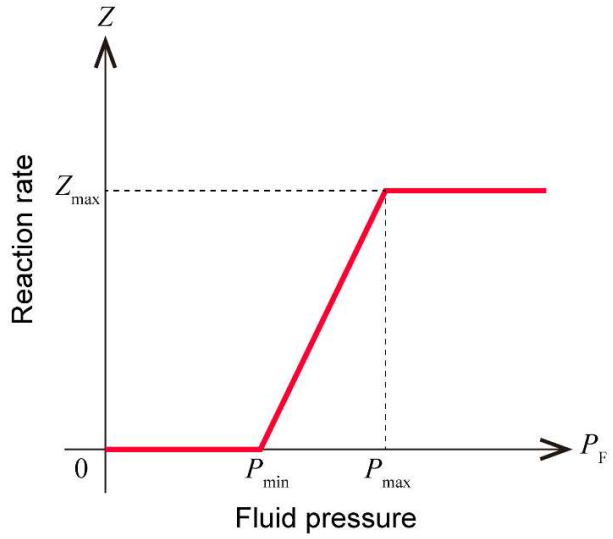

Fig. 3.7. Reaction rate as a function of fluid pressure.

3.3.2. Simulation conditions and parameter setting

Mechanical properties

The density (ρ) and Young's modulus (E) of the non-reactive material are for plagioclase (ρ = 2630 kg m^{-3}, E = 70 GPa; Mavko et al., 2009). On the other hand, ρ and E of reactive particles vary linearly with the degree of reaction from olivine (ρ = 3320 kg m^{-3}, E = 200 GPa; Mavko et al., 2009) to serpentinite (ρ = 2520 kg m^{-3}, E = 36 GPa; Christensen, 2008). Unfortunately, the tensile and compressive strengths of olivine, serpentine, and plagioclase could not be found in publications. However, the uniaxial tensile strength of various rocks ranges from 1 MPa to 40 MPa (Pollard *et al.*, 2006), therefore the compressive strength of the DEM model is therefore assumed to be 10 MPa and 100 MPa, respectively. The strength of each elastic element in the DEM model is different from that of the natural rock. Therefore, the tensile and shear strengths of each elastic element were estimated by comparing simulation results with uniaxial compression and tensile tests (Shimizu, 2010). Fluid properties and other conditions were set to simulate a hydrothermal system of oceanic lithosphere (*i.e.*,

300 °C, 30 MPa, compressibility = 1 GPa, $\mu_f = 10^{-4}$ Pa s^{-1}). The effective confining pressure was set to 1 MPa for all models, and P_{min} and P_{max} in were set to 29 MPa and 30 MPa, respectively.

In the rock model, fluid is supplied from the four boundaries of the model and the fluid pressure at each boundary was set to P_{min} + 1 MPa. The mult-grain model simulates a square rock, the same size as the single grain model (6 × 6 mm), but containing nine reactive mineral grains embedded in a non-reactive matrix (Fig. 3.8B). In this model, no flow boundaries are set on the vertical sides of the model, and fluid flow is permitted upwards or downwards in response to changes in fluid pressure ($P_F = P_{max}$ at the top of the model and P_{min} at the bottom). The layered structure model simulates a squared rock with layered structure of reactive and non-reactive materials. The size of the model is 10 × 10 mm in size. The model consists of three reactive layers (100% reactive mineral) and two non-reactive layers (Fig. 3.8C). The boundary conditions are the same as those of the multi-grain model. Time in the simulations was converted to dimensionless time ($t^* = Z_{max}t$) normalized by the reaction rate.

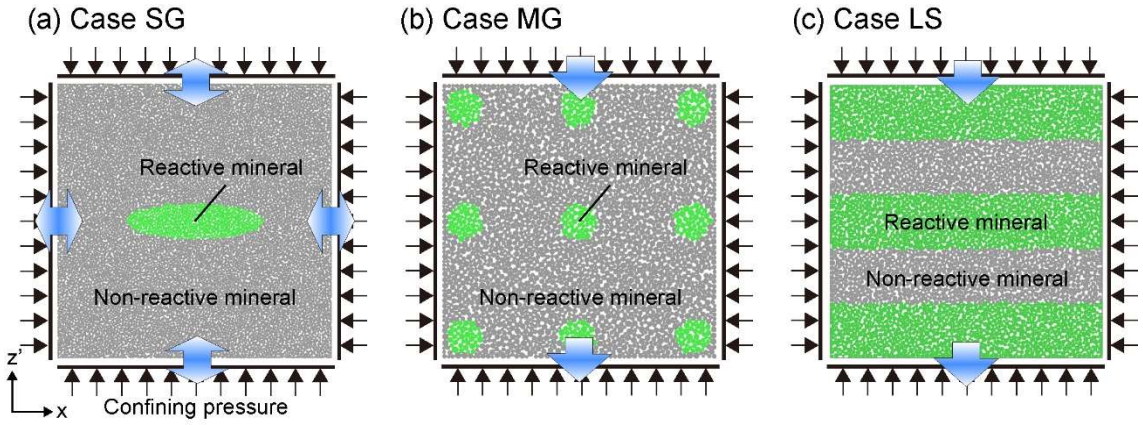

Fig. 3.8. Illustrations of the DEM model systems, which consist of reactive minerals (green) and non-reactive matrix minerals (gray). The blue arrows show permitted fluid flow directions and black arrows indicate the confining pressure. (A) Single grain (SG case). (B) Multiple grains (MG case). (C) Layered structure (LS case).

Parameter settings

The fracture pattern produced by reaction-induced fracturing can be characterized by two dimensionless parameters (Shimizu & Okamoto, 2016): the ratio of the fluid flow rate to the chemical reaction rate in the crack (Ψ_F) and in the matrix (Ψ_M). They are defined by the ratio of the fluid flow rate in the crack (Q_C) and matrix (Q_M) to the reaction rate at the mineral surface (Q_R) as follows:

$$\Psi_F = \frac{Q_C}{Q_R}, \tag{3.22}$$

$$\Psi_M = \frac{Q_M}{Q_R}, \tag{3.23}$$

where Q_C and Q_M are defined as follows:

$$Q_C = \frac{{w_C}^3}{12\mu_f}\frac{\Delta P}{L_{p,avg}}, \tag{3.24}$$

$$Q_M = \frac{{w_M}^3}{12\mu_f}\frac{\Delta P}{L_{p,avg}}, \tag{3.25}$$

where $L_{p,avg}$ is the average channel length. Q_R is defined as follow:

$$Q_R = \alpha Z_{max}\pi r_{avg}^2. \tag{3.26}$$

where r_{avg} is the average radius of the elements.

The fracture pattern is controlled by Ψ_F and Ψ_M (Shimizu and Okamoto, 2016). Mesh-like patterns are formed at high Ψ_F (>10^4) and relatively low Ψ_M (<10). In this study, the Ψ_F and Ψ_M of the reactive material were set to 10^4 and 0-1, respectively, to produce the mesh-like pattern as seen in natural olivine grains. In the SG and MG cases, Ψ_M was set to 0. In the LS case, Ψ_M was set to 1 to represent the presence of pre-existing microcracks, as this is analogous to for relatively large layer formation. In all cases, Ψ_F and Ψ_M were set to 10^4 and 1 for the non-reactive material. The small Ψ_M value replicates the presence of pre-existing microcracks necessary to initiate the reaction.

3.3.3. Mechanical test for parameter calibration

Uniaxial compression and tension tests are conducted to determine mechanical parameters (elastic modulus of the particle, critical normal and shear stresses, and poisson's ratio). The elastic modulus and poisson's ratio of the rock model are calculated from the slope of the stress-strain curve (Fig. 3.9). The parameters used in the DEM simulations are shown in Table 3.1.

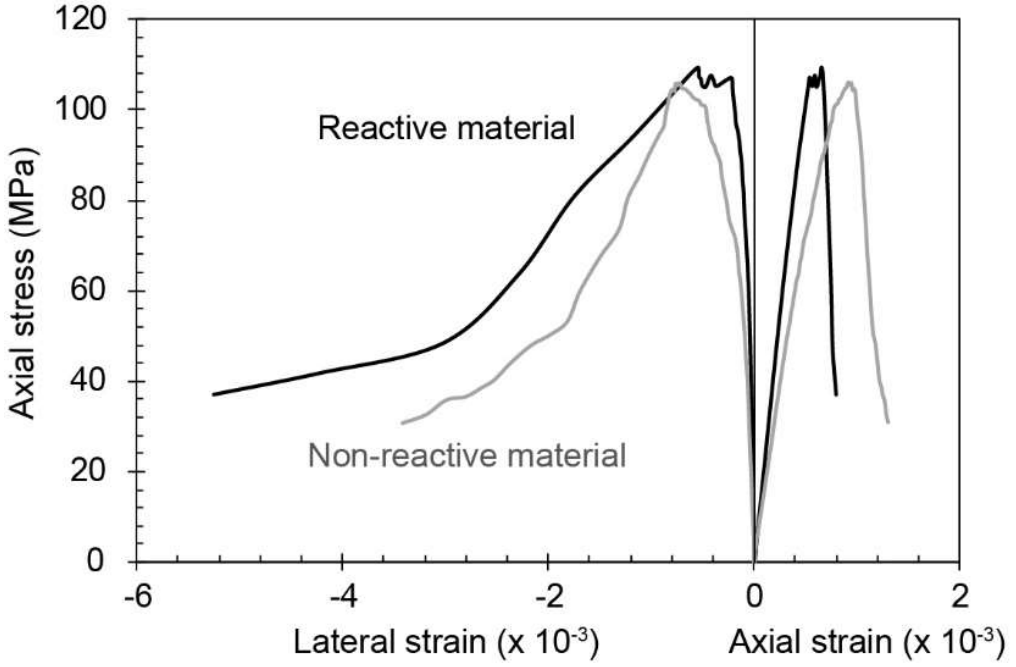

Fig. 3.9. The stress-strain diagrams obtained from the uniaxial compression test of reactive material and non-reactive material. The compression strength and strain were calculated from the force acting on the loading platen and displacements of the monitored particles. The tensile strength and strain were calculated from the force acting both of upper and lower particles and the width of the model.

Table. 3.1. Parameters used in the simulations.

	Case 1	Case 2	Case 3	
Size of rock model	6 × 6	10 × 10	10 × 10	(mm^2)
Total number of particles	8081	4353	4353	
Particle radius	2.2×10^{-2} - 4.4×10^{-2}	0.5×10^{-1} - 1.0×10^{-1}	0.5×10^{-1} - 1.0×10^{-1}	(mm)
Average particle radius	0.033	0.075	0.075	(mm)
Standard deviation of radius	0.6×10^{-2}	0.1×10^{-1}	0.1×10^{-1}	(mm)
Particle density				
Unreacted	3320			(kg/m^3)
Reacted	2520			(kg/m^3)
Non-reactive	2630			(kg/m^3)
Young's modulus of particle				
Unreacted	378			(GPa)
Reacted	150			(GPa)
Non-reactive	320			(GPa)
Shear/normal spring stiffness ratio				
Unreacted	0.45			
Reacted	0.38			
Non-reactive	0.25			
Shear strength of spring				
Unreacted	175			(MPa)
Reacted	17.5			(MPa)
Non-reactive	150			(MPa)
Tensile strength of spring				
Unreacted	28			(MPa)
Reacted	2.8			(MPa)
Non-reactive	30			(MPa)
Friction coefficient of particle	1			
Porosity correlatoin factor	0.01			
Bulk modulus of the fluid	1			(GPa)
Fluid viscosity	1.0×10^{-4}			(Pa·s)
Maximum pore pressure (P_{max})	30			(MPa)
Minimum pore pressure (P_{min})	29			(MPa)
Maximum pressure difference (P_{diff})	1			(MPa)
Reaction rate constant (Z_{max})	100			(1/s)
Proportional constant	0.7			
Volume change factor	1.5			

3.4. Results

3.4.1. Single grain model

The result of the single grain model is shown in Fig 3.10. Snapshots of the reaction ratio, width of the crack aperture, and normalized fluid flux at t*=0.155 (Fig. 3.10A), t*=0.300 (Fig. 3.10B), and t*=0.500 (Fig. 3.10C) are shown, respectively. Figs. 3.11A-C show the time evolution of the reaction ratio (ξ_{Av}, Fig. 3.11A), the crack density within the reactive material and non-reactive material (Fig. 3.11B), and the total fluid flux (Fig. 3.11C).

In the early stages of the hydration reaction (t* = 0 - 0.155), the rock model is initially saturated with water, the hydration reaction begins at the boundary between the reactive and non-reactive material. As the hydration reaction progresses, the fluid pressure in the center of the reactive material decreases, allowing fluid to infiltrate through the matrix from the boundaries between the reactive and non-reactive materials. At this stage, the average reaction rate gradually increases from 0% to 0.4% (Fig. 3.11A). A small number of microcracks develop at the boundaries between reactive and non-reactive materials, resulting in a simultaneous increase in crack density within the reactive and non-reactive matrices from 0% to ~7% (Fig. 3.11B). Because these microcracks are isolated from each other (Fig. 3.10A), the fluid flows uniformly through the non-reactive material and there is no selective fluid flow. The total fluid flow rate is nearly constant (Q_{Total} = ~1.2×10^{-6} m^3/s, Fig. 3.11C).

At t* = 0.16-0.17, the crack density in the reactive matrix increases rapidly from 6% to 18%, while the crack density in the non-reactive matrix increases steadily (Fig. 3.11B). The QTotal value increases from 1.2×10^{-6} to 2.3×10^{-6} m^3/s (Fig. 3.11C). This indicates that fracturing is occurring within the reactive grain in response to the volume expansion of outer of the reactive material, as observed in previous studies (Okamoto and Shimizu, 2015; Røyne *et al.*, 2008; Shimizu and Okamoto, 2016; Ulven *et al.*, 2014). The snapshot at t*=0.300 indicates the initiation of radial fracturing within the non-reactive material, in addition to existing fracturing within the reactive material (Fig. 3.10B). The cracks are highly connected and act as dominant fluid pathways by connecting the inside to the outside of the reactive material (Fig. 3.10B).

At t* = 0.500, the average reaction ratio and fluid flux increase rapidly (Figs 3.10A and C). This rapid increase in reaction ratio and fluid flux is caused by crack connections between the model boundary and the reactive matrix. The radial cracks in the non-reactive matrix are the dominant fluid pathways that enhance the reaction progress of the reactive material (Fig. 3.10C).

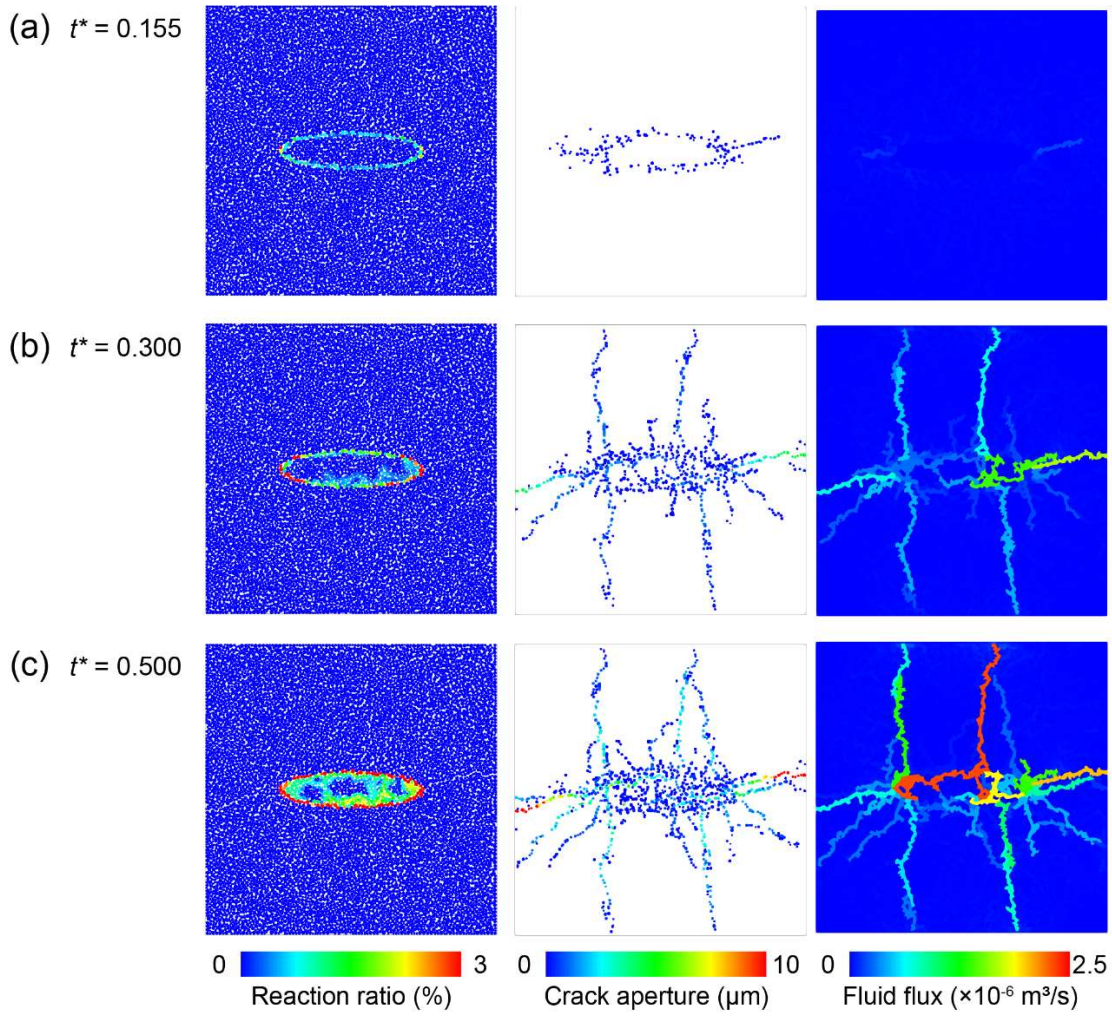

Fig. 3.10. Simulation result of the single grain model. Snapshots of the reaction ratio, fracture aperture, and fluid flux at (A) t* = 0.155 (ξ_{Av} = 0.20, ε_V = 0.07 × 10-2), (B) t* = 0.300 (ξ_{Av} = 0.68, ε_V = 0.5 × 10-2), and (C) t* = 0.500 (ξ_{Av} = 2.07, ε_V = 1.0 × 10-2). ξ_{Av} and ε_V are average reaction ration and volume strain of the reactive grain, respectively.

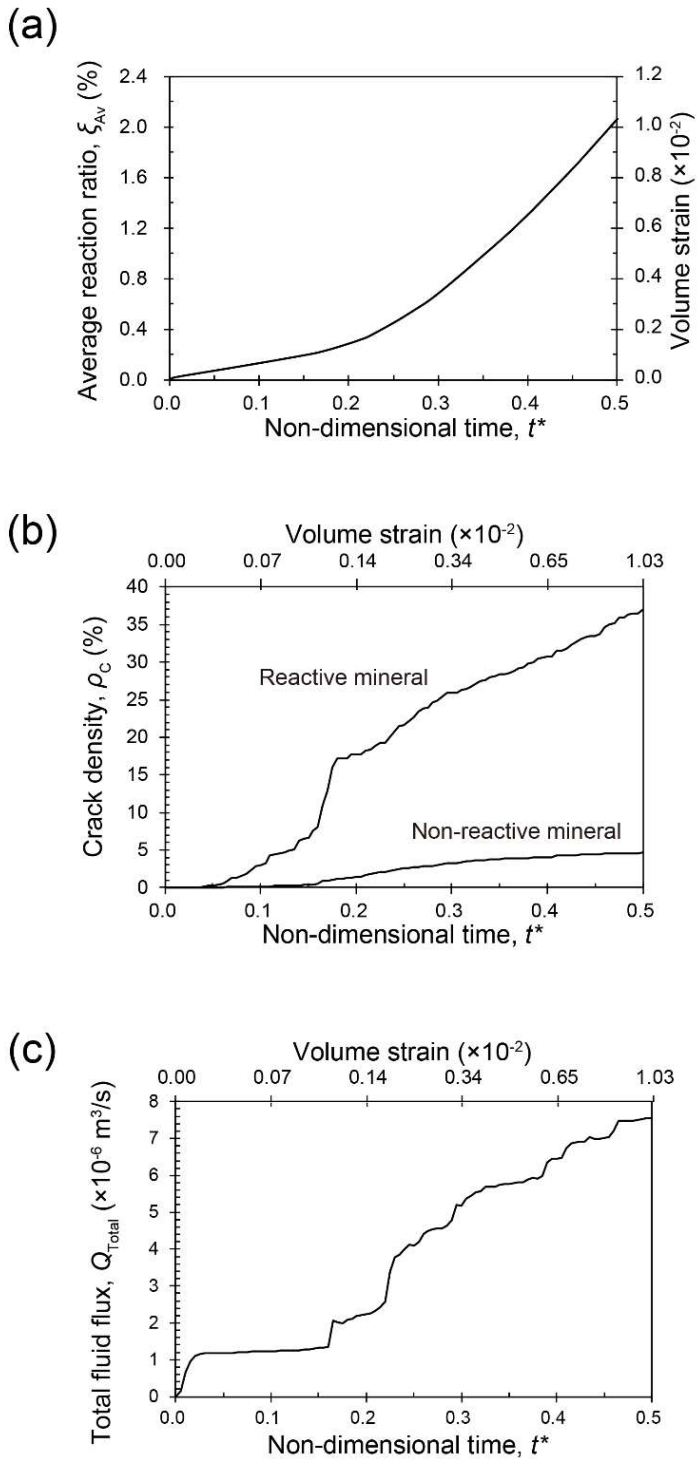

Fig. 3.11. Time evolution of the (A) average reaction ratio, (B) fracture density, and (C) total fluid flux.

3.4.2. Multi-grain model

The result of the multi grain model is shown in Fig 3.12. Snapshots of the reaction ratio, width of crack aperture, and normalized fluid flux are shown for t* = 0.045 (Fig. 3.12A), t* = 0.395 (Fig. 3.12B), and t* = 0.470 (Fig. 3.12C). Fig.s 3.13A-C show the time evolution of the reaction ratio (Fig. 3.13A), crack density within the reactive and non-reactive material (Fig. 3.13B), total fluid flux (Fig. 3.13C), and permeability (Fig. 3.13D). The permeability tests were performed at selected times. Permeability was calculated by fixing the arrangement of elements in the rock model. The fluid flow was assumed to be perpendicular in the z-direction and the boundary in the x-direction was assumed to be a non-permeable boundary.

In the initial phase (t* = 0 - 0.45), as the fluid infiltrate through the non-reactive material from the top to the bottom of the rock model, the reactive grains at the top begin to react (Fig. 3.12A). Snapshots of crack aperture at t* = 0.05, where the crack density of the reactive material increased rapidly (Fig. 3.13B), show that cracks formed within the reactive material grains or at the boundary between the reactive and non-reactive material (Fig. 3.12A).

Thereafter, the crack density within the reactive and non-reactive materials increased gradually until t* = 0.4 (Fig. 3.13B); the profile of fluid flux as a function of t* was similar, with both increasing gradually and Q_{Total} to be doubled by t* = 0.4. The crack density within the reactive material shows a sharp increase at t* = 0.395. At this time, radial cracks form around the reactive grains at the top of the model and the cracks propagate into the second layer of reactive grains (Fig. 3.13B). As the cracks connect to the reactive grains at middle part of the model, the grains within the middle part begin to react. The wide cracks openings tend to increase in size as the reaction progresses and begin to serve as the dominant fluid pathways (Fig. 3.13B). The formation of cracks connecting the grains causes the normalized fluid flux to increase sharply from 2 to 4 between t* = 0.395 and 0.45 (Fig. 3.13C). The snapshot at t* = 0.47 shows that the fracture cuts one of the bottom layer grains and reaches the bottom boundary. This causes a rapid increase in permeability and a reaction progress that leads to further fracture formation.

The results of the multiparticle model indicate that positive feedback between fluid flow, reaction, and fracture formation occurs as the reacting particles are connected by radial fractures, creating a network of fluid flow pathways (Fig. 3.12C). Reaction-induced fractures dynamically change the permeability of the rock. As the fracture network forms between reactive grains, the permeability gradually increases with increasing average reaction ratio (Fig. 3.13D). To summarize the result, The reaction proceeds with limited fluid supply in the early stages of the reaction. In the later stages of the reaction, the formation of a network of connected cracks increases the fluid supply.

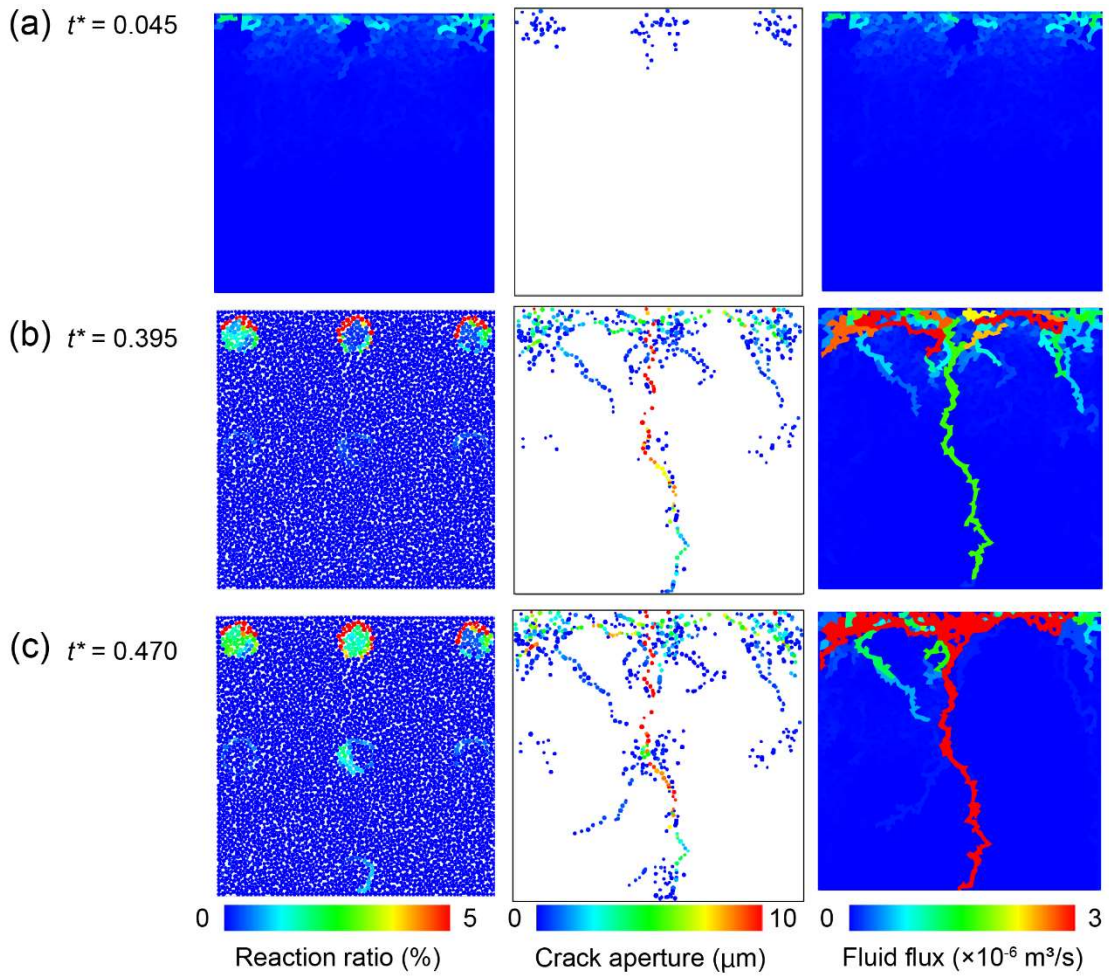

Fig. 3.12. Results of the MG simulation. (a–c) Snapshots showing the reaction ratio, fracture aperture, and fluid flux at (A) t* = 0.045 (ξ_{Av} = 0.1 %, $\varepsilon_V = 0.01 \times 10^{-2}$), (B) t* = 0.40 ($\xi_{Av}$ = 1.4, $\varepsilon_V = 0.7 \times 10^{-2}$), and (C) t* = 0.47 ($\xi_{Av}$ = 2.2, $\varepsilon_V = 0.9 \times 10^{-2}$). ξ_{Av} and ε_V are average reaction ration and volume strain of the reactive grain, respectively.

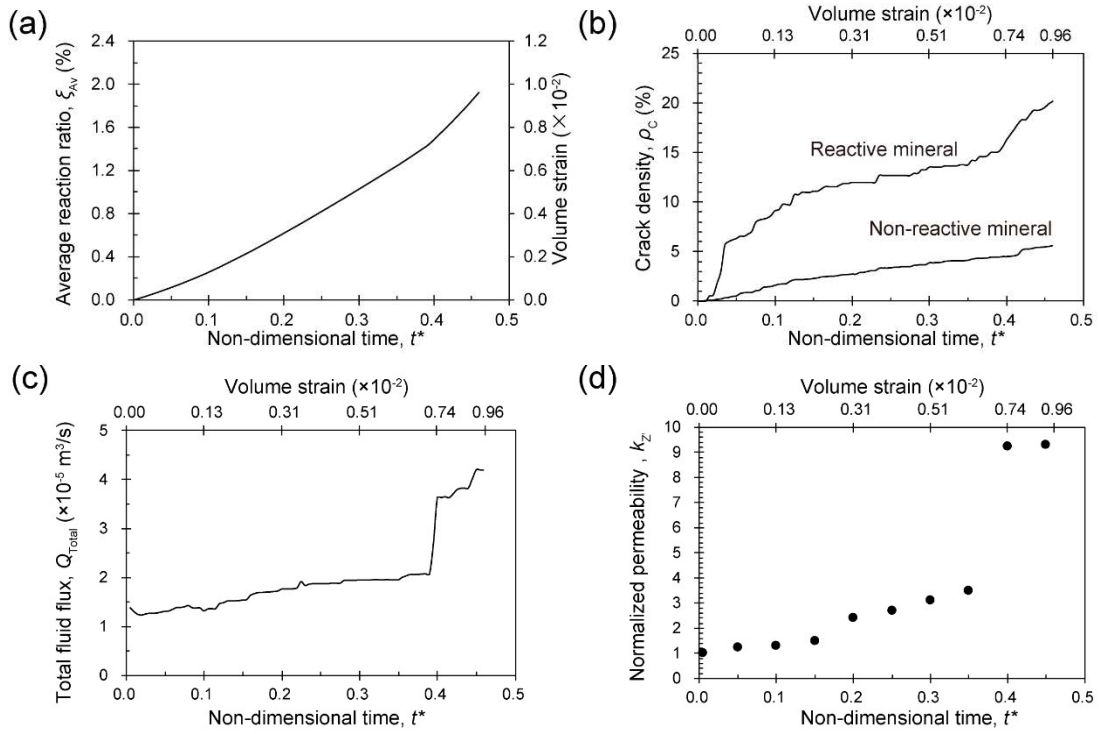

Fig. 3.13. Temporal evolution of the (A) average reaction ratio, (B) crack density within reactive mineral and non-reactive mineral, (C) total fluid flux, and (D) permeability normalized to the initial permeability.

3.4.3. Layered structure condition

The result of the layered sturcture model is shown in Fig 3.14. Snapshots of the reaction ratio, fracture aperture, and normalized fluid flux were shown for t* = 0.120 (Fig. 3.14A), t* = 0.170 (Fig. 3.14B) and t* = 0.240 (Fig. 3.14C). Figs 3.15A-C show the time evolution of the reaction ratio (Fig. 3.15A), the crack density within the reactive and non-reactive material (Fig. 3.15B), the normalized total fluid flux (Fig. 3.15C), and the penetration rate (Fig. 3.15D).

In the initial phase (t* = 0 - 0.12), the reaction begins in the first reaction layer, which is in contact with the top of the model. During this phase, the fracture density increases in the first reaction layer more than in the non-reaction layer. The cracks within the reactive layer are uniformly distributed, whereas the cracks in the non-reactive layers tend to be localized, vertically oriented cracks (Fig. 3.14A). Some cracks propagate into the non-reactive layer and the second reactive layer (Fig. 3.14A). The the fluid flux within the cracks is higher than in the non-reactive layeres (Fig. 3.14A), indicating that the cracks are dominant fluid pathways. The total fluid flux is nearly constant at this stage (Q_{Total} = ~0.4 × 10^{-4} ; Fig. 3.15C).

Between t* = 0.12 and 0.17, Q_{Total} increases sharply by ~17 times. The snapshot at t* = 0.17 shows several large fractures with wide openings that allow fluid flow into the second reaction layer (Fig. 3.14B). A rapid increase in fluid flow is also observed at t* = 0.12, t* = 0.15, 0.18 (Fig. 3.15C).

The snapshot at t*=0.24 shows that the fracture network has reached the lower boundary of the rock model (Fig. 3.14C). The fracture network serves as the main fluid path through several reactive layers (Fig. 3.14C). Vertical cracks develop because the reactive layer expands parallel to the laminae, causing tensile cracks perpendicular to the laminae (Okamoto & Shimizu, 2015).

Fig. 3.16 shows a histogram of the orientation of microcracks in the reactive and non-reactive layers, respectively, at t* = 0.24 (Fig. 3.14C). In the reactive layer, the orientation of microcracks is uniform, while in the non-reactive layer, microcracks form preferentially in the vertical direction. These results are consistent with the orientation of the olivine-rich and plagioclase-rich layers in troctolite (Fig. 3.3). The simulations show that in layered structures with alternating reactive and non-reactive minerals, fracture propagation within the non-reactive material in a direction perpendicular to the layered structure promotes fluid permeation in a direction perpendicular to the layered structure.

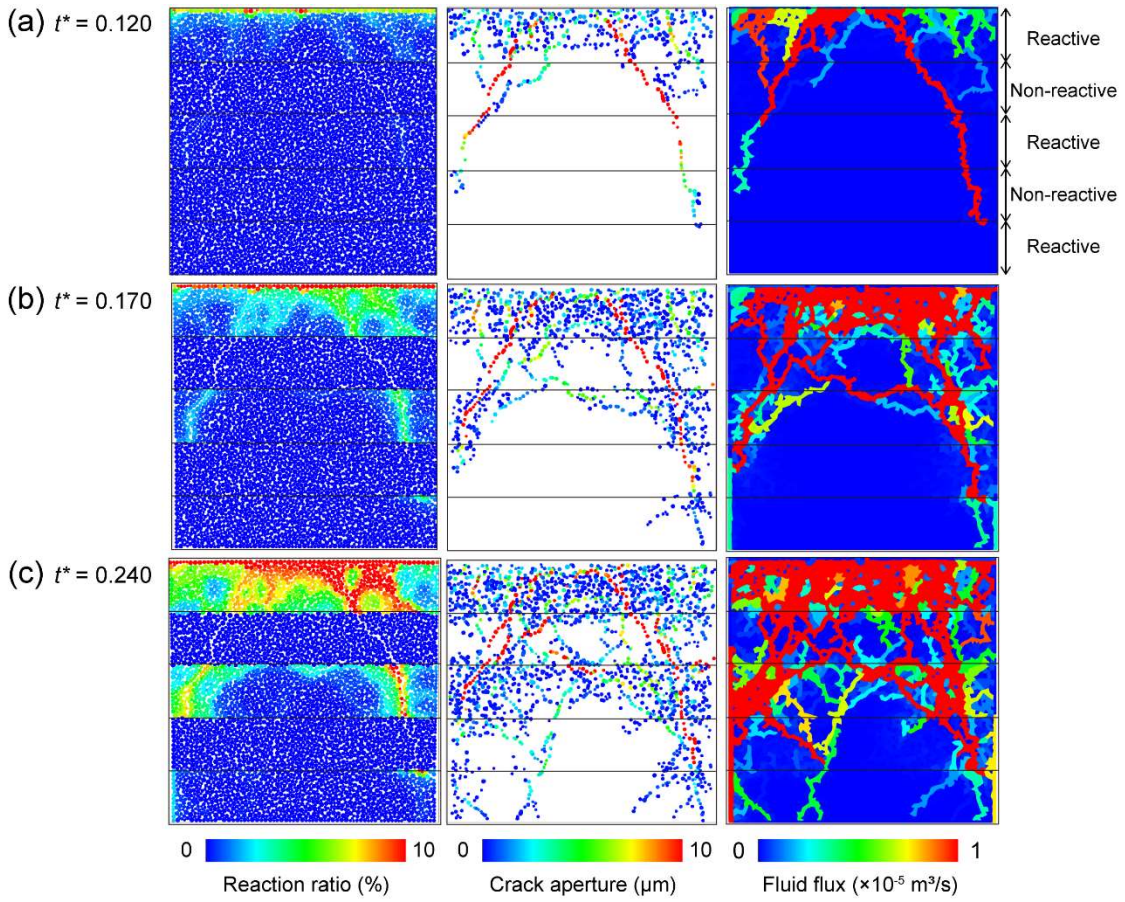

Fig. 3.14. Results of the layered structure model. (A-C) Snapshots showing the reaction ratio, fracture aperture, and fluid flux at (A) t* = 0.12 (ξ_{Av} = 0.4 %, $\varepsilon_V = 0.2 \times 10^{-2}$), (B) t* = 0.17 ($\xi_{Av}$ = 1.1, $\varepsilon_V = 0.6 \times 10^{-2}$), and (C) t* = 0.24 ($\xi_{Av}$ = 3.2, $\varepsilon_V = 1.6 \times 10^{-2}$). ξ_{Av} and ε_V are average reaction ration and volume strain of the reactive grain, respectively.

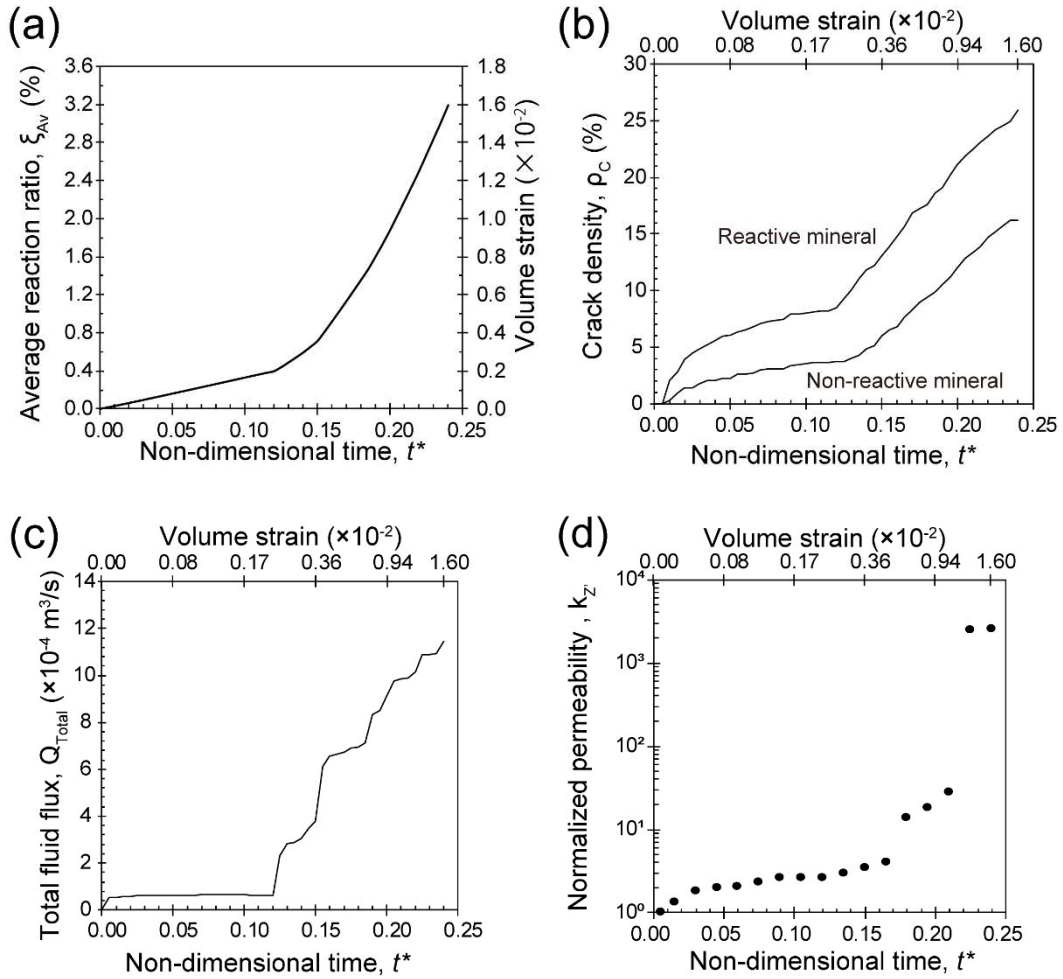

Fig. 3.15. Temporal evolution of the (A) average reaction ratio, (B) crack density within reactive mineral and non-reactive mineral, (C) total fluid flux, and (D) permeability normalized to the initial permeability.

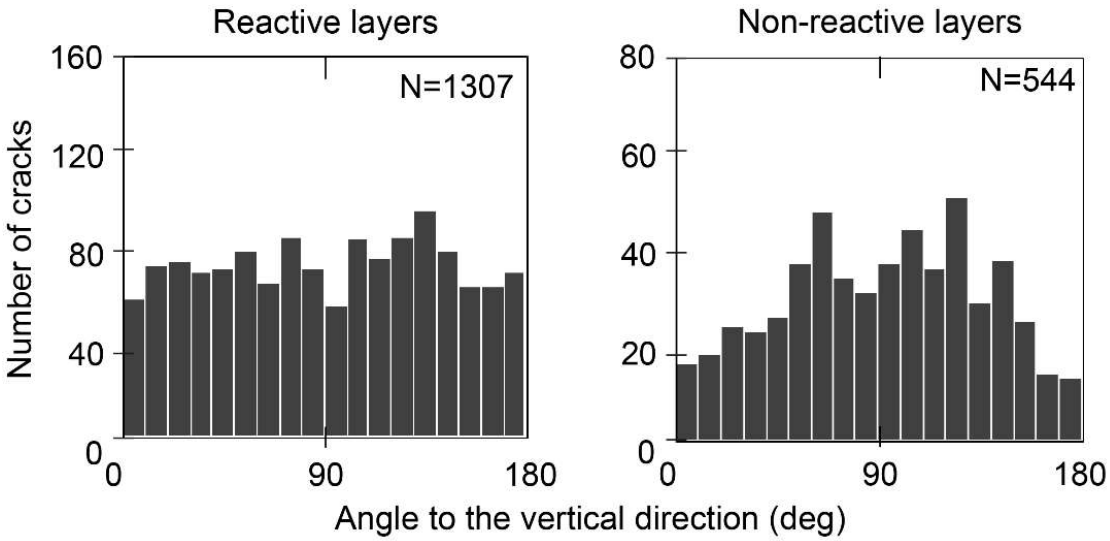

Fig. 3.16. Distribution of crack orientations in reactive and non-reactive layers at t* = 0.24.

3.5. Discussion

3.5.1. Comparison with natural samples

The fracture patterns of the serpentinized olivine in the gabbroic rocks are similar to the results from the DEM simulations conducted in this study. The mesh-like texture within the reactive material and the radial cracks developed in the non-reactive material reproduced by the single particle model simulation (Fig. 3.10). These textures are similar to the mesh texture of partly serpentinized olivine grains and the radial cracks developed in the plagioclase and clinopyroxene around serpentinized olivine (Fig. 3.1). An interesting observation from the DEM simulations in the single grain model is the simultaneous development of the mesh texture and radial cracks (Fig. 3.10). As the reaction progresses, most of the cracks in the reactive grains are narrow, but some cracks become wider and act as the dominant fluid pathways (Fig. 3.10B-C). Narrow and wide cracks within the reactive grains may correspond to Type 1 and Type 2 mesh texture observed in natural gabbroic rocks (Chapter 2, Fig. 2.9). The multi-grain model simulations show a network of cracks connecting reactive grains as observed in gabbroic rocks (Fig. 3.1). The results of the layered structure model simulations (Figs. 3.14 and 3.16) are consistent with the characteristic development of cracks perpendicular to the layered structure in the plagioclase layers compared to the randomly oriented cracks in the olivine-rich layers in the troctolite (Fig. 3.2B). Such fractures perpendicular to the layered structure were also observed in the field observation (Fig. 2.2E). On the other hand, the natural samples also show microstructures that were not reproduced by the simulation. Homogeneous serpentinization without mesh texture formation was observed around serpentine veins in the gabbroic rocks (Fig. 2.19D). Such homogeneous textures are thought to occur when fluid transport dominates over reaction rates (Shimizu and Okamoto., 2016). Since a reasonable mechanism for accelerated fluid transport is unlikely, such a microstructure could have resulted from a relative decrease in reaction rate rather than fluid transport due to a decrease in

temperature during the late stage of serpentinization. In general, the fracture patterns observed in the gabbroic rocks of the Oman Ophiolite are well reproduced by these numerical models.

The results of the simulations with elastic parameters for olivine and plagioclase (Table 3.1) suggest that ~0.01 of volume strain is enough to develop cracks similar to the natural samples. The numerical model assumes 50% of volume increase reaction, ~0.01 of volume strain is accumulated during 2%–3% of the reaction ratio. In the natural gabbroic rocks, the extent of serpentinization is 60%–70% in samples 09Z03, 47Z02, and 48Z03, and ~10% in sample 113Z03. Assuming a 50% volume increase due to the reaction, the volume strain of olivine is estimated to be 0.30–0.35 and 0.07, respectively. The similarity in the geometric patterns between the natural samples and simulation results at different extents of serpentinization suggests that the main geometric pattern is formed in the early stages of the reaction. Indeed, for the single grain model, the slope of the crack density becomes lower with time (Fig. 3.11B), meaning that the number of cracks becomes constant. The snapshots of the single grain model indicate that the width of the crack aperture increases with reaction progress (Fig. 3.10). Similar trends for crack density and crack width were recognized in hydration experiments of MgO in polycrystalline calcite (Kuleci et al., 2017).

3.5.2. Effect of confining pressure

In this study, simulations were performed assuming a low effective confining pressure (1 MPa). Therefore, to evaluate the effect of effective wind pressure, a single-particle model was simulated with effective confining pressure varying between 5 MPa and 10 MPa (Fig. 3.15). In both cases, cracking of the olivine grains and radial cracking of the surrounding matrix were observed (Fig. 3.17A). However, as the effective confining pressure increased, the radial cracking tended to be localized (Fig. 3.18A) and the serpentinization progressed more slowly (Fig. 3.18B).

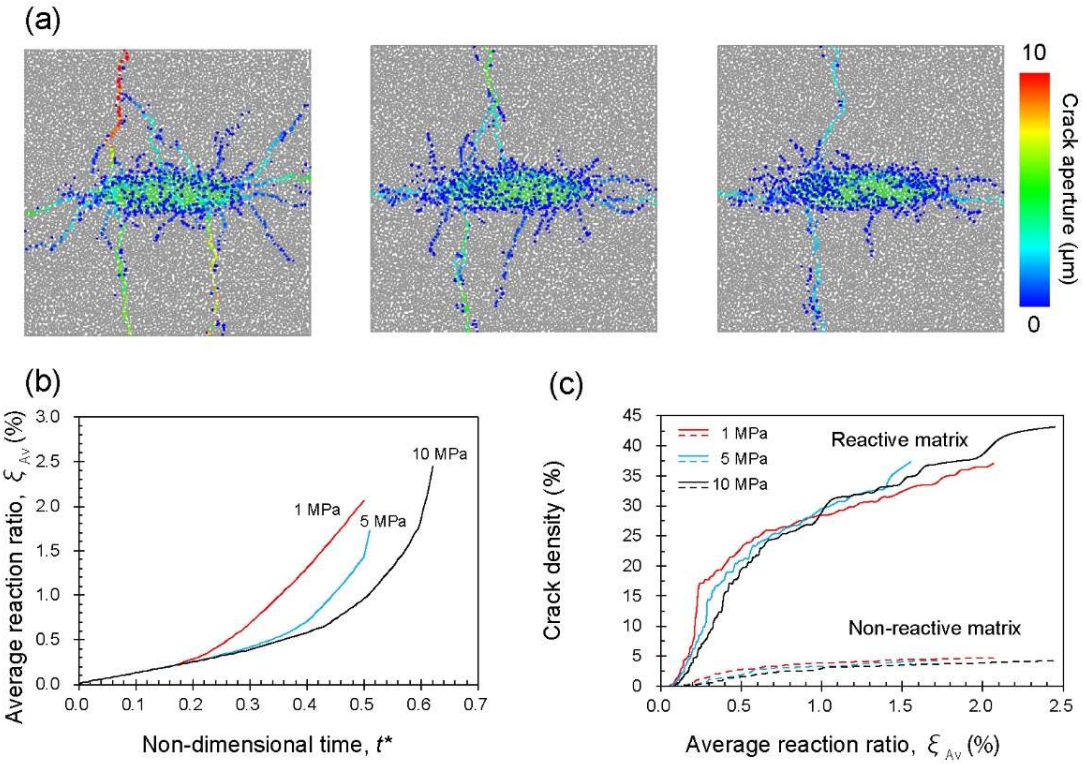

Fig. 3.17. Effect of the effective confining pressure on the development of fractures with progressive olivine hydration in the same configuration as the SG case (Fig. 3.10). (A) Snapshots of crack aperture at a reaction ratio, ξ_{Av}, of 1.6% ($\varepsilon_V = 0.80 \times 10^{-2}$) under an effective confining pressure of 1 MPa (left), 5 MPa (middle), and 10 MPa (right). Parameters other than the effective confining pressure are similar to the simulation of the SC case (Fig. 3.10; Table 3.1). (B) The average reaction ratio with respect to non-dimensional time. (C) Crack density in a reactive mineral (solid line) and non-reactive mineral (dashed line) as a function of the average reaction ratio.

3.5.3. Other fracturing mechanisms

Normal fault systems are commonly developed at mid-ocean ridges, where they form in response to extensional tectonic settings (Bicknell *et al.*, 1987; Buck *et al.*, 2005). However, it is unclear whether the external differential stress that causes faulting on a regional scale affected grain-scale fracturing as observed in this study. In addition, thermal stress is thought to be a main cause of fracturing within the crust during the cooling oceanic lithosphere (Boudier *et al.*, 2005; Cooper and Simmons, 1977; Korenaga, 2007; Nicolas, 2003). There are several evidences of high temperature (>700 ˚C) hydrothermal alteration of gabbro and Moho transition zone within the Oman ophiolite, which is explained by fluid infiltration along the vertical fractures generated by thermal contraction at the fast-spreading ridge (Bosch *et al.*, 2004; Boudier *et al.*, 2005; Nicolas, 2003). Therefore, to assess the influences of fracturing processes induced by tectonic stress and/or thermal stress on grain-scale fracturing observed in this study, I conducted additional simulations on fracturing using a model of olivine grain in matrix with the same mechanical properties and geometry as the SG model case (Fig. 3.18).

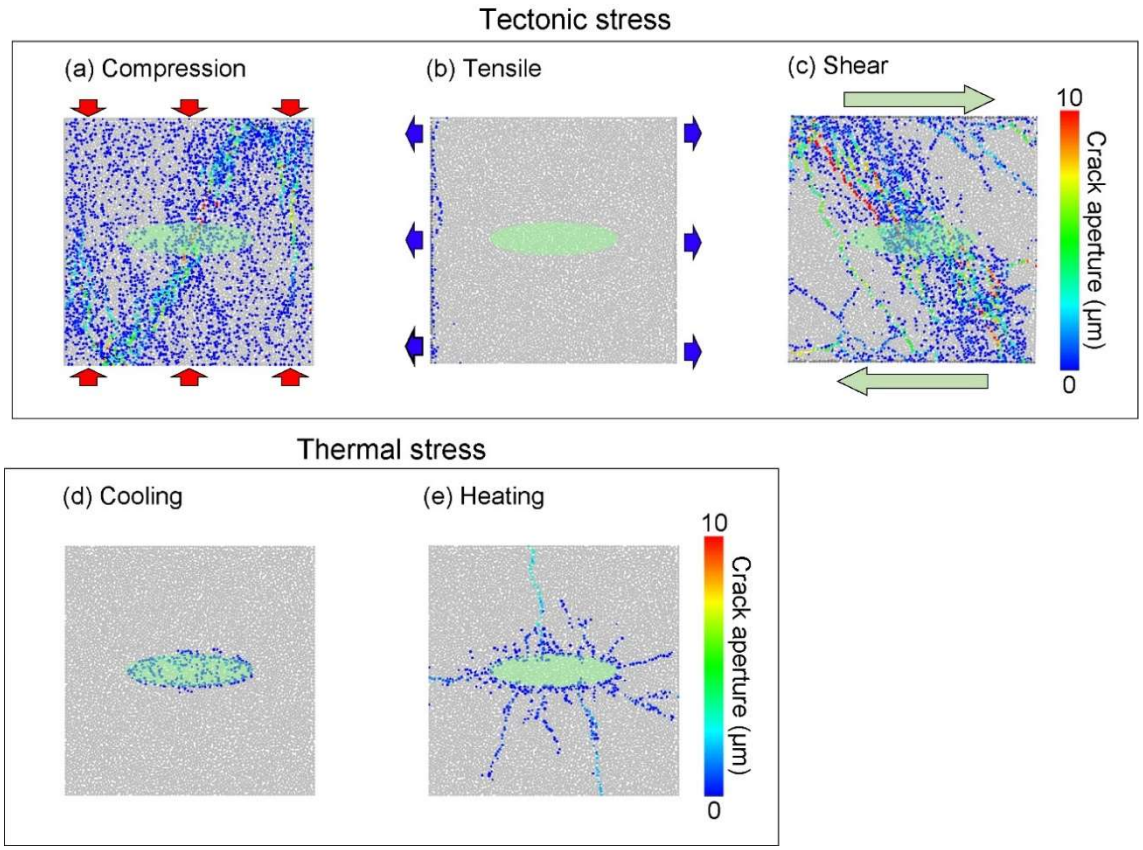

Fig. 3.18. Simulation result of the effect of tectonic stress. (A) compression at axial strain = 1.4×10^{-3}, (B) tensile at lateral strain = -2.6×10^{-5} and (C) shear stress at horizonal displacement = 0.08 mm. (D, E) simulation results of the effect of thermal stress at volume strain = 5×10^{-3}. (D) cooling, (E) heating. The olivine grain is shown in green.

Tectonic stress

The compression tests, tension tests, and shear deformation of the SG model case were conducted (Fig. 3.17). The confining pressure was set to 1 MPa. The strain rates were set to 0.1 s^{-1} for the compression test, -0.05 s^{-1} for the tension test, and 20 s^{-1} for the shear deformation test. It is noted that the fracture pattern generated was not significantly affected by the strain rate, when the strain rate is adequately slow (c.f., Okamoto et al., 2020). In the compression test, numerous tensile and shear cracks were generated normal to the compression axis (Fig. 3.17A).

The cracks were distributed relatively homogeneously throughout the model rock. As strain increased, the model rock broke and large fractures formed in sloped direction. In the tension test, a single fracture oriented normal to the minimum principal stress was generated by connections among smaller tensile fractures (Fig. 3.17B). In the shear deformation test, an en-echelon array of fractures, formed by connected tensile fractures, developed at 40°–50° to the shear plane (Fig. 3.17C). This feature of the tension test is consistent with the results of other DEM simulations of shearing under low confining pressure (Okamoto et al., 2020). In these three cases, there is no difference in the fracture pattern within the olivine and unreactive matrix (Fig. 3.17A–C), in spite of the different Young's modulus of each mineral.

In the natural troctolite described in this study, fractures in olivine are oriented rather uniformly, and most of the fractures within plagioclase are oriented radially or normal to the layering (Fig. 3.1). These features within olivine and plagioclase in natural samples were not reproduced by the DEM modeling in which deformation is induced by the tectonic stress (Fig. 3.18).

Thermal stress

Thermal stresses can be caused by: (1) differences in thermal expansion coefficients between minerals, (2) thermal expansion coefficient anisotropy, and (3) thermal gradients within the rock (Boudier *et al.*, 2005; Cooper and Simmons, 1977; Nicolas, 2003). Here, I investigated grain-scale thermal cracking in response to differences in thermal expansion coefficients between olivine and plagioclase. I simulated the thermal fracture of an olivine grain embedded in a plagioclase matrix during cooling and heating. For a given temperature difference ($\Delta T = T - T_0$), the ratio of the particle radius to the initial radius (r/r0) can be calculated using $r/r_0 = \beta_l \Delta T$, where β_l is the linear thermal expansion coefficient (Wanne and Young, 2008). The material was assumed to be isotropic, so β_l was set to $\beta_v/3$, where β_v is the volumetric thermal expansion coefficient. The linear thermal expansion coefficients of olivine ($\alpha_l = 1.09 \times 10^{-5}$ K^{-1}) and plagioclase ($\beta_l = 0.50 \times 10^{-5}$ K^{-1}) were calculated from the volumetric thermal expansion coefficients (olivine: 3.26×10^{-5} K^{-1} and plagioclase: 1.51×10^{-5} K^{-1}) (Robertson, 1988).

During cooling from 700 to 300°C, olivine and plagioclase grains contract with volume strains up to -1.3×10^{-2} for olivine and -0.6×10^{-2} for plagioclase (Fig. 3.19A). Tensile fractures were preferentially generated within the olivine grain and at the olivine/plagioclase interface (Fig. 3.19C). During progressive cooling, the crack density preferentially increases by up to 20% within the olivine grains, while the crack density in the plagioclase matrix is <0.2% (Fig. 3.19B). Most cracks form in the early cooling stage ($|\Delta T| < 100$ °C; Fig. 3.19B), suggesting that thermal cracking dominates at relatively higher temperatures. Preferential fracturing of olivine grains occurs in response to the higher αv value of olivine relative to that of plagioclase. Similar fracture patterns would also be produced if the matrix mineral were clinopyroxene ($\alpha v = 2.19 \times 10^{-5}$ K^{-1}).

In the natural samples analyzed in this study, the less serpentinized olivine grains show fractures, but they are not accompanied by radial fractures in the surrounding minerals (Fig. 3.1D), which is similar to the results of cooling (Figs. 3.19C). These lines of evidence suggest that olivine fracturing may be initiated by thermal fracturing during cooling and important for initial stage of serpentinization.

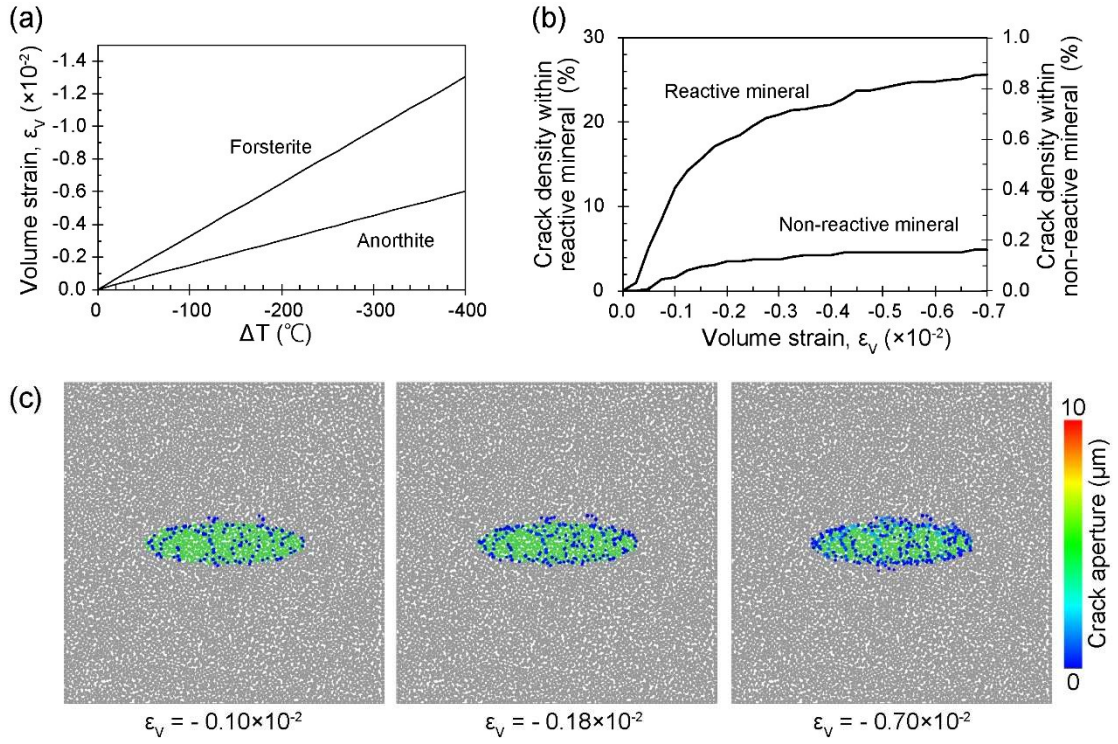

Fig. 3.19. Thermal cracking during cooling for the same configuration as the SG case, where an olivine grain is embedded in plagioclase matrix. (A) Volume strain of forsterite and anorthite with respect to the temperature difference, $\Delta T = T - T_0$, where T_0 is the initial temperature. (B) The evolution of crack density in simulations for thermal cracking during cooling (volume decrease). (C) Snapshots showing the crack apertures at volume strains of $\varepsilon V = -0.10 \times 10^{-2}$, -0.18×10^{-2}, and -0.70×10^{-2}. The olivine grain is shown in green.

3.5.4. Transition from closed to open system during serpentinization

Multi-stages of serpentinization reactions characterized by the Al and Fe concentrations in the serpentine were observed in the gabbroic rocks: (1) mesh texture composed of lizardite+brucite+mag (Type 1 mesh), (2) mesh texture composed of Al-rich serpentine + magnetite (Type 2 mesh), (3) Al-rich yellow colored serpentine in mesh core, and (4) Al-rich serpentine veins. Such multistage serpentinization can result from evolution from a closed to an open system, as discussed below. The earliest Type 1 mesh textures are characterized by lizardite + brucite + magnetite. The lizardite + brucite mineral assemblage indicates that serpentinization began at temperatures below 350°C (Klein *et al.*, 2009) and that serpentinization that serpentinization occurs under low silica activity, corresponding to a olivine dominant closed system with no elemental transport except for H_2O (Beard *et al.*, 2009; Katayama *et al.*, 2010; Oyanagi *et al.*, 2018). In the MgO-SiO_2-H_2O system, this reaction can be written as follows:

$$MgSiO_4 + H_2O = Mg_3Si_2O_5(OH)_4 + Mg(OH)_2 \quad \text{(R2.2)}$$

On the other hand, the type 2 mesh texture is characterized by Al-rich serpentine + magnetite. The serpentinization without brucite can be caused by addition of silica supplied by pyroxene and plagioclase, as observed in harzburgite, lherzorite, and troctolite in previous studies (Beard *et al.*, 2009; Katayama *et al.*, 2010; Oyanagi *et al.*, 2018). In MgO-SiO2-H2O system, this reaction can be written as follows:

$$3Mg_2SiO_4 + 4H_2O + SiO_{2,aq} = 2Mg_3Si_2O_5(OH)_4 \quad \text{(R2.3)}$$

Hydrothermal experiments of olivine with silica-rich minerals (plagioclase or quartz) show that brucite is not produced near the Si-rich minerals (Ogasawara *et al.*, 2013; Oyanagi *et al.*, 2018). Alteration of Al-rich minerals (plagioclase and/or clinopyroxene) can supply Al to the serpentine, forming Al-rich serpentine (Oyanagi *et al.*, 2018).

The area around the serpentine veins that cut the host rock mesh texture was completely serpentinized, and the mesh core was replaced by Al- and Fe-rich yellow colored serpentine. Even in the highly altered gabboric rocks, the clinopyroxene was not altered, suggesting that the main source of Al and Si was most likely plagioclase. Radial cracks (now filled by chlorite, prehnite, or serpenitne) were observed in the plagioclase and clinopyroxene around the serpentinized olivine grains. In the layered gabbro (Fig. 2.2E), fractures (now filled by serpentine) vertical to the layered structure were observed in the plagioclase-rich layers surrounded by olivine-rich layers.

These cracks can increase the surface area in Al-rich mienrals and may enhance the supply of Al and Si. Thermodynamic modeling of olivine and plagioclase alteration under greenstone facies conditions also indicates that the silica potential for plagioclase alteration to form prehnite + chlorite may be higher than that of olivine serpentinization (Nozaka and Tateishi, 2023). This is consistent with the interpretation that Si activity was increased by plagioclase alteration.

The area around the serpentine veins that cut the host rock mesh texture was completely serpentinized, and the mesh core was replaced by Al- and Fe-rich yellow colored serpentine. Even in the highly altered gabboric rocks, the clinopyroxene was not altered, suggesting that the main source of Al and Si was most likely plagioclase. Radial cracks (now filled by chlorite, prehnite, or serpenitne) were observed in the plagioclase and clinopyroxene around the serpentinized olivine grains. In the layered gabbro (Fig. 2.2E), fractures (now filled by serpentine) vertical to the layered structure were observed in the plagioclase-rich layers surrounded by olivine-rich layers.

These fractures may increase the surface area of Al-rich minerals and may enhance the supply of Al and Si. Thermodynamic modeling of olivine and plagioclase alteration under greenstone facies conditions also suggests that the silica potential for plagioclase alteration to form prehnite + chlorite may be higher than that for olivine serpentinization (Nozaka and Tateishi, 2023). This is consistent with

the interpretation that Si activity was increased by plagioclase alteration.

Based on these observations, the serpentinization reaction microstructure of the gabbroic rocks records a transition from a closed system except for water (type 1 mesh texture) to an open system with addition of Al and Si and an increase in the water/rock ratio (Al-rich serpentine in type 2 mesh texture, serpentine veins, and Al-rich mesh core). Transitions from closed to open systems have also been observed in serpentinized troctolites on the seafloor (Beard *et al.*, 2009) and in harzburgites and wherlite (Oyanagi *et al.*, 2018). This trend of higher water to rock ratios with mineral vein formation during serpentinization is consistent with the interpretations discussed in previous studies (Frost *et al.*, 2013; Schwarzenbach *et al.*, 2016). Andreani et al. (2007) suggested the transition from a closed system to an open system during serpentinization on the mid-Atlantic ridge, based on detailed observations of vein systems within serpentinized peridotites. They discussed that this transition was caused by unroofing at a detachment fault. The results of this chapter indicate that, In addition to such tectonic processes, enhancement of mass transfer can be induced by reaction-induced fracturing (e.g., Jamtveit et al., 2008; Kelemen and Hirth, 2012), as shown by radial fracturing within troctolite. As fluid flow is considered explicitly in the model, I show that permeability increases to several times the initial value during the hydration (Fig. 3.14D and 3.15D). Stresses produced by serpentinization reactions, inferred from reaction Gibbs energies, are believed to be sufficient to form fractures even at several kilometers to tens of kilometers below ground (Kelemen and Hirth, 2014; Malvoisin et al., 2017). Therefore, the increase in permeability and change from a closed to a liberated system due to such reactions may also occur deep underground.

In summary, the observed fracture patterns are reproduced well by the modeled fracturing induced by serpentinization reaction and support the inference of permeability enhancement during serpentinization. The enhanced permeability by the formation of fracture network could enlarge the effective distance of element transfer (such as silica and aluminum), which change the serpentinization reactions.

3.6. Summaries

Chapter 3 focused on microcracks and fractures in the gabbroic rocks. A layered structure of olivine-rich and plagioclase-rich layers was observed in the lower crust. In the field observation, fractures perpendicular to the layered structure were observed in the plagioclase-rich layer. Microscopic observation revealed radial cracks in plagioclase and pyroxene around partially serpentinized olivine in the gabbroic rocks. The orientation of microcracks in troctolites at the boundary between olivine-rich and plagioclase-rich layers was predominantly perpendicular to the layered structure in the plagioclase-rich layers, while the olivine-rich layers showed relatively random orientation.

The coupled mechanical-chemical-hydrological two-dimensional numerical simulations was performed to gain insight into the formation mechanism of the microcracks and fractures in natural samples. As a result, in the single grain model, cracks with mesh texture were formed in the interior of

the reactive material and radial cracks were formed in the non-reactive material surrounding the reactive material. In the layered structure model, cracks predominating in the perpendicular to the layered structure were formed in the non-reactive material layers. These features are consistent with natural observations.

Simulations of the multi grain model indicate the formation of a network of cracks link between each reactive material grains, which increase the permeability by more than one order of magnitude after the percolation. The layered structure model results also indicate that hydration of the reactive material layer promote vertical fluid flow by forming vertical fractures in the non-reactive material layers above and below it.

The change from low to high permeability in the early stages of the reaction, as indicated by numerical simulations, is consistent with the change from a closed to a open system observed in natural samples. In addition, the cracks developed in the plagioclase or clinopyroxene increase the reaction suface area and may enhance dissolution of these mienrals. It result the addition of Al and Si to the serpentine in the later stage serpentinization as observed in the natural samples. These features suggest that reaction-induced fracturing causes a transition from a closed to an open system, and enhances fluid infiltration through the initially less permeable lower crust and into the deeper oceanic lithosphere.

Part of the content of the Chapter 3 has been published as the following publication:
Yoshida, K., Okamoto, A., Shimizu, H., Oyanagi, R., Tsuchiya, N., Oman Drilling Project Phase 2 Science Party, “Fluid Infiltration Through Oceanic Lower Crust in Response to Reaction-Induced Fracturing: Insights From Serpentinized Troctolite and Numerical Models”, *Journal of Geophysical Research: Solid Earth*, 125, 11, 2020, DOI:10.1029/2020JB020268.

Chapter 4: Fluid flow in through fracture network in serpentinites

4.1. Introduction

Mineral veins are record of fluid flow pathways. In serpentinite, mineral veins can be observed at various scales from the micrometer scale to the outcrop scale. While the importance of microcracks highlighted in Chapter 3, relatively large-scale fractures observed at outcrop scale from thin sections scale may play an important role as the high flux fluid pathway. However, it is not well known how long the mineral veins found in natural serpentinites formed and how much fluid flowed through the fracture. Local mass transport caused by fluid flow along a fracture in the rock can cause the sides of the fluid pathway to be replaced by minerals that are different from the host rock. Such structures are called "reaction zone" and provide unique insights into water-rock interactions. Several recent studies have analyzed the width and elemental profiles of reaction zones along mineral veins to constrain the time scale of fluid-rock interactions in subducting oceanic crust (John et al., 2012) and middle continental crust (Mindaleva et al., 2020), as well as temperature-pressure conditions and fluid activity times and fluid flow velocities. These studies suggest that fluid infiltration events can occur over short time intervals (10^{-3}-10^{2} years) compared to the full duration of regional metamorphism (10^{5}-10^{7} years). However, because geologic structures that capture the time scale of fluid-rock interactions are rare, to my knowledge, there are no studies that provide geologic constraints on the time scale and velocity of fluid flow in the formation of antigorite veins in serpentinite.

In this chapter, I examine the occurrence of an antigorite±chrysotile vein network developed in hydrated ultramafic rocks in the Oman ophiolite. The antigorite-chrysotile veins with brucite-rich reaction zones provide a unique insight into the conditions and timescale of antigorite formation, and fluid flow in subduction zone. Based on detailed microstructural observations, mass balance and mineral-fluid equilibrium calculations, coupled with a diffusion model for the reaction zone, I estimated the timescale of vein formation and the fluid flow rate through the fractures. The results indicate that a large amount of fluid flowed in a short period of time (several months to several years).

4.2. Samples and Methods

4.2.1. Samples

The analyzed samples were core samples of dunite recovered in CM1A and CM2B by the Oman Drillin Project, located in the Wadi Tayn massif, Oman. A total of 41 thin sections from the lower crust to the upper mantle were examined for the distribution of antigorite±chrysotile veins.

4.2.2. Transmission electron microscope

An electron-transparent foil across the reaction zone was prepared using a focused ion beam (FIB) – SEM (TFS Helios G3 Nanolab; Utrecht University, the Netherlands). Subsequent analysis of the foil was carried out in a transmission electron microscopy (TEM; TFS Talos F200X; Utrecht University, the Netherlands) using both bright-field TEM imaging and scanning TEM imaging modes as well as energy-dispersive X-ray analysis.

4.3. Results

4.3.1. Distribution of antigorite veins

Fig. 4.1 shows X-ray computed tomography (CT) and transmitted light thin section photographs of typical serpentinized dunite samples with antigorite ± chrysotile in the crust-mantle transition zone (CM1A-90Z2-48-53 and CM1A-137Z3-46-54). The orientation of the antigorite±chrysotile veins vary with borehole depth and are cut by later chrysotile veins (Kelemen et al., 2020) (Fig. 4.1B). The serpentinized dunite samples consist of lizardite, brucite, magnetite and Cr-rich spinel. Fresh olivine was not observed. The sample has a mesh texture developed during serpentinization. Some dunite samples were weathered (i.e., coalingite, oxyhydroxides, and clays (Kelemen et al., 2020; Fig. 4.1B). Antigorite ± chrysotile veins in some dunites have brucite-rich reaction zones extending from the vein wall into the host rock along the vein (Fig. 4.1A). The antigorite ± chrysotile vein with reaction zones is characterized by higher X-ray absorption in X-ray CT images (Fig. 4.1A) compared to the host rock matrix. In contrast, there is little contrast in CT images of samples from depths near the mantle section that do not have reaction zones (Fig. 4.1B).

Thin section observations reveal the discrete and widespread presence of antigorite ± chrysotile veins (Fig. 4.2). In hole CM1A, antigorite ± chrysotile veins are present in serpentinized dunite in the crust-mantle transition zone (160-180 m depth) and in several thin dunite layers in the upper mantle section (Fig. 4.2). In CM2B, antigorite±chrysotile veins are observed in serpentinized dunites at 0-30 m depth in the crust-mantle transition zone and in serpentinized harzburgites in the upper mantle at 140-200 m depth.

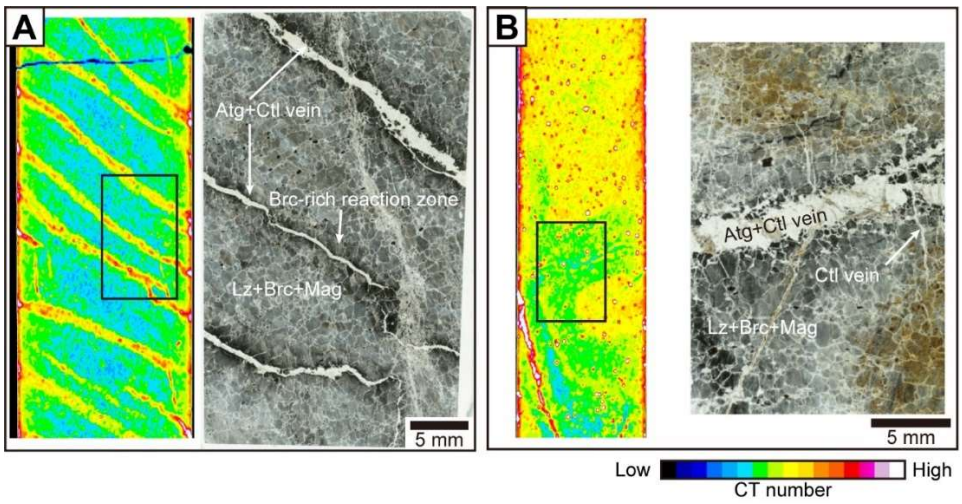

Fig. 4.1. X-ray CT images and thin sections of typical dunite with antigorite+chrysotile veins. (A) CM1A-90Z-2-48-53 and (B) CM1A-137Z-3-46-54.

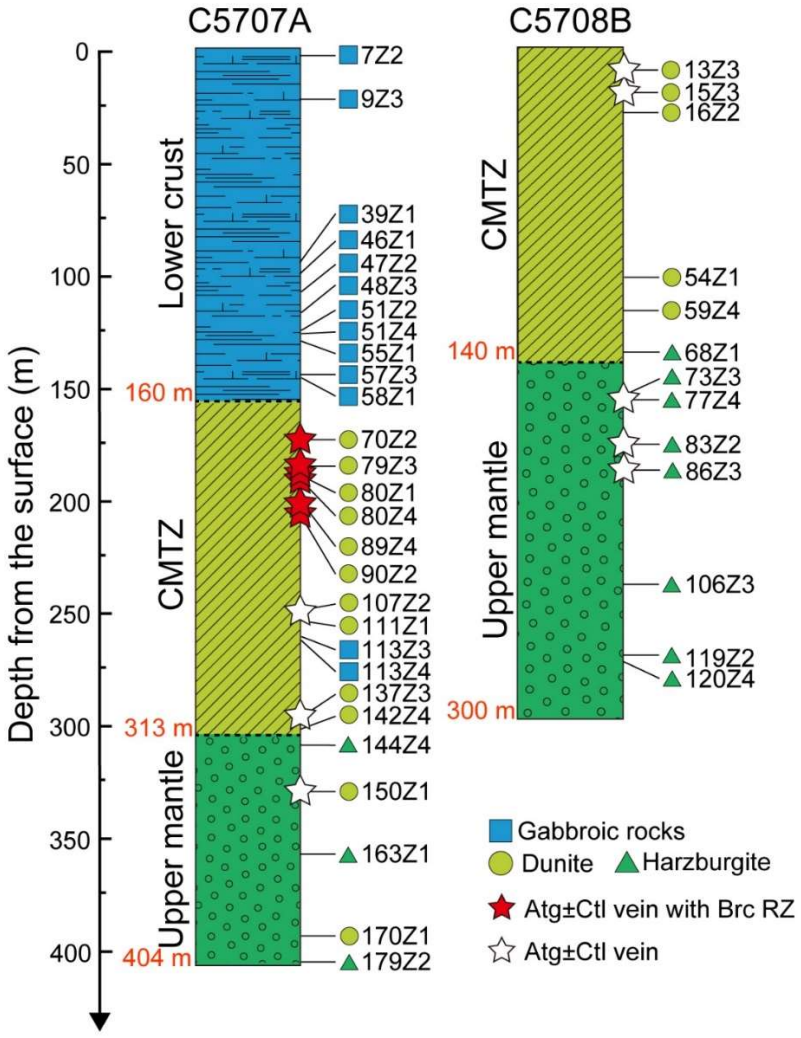

Fig. 4.2. Columnar sections of CM1A and CM2B. Distribution of Atg±Ctl vein with and without Brc-rich reaction zones (RZs) are indicated by red and white stars, respectively; CMTZ is the crust-mantle transition zone.

4.3.2. Microstructures and chemical characteristics

A typical dunite with antigorite+chrysotile vein with brucite-rich reaction zones was analyzed in detail for microstructure and chemical composition (CM1A-90Z2-48-53). The brucite-rich reaction zones are characterized by Si-poor regions in the Si elemental map (Fig. 4.3A). Within the reaction zone, brucite preferentially occurs in the mesh cores, while the mesh rims are replaced by chrysotile (Fig. 4.3B). Within the antigorite+chrysotile veins, ~10-100 μm long blade-shaped antigorite crystals (X_{Mg} = 0.97-0.98) is randomly oriented, and fine-grained chrysotile (X_{Mg} [$Mg^{2+}/(Mg^{2+} + Fe^{2+})$] = 0.97-0.98) fills the spaces between antigorite crystals (Fig. 4.4A). The host rock matrix consists of lizardite (97.5% by area; X_{Mg} = 0.97), brucite (0.5% by area; X_{Mg} = 0.85), and magnetite (2.0% by area; ~1-2 μm size; Fig. 4.4B). The reaction zone consists of brucite (41.0 area%; X_{Mg} =0.88), chrysotile (55.3 area%; X_{Mg} =0.97), and magnetite (3.0 area%; ~1-2 μm size; Fig. 4.4C).

A spontaneous channeling structures called "wormholes" (Szymczak et al., 2009; Devauchelle et al., 2017) developed in the brucite-rich reaction zone. The wormholes propagated from the vein wall into the reaction zones (Fig. 4.5). The wormholes are coated by magnetite at their boundaries to the brucite / matrix serpentine. The interior of the wormhole is filled with chrysotile (X_{Mg} = 0.96-0.97).

The nanostructure of the reaction front was observed by transmission electron microscopy (TEM). TEM observations show that the chrysotile crystals are located in the spaces between the brucite crystals in the reaction zone, and pores occur around the brucite grains in the host rock matrix (Fig. 4.6). The reaction zone has a sharp boundary with the matrix on the millimeter- (Fig. 4.3A) to nanometer scale (Fig. 4.6A) with preservation of the mesh textures (Fig. 4.3A).

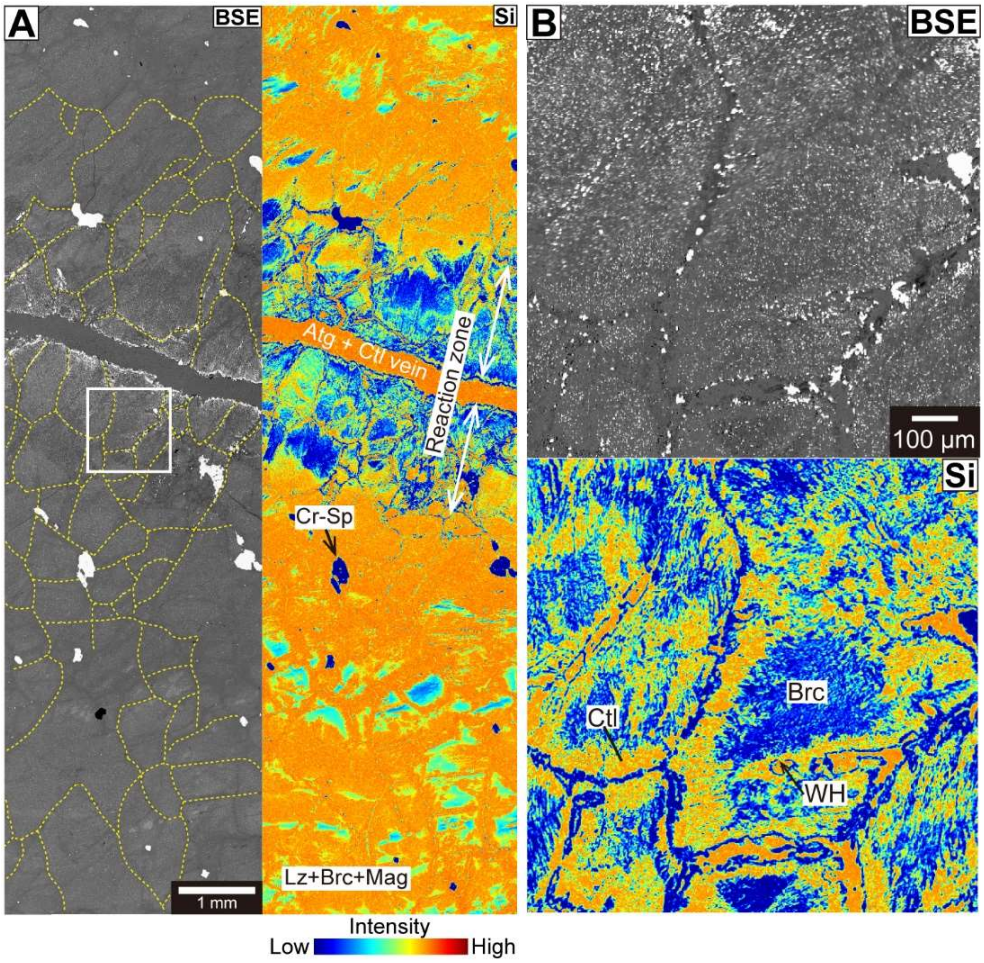

Fig. 4.3. Microstructure of the reaction zone and antigorite-chrysotile vein in a dunite sample (90Z2). (A) Back-scattered electron (BSE) image and Si elemental map of the brucite-rich reaction zone. The yellow dotted lines represent the boundaries of mesh domains. (B) BSE image and Si elemental map of the region indicated by the white box in (A). The reaction zone has a brucite mesh core and chrysotile mesh rim.

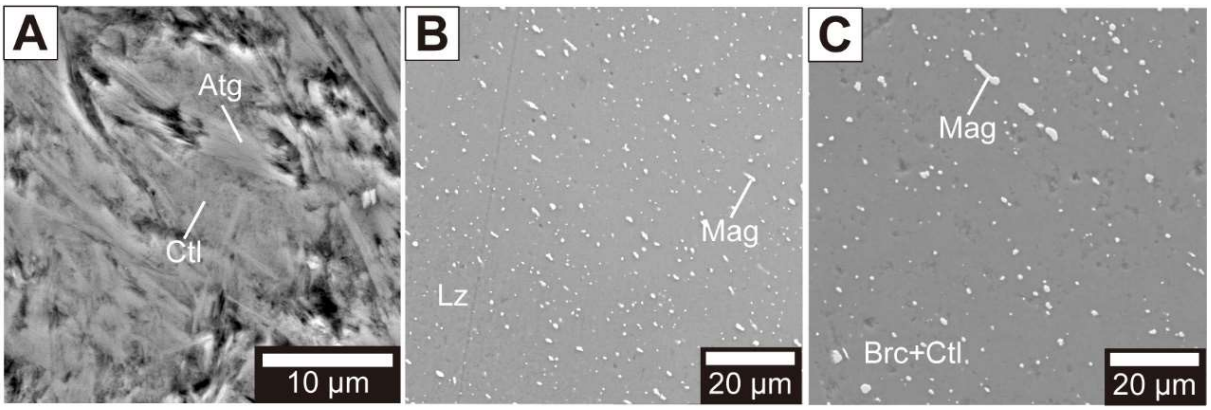

Fig. 4.4. SEM images of the (A) antigorite±chrysotile vein, (B) host rock matrix, and (C) brucite-rich reaction zone..

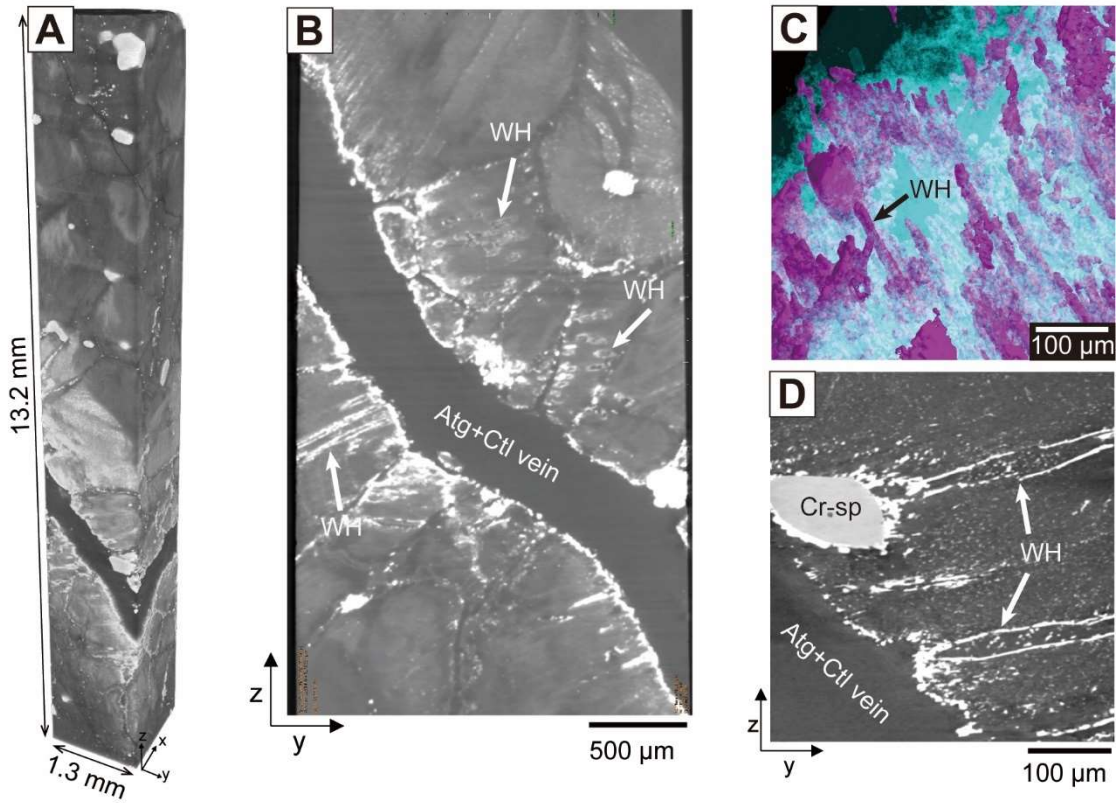

Fig. 4.5. (A) Micro-focused X-ray CT image of the antigorite vein and surrounding rock. (B) Image of the Z–Y cross-section. (C) Three-dimensional structure of the wormhole. (D) Close up view of the Z-Y cross-section focus on the wormholes. White arrows indicate wormholes, which are 60 μm in diameter and connected to the antigorite-chrysotile vein. Atg = antigorite, Ctl = chrysotile, WH = wormhole.

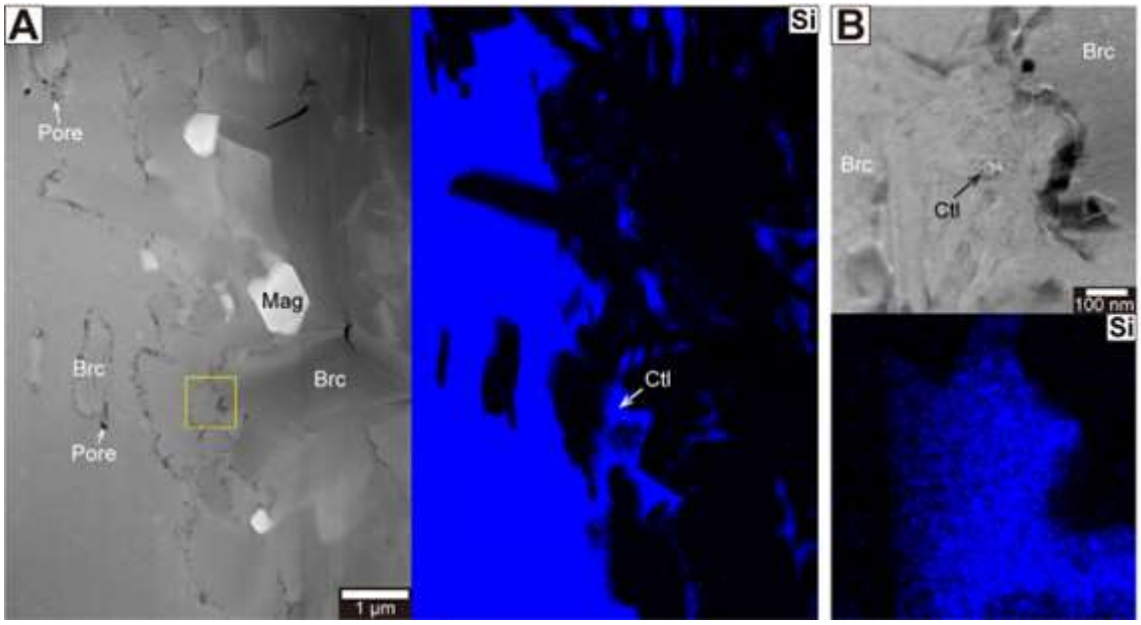

Fig. 4.6. TEM image at the boundary of host rock and brucite-rich reaction zone. (A) Wide view of TEM image and EDX Si-map of the reaction front. (B) Close up view of the region indicated by the yellow box in (A). Brc = brucite; Ctl = chrysotile; Mag = magnetite.

4.3.3. Measurement of the reaction zone widths from X-ray CT imaging

X-ray micro-computed tomography showed high X-ray CT absorption in the reaction zone. The width of the reaction zone was determined by image processing using ImageJ software (Schneider, Rasband, and Eliceiri 2012). A Euclid distance map represents the distance to the nearest background pixel as a value for each pixel. Thus, the pixel near the center of the reaction zone has a value equal to the width of the reaction zone. The center pixel was obtained by a thinning process and the value of the pixel was used as the width of the reaction zone. The obtained width of brucite-rich reaction zones ranges from 0.5 to 1.3 mm (average = 0.88 mm; Fig. 4.7) and is independent of the distribution of wormholes.

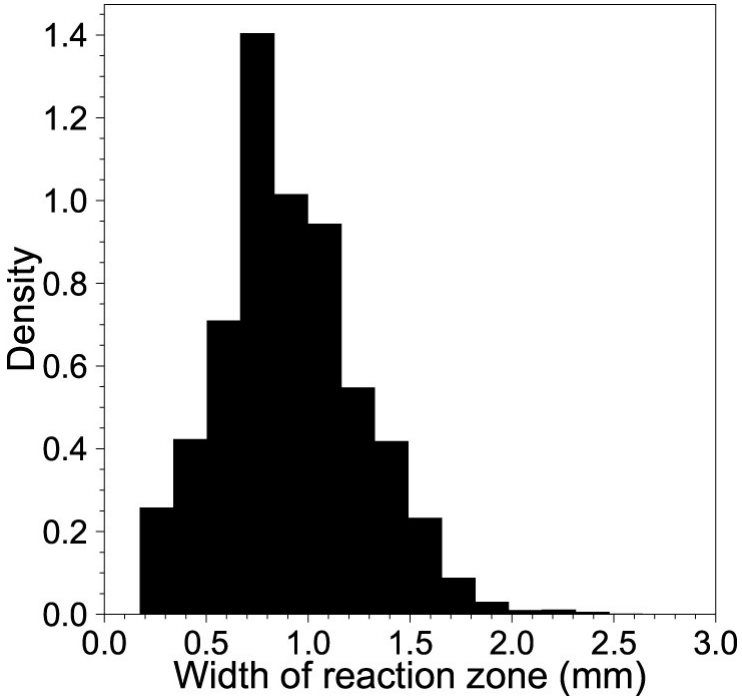

Fig. 4.7. Histgram of the reaction zone width in CM1A-90Z2-48-53.

4.3.4. Estimation of porosity in the reaction zone

TEM image analysis indicates that the porosity of the host rock is approximately 3%, which is consistent with the reported porosity (2.54 ± 1.51%; Katayama et al. 2020; Kelemen et al. 2020) for serpentinized dunite in the Oman ophiolite. The porosity in the reaction zone was estimated based on two types of microstructural observations. TEM observation of the brucite-rich reaction zone near the reaction front showed that aggregates of needle-like chrysotile crystals were formed in the spaces between the brucite crystals (Fig. 4.6). This indicates that chrysotile crystals precipitated from the solution into the interstices. If the chrysotile present in the reaction zone was a void at the time of reaction zone formation, the TEM image analysis indicates a porosity of ~10% in the reaction zone. The

mesh rims in the brucite-rich reaction zone are preferentially replaced by chrysotile (Fig. 4.3B), indicating that brucite reacted with silica-rich fluids to form chrysotile, as follows:

$$Mg(OH)_2 + 2SiO_{2,aq} = Mg_3Si_2O_5(OH)_4 + H_2O \quad (R4.1)$$

This is a volume-increasing reaction with V/V0 = 1.44. Using the V/V0 value and the modal abundance of chrysotile (55.3%; Fig. 4.8), as well as the preservation of the outline of the reticulate region within the reaction zone, the maximum porosity of the brucite reaction zone prior to chrysotile formation is 17%. Based on the porosity estimates for the two microstructures, the range of porosities is estimated between 10% and 17%. This value for the reaction zone is higher than that observed for the host rock matrix (~3%). The high porosity in the reaction zone is likely caused by porosity formed by mineral replacement reactions (Beaudoin *et al.*, 2018; Beinlich *et al.*, 2020; Plümper *et al.*, 2017; Putnis, 2002).

4.3.5. Mass balance calculation

To calculate the gain or loss of elements in the formation of the reaction zone, a mass balance calculation based on Gresens' equation (Gresens 1967) was conducted based on the modal abundance and chemical composition of the minerals. In Gresens' equation, mass transfer is calculated by assuming volume and bulk composition before and after alteration. The bulk compositions of the reaction zone and host rock matrix were determined from the mineral phase map based on EPMA elemental maps (Fig. 4.8). The mineral chemistry of each mineral is based on EPMA data for each mineral. Some assumptions were made in the calculation of the mineral mode of the reaction zone. Chrysotile was observed along the mesh rims of the reaction zone (Fig. 4.3B), suggesting that brucite (Tutolo et al. 2018) silicified after the formation of the reaction zone (Fig. 4.3). Therefore, the volume of chrysotile was recalculated as the volume of brucite, assuming that the reaction zone consisted only of brucite and magnetite (Reaction R4.1).

The reaction zone and host rock matrix contain fine-grained magnetite (~1 μm), but it is difficult to identify these minerals in the EPMA maps (c.f. probe diameter = ~1-2 μm). Therefore, the amount of fine-grained magnetite was determined from backscattered electron images (Fig. 4.4B; matrix = 2.0 area%, Fig. 4.4C; reaction zone = 1.8 area%). Therefore, the reaction zone was assumed to consist of 97.0 area percent brucite [$Mg_{0.88}Fe_{0.12}(OH)_2$] and 3.0 area percent magnetite. The mineral mode of the host rock matrix is determined to be 97.5 area percent lizardite [$Mg_{1.9}FeSi_{0.1}O_5(OH)_2$], 0.5 area percent brucite [$Mg_{0.85}Fe_{0.15}(OH)_2$], and 2.0 area percent magnetite. The mineral phase map (Fig. 4.8) based on elemental maps of Si, Mg, Fe, and Cr was generated using XMapTools (Lanari et al. 2014).

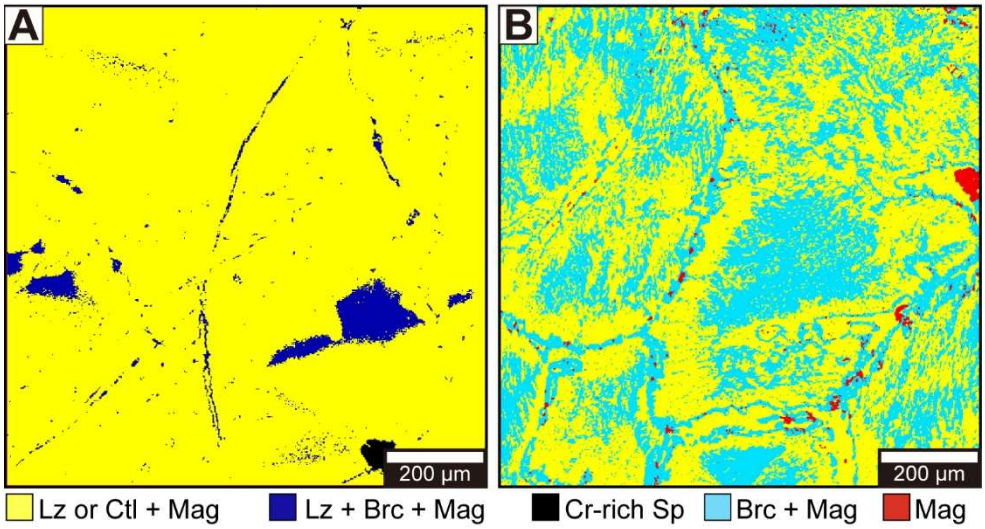

Fig. 4.8. Mineral phase map obtained with XMapTools. (A) The matrix consists of lizardite + magnetite (94.5 area %), brucite + lizardite + magnetite (3.8 area %), and Cr-rich spinel (0.4 area %). (B) The reaction zone consists of chrysotile + magnetite (56.3 area %), brucite + magnetite (41.8 area %), and magnetite (1.2 area %). Lz = lizardite, Ctl = chrysotile, Mag = magnetite, Brc = brucite, Sp = spinel.

The mass balance was calculated using the Gresens equation (Gresens 1967):

$$f_{\mathrm{v}}\left(\frac{\rho_{\mathrm{RZ}}}{\rho_{\mathrm{Wall\ rock}}}\right)c_{\mathrm{n}}^{\mathrm{RZ}} - c_{\mathrm{n}}^{\mathrm{Wall\ rock}} = x_{\mathrm{n}}, \tag{4.1}$$

where, f_{v} is the volume factor, and ρ_{RZ} and ρ_{Matrix} are the average density of the reaction zone and matrix, respectively, as follows:

$$\rho_{\mathrm{Matrix}} = \frac{A_{\mathrm{Lz}}\rho_{\mathrm{Lz}} + A_{\mathrm{Brc}}\rho_{\mathrm{Brc}} + A_{\mathrm{Mag}}\rho_{\mathrm{Mag}}}{A_{\mathrm{Lz}} + A_{\mathrm{Brc}} + A_{\mathrm{Mag}}}, \tag{4.2}$$

$$\rho_{\mathrm{RZ}} = \frac{A_{\mathrm{Brc}}\rho_{\mathrm{Brc}} + A_{\mathrm{Mag}}\rho_{\mathrm{Mag}}}{A_{\mathrm{Brc}} + A_{\mathrm{Mag}}}, \tag{4.3}$$

where, $c_{\mathrm{n}}^{\mathrm{RZ}}$ and $c_{\mathrm{n}}^{\mathrm{Matrix}}$ are the weight fractions of component *n* in the reaction zone and matrix, respectively, and x_{n} is the gain or loss for each component. The bulk rock composition used to calculate the mass balance is shown in Table 4.2.

$$c_{\mathrm{n}}^{\mathrm{Matrix}} = \frac{A_{\mathrm{Lz}}\rho_{\mathrm{Lz}}c_{\mathrm{Lz}}^{\mathrm{n}} + A_{\mathrm{Brc}}\rho_{\mathrm{Brc}}c_{\mathrm{Brc}}^{\mathrm{n}} + A_{\mathrm{Mag}}\rho_{\mathrm{Mag}}c_{\mathrm{Mag}}^{\mathrm{n}}}{\sum\left(A_{\mathrm{Lz}}\rho_{\mathrm{Lz}}c_{\mathrm{Lz}}^{\mathrm{n}} + A_{\mathrm{Brc}}\rho_{\mathrm{Brc}}c_{\mathrm{Brc}}^{\mathrm{n}} + A_{\mathrm{Mag}}\rho_{\mathrm{Mag}}c_{\mathrm{Mag}}^{\mathrm{n}}\right)}, \tag{4.4}$$

$$c_{\mathrm{n}}^{\mathrm{RZ}} = \frac{(A_{\mathrm{Brc}} - A_{\mathrm{Pore}})\rho_{\mathrm{Brc}}c_{\mathrm{Brc}}^{\mathrm{n}} + A_{\mathrm{Mag}}\rho_{\mathrm{Mag}}c_{\mathrm{Mag}}^{\mathrm{n}}}{\sum\left(A_{\mathrm{Brc}}\rho_{\mathrm{Brc}}c_{\mathrm{Brc}}^{\mathrm{n}} + A_{\mathrm{Mag}}\rho_{\mathrm{Mag}}c_{\mathrm{Mag}}^{\mathrm{n}}\right)}. \tag{4.5}$$

Table 4.2. Mineralogy, average density, and major element compositions of the reaction zone and matrix.

	Area %				Bulk composition (wt. %)				
	Lizardite	Brucite	Magnetite	Avg. density (g cm^{-3})	SiO_2	Fe_2O_3	MgO	FeO	H_2O
Matrix	97.5	0.5	2.0	2.6	41.0	2.7	40.3	3.5	12.4
RZ	0.0	97.0	3.0	2.5	0.0	4.3	53.5	15.0	27.2

Note: RZ = reaction zone.

Fig. 4.9 shows the gains and losses of each element during the formation of the brucite-rich reaction zone by replacement of the host rock matrix (lizardite + brucite + magnetite), calculated using the Gresens equation. MgO, FeO and H_2O increase with decreasing volume factor (f_v = ratio of solid volume to initial solid volume). On the other hand, since the product mineral (brucite) does not contain SiO_2 [c.f. chemical formula of brucite: $(Mg_x,Fe_{1-x})(OH)_2$], a significant amount of SiO_2 (40 g SiO_2/100 g host rock matrix) should be removed from the host rock matrix (Fig. 4.9). The estimated porosity of 10%–17% corresponds to f_v = 0.83–0.90, which is similar to the value obtained from minimizing the total mass transport (fv = 0.80; Fig. 4.9). Using fv = 0.87 (i.e., the mid-value of the range 0.83–0.90), the reaction that resulted in the development of the brucite reaction zone is as follows:

$$\begin{aligned} &Mg_{2.91}Fe_{0.09}Si_2O_5(OH)_4\ [\text{lizardite}] + 0.02Mg_{0.85}Fe_{0.15}(OH)_2\ [\text{brucite in host rock}] + 0.40MgO \\ &\quad + 0.35FeO + 1.76H_2O \\ &\quad = 3.78Mg_{0.88}Fe_{0.12}(OH)_2[\text{brucite in reaction zone}] + 0.02Fe_2O_3 + 2SiO_{2,aq} \end{aligned} \tag{R4.2}$$

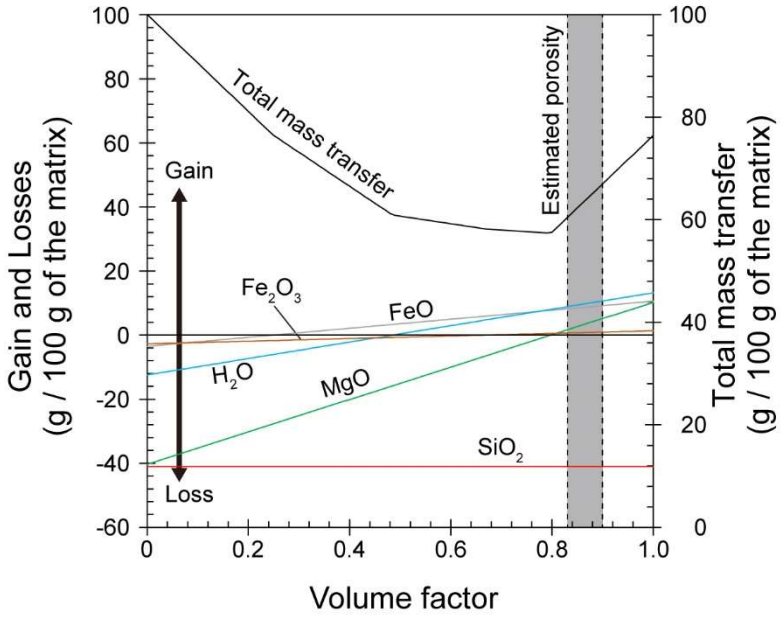

Fig. 4.9. Gains and losses of species per unit volume of rock due to volume changes. The total mass transfer was calculated from the sum of the absolute values for each species. The gray area indicates the porosity in the reaction zone, as inferred from microstructural observations.

4.4. Discussion

4.4.1. Formation conditions of antigorite-chrysotile vein

The conditions for the formation of antigorite + chrysotile veins were considered based on microstructural observations and thermodynamic calculations. Chrysotile occurs between the antigorite blades of the antigorite-chrysotile vein (Fig. 4.4A) and in the replacement of wormholes and mesh rims in the brucite-rich reaction zone (Fig. 4.3B). In addition, TEM observations of the reaction front of the brucite-rich reaction zone show that chrysotile crystals occur in the interstices between brucite crystals (Fig. 4.6). These phenomena suggest that chrysotile formation followed the formation of antigorite in the vein and reaction zone. Based on the natural occurrence of serpentine minerals, antigorite is thought to be more stable at high temperatures than lizardite (Evans 2004; Schwartz et al. 2013), which is consistent with the fact that antigorite formation has only been observed at high temperatures in many laboratory experiments (Wunder and Schreyer, 1997; Nakatani and Nakamura, 2016). Experimental studies of antigorite formation from olivine at low pressures (<0.5 GPa) are lacking, but thermodynamic data suggest that antigorite + brucite mineral assemblages would be stable at 300-450 °C and 0.1-0.5 GPa (Evans 2004). In addition, Infiltration of silica-rich fluids could induce crystallization of antigorite (Roumejion et al., 2019; Falk and Kelemen., 2015). Therefore, in order to consider the formation of antigorite, it is necessary to consider silica activity in addition to temperature and pressure.

When considering the precipitation reaction of a mineral from a solution, the thermodynamically stable mineral that precipitates at a given temperature, pressure, and solution composition can be determined by calculating the reaction Gibbs energy ($\Delta_r G$). The precipitation reaction of the minerals commonly found in serpentinite: antigorite (Atg), lizardite (Lz), chrysotile (Ctl), talc (Tlc), brucite (Brc), and forsterite (Fo), can be written as follows:

$$48Mg^{2+} - 96H^{+} + 79H_2O + 34SiO_{2,aq} = Mg_{48}Si_{34}O_{85}(OH)_{62}\ [Atg] \quad (R4.3)$$

$$48Mg^{2+} - 96H^{+} + 80H_2O + 32SiO_{2,aq} = 16Mg_3Si_2O_5(OH)_4\ [Lz/Ctl] \quad (R4.4)$$

$$48Mg^{2+} - 96H^{+} + 64H_2O + 64SiO_{2,aq} = 16Mg_3Si_4O_{10}(OH)_2\ [Tlc] \quad (R4.5)$$

$$48Mg^{2+} - 96H^{+} + 96H_2O = 48Mg(OH)_2\ [Brc] \quad (R4.6)$$

$$48Mg^{2+} - 96H^{+} + 48H_2O + 24SiO_{2,aq} = 24Mg_2SiO_4\ [Fo] \quad (R4.7)$$

In each precipitation reaction, positive reaction occurs spontaneously when $\Delta_r G$ <0, and minerals are precipitated; minerals with the smallest $\Delta_r G$ are thermodynamically stable. Next, the change in $\Delta_r G$ in each precipitation reaction was calculated when Mg^{2+} and H^{+} in solution were constant and only the

composition of $SiO_{2,aq}$ was changed. The reaction quotient (Q) for the precipitation reaction of each mineral can be written as follows, assuming the activity of the solid and liquid to be unity (activity = 1).

$$Q_{\mathrm{Atg}} = \frac{1}{\left(a_{\mathrm{Mg^{2+}}}\right)^{48}\left(a_{\mathrm{H^{+}}}\right)^{-96}\left(a_{\mathrm{SiO_{2,aq}}}\right)^{34}} \tag{4.6}$$

$$Q_{\mathrm{Lz}} = \frac{1}{\left(a_{\mathrm{Mg^{2+}}}\right)^{48}\left(a_{\mathrm{H^{+}}}\right)^{-96}\left(a_{\mathrm{SiO_{2,aq}}}\right)^{32}} \tag{4.7}$$

$$Q_{\mathrm{Ctl}} = \frac{1}{\left(a_{\mathrm{Mg^{2+}}}\right)^{48}\left(a_{\mathrm{H^{+}}}\right)^{-96}\left(a_{\mathrm{SiO_{2,aq}}}\right)^{32}} \tag{4.8}$$

$$Q_{\mathrm{Tlc}} = \frac{1}{\left(a_{\mathrm{Mg^{2+}}}\right)^{48}\left(a_{\mathrm{H^{+}}}\right)^{-96}\left(a_{\mathrm{SiO_{2,aq}}}\right)^{64}} \tag{4.9}$$

$$Q_{\mathrm{Brc}} = \frac{1}{\left(a_{\mathrm{Mg^{2+}}}\right)^{48}\left(a_{\mathrm{H^{+}}}\right)^{-96}} \tag{4.10}$$

$$Q_{\mathrm{Fo}} = \frac{1}{\left(a_{\mathrm{Mg^{2+}}}\right)^{48}\left(a_{\mathrm{H^{+}}}\right)^{-96}\left(a_{\mathrm{SiO_{2,aq}}}\right)^{24}} \tag{4.11}$$

The reaction Gibbs energy for the each precipitation reaction is obtained from the each reaction quotient (Q) and the standard reaction Gibbs energy ($\Delta_r G^{\ominus}$) for each reaction as follows:

$$\Delta_r G = \Delta_r G^{\ominus} + RT\ln Q \tag{4.12}$$

Where, R is gas constant, T is temperature. In the reaction equilibrium conditions, since $\Delta_r G = 0$, the standard reaction Gibbs energy can be written using the equilibrium constant (K) as follows:

$$\Delta_r G^{\ominus} = -RT\ln K \tag{4.13}$$

The relationship between the reaction Gibbs energy and the solution composition are given by substituting Eq. 4.12 into Eq. 4.13 and substituting the reaction quotient for each mineral, as follows:

$$\Delta_r G_{\mathrm{Atg}} = -RT\ln K_1 - 34RT\ln\left(a_{\mathrm{SiO_{2,aq}}}\right) - 48RT\ln\left(\frac{a_{\mathrm{Mg^{2+}}}}{(a_{\mathrm{H^+}})^2}\right) \tag{4.14}$$

$$\Delta_r G_{\mathrm{Lz}} = -RT\ln K_2 - 32RT\ln\left(a_{\mathrm{SiO_{2,aq}}}\right) - 48RT\ln\left(\frac{a_{\mathrm{Mg^{2+}}}}{(a_{\mathrm{H^+}})^2}\right) \tag{4.15}$$

$$\Delta_r G_{\mathrm{Ctl}} = -RT\ln K_3 - 32RT\ln\left(a_{\mathrm{SiO_{2,aq}}}\right) - 48RT\ln\left(\frac{a_{\mathrm{Mg^{2+}}}}{(a_{\mathrm{H^+}})^2}\right) \tag{4.16}$$

$$\Delta_r G_{\mathrm{Tlc}} = -RT\ln K_4 - 64RT\ln\left(a_{\mathrm{SiO_{2,aq}}}\right) - 48RT\ln\left(\frac{a_{\mathrm{Mg^{2+}}}}{(a_{\mathrm{H^+}})^2}\right) \tag{4.17}$$

$$\Delta_r G_{\mathrm{Brc}} = -RT\ln K_5 - 48RT\ln\left(\frac{a_{\mathrm{Mg^{2+}}}}{(a_{\mathrm{H^+}})^2}\right) \tag{4.18}$$

$$\Delta_r G_{\mathrm{Fo}} = -RT\ln K_6 - 24RT\ln\left(a_{\mathrm{SiO_{2,aq}}}\right) - 48RT\ln\left(\frac{a_{\mathrm{Mg^{2+}}}}{(a_{\mathrm{H^+}})^2}\right) \tag{4.19}$$

The phase diagram can be made by assuming that the mineral with the lowest reaction Gibbs energy is stable. Equilibrium constants at each temperature and pressure were calculated using SUPCRTBL software (Zimmer et al., 2016), which based on thermodynamic data set of Holland and Powell (2011). Fig. 4.10 is a stability phase diagram of temperature–silica activity at 200 MPa in the MgO–SiO_2–H_2O system. The diagram suggests that antigorite is stable at higher temperatures and silica activities than lizardite (Fig. 4.10), which is consistent with natural occurrences of antigorite at high temperatures (Evans 2004) or high silica activities even at low temperatures (Roumejion et al., 2019; Falk and Kelemen., 2015). Chrysotile does not appear in the phase diagram because it is metastable (Evans 2004).

Previous studies of abyssal serpentinites have shown that the occurrence of antigorite veins associated with talc indicates that antigorite crystallization is caused by infiltration of silica-rich fluids (Roumejion et al., 2019). However, it is unlikely that the antigorite+chrysotile veins are associated with brucite-rich reaction zones because brucite is only stable at low silica activities (i.e., several orders of magnitude lower than talc) (Fig. 4.10). Therefore, it is more likely that the relatively high temperature fluid (300-450°C) precipitated the antigorite into the fractures to form the brucite-rich reaction zones.

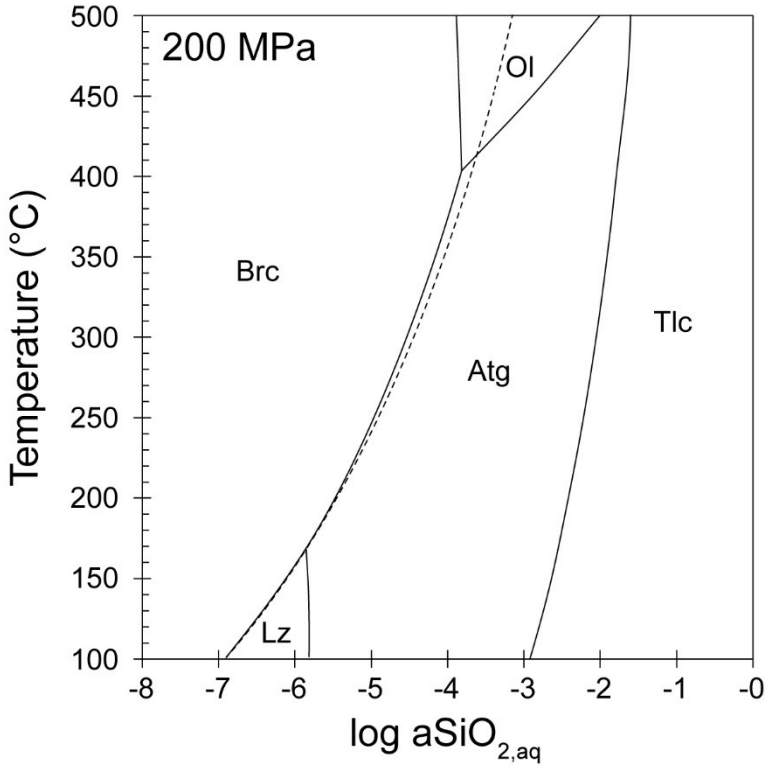

Fig. 4.10. $SiO_{2,aq}$ activity–temperature phase diagram of a MgO–SiO_2–H_2O system at 200 MPa. The dashed line shows the lizardite–brucite equilibrium.

4.4.2. Brucite-rich reaction zone formation

Mass balance calculations indicate that a significant amount of SiO_2 (40 g SiO_2/100 g of host rock) must be removed from the host rock matrix during the formation of the brucite-rich reaction zone via matrix replacement (Fig. 4.9). To understand the chemical driving force for the formation of the brucite-rich reaction zone, the chemical potential gradients were determined based on local equilibrium assumptions for the MgO-SiO_2-H_2O system under typical T-P conditions. For the Mg-fixed system, the antigorite-brucite (Atg-Brc) and lizardite-brucite (Lz-Brc) equilibrium are written as follows:

$$48\mathrm{Mg(OH)_2\ [brucite]} + 34\mathrm{SiO_{2,aq}} = \mathrm{Mg_{48}Si_{34}O_{85}(OH)_{62}[antigorite]} + 17\mathrm{H_2O} \quad \text{(R4.8)}$$

$$48\mathrm{Mg(OH)_2\ [brucite]} + 32\mathrm{SiO_{2,aq}} = 16\mathrm{Mg_3Si_2O_5(OH)_4[lizardite]} + 17\mathrm{H_2O} \quad \text{(R4.9)}$$

The reaction Gibbs free energy for each reaction is as follow:

$$\Delta_r G_{\mathrm{Atg-Brc}} = -RT\ln K_{R1} - 34RT\ln\left(a_{\mathrm{SiO_{2,aq}}}\right) \quad (4.20)$$

$$\Delta_r G_{\mathrm{Lz-Br}} = -RT\ln K_{R2} - 32RT\ln\left(a_{\mathrm{SiO_{2,aq}}}\right) \quad (4.21)$$

where, K_{R1} and K_{R2} are the equilibrium constant for Reaction R4.8 and R4.9, respectively. The equations 4.20 and 4.21 show that antigorite is steeper than lizardite in the Gibbs free energy versus silica activity plot (Fig. 4.11). This relationship depends only on the coefficient of $RT\ln\left(a_{\mathrm{SiO_{2,aq}}}\right)$ for antigorite (-34) and lizardite (-32), respectively. This topological relationship is a result of the difference in the chemical formulas of lizardite and antigorite. This difference results in different values of $RT\ln\left(a_{\mathrm{SiO_{2,aq}}}\right)$ for antigorite and lizardite, which in turn results in different chemical potentials. The silica activity at each equilibrium ($\Delta_r G = 0$) is obtained as follows:

$$\ln\left(a_{\mathrm{SiO_{2,aq}}}\right) = -\frac{K_{R1}}{34} \tag{4.22}$$

$$\ln\left(a_{\mathrm{SiO_{2,aq}}}\right) = -\frac{K_{R1}}{32} \tag{4.23}$$

At low temperature (c.f. 100°C), when lizardite is stable, the silica activity at the lizardite-brucite equilibrium [$\log\left(a_{\mathrm{SiO_{2,aq}}}\right)$=-7.05] is higher than at the Atg-Brc equilibrium [$\log\left(a_{\mathrm{SiO_{2,aq}}}\right)$=-7.00] (Fig. 4.11C). On the other hand, at high temperature (c.f. 350 °C), when antigorite is stable, silica activity at the reaction front [lizardite-brucite equilibrium; $\log\left(a_{\mathrm{SiO_{2,aq}}}\right)$=-4.02] is higher than at the vein wall (antigorite-brucite equilibrium; $\log\left(a_{\mathrm{SiO_{2,aq}}}\right)$=-4.11) (Fig. 4.11D). The difference in silica concentration between the host rock (lizardite-brucite equilibrium) and the antigorite vein wall (antigorite-brucite equilibrium) can cause aqueous silica diffusion, forming a silica-depleted brucite-rich reaction zone. This concentration difference, assuming an ideal solution (activity = concentration), can be written as follow:

$$\Delta C_{\mathrm{SiO_{2,aq}}} = 10^{-\frac{K_{R1}}{32}} - 10^{-\frac{K_{R1}}{34}} \tag{4.24}$$

These results indicate that antigorite-brucite is stable only when infiltrated by high temperature fluid (c.f. 350 °C; Fig. 4.12).

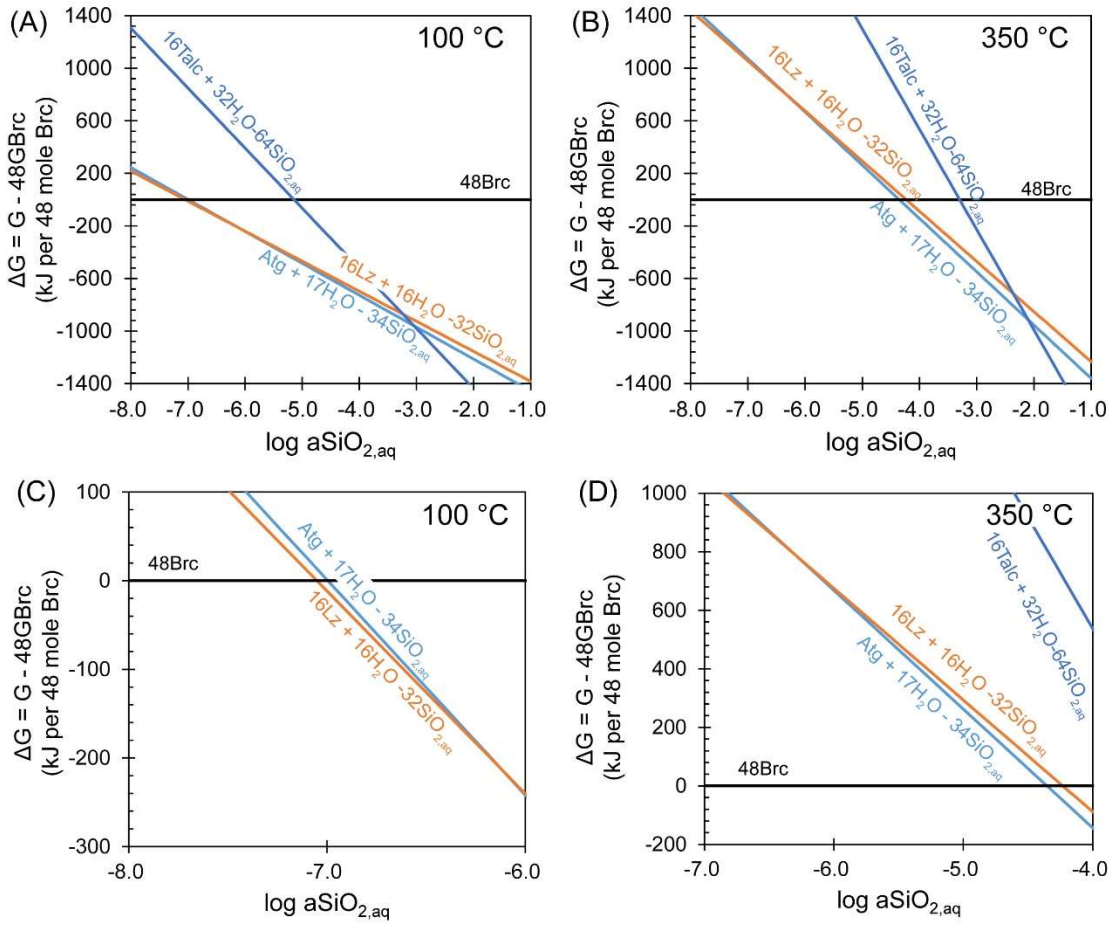

Fig. 4.11. Gibbs free energy (kJ / 48 mol brucite) versus silica activity at 1 kbar at (A) 350 °C and (B) 100 °C. (C-D)Close-up of the plot at 350 °C (C) and 100 °C (D).

Based on microstructural observations and thermodynamic considerations, antigorite+chrysotile veins with brucite-rich reaction zones may have formed as follows: (1) Fractures are formed that provide a fluid pathway (Fig. 4.12A). (2) Silica-poor, high-temperature fluid (c.f. 350 °C) penetrates along the fracture, precipitating antigorite in the fracture and forming a brucite-rich reaction zones (Fig. 4.12B). (3) The later stage fluid dissolves the brucite and forms wormholes in the brucite reaction zone (Fig. 4.12C). (4) Brucite-rich reaction zone is partly replaced by chrysotile (Fig. 4.12D).

The formation of the brucite-rich reaction zone required the removal of silica, while other elements were relatively immobile during the reaction zone formation (Fig. 4.9). This elemental mobilization is in contrast to most reaction zones in metamorphic rocks, which are caused by the addition of elements from fluids (e.g., Cl (Mindaleva *et al.*, 2020), CO_2 (Beinlich *et al.*, 2020; Okamoto *et al.*, 2021)). The formation of reaction zones due to element removal has been reported in rock zones associated with quartz (Fisher and Brantley, 2014) and quartz + kyanite veins (Ague, 2011) and is attributed to the low solubility of quartz in open fractures. In the case of this study, the silica activity gradient was caused by the serpentine-brucite equilibrium. The silica mobilization and pseudo-

replacement of the host rock mesh textures (Fig. 4.3B) suggest that prior to chrysotile precipitation in reaction-induced pore spaces (Fig. 4.6) or replacement of brucite by chrysotile (Fig. 4.3B), the high porosity (~10% to 17%) suggests that the development of the long-term presence of such pores along fractures may also affect the Vp/Vs anisotropy within the mantle wedge (Kuster and Toksöz, 1974).

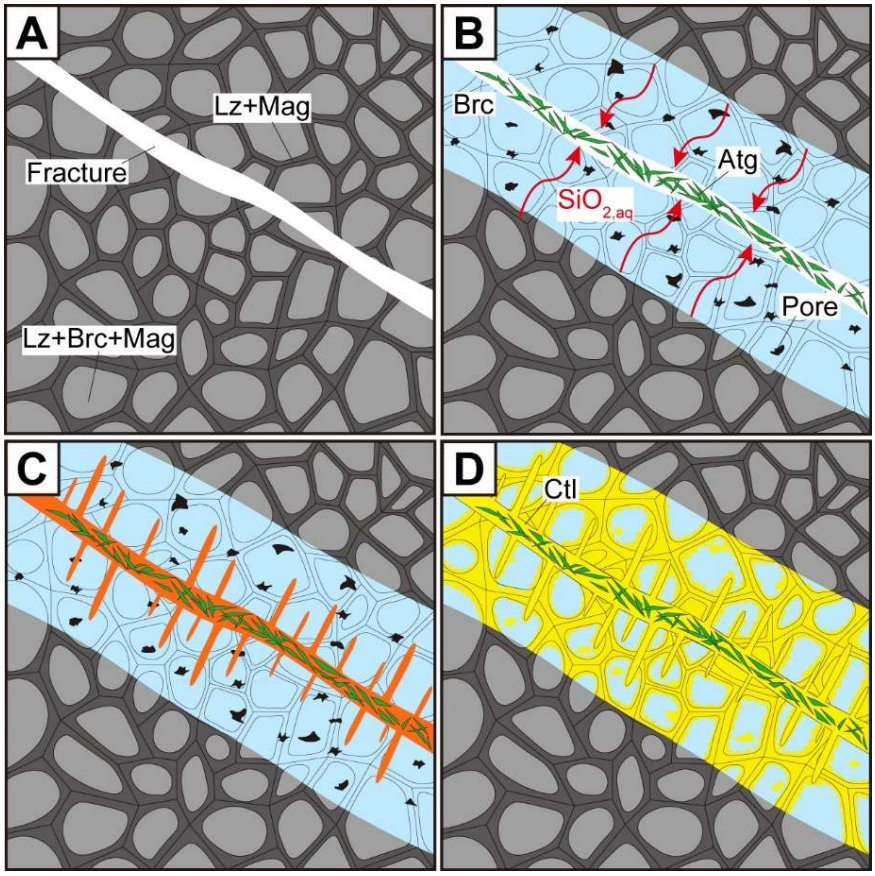

Fig. 4.12. Schematic model for reaction zone formation. The brucite reaction zone (blue) forms during antigorite crystallization. Brucite is rapidly dissolved by later fluid infiltration (orange) to form the wormhole texture. Brucite is partly silicified along the mesh texture and converted to chrysotile (yellow). Atg = antigorite; Lz = lizardite; Ctl = chrysotile; Brc = brucite; Tlc = talc; Fo = forsterite; Mag = magnetite; WH = wormhole.

4.4.3. Time scale and fluid flow velocity for the reaction zone formation

The time-integrated fluid flux, duration, and fluid velocity along the fractures can be constrained by the presence of the brucite-rich reaction zones. The mass balance calculation and thermodynamic relationship suggest that silica was removed to form these reaction zones. Assuming that the silica concentration at the vein wall was zero, a minimum duration of reaction zone formation can be obtained. Alternatively, the fracture is filled with antigorite. Hence, the silica concentration at Atg-Brc equilibrium is assumed to be the maximum silica concentration at the vein wall.

Time scale for the reaction zone formation

The sharp reaction front of the brucite reaction zone (Figs. 4.3A and 4.6, and Fig.2.27 in Chapter 2) suggests that the migration of the front is rate limited by diffusive transport rather than surface reaction (Lichtner, 1988). The diffusive flux of silica ($Q_{\mathrm{SiO_{2,aq}}}$ [mol m^{-2} s^{-1}]) from the reaction zone is given by:

$$Q_{\mathrm{SiO_{2,aq}}} = D_{\mathrm{SiO_{2,aq}}}\varphi_{\mathrm{RZ}}\frac{dC_{\mathrm{SiO_{2,aq}}}}{dx} \approx D_{\mathrm{SiO2,aq}}\varphi_{\mathrm{RZ}}\frac{\left(C_{\mathrm{SiO_{2,aq}}}^{\text{Reaction front}} - C_{\mathrm{SiO_{2,aq}}}^{\text{Vein wall}}\right)\rho_{\mathrm{w}}}{x}, \tag{4.25}$$

where $D_{\mathrm{SiO_{2,aq}}}$ (m^2 s^{-1}) is the diffusion coefficient of silica in water; $C_{\mathrm{SiO_{2,aq}}}^{\text{Reaction front}}$ and $C_{\mathrm{SiO_{2,aq}}}^{\text{Vein wall}}$ (mol kg^{-1}$_{\text{(water)}}$) are the silica concentrations at the reaction front and vein wall, respectively. ρ_{RZ} and ρ_{w} are the densities of the reaction zone and water, respectively; x is the distance from the reaction front to the fluid; and φ_{RZ} is the porosity of the reaction zone. The migration rate of the reaction zone is given by

$$\frac{dx}{dt} = \frac{Q_{\mathrm{SiO_{2,aq}}}}{n_{RZ}}, \tag{4.26}$$

where t (s) is the time and n_{RZ} (mol m^{-3}$_{\text{(RZ)}}$) is the number of moles of $SiO_{2,aq}$ that are produced to form a reaction zone with a volume of 1 m^3. Combining Eqs. 4.25 and 4.26, the time scale to form a reaction zone with a width of w_{RZ} can be written as follows:

$$t_{RZ} = \frac{1}{2}\frac{n_{\mathrm{RZ}}}{D_{\mathrm{SiO_{2,aq}}}\varphi_{\mathrm{RZ}}\left(C_{\mathrm{SiO_{2,aq}}}^{\text{Reaction front}} - C_{\mathrm{SiO_{2,aq}}}^{\text{Vein wall}}\right)\rho_{\mathrm{w}}}{w_{\mathrm{RZ}}}^2. \tag{4.27}$$

$D_{\mathrm{SiO2,aq}}$ was set to 2.5 × 10^{-8} m^2 s^{-1}, considering that the diffusivity for aqueous ionic species at 350°C and 100–300 MPa varies from 1 × 10^{-8} to 5 × 10^{-8} m^2 s^{-1} (Oelkers and Helgeson, 1988). The width of reaction zone (w_{RZ}) is set to the observed width of the brucite-rich reaction zones (0.5–1.3 mm; Fig. 4.7) and φ_{RZ} to 10-17%. All parameters used in the calculation shown in Table 4.3.

Using the diffusion-controlled transport model for aqueous silica, a maximum duration of reaction zone formation (t_{RZ}) is obtained of 2.1 × 10^{-1} to 1.1 × 10^{1} yr. The time scale is a maximum estimate because increasing advective transport would enhance the migration rate of the reaction front. Even though advection was neglected, this time scale is shorter than those estimated for vein formation in eclogites (~200 yr (John *et al.*, 2012)) and carbonation reactions related to ophiolite emplacement (~20 yr (Beinlich *et al.*, 2020)).

Table 4.3. Parameters used in the calculations for formation time of the reaction zone (tRZ), time-integrated fluid flux (Q_{TI}), and fluid velocity (v).

Parameter	Description	Value		Units
n_{RZ}	Number of moles of $SiO_{2,aq}$ that are produced to form a reaction zone with a volume of 1 m^3	1.8E+04		mol $m^{-3}_{(RZ)}$
n_{Atg}	Number of moles of $SiO_{2,aq}$ that are consumed to form antigorite with a volume of 1 m^4	1.9E+04		mol $m^{-3}_{(Atg)}$
$D_{SiO2,aq}$	Diffusion coefficient of silica in water	2.5E-08		$m^2\ s^{-1}$
Φ_{RZ}	Porosity in the reaction zone	0.10	- 0.17	
$C^{Reaction\ front}_{SiO2,aq}$	Silica concentration at the reaction front	9.5E-05		mol kg^{-1}(water)
$C^{Vein\ wall}_{SiO2,aq}$	Silica concentration at the vein wall	0.0	- 7.4E-05	mol kg^{-1}(water)
ρ_{RZ}	Density of the reaction zone	2400		kg m^{-3}
ρ_{Atg}	Density of antigorite	2550		kg m^{-3}
ρ_W	Density of water (200MPa, 350°C)	840		kg m^{-3}
w_{RZ}	Width of the reaction zones	5.0E-04	- 1.3E-03	m
w_F	Width of the fracture	4.0E-04	- 5.0E-04	m

Fluid flow velocity

A unit volume (1 × 1 × 1 m) of host rock with a single fracture and reaction zones on both sides of the fracture is considered to determine the fluid flow velocity. The total amount of fluid flow that passes across an area of the fracture (Q_{TI}; $m^3_{(water)}$) is approximately as follows:

$$Q_{\mathrm{TI}} \approx \frac{\xi_{\mathrm{RZ}} n_{\mathrm{RZ}} - \xi_{\mathrm{vein}} n_{\mathrm{Atg}}}{C^{\mathrm{Vein\ wall}}_{\mathrm{SiO_{2,aq}}} \rho_{\mathrm{w}}}, \tag{4.28}$$

where ξ_{RZ} (= $2w_{RZ}$/unit length) and ξ_F (= w_F/unit length) are the volume fractions of the reaction zone and fracture. The numerator represents the amount of silica that must be transported by the fluid (7.7–37.3 moles). The calculated total amount of fluid flow is 1.0×10^2 – 4.8×10^2 m^2. The average fluid flow velocity v (m s^{-1}) is given by the cross-sectional area of the fracture (A_F = w_F×unit length) and duration of the fluid flow (t_{RZ}), $v = Q_{TI}/(A_F t_{RZ})$.

Assuming that the silica concentration of the fluid in the fracture was zero, flow velocity, v, of 2.7×10^{-3} to 4.9×10^{-2} m s^{-1} is obtained. This velocity along the fractures in the mantle wedge is lower than that estimated for fluid flow related to earthquakes in the crust (~10^{-1} – 10^1 m s^{-1} (Cox and Munroe, 2016; Oliver *et al.*, 2006)), but similar to that estimated for tensile quartz veins in high-pressure metamorphic rocks in ancient subduction zones (~10^{-2}–10^{-1} m s^{-1} (Okamoto and Tsuchiya, 2009)).

The drill core from Hole CM1A contains abundant vein networks in the mantle, crust-mantle transition zone, and lower crust. The antigorite–chrysotile veins occur mainly at depths of 160–180 m in Hole CM1A, where intense fault zones are commonly developed (Fig. 4.2), suggesting that these vein networks formed in association with faulting events. The occurrence of antigorite–chrysotile veins and their trace element compositions (Figs. 2.47 and 2.48 in Chapter 2) indicate that infiltration of slab-derived fluids occurs in supra-subduction zones. The absence of banded texture (Tarling *et al.*, 2021) in the antigorite-chrysotile veins suggests that each vein resulted from a single fluid flow event. Additionally, it indicates that an open fracture persisted until mineral precipitation filled the fracture (Fisher *et al.*, 2021). This fluid could have been at higher temperatures (Atg–Brc equilibrium) than the

host rock in which Lz–Brc was stable, although the precise temperature difference is not clear. Similar antigorite vein networks have been reported in several ophiolites in supra-subduction settings (Carter *et al.*, 2021; Dandar *et al.*, 2021; Ulrich *et al.*, 2020), suggesting that channelized fluid flow along fracture networks is common in supra-subduction zones. In general, while it seems that each individual vein was created by a single fluid flow event, the fact that the antigorite-chrysotile veins intersect each other (Fig. 2.22) indicates that multiple fracturing and fluid flow events occurred to create the entire vein network.

4.4.4. Comparison with fluid flow velocities of geological and geophysical processes

The velocity of the fluid through the serpentinite in the subduction zone, calculated from the permeability, is ~10^{-9} m s^{-1} (Kawano *et al.*, 2011), which is several orders of magnitude slower than the velocity of fluid movement obtained here. It is also slower than the velocity of fluid moving through the fracture zone of the fault. On the other hand, it is similar to the velocity of fluid flowing through a crack in a subduction zone (Okamoto and Tsuchiya, 2009).

Subduction zone seismicity is closely linked to pore fluid pressure (Audet *et al.*, 2009; Kodaira *et al.*, 2004; Saffer and Tobin, 2011). The migration of epicenters and slip events above the subduction plate boundary has been observed in several subduction zones, such as Nankai and Cascadia (Dragert *et al.*, 2004; Halpaap *et al.*, 2019; Kostoglodov *et al.*, 2003; Nakajima and Uchida, 2018; Nippress and Rietbrock, 2007). The epicenters move relatively slowly (~10^{-4} to 10^{-3} m s^{-1} (Dragert *et al.*, 2004; Nakajima and Uchida, 2018; Nippress and Rietbrock, 2007)) as compared with the rupture velocity during major earthquakes (~10^{3} m s^{-1} (Rowe and Griffith, 2015)). The migration of epicenters has been observed at the depth of forearc mantle and is thought to represent fluid injection into the mantle wedge (Halpaap *et al.*, 2019; Nakajima and Uchida, 2018; Nippress and Rietbrock, 2007), which possibly lowers the pore fluid pressure at the subduction zone megathrust. I compared geophysical observations in the subduction zones with the estimate of the timescale and fluid flow velocity (Fig. 4.13). Interestingly, the estimate of the timescale of reaction zone formation (2.1×10^{-1} to 1.1×10^{1} yr) is close to the seismically observed timescale of fluid activity inferred from supra-slab seismicity (~10^{-1} yr (Nakajima and Uchida, 2018; Nippress and Rietbrock, 2007)), silent earthquakes (silent EQ, 10^{-1} to 10^{0} yr (Kostoglodov *et al.*, 2003; Ozawa *et al.*, 2002)), and slow slip events (SSEs, 10^{-3} to 10^{-1} yr (Hirose and Obara, 2005)). In addition, the fluid velocity estimated for the antigorite–chrysotile veins (2.7×10^{-3} to 4.9×10^{-2} m s^{-1}) of the present study is similar to the observed propagation velocities of episodic tremor and slip (ETS, ~10^{-1} m s^{-1} (Dragert *et al.*, 2004; Obara, 2002)), long-term SSE (~10^{-3} to 10^{-2} m s^{-1} (Hirose and Obara, 2005)), and silent EQ (~10^{-3} to 10^{-2} m s^{-1} (Kostoglodov *et al.*, 2003; Ozawa *et al.*, 2002)). The comparison of the geological evidence with geophysical observations suggests that, in contrast to the continuous nature of fluid supply from the subducting slab (Fig. 4.14A), some of the fluid drainage into the overlying plate occurs as transient pulses, possibly related to the migration of micro-seismicity (Fig. 4.14B). Such episodic fluid drainage causes rapid water–rock interactions within the mantle wedge. Moreover, we suggest that large, short-lived fluid fluxes through the mantle wedge can result in a decrease in pore fluid pressure, thereby influencing seismicity at a plate boundary.

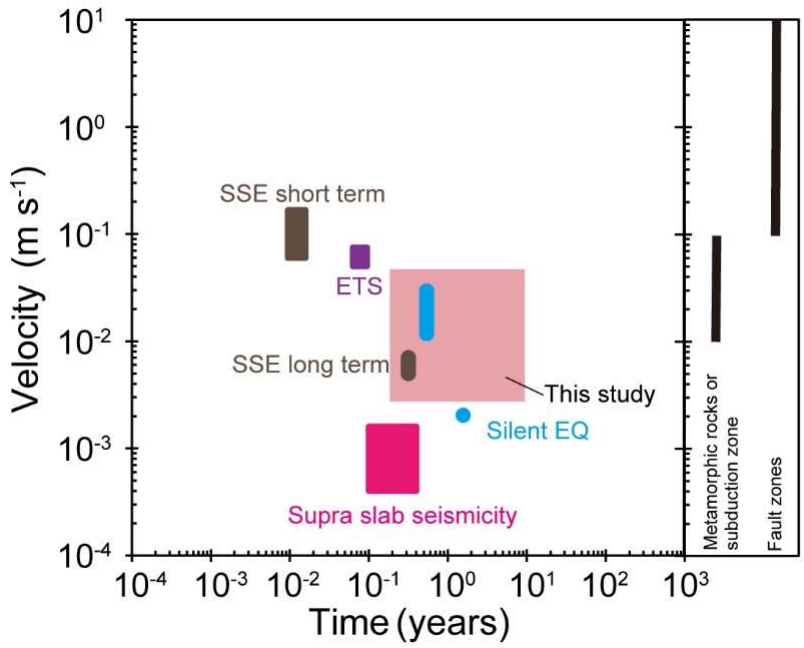

Fig. 4.13. Comparison of the characteristic velocities of propagation of seismic events and fluid flow estimated by petrological observations. The plot shows velocities and timescale of fluid flow for data obtained in this study (highlighted in red), as compared with the propagation velocities of slow slip events (SSEs) (Hirose and Obara, 2005), episodic tremor and slip (ETS) (Dragert *et al.*, 2004), silent earthquake (EQ) (Kostoglodov *et al.*, 2003; Ozawa *et al.*, 2002), and supra-slab seismicity (Nakajima and Uchida, 2018; Nippress and Rietbrock, 2007). Fluid flow velocities in metamorphic rocks in ancient subduction zones (Okamoto and Tsuchiya, 2009), and fault zones (Cox and Munroe, 2016; Oliver *et al.*, 2006) estimated based on geological observation are shown on the right-hand side.

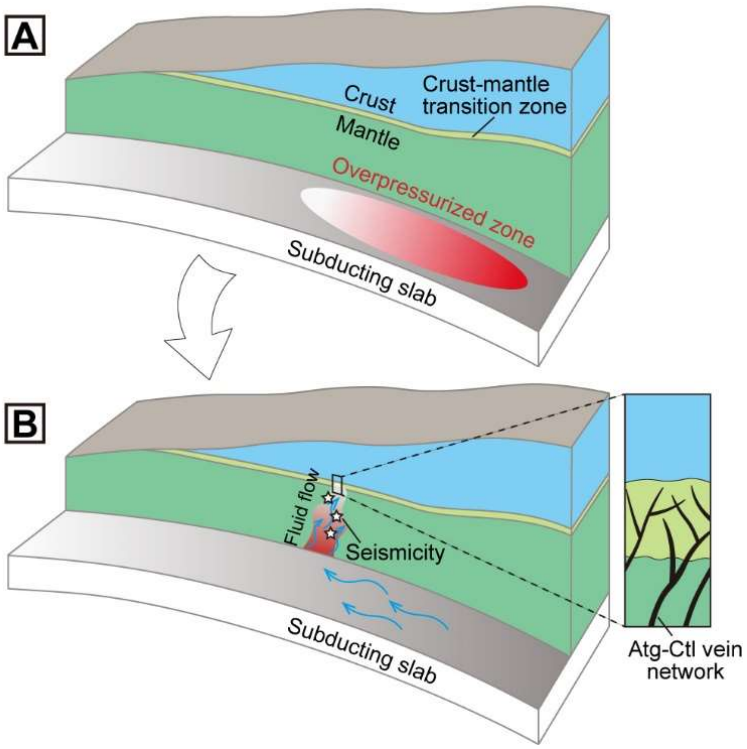

Fig. 4.14. Schematic model of subduction zone and a close-up view of the fracture zone. (A)Accumulation of fluids from subducting plate and buildup of pore fluid pressure. (B) Fluid flow through fracture network triggered by seismicity (white stars).

4.5. Summaries

In this chapter, I focused on serpentine (antigorite) veins and estimate the timing of their formation, the time scale, and the velocity of the fluid flow. Trace element analyses and thermodynamic calculations suggest that the antigorite veins were formed by subduction zone setting of high-temperature fluids after serpentinization of the main stage of lizardite. It is also clear that antigorite precipitation occurred within a short period of time, ranging from a few months to a few years. These results suggest that cracks that form in serpentinite are closed in a short period of time and that it is difficult to maintain high permeability. Therefore, for high permeability to be maintained continuously over a long period of time, such as the timescale of serpentinization progression, fractures must be periodically generated by events such as earthquakes.

Part of the content of the Chapter 2 has been published as the following publications:
Kazuki Yoshida, Ryosuke Oyanagi, Masao Kimura, Oliver Plümper, Mayuko Fukuyama, Atsushi Okamoto, “Geological recordsof transient fluid drainage into the shallow mantlewedge”, *Science Advances*, 9, 14, 2023, DOI:10.1126/sciadv.ade6674.

Chapter 5: Hydrogen production during serpentinization of the lower crust to upper mantle

5.1. Introduction

Hydrogen produced by serpentinization reactions plays an important role in a variety of geological processes, such as supporting diverse biological systems on the seafloor and controlling redox conditions in subduction zones (Debret *et al.*, 2014; Früh-Green *et al.*, 2004a; Kelley *et al.*, 2005). The hydrogen produced by serpentinization is an important energy source for the energy-poor deep subsurface microbiosphere due to the lack of sunlight and is attracting attention as a key to understanding the expansion of the deep subsurface biosphere and the survival mode of early life before photosynthesis. In the serpentinization reaction, a substantial amount of hydrogen is produced by reducing water as the divalent iron in the reaction minerals, such as olivine and pyroxene, is converted to trivalent iron in the product minerals, such as magnetite and serpentine. The conditions for magnetite formation are relatively well studied (Beard *et al.*, 2009; Frost *et al.*, 2013; Klein *et al.*, 2014; Schwarzenbach *et al.*, 2016). Hydrogen production in serpentinization is often discussed in terms of the redox state of iron and magnetite content of the bulk rock (Albers *et al.*, 2021; Evans, 2008). This is because local analysis of the redox state of iron is generally difficult. However, this method has difficulty in avoiding the influence of weathered minerals and may estimate a large amount of hydrogen production. The control on hydrogen production is the formation of magnetite and serpentine, which can contain Fe^{3+}. However, since bulk rock analysis cannot examine the redox state of each mineral separately, it is not well understood how much Fe^{3+} serpentine contains and what factors control the $Fe^{3+}/\Sigma Fe$ in serpentine. Andreani et al (2013) found that the redox state of serpentinite microstructures using μXANES revealed that $Fe^{3+}/\Sigma Fe$ in serpentine varies with W/R. On the other hand, the effect of silica activity is not well understood.

In Chapter 5, I conducted bulk rock and local chemical analyses including the iron redox state. Three type of rocks are analyzed: lower crustal gabbroic rocks, dunite at the crust-mantle boundary, and harzburgite in the upper mantle. The contribution of each mineral to the Fe content in the rocks was determined from chemical composition analysis of bulk rocks, thermogravimetric analysis, and chemical composition of minerals. Mapping of the redox state of iron in each mineral using synchrotron X-ray absorption fine structure spectroscopy (XANES) was performed to investigate the redox state of iron in each mineral and to determine the hydrogen production history recorded in the rock texture.

5.2. Sample and Methods

5.2.1. Samples

Total 75 samples from Oman Drilling Project CM sites (18 gabbroic rocks from CM1A, 10 dunites from CM1A, 10 dunite from CM2B, 9 harzburgites from CM1A, and 28 harzburgite from CM2B) were analyzed for investigating iron partition and redox state of iron during serpentinization (Tables 5.1-5.3). Details of the petrographic observations of these rocks are described in Chapter 2. EPMA and Raman spectroscopic microscopy were used for mineral identification and chemical composition analysis. Bulk-rock chemical composition and the amount of hydrous minerals were determined and quantified by WDX-XRF and TG.

Table 5.1. Sample list of gabbroic rock samples with total iron (wt. %) and loss on ignition (LOI) (wt. %).

Sample name	Lithology	Fe_2O_3* (wt%)	LOI (wt%)
CM1A-7Z1-43-45	gabbroic	13.92	7.77
CM1A-7Z2-38-42	gabbroic	12.47	7.82
CM1A-8Z2-10-14	gabbroic	9.50	6.68
CM1A-28Z1-85-88	gabbroic	5.25	4.59
CM1A-32Z1-53-55	gabbroic	16.42	5.76
CM1A-39Z1-84-88	gabbroic	3.84	1.88
CM1A-46Z1-34-39	gabbroic	3.26	1.98
CM1A-47Z2-62-67	gabbroic	6.42	4.66
CM1A-48Z3-10-15	gabbroic	6.73	7.25
CM1A-51Z2-72-77	gabbroic	5.83	8.35
CM1A-51Z4-72-77	gabbroic	4.50	5.73
CM1A-55Z1-76-81	gabbroic	13.81	5.09
CM1A-57Z3-12-17	gabbroic	20.22	9.47
CM1A-57Z3-43-48	gabbroic	9.17	7.51
CM1A-58Z1-50-54	gabbroic	8.33	7.11
CM1A-113Z3-25-30	gabbroic	3.67	1.88
CM1A-113Z4-11-16	gabbroic	3.95	6.48
CM1A-124Z1-40-48	gabbroic	4.25	4.95

*Fe calculated as Fe_2O_3

Table 5.2. Sample list of dunite samples with total iron (wt. %) and loss on ignition (LOI) (wt. %).

Sample name	Lithology	Fe_2O_3* (wt%)	LOI (wt%)	Titration
CM1A-70Z2-26-31	dunite	11.00	15.14	
CM1A-79Z3-6-9	dunite	11.07	14.76	○
CM1A-79Z3-40-45	dunite	12.77	14.28	
CM1A-80Z1-26-31	dunite	8.68	14.82	
CM1A-80Z4-24-29	dunite	9.00	15.03	
CM1A-89Z4-12-17	dunite	11.48	15.01	
CM1A-90Z2-48-53	dunite	9.48	15.83	
CM1A-137Z3-46-54	dunite	10.84	14.17	
CM1A-138Z2-18-26	dunite	9.39	14.03	
CM1A-142Z4-3-11	dunite	10.30	15.10	
CM2B-13Z3-7-12	dunite	9.58	15.64	
CM2B-15Z3-7-12	dunite	10.74	14.93	○
CM2B-15Z3-38-43	dunite	10.78	14.68	○
CM2B-16Z2-34-35	dunite	10.75	14.83	○
CM2B-24Z1-14-19	dunite	10.02	15.13	
CM2B-52Z3-16-21	dunite	14.97	14.42	○
CM2B-54Z1-29-34	dunite	10.05	14.62	
CM2B-56Z3-51-56	dunite	9.75	14.94	
CM2B-59Z4-11-16	dunite	10.36	16.21	○
CM2B-63Z3-37-42	dunite	11.60	15.97	○

*Fe calculated as Fe_2O_3

Table 5.3. Sample list of harzburgite samples with total iron (wt. %) and loss on ignition (LOI) (wt. %).

Sample name	Lithology	Fe_2O_3* (wt%)	LOI (wt%)	Titration
CM1A-107Z2-5-10	harzburgite	11.98	13.40	○
CM1A-144Z2-24-32	harzburgite	8.11	14.75	
CM1A-144Z4-60-68	harzburgite	8.83	10.91	○
CM1A-150Z1-24-32	harzburgite	7.90	15.50	
CM1A-160Z3-47-55	harzburgite	7.82	13.84	
CM1A-163Z1-12-20	harzburgite	8.57	13.00	
CM1A-170Z1-31-39	harzburgite	7.90	14.72	
CM1A-179Z2-30-38	harzburgite	7.74	13.49	
CM1A-179Z3-18-26	harzburgite	8.73	13.85	○
CM2B-68Z1-27-31	harzburgite	8.58	14.86	○
CM2B-73Z3-64-69	harzburgite	9.60	13.51	
CM2B-77Z4-70-75	harzburgite	8.62	11.26	○
CM2B-83Z2-8-13	harzburgite	8.42	12.47	
CM2B-86Z3-10-15	harzburgite	8.65	14.53	○
CM2B-90Z3-40-45	harzburgite	8.70	12.41	○
CM2B-90Z4-65-70	harzburgite	8.99	11.02	
CM2B-92Z4-35-40	harzburgite	8.89	11.59	
CM2B-92Z4-80-85	harzburgite	8.93	11.83	
CM2B-99Z2-68-73	harzburgite	8.89	10.95	○
CM2B-100Z2-15-20	harzburgite	8.75	10.71	
CM2B-100Z2-65-70	harzburgite	9.02	11.33	
CM2B-100Z2-80-85	harzburgite	9.35	12.39	○
CM2B-100Z2-85-90	harzburgite	8.24	12.89	
CM2B-104Z1-33-38	harzburgite	8.59	11.20	
CM2B-106Z2-16-21	harzburgite	7.80	15.18	○
CM2B-106Z3-16-21	harzburgite	8.18	13.56	
CM2B-106Z3-33-38	harzburgite	8.65	13.88	
CM2B-106Z3-45-50	harzburgite	8.72	13.05	
CM2B-110Z1-57-62	harzburgite	8.13	13.04	
CM2B-110Z1-62-67	harzburgite	8.10	13.53	
CM2B-112Z4-47-52	harzburgite	7.70	13.00	
CM2B-119Z1-34-39	harzburgite	8.86	13.04	
CM2B-119Z2-7-12	harzburgite	8.49	9.34	○
CM2B-119Z3-78-83	harzburgite	8.42	13.81	
CM2B-120Z3-8-13	harzburgite	8.22	13.79	
CM2B-120Z4-82-87	harzburgite	8.44	11.38	
CM2B-121Z4-55-60	harzburgite	10.73	13.71	

*Fe calculated as Fe_2O_3

5.2.2. Potassium dichromate titration

The mass fraction of ferrous iron (FeO) of 18 selected serpentinites were determined by potassium dichromate titration at the Palynosurvery Co. Ltd. (www.palyno.co.jp) (Table 5.2 and 5.3). The powdered samples were digested using a sulfuric acid and hydrofluoric acid mixture until no residue remained (Geological Survey of Japan, 1978). The mass fraction of ferric iron (Fe_2O_3) and molar ratio of ferric to total iron ($Fe^{3+}/\Sigma Fe$) was calculated from the $Fe_2O_3{}^*$ determined by WDX-XRF and FeO determined by the titration as following:

$$Fe_2O_3 = \frac{159.69}{2}\left(\frac{Fe_2O_3{}^*}{159.69} \times 2 - \frac{FeO}{71.84}\right) \cong Fe_2O_3{}^* - 1.11FeO\ (wt.\%), \quad (5.1)$$

$$Fe^{3+}/\Sigma Fe = \frac{2Fe_2O_3/159.69}{FeO/71.84 + 2Fe_2O_3/159.69}. \quad (5.2)$$

5.2.3. Measurements of magnetic properties and magnetite contents

Bulk-rock magnetic properties were measued from magnetic hysteresis loops for powdered samples using a vibrating sample magnetometer (VSM) at the Center for Advanced Marine Core Research (CMCR), Kochi University. The magnetic field of the magnetometer varied in the range from -1.0 to + 1.0 T. The amount of magnetite is determined by dividing the measured volume saturation magnetization by a representative value of the saturation magnetitation of magnetite (usually 92 Am^2/kg, the value of pure magnetite) (Maffine et al., 2014; Fuji et al., 2016).

$$m = \frac{Ms}{Ms_{\mathrm{Ref}}} \times 100\ (wt.\%) \quad (5.3)$$

where m is the mass% of magnetite in the sample, *Ms* is the volume saturation magnetization, and Ms_{Ref} is a reference value for the saturation magnetization of magnetite. When determining the amount of magnetite using this method, it is necessary to assume that only magnetite contributes to saturation magnetization in the sample.

5.2.4. X-ray absorption near-edge structure spectroscopy

Bulk-rock XANES

Bulk-rock x-ray absorption near-edge structure (XANES) spectra of mineral standards,

olivine–magnetite mixtures, and natural serpentinite were measured at beamline BL-12C of the Photon Factory A A pellet 10 mm in diameter was prepared by pressing mixed fine-grained rock or mineral (10–30 mg) and boron nitride (100 mg) powders for quick X-ray absorption fine structure (XAFS) transmission analyses. An Si(111) double crystal monochromator and a focusing mirror were installed upstream of the beamline. The ring energy was 2.5 GeV and the current was 450 mA. Measurements were performed using an energy of 6600–8200 eV and an energy width of 0.4 eV. The X-ray energy calibration was based on the first inflection point of absorbance at the K edge of Fe metal foil at 7112.0 eV (Bearden and Burr, 1967). Measured XANES spectra were normalized and flattened using Larch version 0.9.70 (Newville, 2013). The flattening range was adjusted by checking the absorption before the pre-edge (7000–7050 eV) and post-edge (7200–7400 eV) regions were flattened to 0 and 1, respectively.

Iron redox state ($Fe^{3+}/\Sigma Fe$ ratios) were estimated from the XANES spectra by LCF using standard spectra following Sutton et al. (2017) and using Larch version 0.9.70 (Newville, 2013). In LCF, a spectrum from the unknown sample is modeled as a linear combination of spectra from standard samples, and the combined spectrum is optimized using a non-linear least squares method (Newville, 2013). The spectrum between 7080 and 7200 eV was used for fitting. $Fe^{3+}/\Sigma Fe$ ratios were calculated by summing the weight calculated by LCF multiplied by the $Fe^{3+}/\Sigma Fe$ ratio of each standard sample. We used eight mineral standards with variable Fe oxidation states and coordination, including octahedrally coordinated ferric iron $^{VI}Fe^{2+}$-bearing minerals (olivine), octahedrally coordinated ferrous iron $^{VI}Fe^{3+}$-bearing minerals (andradite), and tetrahedrally coordinated ferrous iron $^{IV}Fe^{3+}$-bearing minerals (sanidine).

2D imaging XANES

2D imaging XANES were measured at beamline NW-2A of the Photon Factory – Advanced Ring (PF-AR) equipped with Si(111) double-crystal monochrometer and CMOS image sensor (ORCA Flash 2.8) at the High Energy Accelerator Research Organization (KEK), Tsukuba, Japan. The ring energy was 6.5 GeV and the current was 60 mA. The Si(111) double-crystal monochrometer. XANES mapping was performed by recording a stack of 209 points with the following steps: (i)7009.2 – 7104.20 eV with 2.50 eV/step, (ii) 7104.20 – 7139.20 eV with 0.35 eV/step, (iii) 7139.20 – 7181.20 eV with 1.4 eV/step, (iv) 7181.20 -7321.20 eV with 3.5 eV/step. The exposure time was 0.4 s for one energy point. The X-ray energy calibration was based on the first inflection point of absorbance at the K edge of Fe metal foil at 7112.0 eV (Bearden and Burr, 1967). Measured XANES images were analyzed using ImageJ Fiji software with NW2A ImagingXAFS plugin. Redox state mapping of iron was created by linear combination fitting using olivine, andradite, and sanidine as standards after a 2-pixel binning process.

5.2.5. Synchrotron radiation nanoscopic X-ray CT

The nanoscale three-dimensional structure of magnetite in serpentinites was obtained by synchrotron radiation nanoscopic X-ray computed tomography (SR-XCT). Sample preparation for SR-XCT was performed using a focused ion beam scanning electron microscope (FIB-SEM; Thermo Fisher Scientific Helios NanoLab G4 at the Japan Agency for Marine-Earth Science and Technology (JAMSTEC), Yokosuka, Japan). A specific part in a thin section of the sample was made into a cylindrical shape with a diameter of ~15 μm and a height of ~20 μm using FIB-SEM. The cylindrical sample was attached to the tip of a tungsten needle by Pt welding. The FIB-SEM was performed with a gallium ion (Ga+) source at a voltage of 30 kV with a current of 0.09-20 nA.

The SR-XCT measurements were performed with a transmission x-ray microscope (TXM) system at beamline NW-2A at IMSS, PF-AR, KEK (Niwa et al., 2019). The voxel size was 19.2 nm, and the energy of the X-ray beam was fixed at 7118 eV and 7120 eV, respectively. The transmission X-ray images for CT were obtained by rotating the sample state from -90° to 90°, a total of 1441 images were obtained with an exposure time of 2 s. I used ilastik software (version 1.3.3post3) for segmentation of the X-ray CT data (Berg et al., 2019). Fiji software was also used for image processing (Schindelin et al., 2012). Dragonfly software (version 2022.2.0.1409) was used for visualization and volume and surface area quantification. The calculation of the volume and surface area is based on weighted local configurations method (Lindblad, 2005). The data processing process is shown in Fig. 5.1.

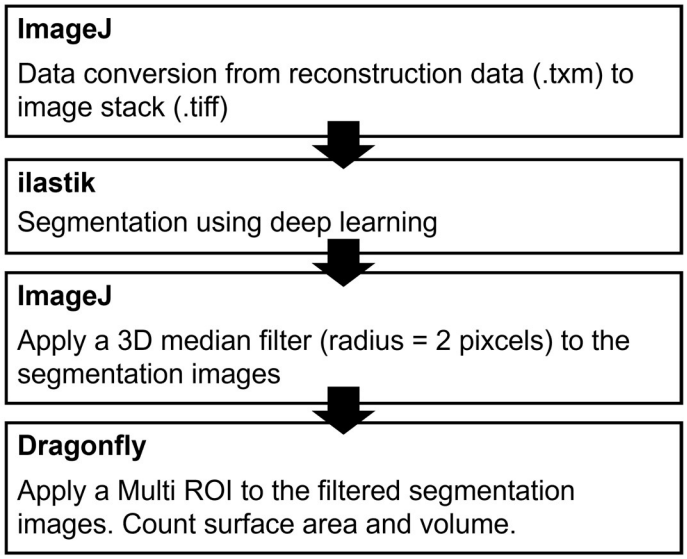

Fig. 5.1. Scheme for the X-ray CT data processing.

5.2.6. Micro X-ray fluorescence microscope

Thin section scale elemental maps of gabbroic rocks were obtained by micro x-ray fluorescence (XRF) microscope (Bulker M4 Tornado at Graduate School of Environmental Studies, Tohoku University, Japan) equipped with an energy dispersive spectrometer (EDS) for element mapping. The micro-XRF analysis were conducted at an accelerating voltage of 50 kV and beam current was 300 μA. The scan time was 20 ms per pixcel. The resolution of the elemental mapping is set to 20 um with beam diameter of 20 um.

5.2.7. Thermodynamic calculations

Calculations of equilibrium constants for mineral dissolution, dissolved species, and redox reactions were performed using SUPCRTBL software, which is an extension of SUPCRT92 and includes the thermodynamic database from Holland and Powell (2011). Thermodynamic data for Hisingerite ($\square Fe^{3+}{}_2Si_2O_5(OH)_4$) and Fe-bruite ($Fe(OH)_2$) were from Klein et al. (2009) and for cronstedite from Klein et al. (2013). Phase diagrams in the Fe-fixed Fe-Si-O-H system were created to investigate stable minerals in arbitrary $H_{2,aq}$ and $SiO_{2,aq}$. In the phase diagram, the stable phase was the mineral with the lowest reaction Gibbs energy for the dissolution reaction of each mineral. The reaction Gibbs free energy can be written as

$$\Delta_r G = \Delta_r G° + RT\ln Q \tag{5.4}$$

where $\Delta_r G$ is the reaction Gibbs energy for a given reaction, $\Delta_r G°$ is the standard reaction Gibbs energy, R is the gas constant, T is the temperature, and Q is the reaction ratio. Equation x can be rewritten using the equilibrium constant K from the relation $\Delta_r G° = -RT\ln K$ as follows:

$$\Delta_r G = -RT\ln K + RT\ln Q \tag{5.5}$$

Since the equilibrium constant output by SUPCRTBL is logK (10 is the bottom), it can be rewritten by transforming the bottom as follows:

$$\Delta_r G = -\ln(10)\, RT\log_{10} K + \ln(10)\, RT\log_{10} Q \tag{5.6}$$

Since logK is uniquely obtained for a given temperature pressure, Eq. 5.6 represents the reaction Gibbs energy for a given composition (Q). For a given composition, the mineral with the lowest reaction Gibbs energy is assumed to be stable, and a phase diagram is created.

5.3. Results

5.3.1. Bulk-rock analysis

Bulk-rock composition and iron redox state

The Fe content and $Fe^{3+}/\Sigma Fe$ of each lithology are listed in Table 5.4. The dunite samples are the most Fe-rich (Fe_2O_3*=10.63±1.37 wt. %), while the harzburgite and gabbroic rocks contain on average about the same amount of iron (Gabbroic rocks: Fe_2O_3*=8.42±4.87 wt. %, Harzburgite: Fe_2O_3*=8.65±0.79 wt. %). The Fe content of the gabbroic rocks is highly variable; $Fe^{3+}/\Sigma Fe$ values are nearly identical for dunite and harzburgite, while the gabbroic rocks have lower values. The $Fe^{3+}/\Sigma Fe$ of all rocks tends to increase with increasing loss on ignition (Fig. 5.2).

Table 5.4. Average bulk rock total iron (Fe_2O_3*), $Fe^{3+}/\Sigma Fe$, FeO, and Fe_2O_3 for each lithology.

Lithology	Gabbroic rocks		Dunite		Harzburgite	
N	18		20		37	
	Avg.	Std.	Avg.	Std.	Avg.	Std.
Fe_2O_3* (wt%)	8.42	4.87	10.63	1.37	8.65	0.79
$Fe^{3+}/\Sigma Fe$	0.31	0.08	0.63	0.05	0.61	0.08
FeO (wt%)	5.26	2.72	3.31	0.42	2.97	0.68
Fe_2O_3 (wt%)	2.60	1.94	5.73	1.04	4.57	0.72

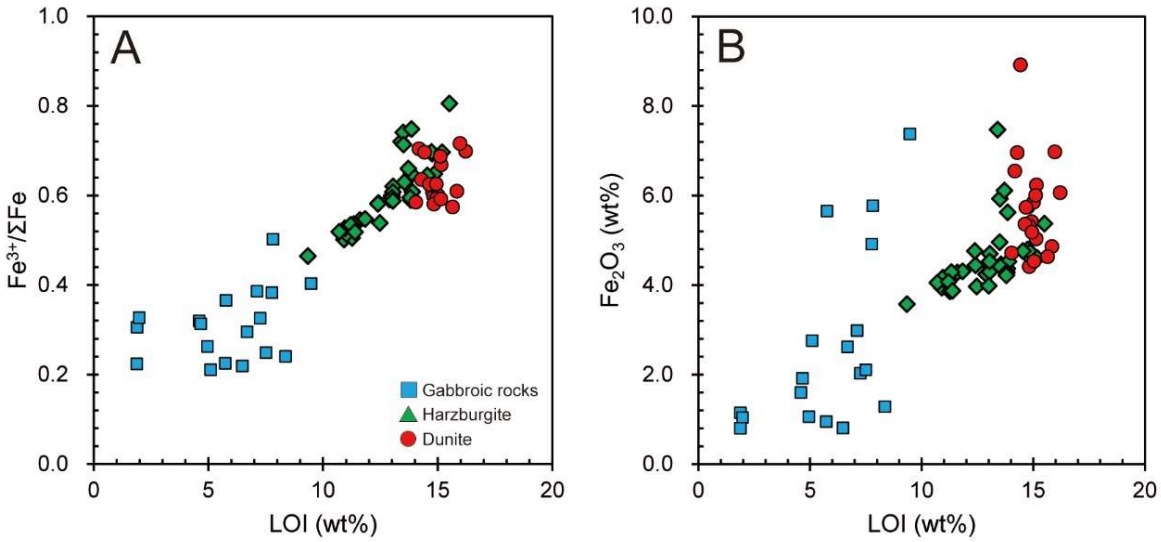

Fig. 5.2. (A)Bulk rock iron redox state ($Fe^{3+}/\Sigma Fe$) vs loss on ignition (LOI). (B)Bulk rock Fe_2O_3 vs LOI.

Magnetic properties and magnetite content

Fig. 5.3. shows the magnetic hysteresis curve of a typical sample. Different samples show different magnetic hysteresis curves. The mass fraction of magnetite was calculated from the saturation magnetization of each sample. Magnetite is assumed to be the only mineral contributing to the saturation magnetization. The average values of saturation magnetization and magnetite content for each lithology are shown in Table 5.5. The saturation magnetization of the samples was 1.5±2.0 $Am^2 kg^{-1}$ for gabbroic rocks, 3.2±1.7 $Am^2 kg^{-1}$ for dunite, and 1.2±1.3 $Am^2 kg^{-1}$ for harzburgite. Magnetite content in each lithology ranges from 1.6±2.2 wt. % in gabbroic rocks, 3.5±1.9 wt. % in dunite, and 1.3±1.5 wt. % in harzburgite. The gabbroic rocks have large variation in magnetite content. Dunite contains more magnetite than harzburgite. The relationship between magnetite content and loss on ignition shows magnetite content increases sharply at loss on ignition of 5-7 wt. % in the case of the gabbroic rocks (Fig. 5.4). For dunite and harzburgite, magnetite content increases sharply at LOI of 13-15 wt. %.

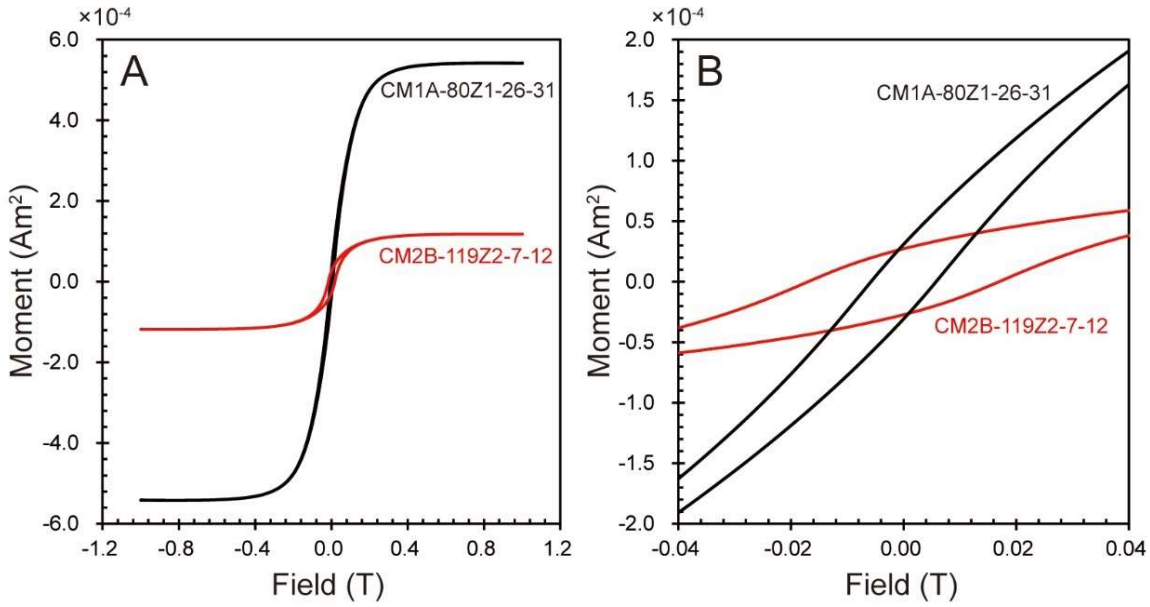

Fig. 5.3. Magnetic hysteresis curve of a typical sample (CM1A-80Z1-26-31(Dunite) and CM2B-119Z2-7-12(Harzburgite)).

Table 5.5. The saturation magnetization (*Ms*) and magnetite content calculated from the *Ms* (wt. %).

Lithology	Gabbroic rocks		Dunite		Harzburgite	
N	18		20		37	
	Avg.	Std.	Avg.	Std.	Avg.	Std.
Ms (Am^2/kg)	1.2	1.7	3.3	1.4	1.4	1.6
Magnetite (wt%)	1.3	1.9	3.6	1.5	1.5	1.8

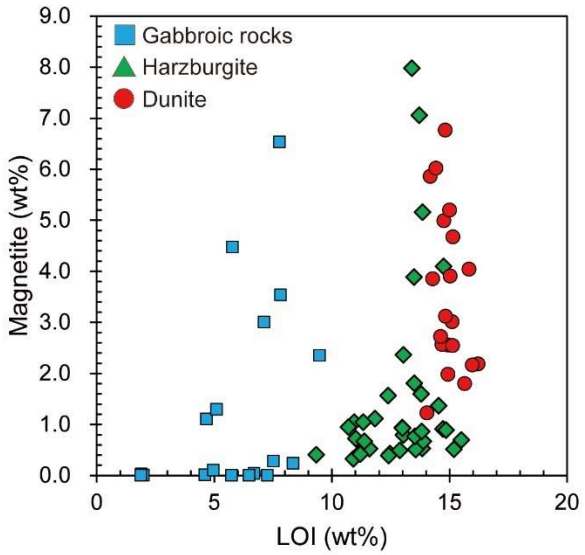

Fig. 5.4. Loss on ignition (LOI) vs magnetite content (wt. %).

5.3.2. Microtexture and iron redox state mapping

The iron content of olivine, serpentine, and brucite in gabbroic rocks, dunite, and harzburgite were investigated. A detailed description of the samples analyzed is given in Chapter 2. The focus here is on serpentine and related minerals (brucite and magnetite). The main serpentinization stage of gabbroic rock, dunite, and harzburgite is characterized by mesh texture that replace olivine (Fig. 5.5). Fig. 5.6 shows depth profile of X_{Mg} [=Mg/(Mg+Fe^{2+})] of olivine, mesh texture serpentine and brucite that replacing olivine. The X_{Mg} of olivine in the gabbroic rocks is higher (X_{Mg} = 0.80-0.87) than that of dunite and harzburgite (X_{Mg} = 0.91-0.92). X_{Mg} of olivine in gabbroic rocks shows a decreasing trend with increasing depth. Despite the variation in X_{Mg} of olivine, the X_{Mg} of serpentine in the mesh texture replacing olivine almost unchanged at range of 0.9-1.0. On the other hands, the X_{Mg} of brucite in the mesh texture shows variations depending on the lithology. The X_{Mg} of brucite in dunite shows higher X_{Mg} (X_{Mg} = 0.72-0.94, Average 0.85, N = 9) than in gabbroic rocks (X_{Mg} = 0.50-0.73, Average 0.60, N = 4) and harzburgite (X_{Mg} = 0.65-0.84, Average 0.76, N = 6). Serpentinite replacing orthopyroxene (X_{Mg} = 0.91-0.96, Average 0.93, N = 4) in harzburgite is richer in Fe than serpentinite replacing olivine.

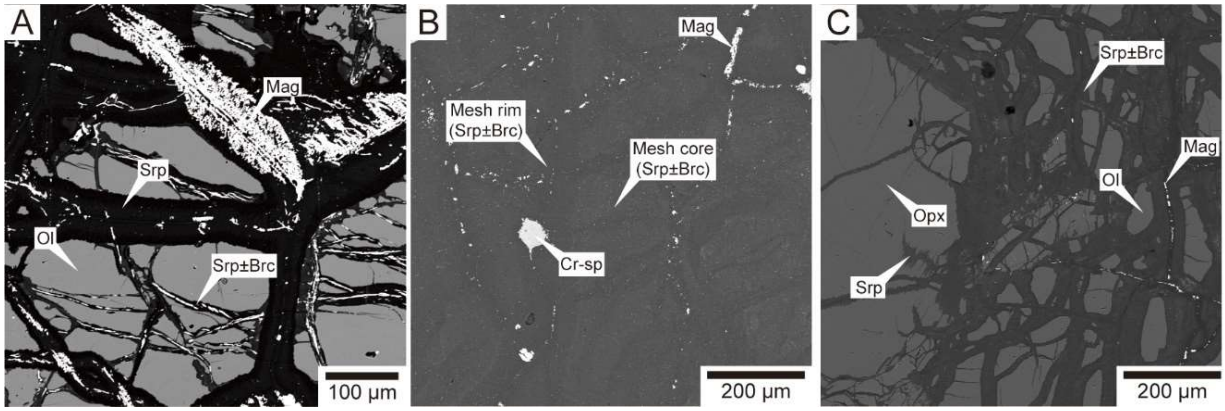

Fig. 5.5. Mesh texture serpentinization in (A)Gabbroic rock (CM1A-9Z3-26-30), (B)Dunite (CM2B-16Z2-34-35), (C)Harzburgite (CM1A-144Z4-60-68).

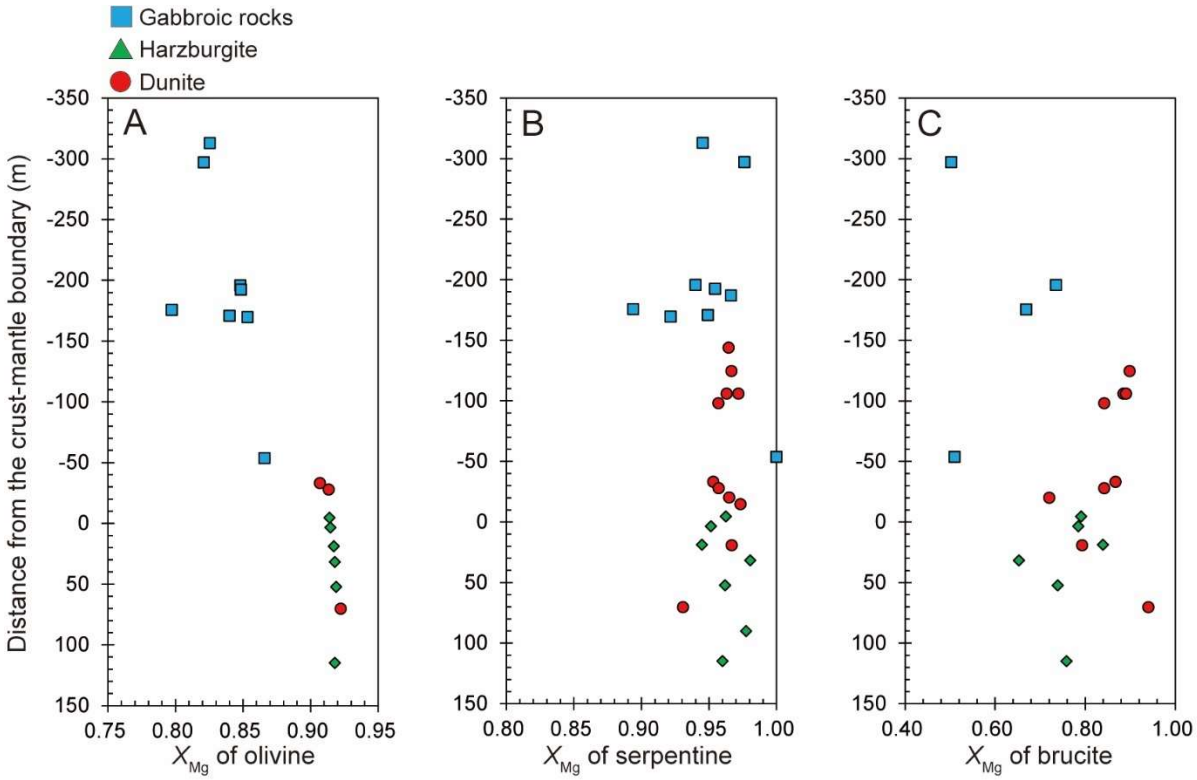

Fig. 5.6. X_{Mg} [=Mg/(Mg+Fe^{2+})] depth profiles of olivine, mesh texture serpentine and brucite.

Gabbroic rocks

The gabbroic rocks are composed of olivine, plagioclase, and orthopyroxene, with the 50-80% serpentinized olivine with a mesh texture. The mesh texture is composed of serpentine (lizardite: X_{Mg}=0.96-0.97) and magnetite. Fe-redox mapping shows that serpentine has a lower $Fe^{3+}/\Sigma Fe$ than magnetite. Serpentine near the boundary with olivine has lower $Fe^{3+}/\Sigma Fe$ than mesh rim (Fig. 5.7).

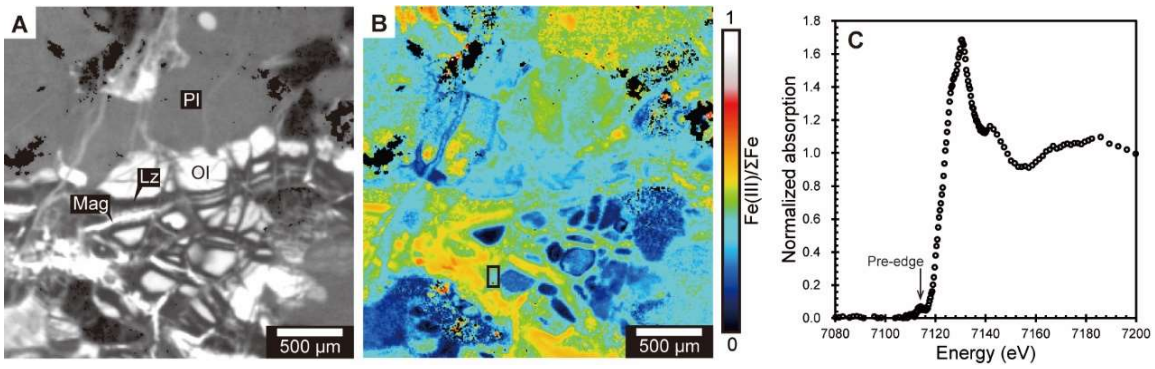

Fig.5.7. 2D imaging XANES of olivine gabbro (CM1A-47Z2). (A)Map of Iron K-edge jump. (B)Map of Iron redox state. (C) XANES spectra of mesh rim.

Dunite

The dunite is completely serpentinized with a mesh texture. The mesh core is composed of lizardite (X_{Mg} = 0.94) and particulate magnetite, while the mesh rim is composed of mixture of lizardite (X_{Mg} = 0.96) and brucite (X_{Mg}=0.83). In dunite, the mesh core has higher $Fe^{3+}/\Sigma Fe$ than the mesh rim (Fig. 5.8). The $Fe^{3+}/\Sigma Fe$ of mesh rim is 0.1-0.2, mesh core has higher $Fe^{3+}/\Sigma Fe$ of 0.8-0.9. Serpentine around veins has higher $Fe^{3+}/\Sigma Fe$, ~1.0. The XANES spectrum of serpentine in the mesh core and mesh rim has a small pre-edge (Fig. 5.8C and 5.8D).

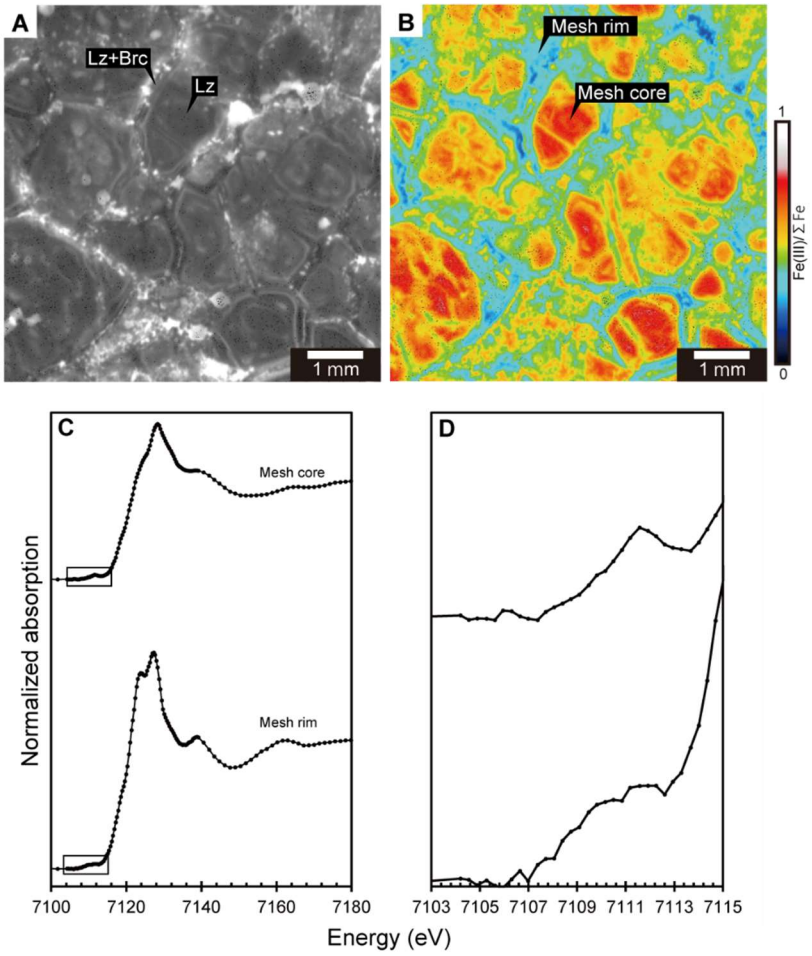

Fig. 5.8. Iron redox state mapping of dunite (CM2B-16Z3). (A)Map of Iron K-edge jump. (B)Map of Iron redox state. (C-D) XANES spectra of (C)Mesh core and mesh rim. (D)Close up of the pre-edge region shown in rectangle in Fig. C.

Harzburgite

Harzburgite is about 65-80% serpentinized with a mesh texture. Rectangular pyroxene is less serpentinized than olivine. Veins with magnetite often occur in harzburgite, and both olivine and orthopyroxene are completely serpentinized around the veins. The mesh texture is a mixture of lizardite, chrysotile, and brucite. The X_{Mg} of the serpentine in the mesh structure is 0.97, and that of the brucite is 0.74. Bastite is a mixture of lizardite and chrysotile without brucite. It has an X_{Mg} of 0.86 and is richer in iron than the mesh-structure serpentine. The magnetite veins are composed of serpentine (lizardite) and magnetite and do not contain brucite. The X_{Mg} of this serpentine is 0.97. The chrysotile vein, thought to have formed in the last stage, has an X_{Mg} of 0.91.

Serpentinized harzburgites have various $Fe^{3+}/\Sigma Fe$ depending on the microstructure (Fig. 5.9). Serpentine in the vicinity of veins have higher $Fe^{3+}/\Sigma Fe$ compared to mesh textures and bastite away from veins. Late-stage chrysotile veins have low $Fe^{3+}/\Sigma Fe$. When the mesh texture is expanded, the mesh rim has higher $Fe^{3+}/\Sigma Fe$ than the olivine-serpentine boundary, which is a reaction front. A similar trend has been reported in previous studies (Andreani et al., 2013). Bastite has low $Fe^{3+}/\Sigma Fe$ in the core, whereas the rim shows high $Fe^{3+}/\Sigma Fe$. XANES spectra of the mesh texture, bastite, and chrysotile veins commonly show low pre-edges (Fig. 5.10). The $Fe^{3+}/\Sigma Fe$ of the mesh texture is 0.29-0.35. This is in agreement with the value obtained by the Mössbauer method in a previous study ($Fe^{3+}/\Sigma Fe$ = 0.30-0.68; Klein et al., 2009). The fully serpentinized orthopyroxene (bastite) shows similar $Fe^{3+}/\Sigma Fe$ (=0.35) as mesh texture. The $Fe^{3+}/\Sigma Fe$ of serpentine around magnetite veins is 0.5-0.6, which is high compared to the mesh texture. On the other hands, chrysotile veins perpendicular to the magnetite vein have low $Fe^{3+}/\Sigma Fe$ (~0.2). Although it is possible that minerals with low Fe content (FeO = a few wt. %) were photo-oxidized by synchrotron radiation during the measurements (Reynard et al. 2022), considering the low $Fe^{3+}/\Sigma Fe$ of chlorite (FeO = 3.2±0.9 wt. %) in the same area of analysis, it is likely that the effect of photo-oxidation was negligible.

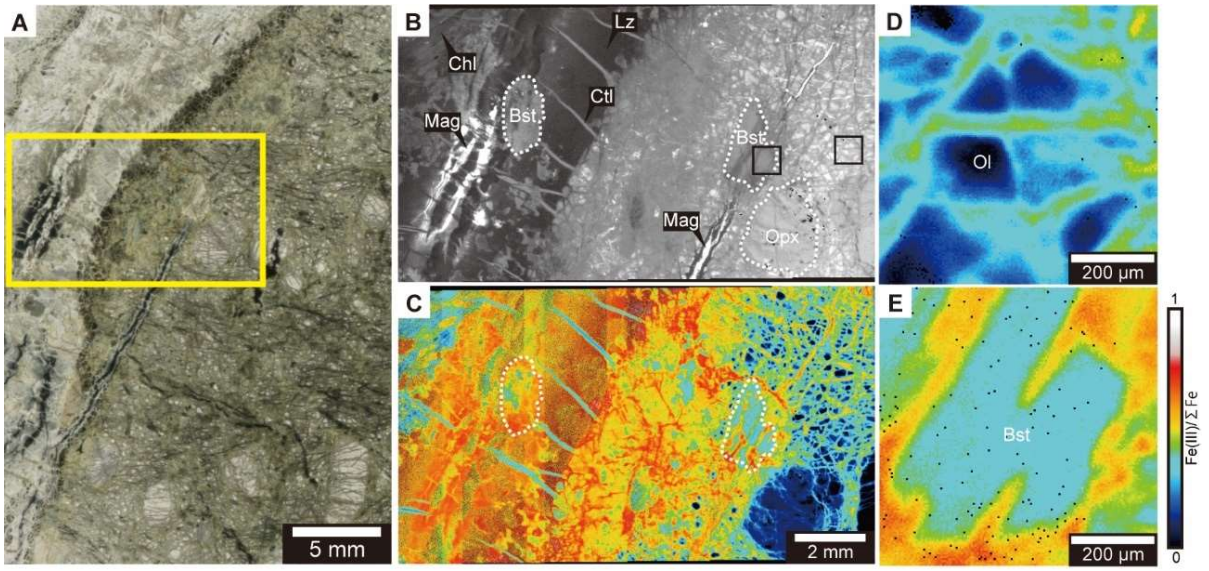

Fig. 5.9. Iron redox state mapping of harzburgite (CM2B-119Z2-7-12). (A)Thin section scan. (B)Map of Iron K-edge jump. (C)Map of Iron redox state. (D)Close up view of the iron redox state map of mesh texture. (E)Close up view of the iron redox state map of bastite (serpentinized orthopyroxene).

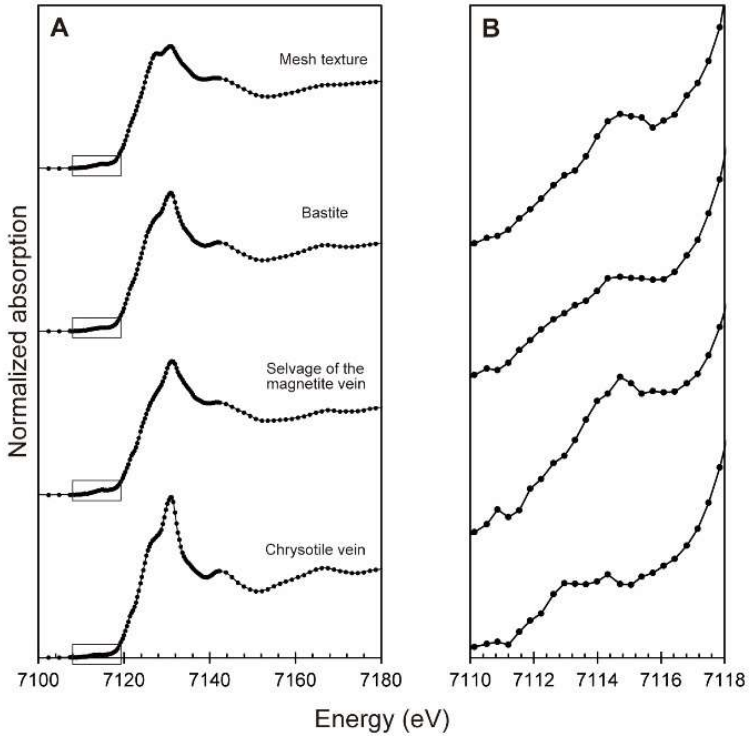

Fig. 5.10. XANES spectra of mesh texture (A), bastite (B), selvage of the magnetite vein (C), and chrysotile vein (D).

5.3.3. Microtexture of magnetite

Magnetite in host rock matrix

Here, magnetite features in each lithology are described, and the volume ratio of magnetite to serpentine is quantified by using image analysis. The magnetite geometry characteristics (surface area, volume, and aspect ratio) in each lithology were also investigated by nanoscale structural observations using synchrotron radiation X-ray computed tomography (SR-XCT).

In gabbroic rocks, magnetite grains show dendritically at the mesh rim, away from the olivine (Fig. 5.11A). Similar microstructures are also found in seafloor drilling samples (Hess Deep, Nozaka et al., 2017, Lithos). The volume ratio of serpentine to magnetite (V_{Mag}/V_{Srp}) in the gabbroic rocks determined from image analysis is ~0.05-0.09. Magnetite in the rims has a rough surface (Fig. 5.11C and D). Where magnetite grows prominently, magnetite is connected at the micrometer scale (Fig. 5.11C). Magnetite is abundant at the rim and discretely distributed away from the rim (Fig. 5.11D).

Two types of magnetite were observed in the dunite host rock matrix: (A) magnetite veins at mesh rims and (B) homogeneously distributed particulate magnetite (Figs. 5.12A and B). Particulate magnetite is also observed in fresh olivine grains. Such occurrences of magnetite in olivine have been reported in Oman and other ophiolites (Arai et al., 2021, Lithos). The amount of particulate magnetite calculated by image analysis ranged from ~0.6-1.3 vol%, and the amount of magnetite in the mesh rims ranged from ~0.3-0.8 vol%. The volume ratio of serpentine to magnetite in the dunite determined from image analysis is ~8.0×10^{-3} – 1.5×10^{-2}. Particulate magnetite in mesh cores and olivine has a flattened shape with a smooth surface (Figs. 5.12C-D). In contrast, magnetite in mesh rims has a rough surface (Fig. 5.12E). The aspect ratios and volumes of platy magnetite in olivine and serpentinized mesh cores are similar (Fig. 5.13).

In harzburgite, magnetite veins are distributed on the mesh rims (Fig. 5.14A). The volume ratio of serpentine to magnetite in the gabbroic rocks determined from image analysis is ~$2.0\text{-}3.0\times10^{-3}$. The mesh rim of harzburgite also shows magnetite with a rough surface similar to gabbroic rocks and dunite (Fig. 5.14B).

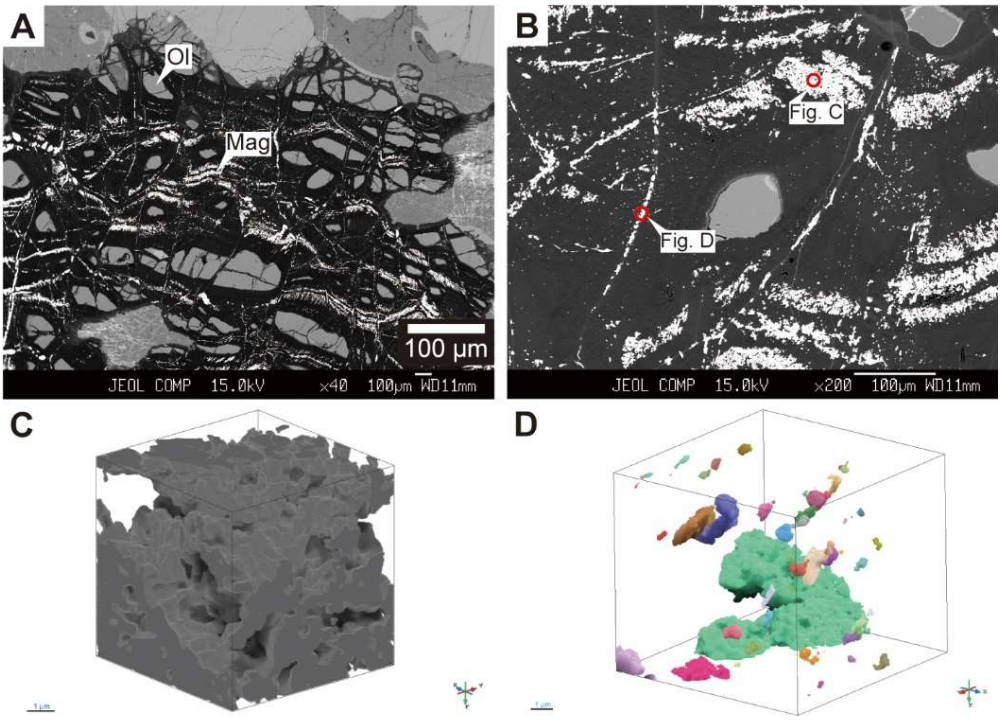

Fig. 5.11. Backscattered electron images (BEI) and SR-XCT of magnetite in olivine gabbro (CM1A-47Z2). (A) BEI of partially serpentinized olivine. (B) Close-up of magnetite. (C) SR-XCT of well-grown magnetite. (D) SR-XCT of mesh rim magnetite.

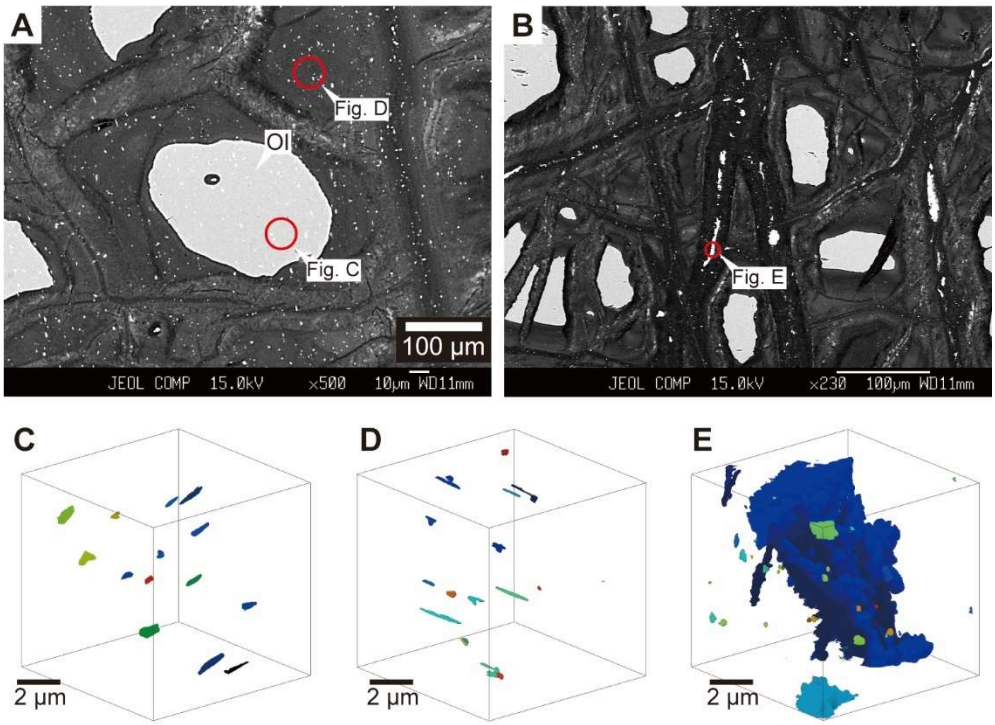

Fig. 5.12. BEI and SR-XCT of dunite. (A) BEI of magnetite in olivine (CM2B-54Z). (B) BEI of magnetite at the mesh rim (CM2B-56Z). SR-XCT of magnetite in the olivine grain (C), the mesh core (D), and the mesh rim (E).

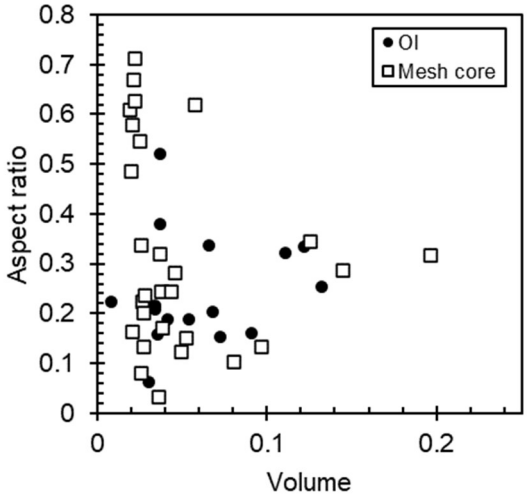

Fig. 5.13. Size and aspect ratio of magnetite in olivine and mesh core of dunite (CM2B-56Z).

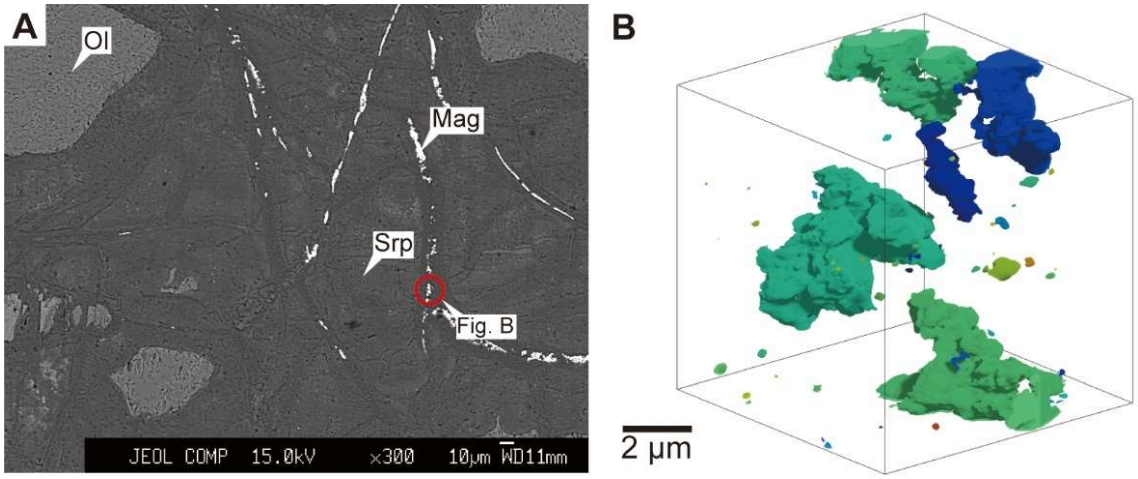

Fig. 5.14. BEI and SR-XCT of harzburgite (CM1A-144Z4). (A)BEI of magnetite in mesh rim. (B)SR-XCT of magnetite in mesh rim.

5.3.4. Ni-Fe alloy and sulfides

Gabbroic rocks

Ni-Fe alloy and Ni-Fe sulfide have less than 1 micrometer in size, were identified on the mesh rims and serpentinized mesh cores of the gabbroic rocks (Fig. 5.15A-D). These minerals are widely distributed on the mesh rim (Fig. 5.16). Semi-quantitative analysis by WDX shows that the Ni-Fe alloys have Ni/Fe = ~0.6 (Fig. 5.17A-B), the composition close to taenite (Botto and Morrison, 1976, Rossetti and Zucchetti, 1988, Frost et al., 2013). Ni-Fe sulfides show Ni/Fe = 0.6-1.2 and (Ni+Fe)/S = 1.7-1.8 (Fig. 5.17C-D), the composition close to pentrandite.

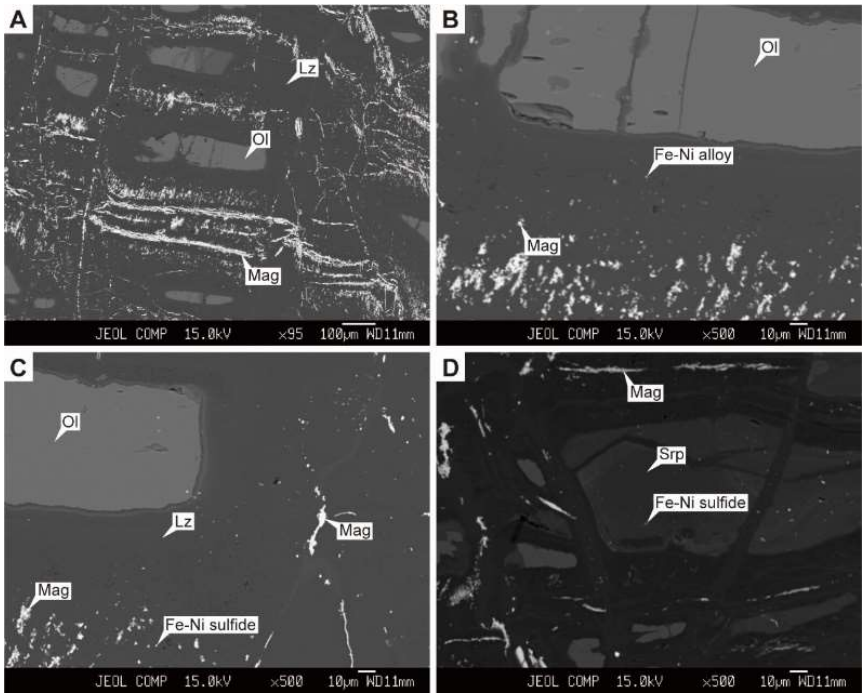

Fig. 5.15. Backscattered electron images of magnetite, Fe-Ni alloy, and Fe-Ni sulfide. (A)Magnetite vein in the mesh rim. (B)Close up view of mesh texture containing Fe-Ni alloy and magnetite. (C)Fe-Ni sulfide in the mesh rim. (D)Fe-Ni sulfide in the serpentinized mesh core. Ol=olivine, Lz=lizardite, Mag=magnetite, Srp=serpentine.

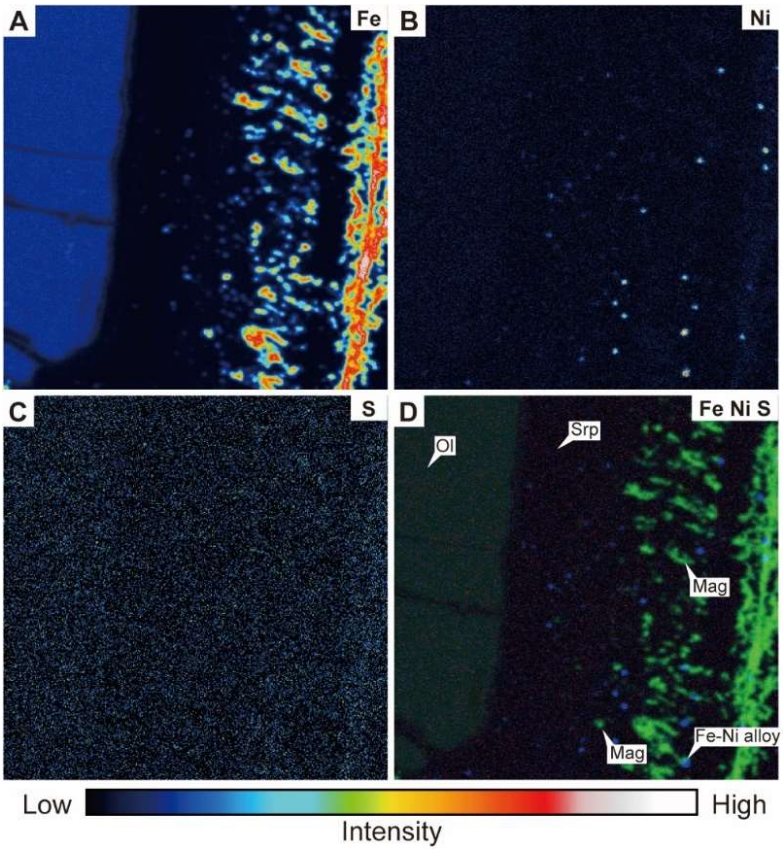

Fig. 5.16. Element mapping of the mesh texture for Fe, Ni and S (A-C). (D)Three element composite map of Fe, Ni, and S.

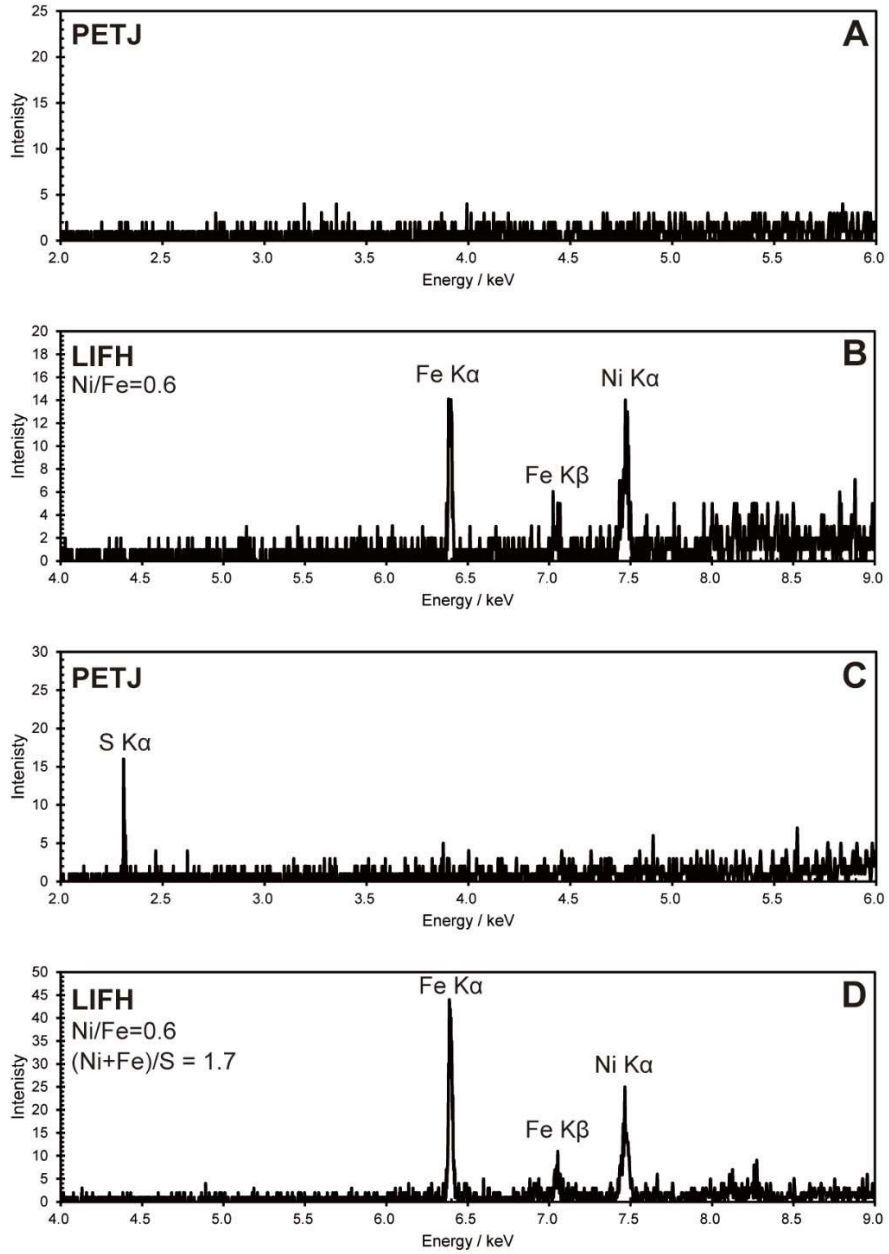

Fig. 5.17. WDX spectra by PETJ and LIFH. (A-B) WDX spectra of Fe-Ni alloy. (C-D) WDX spectra of Fe-Ni sulfide.

Dunite

Fe-Ni alloy have less than 1 micrometer in size, were identified on the mesh rims and mesh cores of the dunites (Fig. 5.18). Elemental map by EPMA shows the distribution of Ni-rich small particles (< ~1 um) on the mesh rim (Fig. 5.19B). Sulfur mapping is below the detection limit (Figs. 5.19C and 5.20C). These minerals are widely distributed on the mesh rims (Figs. 5.19D and 5.20D). Semi-quantitative analysis by WDX shows that the Ni-Fe alloys have Ni/Fe = 1.1-1.3 (Fig. 5.21A-B), the composition close to taenite (Botto and Morrison, 1976; Frost *et al.*, 2013).

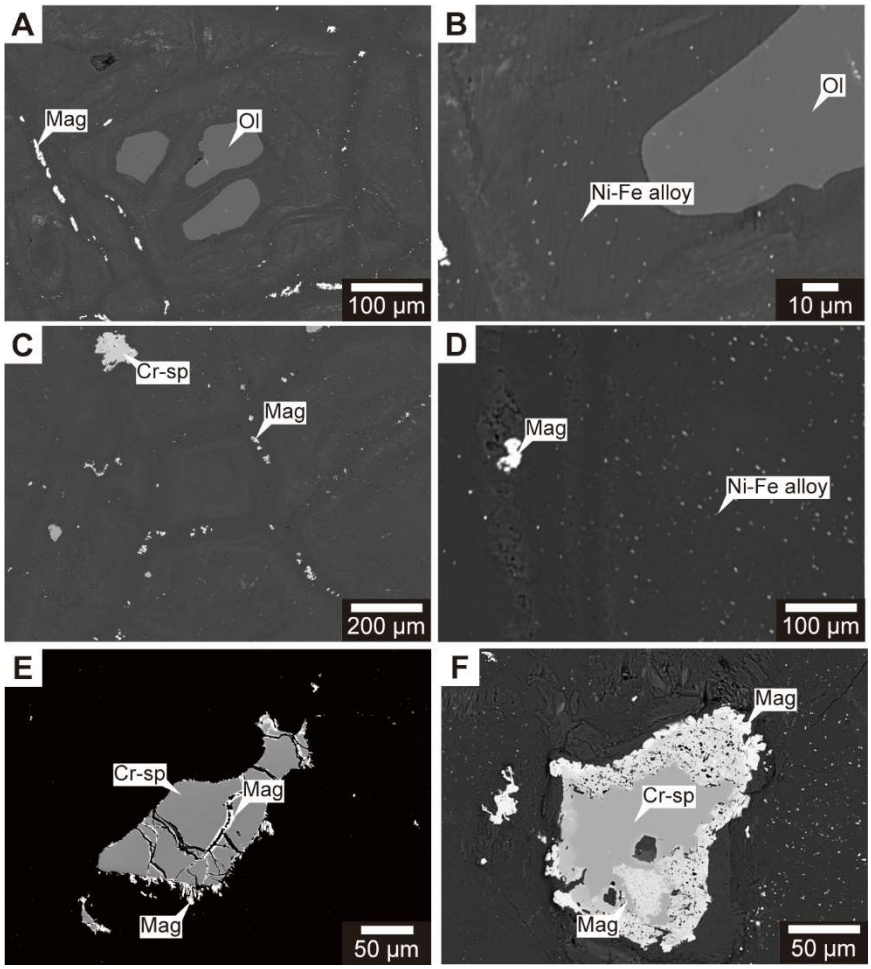

Fig. 5.18. Backscattered electron images of magnetite, Fe-Ni alloy, and Fe-Ni sulfide in dunites. (A)Magnetite vein in mesh rim of partly serpentinized dunite (CM2B-56Z3-51-56). (B)Ni-Fe alloy in the mesh rim. (C)Large grain size (~10 µm) magnetite in mesh rim of completely serpentinized dunite (CM2B-13Z3-7-12). (D) Ni-Fe alloy in the mesh rim. The rim and both side of crack of Cr-spinel replaced to magnetite (E-F).

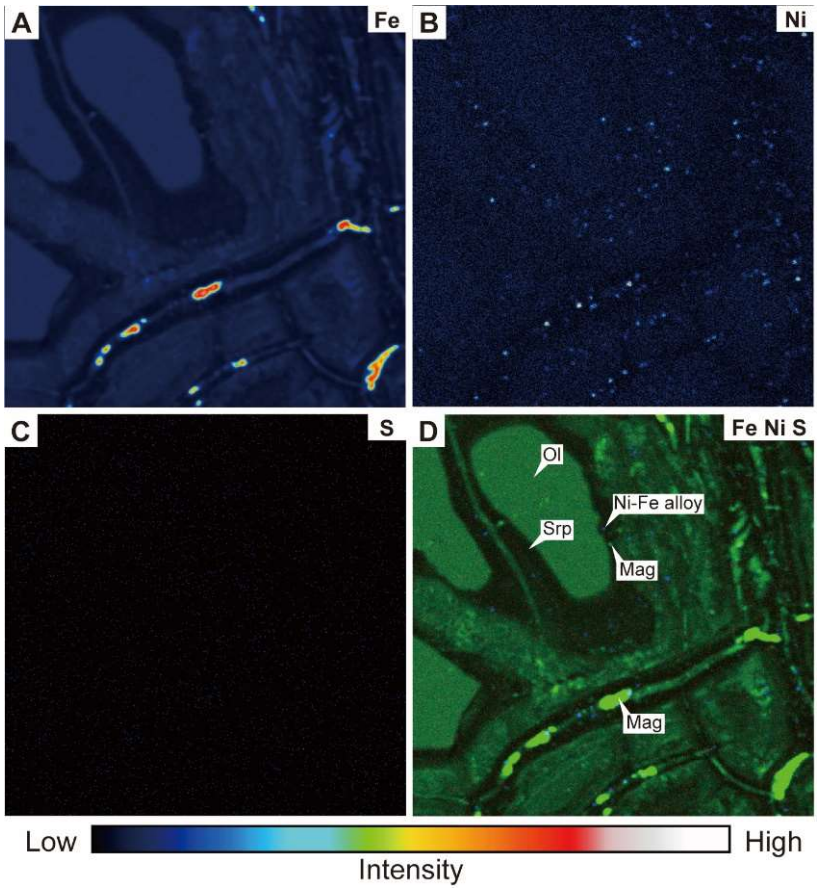

Fig. 5.19. Element mapping of the mesh texture of partly serpentinized dunite (CM2B-56Z3-51-56) for Fe, Ni and S (A-C). (D)Three element composite map of Fe, Ni, and S.

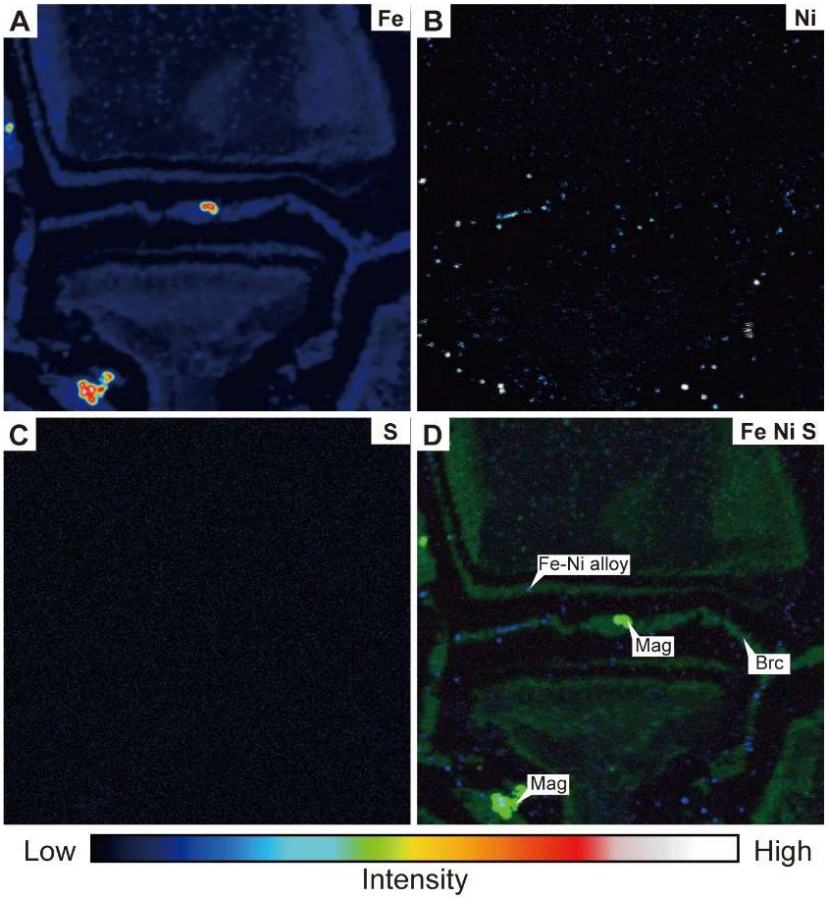

Fig. 5.20. Element mapping of the mesh texture of completely serpentinized dunite (CM2B-13Z3-7-12) for Fe, Ni and S (A-C). (D)Three element composite map of Fe, Ni, and S.

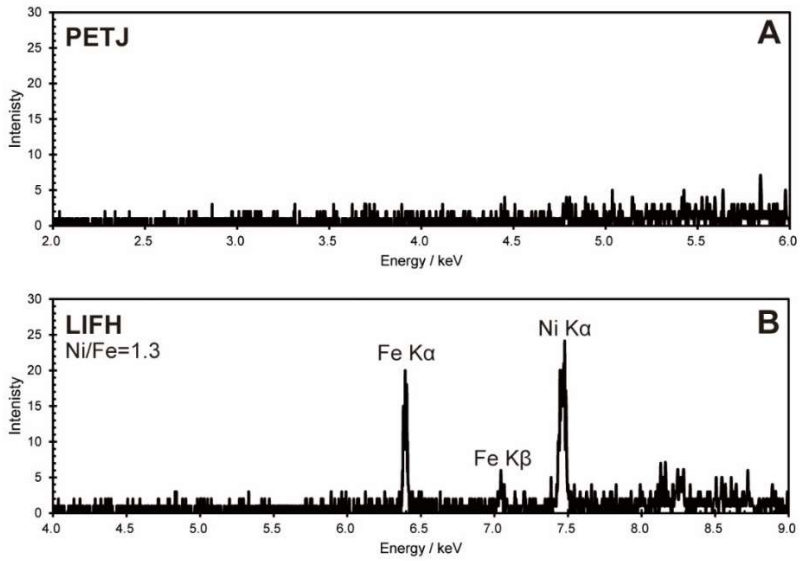

Fig. 5.21. WDX spectra of Ni-Fe alloy from partly serpentinized dunite (CM2B-56Z3-51-56) by PETJ (A) and LIFH (B).

Harzburgite

Ni-Fe alloy have less than 1 micrometer in size, were identified on the mesh rims of the harzburgite (Fig. 5.22A-B). Ni-Fe sulfide with size of ~10 μm observed in mesh texture (Fig. 5.22C-D). Cu-Zn alloys were found in and around tremolite veins (Fig. 5.22E-F). Ni-Fe alloy widely distributed in the mesh rims (Fig. 5.22). Semi-quantitative analysis by WDX shows that the Ni-Fe alloys have Ni/Fe = 2.4-2.6 (Fig. 5.23A-B), the composition close to awaruite (Frost, 1985; Klein et al., 2009; Plumper et al., 2017). The Ni-Fe sulfide shows Ni/Fe = 0.8 and (Ni+Fe)/S = 1.9. The Cu-Zn ally shows Cu/Zn = 5.0 (Fig. 5.24).

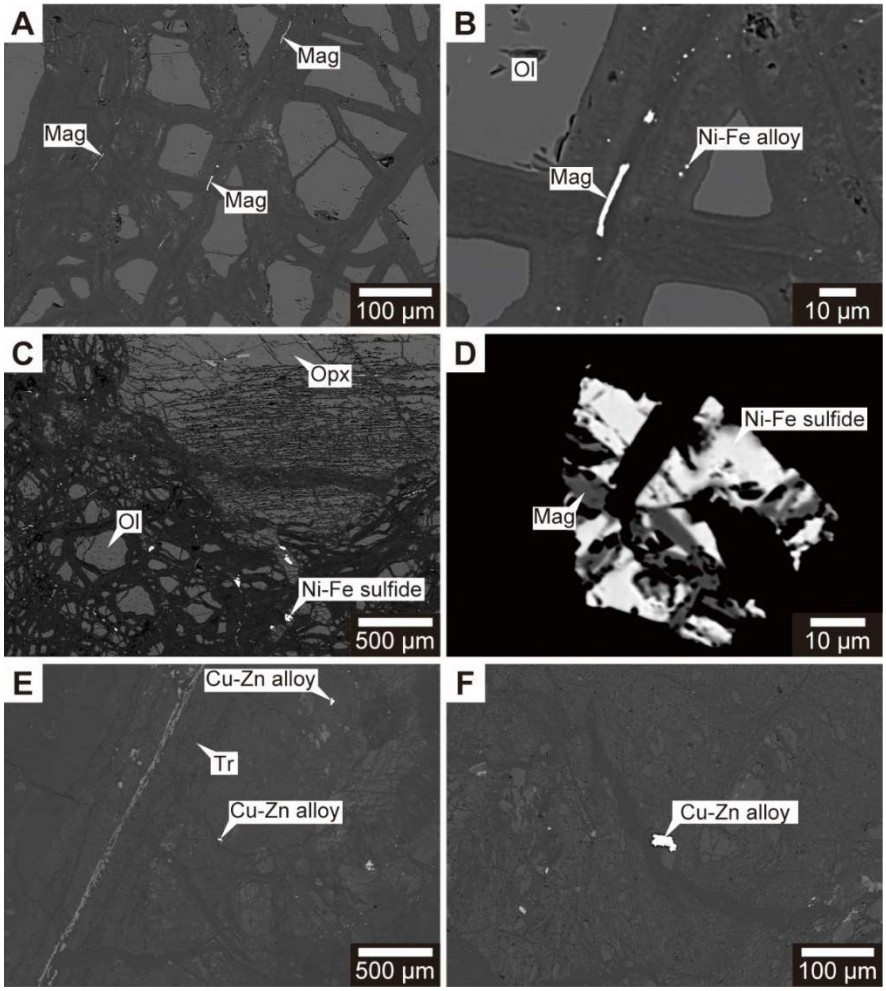

Fig. 5.22. Backscattered electron images of allys and Ni-Fe sulfide in harzburgite. (A)Magnetite, (B)Awaruite, (C)Elemental map. (A-B)CM2B-77Z4-70-75. (C-F)CM2B-83Z2-8-13.

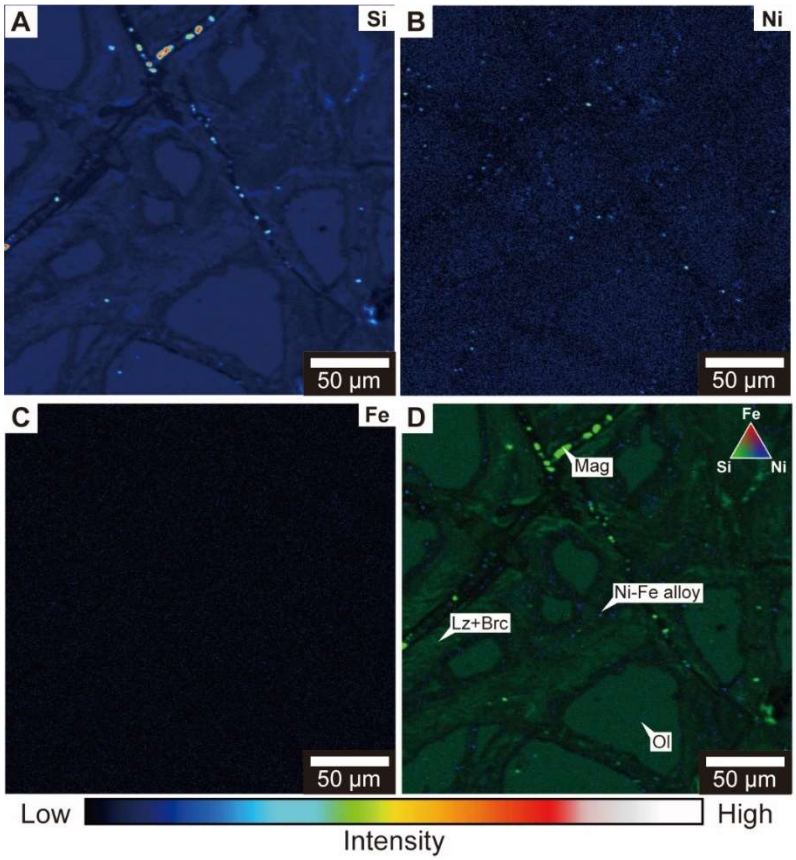

Fig. 5.23. Element mapping of the mesh texture of serpentinized harzburgite (CM2B-83Z2-8-13) for Fe, Ni and S (A-C). (D)Three element composite map of Fe, Ni, and S.

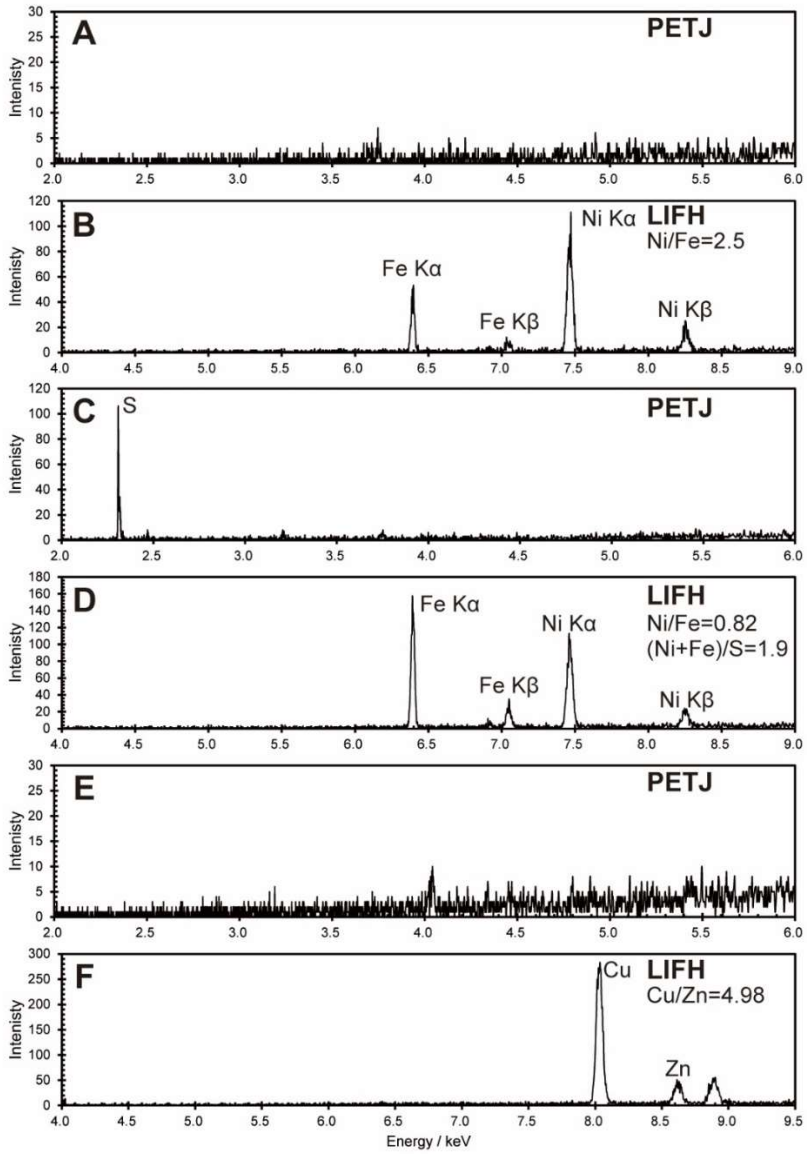

Fig. 5.24. WDX spectra by PETJ and LIFH. Fe-Ni alloy (A-B, CM2B-77Z4-70-75), Fe-Ni sulfide (C-D, CM2B-83Z2-8-13), and Cu-Zn alloy (E-F, CM2B-83Z2-8-13).

5.3.5. Stability fields of minerals in the Fe-Si-O-H system

Phase diagrams were made to investigate the stability of Fe endmembers of minerals found in serpentine with respect to hydrogen and silica activity. The minerals used in the calculations and their dissolution reactions are listed in Table 5.6. The stable mineral phases vary with $H_{2,aq}$ activity and silica activity (Fig. 5.25). At low Si-acitivity (chrysotile-brucite equilibrium), Iron is stable in the most reducing environment (High $H_{2,aq}$ activity). As the solution becomes more oxidizing (Low $H_{2,aq}$ activity), the stable minerals change to Fe-brucite, magnetite, and hematite (goethite at lower temperatures). At high Silica activity (talc-chrysotile equilibrium), Iron is stable in the most reducing environment, and as the solution becomes more oxidizing, the stable minerals change to greenalite and hishingerite. the decrease in $H_{2,aq}$ is due to the increase in W/R and the oxidizing fluid influx (Klein et al., 2009; Ely et al., 2023). The topological relationships of these mineral phases are generally consistent with previous studies (Zolotov 2014; Tutolo et al., 2019). cronstedtite does not appear in the phase diagram produced here because the stable region of cronstedtite overlaps with that of magnetite did not ($aH_{2,aq}$=-2 to -4 and $aSiO_{2,aq}$=-4.5 to -3 at 200 °C, 1 kbar; Tutolo et al., 2019). The thermodynamic properties of cronstedtite have not been measured, and different standard Gibbs free energies have been estimated (Zolotov 2014, Icarus). Therefore, the evaluation of the stability of cronstedtite may contain uncertainties. The upper limit of dissolved hydrogen concentration is determined by $H_{2,g}$=$H_{2,aq}$. From the equilibrium constant for this reaction (K_{H_2}), the $H_{2,aq}$ activity is obtained as

$$\log\left(a_{H_{2,aq}}\right) = \log\left(a_{H_{2,aq}}\right) - \log\left(K_{H_2}\right) \tag{5.7}$$

The solubility of $H_{2,aq}$ is near the magnetite-iron equilibrium (Fig. 5.23).

Table. 5.6. Chemical formula of minerals and their precipitation reaction considered in the stability field diagram.

	Mineral	Chemical formula	Reaction
(1)	Magnetite	$Fe^{2+}Fe^{3+}{}_2O_4$	$6Fe^{2+}+8H_2O= 2Fe^{2+}Fe^{3+}{}_2O_4+12H^++2H_{2,aq}$
(2)	Fayalite	$Fe^{2+}{}_2SiO_4$	$6Fe^{2+}+3SiO_{2,aq}+6H_2O= 3Fe^{2+}{}_2SiO_4+12H^+$
(3)	Iron	Fe^0	$6Fe^{2+}+6H_{2,aq}= 6Fe^0+12H^+$
(4)	Greenalite	$Fe^{2+}{}_3Si_2O_5(OH)_4$	$6Fe^{2+}+10H_2O+4SiO_{2,aq}= 2Fe^{2+}{}_3Si_2O_5(OH)_4+12H^+$
(5)	Fe-brucite	$Fe^{2+}(OH)_2$	$6Fe^{2+}+ 12H_2O= 6Fe^{2+}(OH)_2+12H^+$
(6)	Hisingerite	$3\square Fe^{3+}{}_2Si_2O_5(OH)_4$	$6Fe^{2+}+ 15H_2O+ 6SiO_{2,aq} = 3\square Fe^{3+}{}_2Si_2O_5(OH)_4+12H^++3H_{2,aq}$
(7)	Cronstedtite	$Fe^{2+}{}_2Fe^{3+}(SiFe^{3+})O_5(OH)_4$	$6Fe^{2+}+ 10.5H_2O+ 1.5SiO_{2,aq} = 1.5Fe^{2+}{}_2Fe^{3+}(SiFe^{3+})O_5(OH)_4+12H^++1.5H_{2,aq}$
(8)	Fe-talc	$Fe^{2+}{}_3Si_4O_{10}(OH)_2$	$6Fe^{2+}+ 8H_2O+ 8SiO_{2,aq} = 2Fe^{2+}{}_3Si_4O_{10}(OH)_2+12H^+$
(9)	Hematite	$Fe^{3+}{}_2O_3$	$6Fe^{2+}+ 9H_2O= 3Fe^{3+}{}_2O_3+3H_2+12H^+$
(10)	Goethite	$Fe^{3+}O(OH)$	$6Fe^{2+}+ 12H_2O= 6Fe^{3+}O(OH)+3H_2+12H^+$

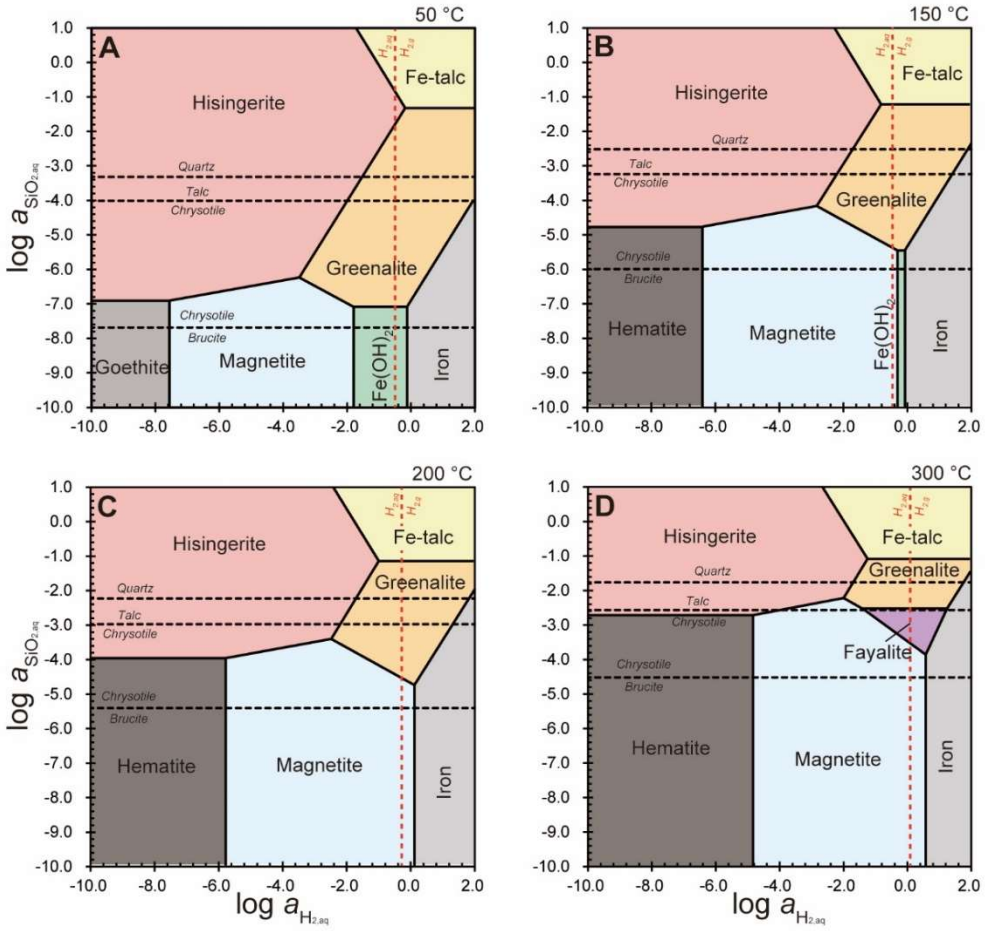

Fig. 5.25. Stability fields of minerals with $H_{2,aq}$ activity and silica activity for the Fe-Si-O-H-system at pressure of 100 MPa and temperatures of (A) 50 °C, (B) 150 °C, (C) 200 °C, and (D) 300 °C. The silica activities of quartz, talc-chrysotile, and chrysotile-brucite are shown in black dashed lines. The upper limit of $H_{2,aq}$ obtained from the reaction of $H_{2,aq}$=$H_{2,g}$ is indicated by the red dotted line.

5.4. Discussion

5.4.1. Hydrogen production by serpentine formation

Serpentine is a mineral that, like magnetite, plays a key role in the production of hydrogen. Serpentine is the key mineral for hydrogen production, especially under conditions where magnetite does not form (high silica activity and/or low temperature: see Fig. 5.25). Here I discuss the effect of serpentine formation on hydrogen production based on the newly obtained redox state and composition data of serpentine.

Iron content and redox state of serpentine

The amount of hydrogen produced by serpentine formation depends on the amount of iron contained and its redox state. The Fe-O-H-Si phase diagram suggests that at low silica activity, oxide or metal (hematite, magnetite, Fe-brucite, Iron) is stable and distribution of Fe to the silicate mineral serpentine is limited, whereas at high silica activity, more Fe is distributed to serpentine (Fig. 5.25). The results of these thermodynamic calculations suggest that in the case of brucite-serpentine equilibrium, the X_{Mg} of serpentine remains high at 0.91-0.97 (Klein *et al.*, 2009, 2013). The X_{Mg} of serpentine in the serpentine-magnetite-brucite coexisting mesh texture was nearly uniform at 0.97, regardless of the lithology. The X_{Mg} of serpentine replacing olivine collected at various locations is 0.90-0.98, independent of their formation temperatures (Fruh-Green *et al.*, 1996; Früh-Green *et al.*, 2004b; Klein *et al.*, 2014; McCollom and Bach, 2009). This supports the results of thermodynamic calculations that the X_{Mg} of serpentine is nearly constant (~0.9-1.0), independent of W/R and temperature (Klein *et al.*, 2009). On the other hand, the serpentinization of Si-rich orthopyroxene (bastite; X_{Mg} = 0.93) and the serpentinization of olivine near altered plagioclase (X_{Mg} = 0.89) have higher iron content than the mesh texture serpentine (X_{Mg} = 0.95-0.98), where no brucite or magnetite was observed. Such Fe-rich serpentine are also found in the highly serpentinized harzburgite and lherzolite (orthopyroxene and clinopyroxene-bearing peridotites) of the Iberia margin (Albers et al., 2021). This is consistent with thermodynamic calculations that show that Fe-rich serpentine are stable when Si activity is higher than magnetite stability field (Klein *et al.*, 2013).

Thermodynamic calculations predict that serpentine with higher $Fe^{3+}/\Sigma Fe$ is more stable at higher water-rock ratios (Klein et al., 2009). At low water-rock ratios (W/R<1), the $Fe^{3+}/\Sigma Fe$ of serpentine is ~0.2-0.3 (Klein et al.) This prediction by thermodynamic calculations is supported by ~0.2 $Fe^{3+}/\Sigma Fe$ of serpentine synthesized by hydrothermal experiments conducted at W/R=1.5 (Marcaillou et al., 2011). At lower water-rock ratios, serpentine has lower $Fe^{3+}/\Sigma Fe$ due to the following Fe^{3+}-serpentine reduction reaction at higher $H_{2,aq}$.

$$2Fe_3Si_2O_5(OH)_4 + 2SiO_{2,aq} + 5H_2O = 3Fe^{3+}{}_2Si_2O_5(OH)_4 + 3H_{2,aq} \quad (R5.1)$$

The presence of awaruite in the mesh texture means that it was in a highly reduced state above $H_{2,aq}$=~340 mM (Frost et al., 1985; McCollom and Bach., 2009). Such a high reduction state requires a low water-rock ratio (W/R<~1) and temperatures around 300 °C, where magnetite formation is maximal (McCollom and Bach., 2009; Klein et al., 2009). These suggest that the mesh texture was formed at low W/R. The 2D imaging XANES results of this study indicate that the $Fe^{3+}/\Sigma Fe$ of the host rock mesh texture is 0.3-0.5 regardless of lithology or starting mineral type (olivine or orthopyroxene; Fig. 5.26), which corresponds to W/R=1-10 in the prediction of thermodynamic calculations (Klein et al. 2009). On the other hand, $Fe^{3+}/\Sigma Fe$ around magnetite veins, which are locally serpentinized, were higher (~0.5~0.6) than in the mesh texture. This is consistent with the fact that water-rock ratios in the vein-forming stages developed in serpentinite are generally considered higher than in serpentinization of the mesh texture (Roumejion et al., 2018, Lithos; Andreani et al., 2013; Lithos). This suggests that the serpentine $Fe^{3+}/\Sigma Fe$ is controlled by water-rock ratio. Taken together, the Fe content of serpentine is mainly controlled by silica activity, and its redox state is controlled by water-rock ratio.

The analytical results and thermodynamic calculations indicate that $Fe^{3+}/\Sigma Fe$ in serpentine is mainly controlled by W/R, with small effects of temperature and silica activity. On the other hand, the concentration of Fe in serpentine is mainly controlled by silica activity. Magnetite formation competes with the formation of Fe-rich serpentine and brucite and is controlled by temperature and silica activity. Serpentine plays an important role in hydrogen production at low temperatures, high W/R, and high silica activity, where magnetite formation is limited. On the other hand, magnetite plays an important role in hydrogen production at relatively high temperature (c.f. >150 °C), low W/R, and low Silica activity.

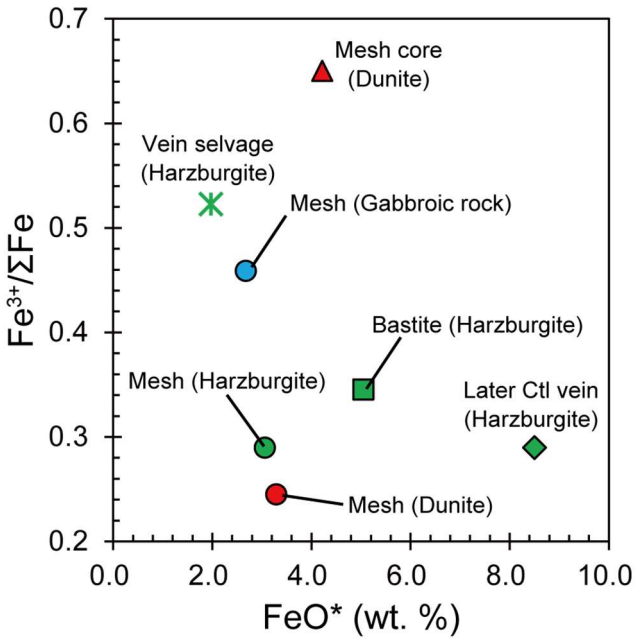

Fig. 5.26. Iron content and iron redox state of each serpentine texture.

5.4.2. Stage of hydrogen production

It is difficult to measure the actual amount of magnetite produced during the mesh texture serpentinization. Here, it was determined from a reaction equation determined from the amount and composition of each mineral. The compositions of olivine, serpentine, and brucite were obtained from EPMA analysis. The amounts of serpentine and brucite were determined from TG. The low abundance of brucite in the gabbroic rocks indicates high silica activity in the serpentinization reaction (Frost and Beard, 2007; Tutolo et al., 2018; Templeton and Ellison., 2020). Fresh olivine in dunite contains magnetite particles (~0.9 wt. %). This magnetite may be formed by dehydrogenation of hydrous olivine (Arai et al., 2021). Such hydrous olivine may be formed near the ridge axis by seawater influx and reaction with melt (Tamura et al., 2022). However, this magnetite formation is obviously not related to serpentinization. In the following discussion, I will exclude this magnetite that is not related to serpentinization. The amount of magnetite obtained from reaction equation was assumed to have been formed during the formation of the mesh texture. The reaction can be written as follows:

$$\underset{\text{Olivine}}{a(Mg_xFe_{1-x})_2SiO_4} + \underset{\text{Water}}{bH_2O} + \underset{\text{Silica}}{cSiO_{2,aq}} = \underset{\text{Serpentine}}{d(Mg_yFe_{1-y})Si_2O_5(OH)_4} + \underset{\text{Brucite}}{e(Mg_zFe_{1-z})(OH)_2} + \underset{\text{Magnetite}}{fFe_3O_4} + \underset{\text{Hydrogen}}{gH_2} \quad \text{(R5.2)}$$

The reaction equations for gabbroic rock, dunite, and harzburgite can be written as follows:

Gabbroic rocks:

$$\underset{\text{Olivine}}{(Mg_{0.84}Fe_{0.16})_2SiO_4} + \underset{\text{Water}}{1.3H_2O} + \underset{\text{Silica}}{0.17SiO_{2,aq}} = \underset{\text{Serpentine}}{0.59(Mg_{0.95}Fe_{0.05})Si_2O_5(OH)_4} + \underset{\text{Magnetite}}{0.79Fe_3O_4} + \underset{\text{Hydrogen}}{0.79H_2} \quad \text{(R5.3)}$$

Dunite:

$$\underset{\text{Olivine}}{(Mg_{0.91}Fe_{0.09})_2SiO_4} + \underset{\text{Water}}{1.4H_2O} + \underset{\text{Silica}}{0.06SiO_{2,aq}} = \underset{\text{Serpentine}}{0.53(Mg_{0.96}Fe_{0.04})Si_2O_5(OH)_4} + \underset{\text{Brucite}}{0.34(Mg_{0.85}Fe_{0.15})(OH)_2} + \underset{\text{Magnetite}}{0.024Fe_3O_4} + \underset{\text{Hydrogen}}{0.024H_2} \quad \text{(R5.4)}$$

Harzburgite:

$$\underset{\text{Olivine}}{(Mg_{0.92}Fe_{0.08})_2SiO_4} + \underset{\text{Water}}{1.4H_2O} + \underset{\text{Silica}}{0.15SiO_{2,aq}}$$

$$= \underset{\text{Serpentine}}{0.57(Mg_{0.96}Fe_{0.04})Si_2O_5(OH)_4} + \underset{\text{Brucite}}{0.23(Mg_{0.79}Fe_{0.21})(OH)_2} + \underset{\text{Magnetite}}{0.015Fe_3O_4} + \underset{\text{Hydrogen}}{0.015H_2} \quad \text{(R5.5)}$$

The mass ratios of the product minerals obtained from these reaction equations are shown in Table 5.6.

Table. 5.6. Calculated mass ratios of the product minerals.

Lithology	Mag (wt%)	Brc (wt%)	Srp (wt%)	Total H_2O (wt%)
Gabbro	10.0	0.0	90.0	11.5
Dunite	2.1	16.6	85.2	15.1
Harzburgite	2.0	8.6	89.4	13.8

Mag = magnetite, Brc = brucite, Srp = serpentine.

The amount of magnetite formed by serpentinization of the mesh texture serpnetinization was determined as the amount of magnetite obtained from these reaction equations as proportional to the loss on ignition. Comparing the amount of magnetite determined by calculation with the amount of magnetite measured from saturation magnetization, some of the dunite and harzburgite samples contain more magnetite than calculated (Fig. 5.27). These magnetites were assumed to be due to magnetite veins in later stages. As mentioned in Chapter 2, gabbroic rocks contain chlorite and prehnite in addition to serpentine. Therefore, note that the LOI of gabbroic rocks may involve other minerals such as chlorite and prehnite in addition to serpentine. This could be one of the reasons for the low amount of magnetite calculated relative to the actual measurements.

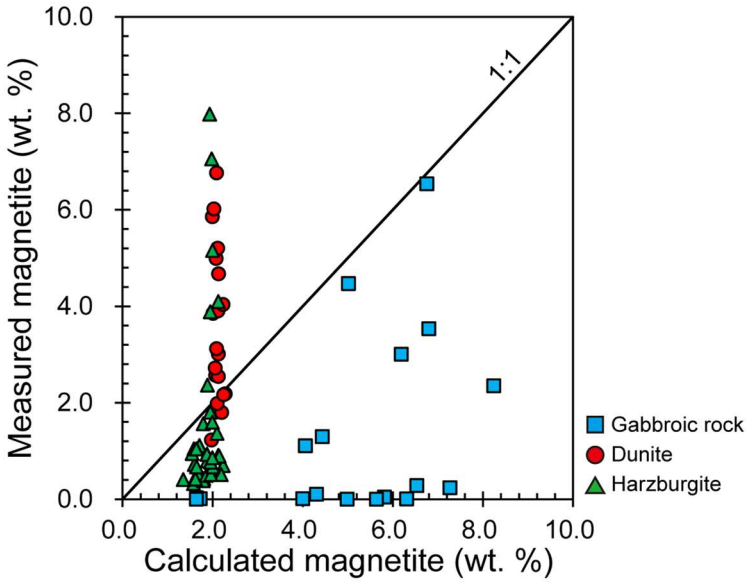

Fig. 5.27. Calculated bulk rock magnetite and measured bulk rock magnetite.

I estimated the contribution of magnetite and serpentine to hydrogen production in each lithology and the hydrogen production stages (Fig. 5.28). The amount of Fe_2O_3 in serpentine and magnetite per kg of rock was calculated from bulk rock data and mineral composition by EPMA and iron redox state from XANES mapping. In this calculation, based on EPMA and XANES mapping results, the $Fe^{3+}/\Sigma Fe$ and X_{Mg} of serpentine were assumed to be 0.4 and 0.97, respectively. The amount of hydrogen produced was estimated from the simplified reaction $Fe_2O_3+H_2=2FeO+H_2O$. The gabbroic rocks produced 84 mM/kg_{rock}, dunite produced 144 mM/kg_{rock}, and harzburgite produced 107 mM/kg_{rock} of hydrogen. The amount of hydrogen production obtained from this equation assumes that all the electrons produced by the oxidation of iron are used for water reduction. Thus, this estimate is the maximum amount that can occur in serpentinization. The presence of nickel-iron alloys (awaruite) suggests that serpentinization occurred in a highly reducing environment, supporting that a substantial amount of hydrogen was generated. Lower crust gabbroic rocks and dunite from crust-mantle transition zone have a large magnetite contribution. The upper mantle has a large contribution of serpentine. The amount of hydrogen formed during serpentinization in harzburgite and dunite is almost the same. This result differs from a previous study that found that harzburgite does not produce as much hydrogen as dunite (Katayama et al., 2010).

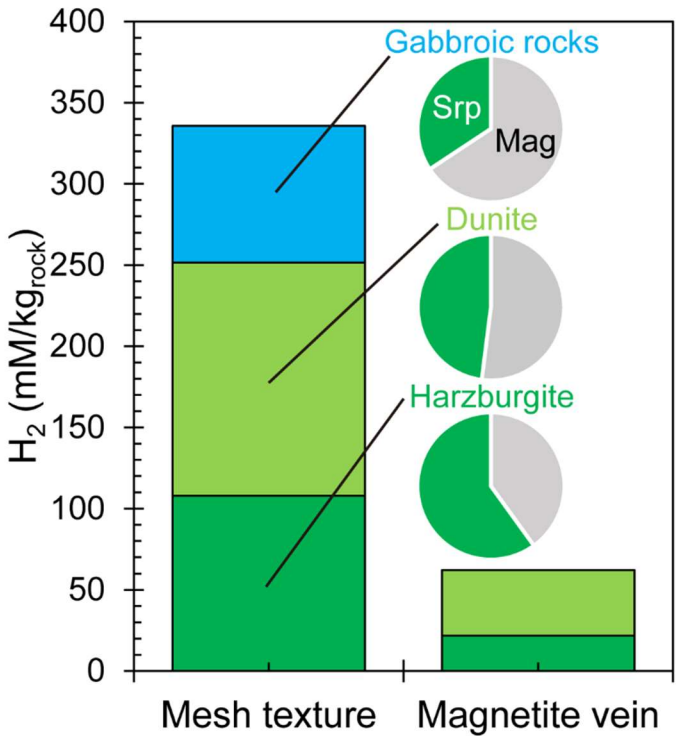

Fig. 5.28. Hydrogen production per unit mass rock and contribution of serpentine and magnetite in each lithology.

5.5. Summaries

In chapter 5, I investigate the microstructure and bulk rock chemistry including the redox state of iron in the gabbroic rocks, dunite, and harzburgite. Serpentine contains substantial amounts of Fe^{3+} ($Fe^{3+}/\Sigma Fe$=0.24-0.46) and plays an important role in hydrogen production in the upper mantle serpentinization. The amount of hydrogen produced per unit mass varies with the amount of olivine in the rock, and olivine-rich gabbro in lower crust also have great potential for hydrogen production.

Comparison of bulk rock analysis and microstructures reveals hydrogen production stages in each lithology. In the gabbroic rocks, magnetite formation during serpentinization is responsible for hydrogen production, and the amount of hydrogen varies with the olivine content. Harzburgite produced hydrogen mainly by serpentinization with mesh structure, and its total hydrogen production was not significantly different from that produced during serpentinization of dunite. Later hydrothermal activity may produce additional hydrogen by magnetite vein formation.

Although previous studies have suggested that harzburgites and gabbroic rocks are unlikely to produce hydrogen because magnetite formation is suppressed by silica-rich minerals, the results of this study indicate that hydrogen is produced by serpentinization of gabbroic rocks and deep harzburgites in oceanic lithosphere.

Chapter 6: Reaction-fracturing-fluid flow interactions on hydrogen production during serpentinization

6.1. Introduction

In this chapter, I integrate and discuss the previous results and discuss how the reaction-destruction-fluid flow interactions affect hydrogen evolution. Many works have been carried out on hydrogen production during serpentinization reactions by laboratory experiments (Marcaillou *et al.*, 2011; McCollom *et al.*, 2020, 2022; Wang *et al.*, 2019), natural observations(Katayama *et al.*, 2010; Klein *et al.*, 2009; Nozaka, 2012; Suda *et al.*, 2014) and thermodynamic calculations (Klein *et al.*, 2009, 2013; McCollom *et al.*, 2022; McCollom and Bach, 2009; Mügler *et al.*, 2016). The results in Chapter 3 indicate that reaction-induced stress form microcracks and increases the permeability of the rock. If silica-rich minerals are present in the rock, the silica activity may increase with the reaction progress because of the formation of microcracks in the silica-rich minerals. The hydrogen production during serpentinization is controlled by temperature, silica activity, and water to rock ratio (Andreani *et al.*, 2013; Klein *et al.*, 2009, 2013, 2014; McCollom *et al.*, 2016, 2020, 2022; McCollom and Bach, 2009). In Chapter 4, I found that regardless of silica activity, serpentine was found to contain a large amount of Fe^{3+} (30-40 wt. % Fe^{3+} in the total Fe). The amount of iron in serpentine is controlled by silica activity while its redox state is controlled by water-rock ratio (Andreani *et al.*, 2013; Klein *et al.*, 2009). These findings suggest that fracture formation associated with the reaction may alter silica activity and water to rock ratio, which in turn may dynamically alter hydrogen production. In this chapter, I integrate the results obtained and discusses how reaction-fracture-fluid interactions affect to the progress of reactions and hydrogen production during serpentinization of oceanic lithospheres.

6.2. Depth profile of the hydrogen production potential

Depth profiles of water content of the drilled core indicate homogeneous serpentinization of mantle rocks. The upper mantle of the Oman ophiolite is more serpentinized than is thought from geophysical observations of the current seafloor. Geophysical observations suggest that serpentinization of oceanic lithosphere is limited before the formation of bending faults near the subduction zone (Grevemeyer et al., 2018; Ivandic et al., 2008). This may indicate that serpentinization of the upper mantle may require reactivation of faults, such as bending faults near trench. In the case of the Oman ophiolite, it is possible that a change in the tectonic setting, such as the over thrusting stage, may have prompted the reactivation of the fault and fluid infiltration into the upper mantle. Thus, there are differences in tectonic processes between the Oman ophiolite and current oceanic lithospheres, and the serpentinization reactions observed in the Oman ophiolite may have been influenced by these processes. However, Oman ophiolite does provide insight into hydrogen generation when typical oceanic lithospheres are serpentinized.

The redox state of iron in all rocks, Fe_2O_3, magnetite content, and loss on ignition show no systematic variation with depth. Dunite in the crust mantle transition zone produces the most hydrogen. However, upper mantle is more abundant than the dunite in the crustal mantle transition zone. The extensive serpentinization of the upper mantle emphasizes its importance as a source of hydrogen production.

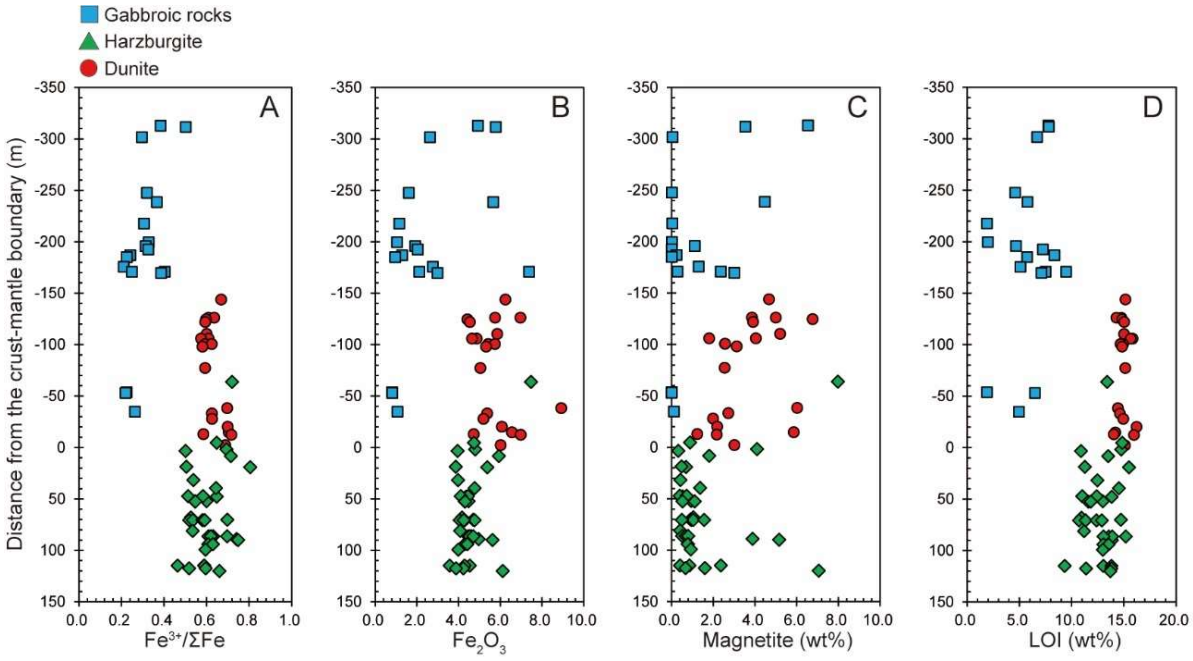

Fig. 6.1. Depth profile of bulk-rock (A)$Fe^{3+}/\Sigma Fe$, (B)Fe_2O_3 (wt. %), (C)Magnetite content (wt. %), (D) Loss on ignition (LOI).

6.3. Reaction-fracturing-fluid flow interaction and hydrogen production during serpentinization

Most of the rocks of the oceanic lithosphere contain silica-rich minerals such as plagioclase and pyroxenes. The results from this study indicate that the serpentinization reaction proceeds by microcrack formation, which enhance fluid penetration and element exchange between different minerals. Numerical and thermodynamic modeling of the serpentinization process in previous studies assume that the olivine and pyroxene in the peridotite reach equilibrium at the same time (Klein *et al.*, 2009, 2013; Malvoisin *et al.*, 2012a; McCollom *et al.*, 2022). However, as shown in this study, microcrack formation in silica-rich minerals (plagioclase and pyroxenes) changes the silica activity of the fluid during the serpentinization. The microcrack formation during the serpentinization reaction increases the silica activity and water to rock mass ratio, which effect on evolution of the hydrogen production during serpentinization. As revealed in Chapter 5, Serpentinization with mesh structure was the main stage of hydrogen production. Therefore, I focus on this mesh texture stage. Next, I discuss the effects of reaction-induced fracturing and enhanced fluid flow on hydrogen production.

6.3.1. Serpentinization at low W/R and low silica activity

Fig. 6.2 schematically illustrates the changes in hydrogen production rates related to reaction-fracturing-fluid interactions during serpentinization of gabbroic rock. The concept is the same for harzburgite, which contains silica-rich mineral (orthopyroxene), although I will use olivine gabbro as an example here. The initial stage of the serpentinization reaction is characterized by low W/R and low Si activity. Possible fluid pathways at this stage are microcracks formed by thermal stress and grain boundaries (Chapter 3). Even in silica-rich gabbric rocks, the preferential microcrack formation in olivine grains due to thermal stresses leads to a large reaction surface of olivine rather than silica-rich minerals (plagioclase), resulting in an olivine-dominated water-rock reaction. Traces of serpentinization with relatively low silica activity during this initial stage were observed as a mesh texture containing brucite in the gabbroic rock (Chapter 3). Fe content of serpentine mainly controlled by silica activity (Chapter 5). The X_{Mg} of the serpentine in the mesh texture is 0.96-0.97 regardless of lithology, suggesting low silica activity. The $Fe^{3+}/\Sigma Fe$ of the mesh texture is 0.3-0.4, independent of lithology, and is lower than that of serpentine surrounding magnetite veins. This suggests that serpentinization of the mesh texture occurred at relatively low W/R. According to thermodynamic modeling by Klein et al. (2009), the $Fe^{3+}/\Sigma Fe$ of this serpentine corresponds to W/R=5-10. The presence of Ni-Fe alloy in the mesh texture also suggests that a highly reduced environment during mesh texture serpentinization, which achieved by low W/R and magnetite formation, and such conditions are achieved in the 250-365°C temperature range (e.g., ~ 340 mM; McCollom and Bach, 2009). In the case of harzburgite, the formation of brucite is inhibited due to the high proportion of silica-rich minerals. Although harzburgite

contains orthopyroxene, a silica-rich mineral, it appears that in the case of the Oman ophiolite it did not react as much in the initial stages, as orthopyroxene is rarely reacted away from the mineral veins. A possible reason for this is the difference in the temperature dependence of the dissolution rates of olivine and orthopyroxene (Janecky & Seyfried, 1986; Okamoto et al., 2011). The preferential reaction of olivine could be due to the fact that the Oman ophiolite harzburgite progressed at relatively low temperatures (200-250 °C; Aupart et al., 2021), where the olivine dissolution rate is relatively faster than that of pyroxene (Ogasawara *et al.*, 2013).

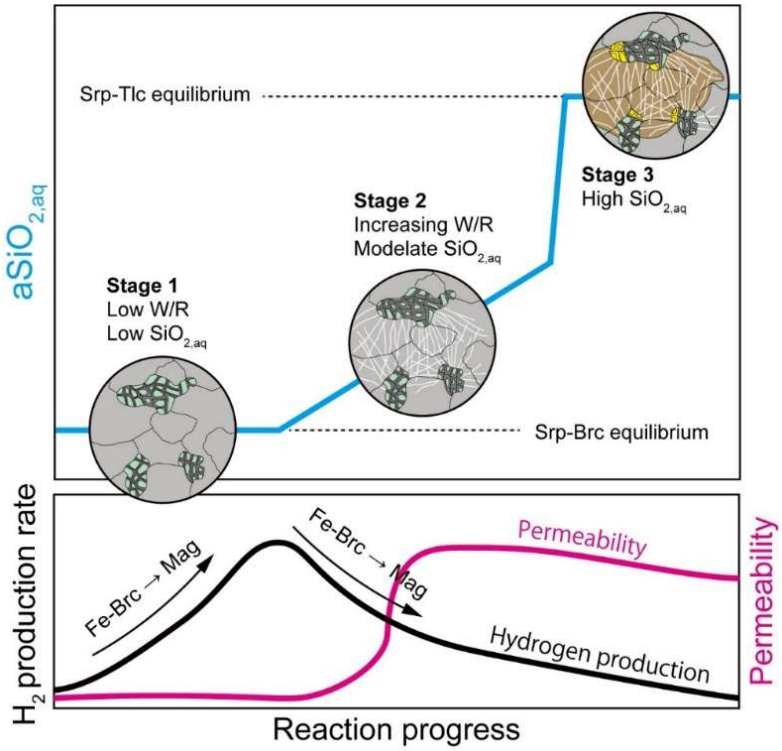

Fig. 6.2. Schematic illustration of the evolution of hydrogen production related to the reaction-fracturing-fluid flow interaction during serpentinization of gabbroic rocks. In Stage 1, olivine-dominated reactions occur at low W/R and low silica activity. In Stage 2, Microcracks formed by the serpentinization of olivine form fluid paths while also increasing the reaction area of silica-rich minerals, resulting increasing silica activity. This decompose the brucite and promotes magnetite formation. Further microcrack propagation will further increase silica activity and water rock ratio. As a result, magnetite is decomposed, and iron-rich serpentinite is formed instead. The increase in W/R reduces the hydrogen concentration and may suppress hydrogen production due to oxygen in the fluid. A similar process occurs in harzburgite, which contains orthopyroxene, a silica-rich mineral.

6.3.2. Increasing W/R and silica activity

Reaction path modeling results show that increased Si activity due to serpentinization of orthopyroxene results in decreased amounts of brucite and increased amounts of magnetite (Klein and Bach., 2013). The increasing of Si activity also can be occurred by alteration of anorthite (Chapter 2). As the serpentinization of olivine progresses, microcracks form due to the volume increase associated with the reaction (Chapter 3). The formation of microcracks increases the permeability of the rock, causing an increase in W/R (Chapter 3). In the case of gabbroic rocks and harzburgite, the formation of microcracks in the silica-rich minerals (orthopyroxene and plagioclase) by serpentinization of olivine increases silica activity (Chapter 3). This change from a near olivine-dominated closed system to an open system with influx of Si and Al also has been reported in many other previous studies (Bach *et al.*, 2006; Beard *et al.*, 2009; Oyanagi *et al.*, 2018; Viti and Mellini, 1998). When brucite is present, silica activity is buffered by the serpentine-brucite equilibrium, and the iron released by the decrease in brucite is primarily used to form magnetite. During this stage, iron content of serpentine is nearly constant. The simplified reaction can be written as follow.

$$2Fe(OH)_2 + SiO_{2,aq} = Fe_2O_3 + H_2O + H_{2,aq} \quad (R6.1)$$

This can increase the amount of hydrogen produced per unit rock; the increase in magnetite content due to increased Si activity will continue until brucite disappears completely. High silica activity has been thought to potentially inhibit magnetite formation during serpentinization of dunite and harzburgite (Katayama *et al.*, 2010; McCollom and Bach, 2009; Oyanagi *et al.*, 2018; Seyfried *et al.*, 2007). However, thermodynamic calculations suggest that magnetite content increases inversely while buffered by serpentine-brucite equilibrium. This result consistent with the petrographic observations of magnetite formation due to increased silica activity (Bach *et al.*, 2006; Miyoshi *et al.*, 2014). Iron in brucite is basically ferrous and therefore does not contribute to hydrogen production in serpentinization reactions. Therefore, iron-rich brucite formed in early-stage serpentinization involving dunite and harzburgite mesh structures may consume iron available for water reduction and inhibit hydrogen production (Klein *et al.*, 2009). However, the present results suggest that Fe-rich brucite formed in the early stages may play an important role in hydrogen production in the later stages of the serpentinization by forming magnetite as the transitions from a closed to open system. Such magnetite formation during the late serpentinization reaction has also been noted from observations of seafloor drilling samples and ophiolitic samples(Bach *et al.*, 2006; Miyoshi *et al.*, 2014). This process may play an important role as a hydrogen production in low-temperature environments where life is more likely to be active (Templeton and Ellison, 2020).

6.3.3. Serpentinization at high Si activity

Lower temperatures are expected in the later stages of the serpentinization reaction. Lower temperatures can generate greater reaction-induced stresses, which can lead to further crack formation (Kelemen and Hirth, 2012). In addition, the decrease in olivine content due to progressive serpentinization is expected to increase the contribution of silica-rich minerals to the olivine serpentinization reaction and further increase silica activity. After complete consumption of brucite, silica activity will be buffered by the serpentine-talc equilibrium. High silica activity leads to the formation of iron-rich serpentine, which is associated with a decrease in magnetite. This reaction consumes $H_{2,aq}$ in solution and decreases the $H_{2,aq}$ activity. This reaction can be written as follow:

$$Fe_3O_4 + H_2O + H_{2,aq} + 2SiO_{2,aq} = Fe_3Si_2O_5(OH)_4 \qquad (R6.2)$$

As shown in Chapter 5, serpentine $Fe^{3+}/\Sigma Fe$ is controlled by W/R. The higher the W/R, the more serpentine is enriched in Fe^{3+} than Fe^{2+}. Therefore, one might assume that if the W/R is high and the $Fe^{3+}/\Sigma Fe$ of the serpentine is high, more hydrogen will be produced. However, such a large amount of hydrogen generation from the formation of serpentine with high $Fe^{3+}/\Sigma Fe$ would be unlikely to occur. First, oxygen in the fluid would inhibit hydrogen generation. First, oxygen in fluid exhibit production of hydrogen during serpentinization because the electrons produced by iron oxidation would be used to reduce $O_{2,aq}$ in the fluid rather than to reduce water (Ely et al., 2023). Under high W/R conditions, where high $Fe^{3+}/\Sigma Fe$ is expected, the effect of oxygen in the fluid will be significant. Thus, the presence of serpentine with high $Fe^{3+}/\Sigma Fe$ does not always imply a large amount of hydrogen generation.

Second, large aperture cracks are necessary to maintain high W/R. However, large aperture cracks formed in serpentine can be closed within a few years to a few months by serpentine precipitation, and high permeability may not be maintained for long (Chapter 4; Farough et al., 2016). In addition, the area of high $Fe^{3+}/\Sigma Fe$ around magnetite veins is limited to a few centimeters and is quite localized. This suggests that the fluid flow that created the magnetite veins is also short-lived. High W/R is likely to be achieved if fluid access is sufficient and if disturbing events such as earthquakes occur with high frequency.

In summary, the formation of microcracks by reaction-induced stress increases the W/R of the rock and, in the case of gabbroic rocks and harzburgite, the formation of microcracks in the orthopyroxene and plagioclase surrounding the olivine increases the reaction area of these minerals, resulting in an increase in silica activity. The reaction and associated cracking formation and enhanced fluid flow promote a change from an olivine-dominated closed system to an open system with influx of Si and Al, controlling the total amount and concentration of hydrogen production during serpentinization. The results of this study show that the amount and concentration of hydrogen generation changes dynamically change as the reaction progresses due to W/R and silica activity associated with crack formation.

6.4. Fluid infiltration, serpentinization and hydrogen production in the Oceanic lithosphere

Here I discuss the serpentinization process and hydrogen production in oceanic lithospheres, based on the findings from the Omani ophiolite. The depth of serpentinization in the oceanic lithosphere is limited by temperature and fluid access. Hydrothermal experiments and thermodynamic calculations performed at various temperatures suggest that serpentinization can progress at temperatures below 350-400°C, corresponding to 5-20 km below the seafloor (Martin and Fyfe., 1970; Evans et al., 2004). Detachment faults near the ridge axis (de Martin *et al.*, 2007; Zihlmann *et al.*, 2018) and bending faults in the outer ridge region (Faccenda *et al.*, 2009; Hatakeyama *et al.*, 2017; Ranero *et al.*, 2003) allow fluid supply to the deeper parts of the oceanic lithosphere. Faults formed near the ridge axis could be the primary fluid flow pathway in the serpentinization of the mantle of the Oman ophiolite (Aupart et al., 2021). Because of the high temperatures at high spreading rate ridge axis, large-scale serpentinization is not usually thought to occur. Hydrothermal activity near the ridge axis may have played an important role in cooling the oceanic lithosphere to temperatures that allowed serpentinization (Bosch *et al.*, 2004; Gregory and Taylor, 1981). Numerical simulations of hydrothermal activity near the ridge axis suggest that at distances greater than about 20 km from the ridge axis, temperatures decrease to temperatures that allow serpentinization of the upper mantle (Iyer *et al.*, 2010). In fact, the CM site is 20 km from the axis of the pareo-ridge axis, where temperatures could decrease to temperatures that allow serpentinization.

While faults are important as major fluid transport pathways, serpentinization of the Oman ophiolite was extensive without localizing it in the vicinity of faults (Chapter 2). The importance of microcracks in such extensive serpentinization has been emphasized (Malvoisin et al.; Aupart et al., 2021). The results of this study highlight that microcrack formation at different mechanisms/stages can cause selective microcrack formation in rocks and dynamically change the amount of hydrogen generation in serpentinization reactions. Based on this, I discuss how the location and amount of hydrogen generation changes over the life of the oceanic lithosphere.

6.4.1. Serpentinization near ridge axis

Near the ridge axis with high spreading rate, the oceanic lithosphere is rapidly cooled by hydrothermal circulation (VanTongeren *et al.*, 2008). Cooling of the oceanic lithosphere as it moves away from the ridge axis is expected to be the first to initiate serpentinization of the lower crust gabbroic rocks above the mantle due to fluid infiltration and hydrothermal circulation (Fig. 6.3B). Thermal stress is the most likely mechanism for microcrack formation in the earliest stages, before serpentinization.

Boudier et al. (2005) showed that microcracks form due to the anisotropic thermal expansion of olivine and plagioclase. They suggested that thermal contraction of the plagioclase-rich lower crust with high thermal expansion anisotropy, occurring near the axis of extension, could produce vertical fractures similar to those observed in high-temperature alteration veins. These vertical fractures could act as fluid pathways for serpentinization in the off-axis (Boudier et al., 2005). In addition to anisotropy in thermal expansion, differences in thermal contraction between different minerals may also cause microcrack formation. As shown in Chapter 3, the thermal expansion of olivine is greater than that of pyroxene and feldspar and may preferentially form microcracks within olivine as temperature decreases. In fact, more microcracks were observed in olivine in the less serpentinized gabbroic rocks than in the surrounding plagioclase and pyroxene (Fig. 3.1D). The higher crack density of olivine relative to silica-rich minerals (plagioclase and pyroxene), resulting olivine-dominant water-rock reactions at early stage of serpentinization. This is supported by the low Al concentration and presence of brucite in the early stage mesh texture (type 1 mesh texture) in gabbroic rocks (Chapter 3). This high temperature and low silica activity serpentinization is favorable for magnetite formation, and hydrogen production is primarily controlled by magnetite formation. In addition to this thermal stress-induced crack formation process, the serpentinization of olivine itself plays an important role in the formation of interconnected microcrack networks formation. As serpentinization progresses, reaction-induced stress develops, and fluid penetration is enhanced in the lower crust gabbroic rocks (Fig. 6.3B). In the case of gabbroic rocks, which contain silica-rich mineral (plagioclase), microcrack development in these minerals increases silica activity and Al concentrations, resulting in production of the relatively Al-rich serpentine and decomposition of brucite. This could result in the production of more magnetite and hydrogen.

6.4.2. Serpentinization at off-axis

As the oceanic lithosphere continues to cool, the temperature isotherm at which the serpentinization reaction occurs reaches the upper mantle, initiating serpentinization of mantle dunite and mantle harzburgite. In contrast to the lower crust, where cracks have already formed, the initial reaction of harzburgite in the upper mantle may be selective olivine crack formation due to anisotropy of thermal stress. On the other hand, in the lower crust, magnetite may become unstable due to hydrothermal alteration of silica-rich minerals (plagioclase and pyroxenes) and increased silica activity. The suppression of magnetite decomposition or formation due to increased silica activity would reduce hydrogen generation in the lower crust, while the upper mantle would play a more important role in hydrogen production. Upper mantle harzburgite may selectively form cracks within the olivine due to thermal stress anisotropy. This may cause the initial stage of upper mantle serpentinization to be selective for olivine. Such selective serpentinization of olivine was observed in this study and has been noted in other studies (Viti and Mellini., 1998).

Furthermore, serpentinization of the Oman ophiolite may have been caused by fluid supply from the subducting slab, in addition to fluid infiltration from the seafloor as discussed previously. In

other ophiolites, fluid supply from subducting slabs has caused massive serpentinization. For example, in the Chandman meta-peridotite body in Mongolia, fluid supply from the subducting slab is the main source of mantle hydration (Dandar *et al.*, 2023). The antigorite + chrysotile veins in the dunite and harzburgite studied in this study suggest that they formed in association with the setting of the subduction zone (Chapter 4). However, the estimated short duration of fluid activity suggests that their contribution to the serpentinization reaction progression was limited. This suggests that the contribution of fluids from the subducting slab was limited in the serpentinization of the Oman ophiolite.

These results suggest that the site of hydrogen production from serpentinization in oceanic lithospheres may transition from the lower crust to the deep mantle. Furthermore, the formation of microcracks at different mechanistic stages may cause selective microcrack formation in minerals in the rocks, highlighting the possibility of dynamic changes in hydrogen evolution during serpentinization reactions. Such changes in hydrogen production in the oceanic lithosphere can lead to temporal and spatial variations in the deep microbial biomass. On the other hand, elements such as carbon and nitrogen are also required for microbial growth. Therefore, an estimate of the extent of the deep biosphere based on the amount of hydrogen production will only give the upper limit of the biosphere. A more realistic estimate of the deep biosphere should also take into account the mass transport of carbon and nitrogen. In addition, hydrogen produced by serpentinization must be transported to a location with a temperature suitable for microbial life (e.g., T<150 °C). Therefore, it is important to develop models that account for the temporal variability of hydrogen production and the transport of elements essential for life, including hydrogen, to explore the possibility of life on other planets as well as the spatial and temporal variability of deep microbial life biomass.

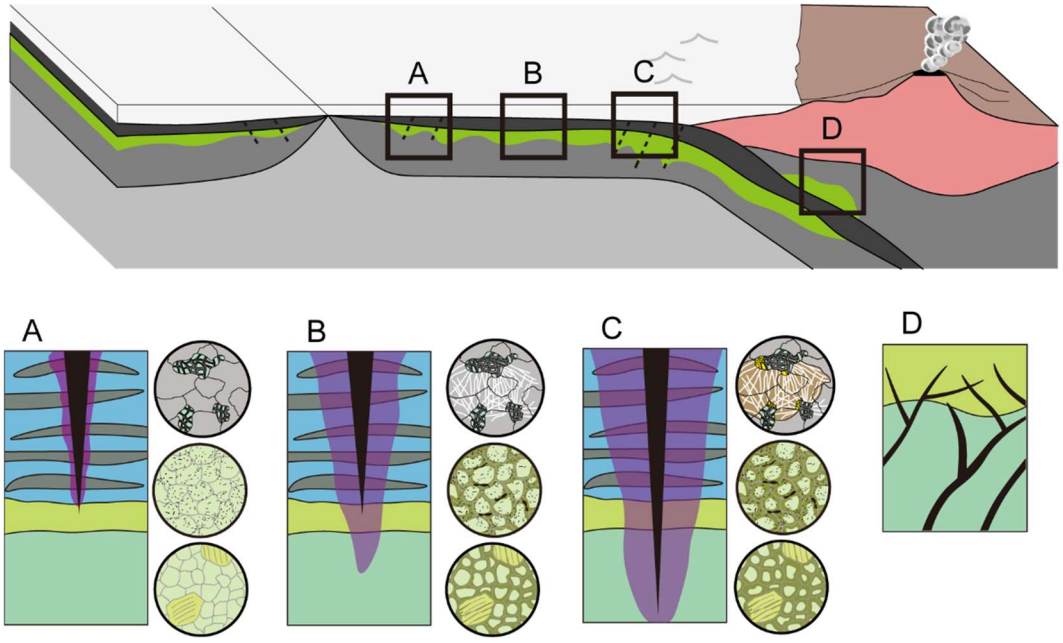

Fig. 6.3. Conceptual illustration of fracturing, reaction, and fluid flow in the seafloor and subduction zone setting. Serpentinization near ridge-axis (A), off-axis (B), bending-fault (C), and subduction zone (D).

6.5. Summaries

Based on all the results obtained in this study, this chapter discusses how the interaction between the reaction and associated microcrack formation and fluid flow affects the serpentinization reaction progression and hydrogen production of rocks in the oceanic lithosphere. The results suggest that cracks produced by volume changes due to olivine serpentinization may have increased the permeability of the lower crust and upper mantle, which have low permeability, and may have played an important role in the several hundred-meter scale serpentinization observed in the Oman Ophiolite. Such widespread serpentinization that is not localized to faults may also be important in the ongoing serpentinization reactions.

The formation of microcracks increases the W/R of the rock and also increases silica activity by forming cracks in the silica-rich minerals (orthopyroxene and plagioclase) around olivine and increasing the reaction area of these minerals. This enhancement of fluid flow and silica activity due to the reaction and associated crack formation, which changes the reaction from a near closed system in the early stages of olivine-dominated serpentinization to an open system with Si and Al influx, has been shown to control the amount and concentration of hydrogen generation that is occurring due to the serpentinization reaction.

The results show that the amount and concentration of hydrogen produced by the serpentinization reaction is dynamically controlled by reaction-fracturing-fluid flow interaction during serpentinization in the oceanic lithosphere. The dynamic changes in hydrogen production may affect the spatial and temporal evolution of the deep biosphere on the seafloor.

Chapter 7: Conclusions

In this study, petrographic observations and chemical analysis, including iron redox state, of rock samples from the lower crust to the upper mantle of the Oman ophiolite were conducted. Combining results from the numerical simulations using coupled reaction-mechanical-fluid flow 2-D discrete element method and thermodynamic calculations, the hydrogen production process in the serpentinization reaction of oceanic lithospheres, where reaction-fracture-fluid transfer interacts, was revealed.

In Chapter 2, rock samples from the lower crust to the upper mantle of the Oman ophiolite were analyzed and observed. Systematic analysis of 404 m of drill core (CM1A) from the lower crust-upper mantle and 300 m of drill core (CM2B) from the crust-mantle boundary-upper mantle revealed homogeneous serpentinization with respect to depth. Serpentinization is particularly advanced around mineral veins in the rock samples, but is limited in extent, and the main serpentinization is extensive with a mesh structure. Trace element analyses of antigorite + chrysotile veins at the crust-mantle boundary indicate that these mineral veins are rich in As and Sb, indicating geoscientific signatures of subducted sediments. These results indicate that the main serpentinization occurred during the seafloor stage.

In Chapter 3, the formation mechanism of microcracks was discussed based on observations of natural samples and numerical simulations coupling fracture-reaction-fluid transfer. Comparison of the numerical simulation results with natural samples revealed that the stress induced by the reaction-induced volume change may play an important role in crack formation as a crack formation mechanism. The microstructures of the natural samples suggest that a change from a closed system to an open system occurred during the serpentinization reaction. Crack formation associated with the reaction enhance reaction progress as well as causing an increase in W/R and Si activity. These results suggest that the reaction-associated crack formation may have caused positive feedback that facilitated fluid movement and further reaction progression.

In Chapter 4, I focused on mineral veins, which are traces of relatively large fractures that may play an important role as high-speed fluid migration pathways. I focused on serpentine veins found in serpentinite and the reaction zones that developed around them to estimate the velocity, timescale, and flow rate of fluid movement through the fractures. The results indicate that minerals precipitate in the cracks for geologically short periods of time (months to years) and that high permeability is not maintained for long periods of time.

In Chapter 5, bulk rock and local chemical analyses, including the redox state of iron, were performed on lower crustal gabbroic rocks, dunite at the crust-mantle boundary, and harzburgite in the upper mantle. Iron redox state mapping using synchrotron X-ray absorption fine structure spectroscopy was used to investigate the redox state of iron in each mineral and to determine the hydrogen production history recorded in the rock texture. Serpentine contains significant amounts of Fe^{3+} and plays an important role in hydrogen production when magnetite is less commonly produced. The contributions

of magnetite and serpentine to hydrogen generation in each lithology were investigated in terms of bulk rock compositions, iron content of each mineral, and detailed microstructures. Estimation of hydrogen generation in serpentinization with mesh texture and subsequent magnetite veins indicates that serpentinization with mesh texture is the main stage. In the serpentinization with mesh texture, gabbroic rocks, dunite, and harzburgite were estimated to have generated 84 mM/kg rock, 144 mM/kg rock, and 107 mM/kg rock of hydrogen, respectively. Calculations of the contribution of serpentine and magnetite to hydrogen generation indicate that magnetite is the major contributor to hydrogen generation in the gabbroic rocks, whereas serpentine is the major contributor in dunite and harzburgite.

These results indicate that the formation of cracks during the serpentinization reaction increases the W/R of the rock and also increases silica activity by forming cracks in the silica-rich minerals (orthopyroxene and plagioclase) around olivine and increasing the reaction area of these minerals. This dynamic change in fluid flow enhancement and silica activity due to the reaction and associated crack formation may control the amount and concentration of hydrogen produced by the serpentinization reaction. Future experimental investigations of the reaction rates of the minerals and development of models that account for changes in silica activity and W/R associated with crack formation involved will provide more accurate predictions of temporal changes in hydrogen generation at the seafloor.

References

Abily, B., Ceuleneer, G. (2013) The dunitic mantle-crust transition zone in the Oman ophiolite: Residue of melt-rock interaction, cumulates from high-MgO melts, or both? *Geology* 41, 67–70.

Agard, P., Yamato, P., Soret, M., Prigent, C., Guillot, S., Plunder, A., Dubacq, B., Chauvet, A., Monié, P. (2016) Plate interface rheological switches during subduction infancy: Control on slab penetration and metamorphic sole formation. *Earth and Planetary Science Letters*. Elsevier B.V. 451, 208–220.

Ague, J.J. (2011) Extreme channelization of fluid and the problem of element mobility during Barrovian metamorphism. *American Mineralogist*. Walter de Gruyter GmbH 96, 333–352.

Alabaster, T., Pearce, J.A., Malpas, J. (1982) The volcanic stratigraphy and petrogenesis of the Oman ophiolite complex. *Contributions to Mineralogy and Petrology* 81, 168–183.

Albers, E., Bach, W., Pérez-Gussinyé, M., McCammon, C., Frederichs, T. (2021) Serpentinization-Driven H2 Production From Continental Break-Up to Mid-Ocean Ridge Spreading: Unexpected High Rates at the West Iberia Margin. *Frontiers in Earth Science*. Frontiers Media S.A. 9.

Andreani, M., Grauby, O., Baronnet, A., Muñoz, M. (2008) Occurrence, composition and growth of polyhedral serpentine. *European Journal of Mineralogy*. Schweizerbart 20, 159–171.

Andreani, M., Mével, C., Boullier, A.M., Escartín, J. (2007) Dynamic control on serpentine crystallization in veins: Constraints on hydration processes in oceanic peridotites. *Geochemistry, Geophysics, Geosystems* 8.

Andreani, M., Muñoz, M., Marcaillou, C., Delacour, A. (2013) μXANES study of iron redox state in serpentine during oceanic serpentinization. *Lithos* 178, 70–83.

Audet, P., Bostock, M.G., Christensen, N.I., Peacock, S.M. (2009) Seismic evidence for overpressured subducted oceanic crust and megathrust fault sealing. *Nature*. Nature Publishing Group 457, 76–8.

Aupart, C., Morales, L., Godard, M., Jamtveit, B. (2021) Seismic faults triggered early stage serpentinization of peridotites from the Samail Ophiolite, Oman. *Earth and Planetary Science Letters*. Elsevier B.V. 574.

Auzende, A.-L., Devouard, B., Guillot, S. phane, Daniel, I., Baronnet, A., Lardeaux, J.-M. (2002) Serpentinites from Central Cuba: petrology and HRTEM study. *European Journal of Mineralogy*. Schweizerbart 14, 905–914.

Bach, W., Irber, W. (1998) Rare earth element mobility in the oceanic lower sheeted dyke complex: evidence from geochemical data and leaching experiments. *Chemical Geology* 151, 309–326.

Bach, W., Paulick, H., Garrido, C.J., Ildefonse, B., Meurer, W.P., Humphris, S.E. (2006) Unraveling the sequence of serpentinization reactions: Petrography, mineral chemistry, and petrophysics of serpentinites from MAR 15°N (ODP Leg 209, Site 1274). *Geophysical Research Letters* 33.

Bar-On, Y.M., Phillips, R., Milo, R. (2018) The biomass distribution on Earth. *Proceedings of the National Academy of Sciences of the United States of America*. National Academy of Sciences 115,

6506–6511.

Beard, J.S., Frost, B.R., Fryer, P., McCaig, A., Searle, R., Ildefonse, B., Zinin, P., Sharma, S.K. (2009) Onset and progression of serpentinization and magnetite formation in Olivine-rich troctolite from IODP hole U1309D. *Journal of Petrology* 50, 387–403.

Beaudoin, N., Hamilton, A., Koehn, D., Shipton, Z.K., Kelka, U. (2018) Reaction-induced porosity fingering: Replacement dynamic and porosity evolution in the KBr-KCl system. *Geochimica et Cosmochimica Acta*. Elsevier Ltd 232, 163–180.

Beinlich, A., John, T., Vrijmoed, J.C., Tominaga, M., Magna, T., Podladchikov, Y.Y. (2020) Instantaneous rock transformations in the deep crust driven by reactive fluid flow. *Nature Geoscience*. Nature Research 13, 307–311.

Belluso, E., Cavallo, A., Halterman, D. (2017) Crystal habit of mineral fibres. *European Mineralogical Union Notes in Mineralogy*. Mineralogical Society 18, 65–109.

Berndt, M.E., Allen, D.E., Seyfried, W.E. (1996) Reduction of CO2 during serpentinization of olivine at 300 °C and 500 bar. *Geology* 24, 351.

Bicknell, J.D., Sempere, J.C., Macdonald, K.C., Fox, P.J. (1987) Tectonics of a fast spreading center: A Deep-Tow and sea beam survey on the East Pacific rise at 19°30′ S. *Marine Geophysical Researches* 9, 25–45.

Blackman, D.K., Ildefonse, B., John, B.E., Ohara, Y., Miller, D.J., MacLeod, C.J., Scientists, the E. 304/305 (2006) Site U1309. *Proceedings of the IODP, 304/305*. Integrated Ocean Drilling Program.

Blanc, P., Vieillard, P., Gailhanou, H., Gaboreau, S., Gaucher, É., Fialips, C.I., Madé, B., Giffaut, E. (2015) A generalized model for predicting the thermodynamic properties of clay minerals. *American Journal of Science*. Yale University 315, 734–780.

Bosch, D., Jamais, M., Boudier, F., Nicolas, A., Dautria, J.M., Agrinier, P. (2004) Deep and high-temperature hydrothermal circulation in the Oman ophiolite - Petrological and isotopic evidence. *Journal of Petrology* 45, 1181–1208.

Botto, R.I., Morrison, G.H. (1976) Josephinite; a unique nickel-iron. *American Journal of Science* 276, 241–274.

Boudier, F., Coleman, R.G. (1981a) Cross Section Through the Peridotite in the Samail Ophiolite, Southeastern Oman Mountains. 86, 2573–2592.

Boudier, F., Coleman, R.G. (1981b) Cross Section Through the Peridotite in the Samail Ophiolite, Southeastern Oman Mountains. *Journal of Geophysical Research* 86, 2573–2592.

Boudier, F., Nicolas, A. (1995) Nature of the moho transition zone in the Oman ophiolite. *Journal of Petrology* 36, 777–796.

Boudier, F., Nicolas, A., Ildefonse, B. (1996) Magma chambers in the oman ophiolite: Fed from the top and the bottom. *Earth and Planetary Science Letters* 144, 239–250.

Boudier, F., Nicolas, A., Mainprice, D. (2005) Does Anisotropy of Thermal Contraction Control Hydrothermal Circulation at the Moho Level below Fast Spreading Oceanic Ridges? *International Geology Review* 47, 101–112.

Buck, W.R., Lavier, L.L., Poliakov, A.N.B. (2005) Modes of faulting at mid-ocean ridges. *Nature* 434, 719–723.

Cai, C., Wiens, D.A., Shen, W., Eimer, M. (2018) Water input into the Mariana subduction zone estimated from ocean-bottom seismic data. *Nature*. Nature Publishing Group 563, 389–392.

Cannat, M. (1993) Emplacement of mantle rocks in the seafloor at mid-ocean ridges. *Journal of Geophysical Research: Solid Earth* 98, 4163–4172.

Cannat, M., Fontaine, F., Escartín, J. (2010) Serpentinization and associated hydrogen and methane fluxes at slow spreading ridges. , 241–264.

Capitani, G., Compagnoni, R., Cossio, R., Botta, S., Mellini, M. (2021) The intracrystalline microstructure of Monte Fico lizardite, by optics, <i>μ</i>-Raman spectroscopy and TEM. *European Journal of Mineralogy*. Copernicus GmbH 33, 425–432.

Carter, E.J., O'Driscoll, B., Burgess, R., Clay, P.L. (2021) Multi-stage fluid infiltration and metasomatism in supra-subduction zone mantle: evidence from halogens and noble gases in the Leka Ophiolite Complex, Norway. *Geochimica et Cosmochimica Acta*. Elsevier Ltd 307, 258–280.

Chen, L., Tian, L., Hu, S.-Y., Gong, X., Dong, Y., Gao, J., Ding, W., Wu, T., Liu, H. (2023) Seafloor hydrothermal circulation at a rifted margin of the South China Sea: Insights from basement epidote veins in IODP Hole U1502B. *Lithos*. Elsevier B.V. 444–445, 107102.

Chernosky, J. V. (1998) The stability of tremolite: New experimental data and a thermodynamic assessment. *American Mineralogist* 83, 726–738.

Christensen, N.I. (1972) The Abundance of Serpentinites in the Oceanic Crust. *The Journal of Geology* 80, 709–719.

Christensen, N.I. (1978) Ophiolites, seismic velocities and oceanic crustal structure. *Tectonophysics* 47, 131–157.

Christensen, N.I. (1996) Poisson's ratio and crustal seismology. *Journal of Geophysical Research: Solid Earth*. American Geophysical Union 101, 3139–3156.

Christensen, N.I. (2004) Serpentinites, Peridotites, and Seismology. *International Geology Review* 46, 795–816.

Christensen, N.I., Salisbury, M.H. (1975) Structure and constitution of the lower oceanic crust. *Reviews of Geophysics* 13, 57–86.

Cluzel, D., Boulvais, P., Iseppi, M., Lahondère, D., Lesimple, S., Maurizot, P., Paquette, J.L., Tarantola, A., Ulrich, M. (2020) Slab-derived origin of tremolite–antigorite veins in a supra-subduction ophiolite: the Peridotite Nappe (New Caledonia) as a case study. *International Journal of Earth Sciences*. Springer 109, 171–196.

Coleman, R.G., Keith, T.E. (1971) A Chemical Study of Serpentinization--Burro Mountain, California. *Journal of Petrology* 12, 311–328.

Colman, D.R., Poudel, S., Stamps, B.W., Boyd, E.S., Spear, J.R. (2017) The deep, hot biosphere: Twenty-five years of retrospection. *Proceedings of the National Academy of Sciences of the United States of America*. National Academy of Sciences, 6895–6903.

Compagnoni, R., Cossio, R., Mellini, M. (2021) Raman anisotropy in serpentine minerals, with a *caveat* on identification. *Journal of Raman Spectroscopy*. John Wiley and Sons Ltd 52, 1334–1345.

Contreras-Reyes, E., Grevemeyer, I., Flueh, E.R., Reichert, C. (2008) Upper lithospheric structure of the subduction zone offshore of southern Arauco peninsula, Chile, at ~38°S. *Journal of Geophysical Research: Solid Earth*. Blackwell Publishing Ltd 113.

Cooper, H.W., Simmons, G. (1977) The effect of cracks on the thermal expansion of rocks. *Earth and Planetary Science Letters* 36, 404–412.

Cowan, R.J., Searle, M.P., Waters, D.J. (2014) Structure of the metamorphic sole to the Oman Ophiolite, Sumeini Window and Wadi Tayyin: Implications for ophiolite obduction processes. *Geological Society Special Publication*. Geological Society of London 392, 155–175.

Cox, S.F., Munroe, S.M. (2016) Breccia formation by particle fluidization in fault zones: Implications for transitory, rupture-controlled fluid flow regimes in hydrothermal systems. *American Journal of Science*. Yale University 316, 241–278.

Dandar, O., Okamoto, A., Uno, M., Tsuchiya, N. (2021) Redistribution of magnetite during multi-stage serpentinization: Evidence from the Taishir Massif, Khantaishir ophiolite, western Mongolia. *Journal of Mineralogical and Petrological Sciences*. Tohoku University 116, 176–181.

Dandar, O., Okamoto, A., Uno, M., Tsuchiya, N. (2023) Mantle hydration initiated by Ca metasomatism in a subduction zone: An example from the Chandman meta-peridotite, western Mongolia. *Lithos*. Elsevier B.V. 452–453.

de Martin, B.J., Reves-Sohn, R.A., Canales, J.P., Humphris, S.E. (2007) Kinematics and geometry of active detachment faulting beneath the Trans-Atlantic geotraverse (TAG) hydrothermal field on the Mid-Atlantic Ridge. *Geology* 35, 711–714.

de Obeso, J.C., Kelemen, P.B., Leong, J.M., Menzel, M.D., Manning, C.E., Godard, M., Cai, Y., Bolge, L. (2022) Deep Sourced Fluids for Peridotite Carbonation in the Shallow Mantle Wedge of a Fossil Subduction Zone: Sr and C Isotope Profiles of OmanDP Hole BT1B. *Journal of Geophysical Research: Solid Earth*. American Geophysical Union (AGU) 127.

Debret, B. *et al.* (2019) Shallow forearc mantle dynamics and geochemistry: New insights from IODP Expedition 366. *Lithos*. Elsevier B.V. 326–327, 230–245.

Debret, B., Andreani, M., Muñoz, M., Bolfan-Casanova, N., Carlut, J., Nicollet, C., Schwartz, S., Trcera, N. (2014) Evolution of Fe redox state in serpentine during subduction. *Earth and Planetary Science Letters*. Elsevier 400, 206–218.

Demichelis, R., De La Pierre, M., Mookherjee, M., Zicovich-Wilson, C.M., Orlando, R. (2016) Serpentine polymorphism: A quantitative insight from first-principles calculations. *CrystEngComm*. Royal Society of Chemistry 18, 4412–4419.

Deschamps, F., Godard, M., Guillot, S., Hattori, K. (2013) Geochemistry of subduction zone serpentinites: A review. *Lithos*. Elsevier B.V. 178, 96–127.

Deschamps, F., Guillot, S., Godard, M., Andreani, M., Hattori, K. (2011) Serpentinites act as sponges for fluid-mobile elements in abyssal and subduction zone environments. *Terra Nova*. John Wiley

& Sons, Ltd 23, 171–178.

Dick, H., Natland, J., Ildefonse, B. (2006) Past and Future Impact of Deep Drilling in the Oceanic Crust and Mantle. *Oceanography* 19, 72–80.

Dick, H.J.B., Lin, J., Schouten, H. (2003) An ultraslow-spreading class of ocean ridge. *Nature* 426, 405–412.

Dragert, H., Wang, K., Rogers, G. (2004) *Geodetic and seismic signatures of episodic tremor and slip in the northern Cascadia subduction zone*. *Earth Planets Space*.

Eggleton, R.A. (1998) Hisingerite: A Ferric Kaolin Mineral with Curved Morphology. *Clays and Clay Minerals* 46, 400–413.

Enju, S., Uehara, S., Inoo, T. (2023) Polygonal Serpentine and Chrysotile in the Kurosegawa Belt, Kyushu, Japan. *The Canadian Journal of Mineralogy and Petrology*. Mineralogical Association of Canada 61, 145–166.

Ernewein, M., Pflumio, I.C., Whitechurch ', H. (1988) *The death of an accretion zone as evidenced by the magmatic history of the Sumail ophiolite (Oman)*. Elsevier Science Publishers B.V.

Evans, B.W. (2008) Control of the products of serpentinization by the Fe2+ Mg-1 exchange potential of olivine and orthopyroxene. *Journal of Petrology* 49, 1873–1887.

Evans, O., Spiegelman, M., Kelemen, P.B. (2020) Phase-Field Modeling of Reaction-Driven Cracking: Determining Conditions for Extensive Olivine Serpentinization. *Journal of Geophysical Research: Solid Earth* 125, 1–21.

Faccenda, M., Gerya, T. V., Burlini, L. (2009) Deep slab hydration induced by bending-related variations in tectonic pressure. *Nature Geoscience* 2, 790–793.

Falk, E.S., Kelemen, P.B. (2015) Geochemistry and petrology of listvenite in the Samail ophiolite, Sultanate of Oman: Complete carbonation of peridotite during ophiolite emplacement. *Geochimica et Cosmochimica Acta*. Elsevier Ltd 160, 70–90.

Farough, A., Moore, D.E., Lockner, D.A., Lowell, R.P. (2016) Evolution of fracture permeability of ultramafic rocks undergoing serpentinization at hydrothermal conditions: An experimental study. *Geochemistry, Geophysics, Geosystems*. Blackwell Publishing Ltd 17, 44–55.

Fisher, D.M., Brantley, S.L. (2014) The role of silica redistribution in the evolution of slip instabilities along subduction interfaces: Constraints from the Kodiak accretionary complex, Alaska. *Journal of Structural Geology*. Elsevier Ltd 69, 395–414.

Fisher, D.M., Hooker, J.N., Smye, A.J., Chen, T.W. (2021) Insights from the geological record of deformation along the subduction interface at depths of seismogenesis. *Geosphere*. GeoScienceWorld 17, 1686–1703.

Földvári, M. 1944- (2011) *Handbook of thermogravimetric system of minerals and its use in geological practice*. Geological Institute of Hungary.

Frost, B.R. (1985) On the Stability of Sulfides, Oxides, and Native Metals in Serpentinite. *Journal of Petrology* 26, 31–63.

Frost, B.R., Evans, K.A., Swapp, S.M., Beard, J.S., Mothersole, F.E. (2013) The process of

serpentinization in dunite from New Caledonia. *Lithos* 178, 24–39.

Früh-Green, G.L., Connolly, J.A.D., Plas, A., Kelley, D.S., Grobety, B. (2004a) Serpentinization of Oceanic Peridotites : Implications for Geochemical Cycles and Biological Activity The Subseafloor Biosphere at Mid-Ocean Ridges. *The Subseafloor Biosphere at Mid-Ocean Ridges* 144, 119–136.

Früh-Green, G.L., Connolly, J.A.D., Plas, A., Kelley, D.S., Grobéty, B. (2004b) Serpentinization of oceanic peridotites: Implications for geochemical cycles and biological activity. *Geophysical Monograph Series*, 119–136.

Früh-Green, G.L., Kelley, D.S., Bernasconi, S.M., Karson, J.A., Ludwig, K.A., Butterfield, D.A., Boschi, C., Proskurowski, G. (2003) 30,000 Years of Hydrothermal Activity at the Lost City Vent Field. *Science* 301, 495–498.

Fruh-Green, G.L., Plas, A., Lecuyer, C. (1996) Petrologic and Stable Isotope Constraints on Hydrothermal Alteration and Serpentinization of the EPR Shallow Mantle at Hess Deep (Site 895). *Proceedings of the Ocean Drilling Program, 147 Scientific Results*.

Fujie, G., Kodaira, S., Yamashita, M., Sato, T., Takahashi, T., Takahashi, N. (2013) Systematic changes in the incoming plate structure at the Kuril trench. *Geophysical Research Letters* 40, 88–93.

Gahlan, H.A., Arai, S., Ahmed, A.H., Ishida, Y., Abdel-Aziz, Y.M., Rahimi, A. (2006) Origin of magnetite veins in serpentinite from the Late Proterozoic Bou-Azzer ophiolite, Anti-Atlas, Morocco: An implication for mobility of iron during serpentinization. *Journal of African Earth Sciences* 46, 318–330.

Garber, J.M., Rioux, M., Kylander-Clark, A.R.C., Hacker, B.R., Vervoort, J.D., Searle, M.P. (2020) Petrochronology of Wadi Tayin Metamorphic Sole Metasediment, With Implications for the Thermal and Tectonic Evolution of the Samail Ophiolite (Oman/UAE). *Tectonics*. John Wiley & Sons, Ltd 39, e2020TC006135.

Garbe-Schönberg, D., Koepke, J., Müller, S., Mock, D., Müller, T. (2022) A Reference Section Through Fast-Spread Lower Oceanic Crust, Wadi Gideah, Samail Ophiolite (Sultanate of Oman): Whole Rock Geochemistry. *Journal of Geophysical Research: Solid Earth*. John Wiley and Sons Inc 127.

Germanovich, L.N., Genc, G., Lowell, R.P., Rona, P.A. (2012) Deformation and surface uplift associated with serpentinization at mid-ocean ridges and subduction zones. *Journal of Geophysical Research: Solid Earth*. Blackwell Publishing Ltd 117.

Gillis, K.M. *et al.* (2014) Expedition 345 summary. 345.

Goslin, J., Beuzart, P., Francheteau, J., Le Pichon, X. (1972) Thickening of the oceanic layer in the Pacific Ocean. *Marine Geophysical Researches* 1, 418–427.

Gregory, R.T., Taylor, H.P. (1981) An oxygen isotope profile in a section of Cretaceous oceanic crust, Samail Ophiolite, Oman: Evidence for δ 18 O buffering of the oceans by deep (>5 km) seawater-hydrothermal circulation at mid-ocean ridges . *Journal of Geophysical Research: Solid Earth* 86, 2737–2755.

Grevemeyer, I., Hayman, N.W., Lange, D., Peirce, C., Papenberg, C., van Avendonk, H.J.A., Schmid,

F., de La Peña, L.G., Dannowski, A. (2019) Constraining the maximum depth of brittle deformation at slow-and ultraslow-spreading ridges using microseismicity. *Geology*. Geological Society of America 47, 1069–1073.

Grevemeyer, I., Hayman, N.W., Peirce, C., Schwardt, M., Van Avendonk, H.J.A., Dannowski, A., Papenberg, C. (2018a) Episodic magmatism and serpentinized mantle exhumation at an ultraslow-spreading centre. *Nature Geoscience*. Nature Publishing Group 11, 444–448.

Grevemeyer, I., Ranero, C.R., Flueh, E.R., Kläschen, D., Bialas, J. (2007) Passive and active seismological study of bending-related faulting and mantle serpentinization at the Middle America trench. *Earth and Planetary Science Letters* 258, 528–542.

Grevemeyer, I., Ranero, C.R., Ivandic, M. (2018b) Structure of oceanic crust and serpentinization at subduction trenches. *Geosphere* 14, 395–418.

Groppo, C., Rinaudo, C., Cairo, S., Gastaldi, D., Compagnoni, R. (2006) Micro-Raman spectroscopy for a quick and reliable identification of serpentine minerals from ultramafics. *European Journal of Mineralogy*. Schweizerbart 18, 319–329.

Guillot, S., Schwartz, S., Reynard, B., Agard, P., Prigent, C. (2015) Tectonic significance of serpentinites. *Tectonophysics*. Elsevier B.V., 1–19.

Hacker, B.R. (1991) The role of deformation in the formation of metamorphic gradients: Ridge subduction beneath the Oman Ophiolite. *Tectonics* 10, 455–473.

Hacker, B.R. (1994) Rapid emplacement of young oceanic lithosphere: Argon geochronology of the oman ophiolite. *Science* 265, 1563–1565.

Hacker, B.R. (2008) H2O subduction beyond arcs. *Geochemistry, Geophysics, Geosystems*. Blackwell Publishing Ltd 9.

Hacker, B.R., Mosenfelder, J.L., Gnos, E. (1996) Rapid emplacement of the Oman ophiolite: Thermal and geochronologic constraints. *Tectonics*. American Geophysical Union 15, 1230–1247.

Halpaap, F., Rondenay, S., Perrin, A., Goes, S., Ottemöller, L., Austrheim, H., Shaw, R., Eeken, T. (2019) Earthquakes track subduction fluids from slab source to mantle wedge sink. *Science Advances* 5.

Hanghøj, K., Kelemen, P.B., Hassler, D., Godard, M. (2010) Composition and Genesis of Depleted Mantle Peridotites from the Wadi Tayin Massif, Oman Ophiolite; Major and Trace Element Geochemistry, and Os Isotope and PGE Systematics. *Journal of Petrology*. Oxford Academic 51, 201–227.

Hasenclever, J., Theissen-Krah, S., Rüpke, L.H., Morgan, J.P., Iyer, K., Petersen, S., Devey, C.W. (2014) Hybrid shallow on-axis and deep off-axis hydrothermal circulation at fast-spreading ridges. *Nature*. Nature Publishing Group 508, 508–512.

Hatakeyama, K., Katayama, I., Hirauchi, K.I., Michibayashi, K. (2017) Mantle hydration along outer-rise faults inferred from serpentinite permeability. *Scientific Reports*. Nature Publishing Group 7.

Hattori, H., Guillot, S. (2003) Volcanic fronts form as a consequence of serpentinite dehydration in the forearc mantle wedge. *Geology* 525.

Hedges, S.B. (2002) The origin and evolution of model organisms. *Nature reviews. Genetics* 3, 838–49.

Hermann, J., Müntener, O., Scambelluri, M. (2000) The importance of serpentinite mylonites for subduction and exhumation of oceanic crust. *Tectonophysics* 327, 225–238.

Hirauchi, K. ichi, Nagata, Y., Kataoka, K., Oyanagi, R., Okamoto, A., Michibayashi, K. (2021) Cataclastic and crystal-plastic deformation in shallow mantle-wedge serpentinite controlled by cyclic changes in pore fluid pressures. *Earth and Planetary Science Letters*. Elsevier B.V. 576.

Hirose, H., Obara, K. (2005) *Repeating short-and long-term slow slip events with deep tremor activity around the Bungo channel region, southwest Japan*. *Earth Planets Space*.

Hofmeister, A.M., Chopelas, A. (1991) Vibrational spectroscopy of end-member silicate garnets. *Physics and Chemistry of Minerals* 17, 503–526.

Holm, N.G., Oze, C., Mousis, O., Waite, J.H., Guilbert-Lepoutre, A. (2015) Serpentinization and the Formation of H2 and CH4 on Celestial Bodies (Planets, Moons, Comets). *Astrobiology*. Mary Ann Liebert Inc. 15, 587–600.

Hopkinson, L., Beard, J.S., Boulter, C.A. (2004) The hydrothermal plumbing of a serpentinite-hosted detachment: Evidence from the West Iberia non-volcanic rifted continental margin. *Marine Geology* 204, 301–315.

Hopson, C.A., Coleman, R.G., Gregory, R.T., Pallister, J.S., Bailey, E.H. (1981) Geologic section through the Samail Ophiolite and associated rocks along a Muscat-Ibra Transect, southeastern Oman Mountains. *Journal of Geophysical Research: Solid Earth*. John Wiley & Sons, Ltd 86, 2527–2544.

Horen, H., Zamora, M., Dubuisson, G. (1996) Seismic waves velocities and anisotropy in serpentinized peridotites from Xigaze ophiolite: Abundance of serpentine in slow spreading ridge. *Geophysical Research Letters* 23, 9–12.

Horita, J., Berndt, M.E. (1999) Abiogenic Methane Formation and Isotopic Fractionation Under Hydrothermal Conditions. *Science* 285, 1055–1057.

Huang, F. *et al.* (2021) Dataset for H2, CH4 and organic compounds formation during experimental serpentinization. *Geoscience Data Journal*. John Wiley and Sons Ltd 8, 90–100.

Hybler, J., Petríček, V., Fábry, J., Durovič, S. (2002) Refinement of the crystal structure of cronstedtite-2H2. *Clays and Clay Minerals* 50, 601–613.

Hyndman, R.D., Drury, M.J. (1976) The physical properties of oceanic basement rocks from deep drilling on the Mid-Atlantic Ridge. *Journal of Geophysical Research* 81, 4042–4052.

Hyndman, R.D., McCrory, P.A., Wech, A., Kao, H., Ague, J. (2015) Cascadia subducting plate fluids channelled to fore-arc mantle corner: ETS and silica deposition. *Journal of Geophysical Research: Solid Earth*. Blackwell Publishing Ltd 120, 4344–4358.

Ishikawa, T., Fujisawa, S., Nagaishi, K., Masuda, T. (2005) Trace element characteristics of the fluid liberated from amphibolite-facies slab: Inference from the metamorphic sole beneath the Oman ophiolite and implication for boninite genesis. *Earth and Planetary Science Letters* 240, 355–377.

Ivandic, M., Grevemeyer, I., Bialas, J., Petersen, C.J. (2010) Serpentinization in the trench-outer rise region offshore of Nicaragua: Constraints from seismic refraction and wide-angle data.

Geophysical Journal International 180, 1253–1264.

Iyer, K., Jamtveit, B., Mathiesen, J., Malthe-Sørenssen, A., Feder, J. (2008) Reaction-assisted hierarchical fracturing during serpentinization. *Earth and Planetary Science Letters* 267, 503–516.

Iyer, K., Rüpke, L.H., Morgan, J.P. (2010) Feedbacks between mantle hydration and hydrothermal convection at ocean spreading centers. *Earth and Planetary Science Letters*. Elsevier B.V. 296, 34–44.

Jamtveit, B., Austrheim, H. (2010) Metamorphism: The role of fluids. *Elements* 6, 153–158.

Jamtveit, B., Austrheim, H., Malthe-Sorenssen, A. (2000) Accelerated hydration of the Earth's deep crust induced by stress perturbations. *Nature* 408, 75–78.

Jamtveit, B., Malthe-Sørenssen, A., Kostenko, O. (2008) Reaction enhanced permeability during retrogressive metamorphism. *Earth and Planetary Science Letters*. Elsevier 267, 620–627.

Jamtveit, B., Putnis, C. V., Malthe-Sørenssen, A. (2009) Reaction induced fracturing during replacement processes. *Contributions to Mineralogy and Petrology* 157, 127–133.

John, T., Gussone, N., Podladchikov, Y.Y., Bebout, G.E., Dohmen, R., Halama, R., Klemd, R., Magna, T., Seitz, H.M. (2012) Volcanic arcs fed by rapid pulsed fluid flow through subducting slabs. *Nature Geoscience* 5, 489–492.

Katayama, I., Kurosaki, I., Hirauchi, K. ichi (2010) Low silica activity for hydrogen generation during serpentinization: An example of natural serpentinites in the Mineoka ophiolite complex, central Japan. *Earth and Planetary Science Letters*. Elsevier B.V. 298, 199–204.

Katayama, I., Terada, T., Okazaki, K., Tanikawa, W. (2012) Episodic tremor and slow slip potentially linked to permeability contrasts at the Moho. *Nature Geoscience*. Nature Publishing Group 5, 731–734.

Kawano, S., Katayama, I., Okazaki, K. (2011) Permeability anisotropy of serpentinite and fluid pathways in a subduction zone. *Geology* 39, 939–942.

Kelemen, P.B., Hirth, G. (2012) Reaction-driven cracking during retrograde metamorphism: Olivine hydration and carbonation. *Earth and Planetary Science Letters*. Elsevier 345–348, 81–89.

Kelemen, P.B., Matter, J., Streit, E.E., Rudge, J.F., Curry, W.B., Blusztajn, J. (2011) Rates and mechanisms of mineral carbonation in peridotite: Natural processes and recipes for enhanced, in situ CO2 capture and storage. *Annual Review of Earth and Planetary Sciences* 39, 545–576.

Kelemen, P.B., Matter, J.M., Teagle, D.A.H., Coggon, J.A., the Oman Drilling Project Science Team (2020) *Proceedings of the Oman Drilling Project*. International Ocean Discovery Program.

Kelley, D.S. *et al.* (2005) A Serpentinite-Hosted Ecosystem: The Lost City Hydrothermal Field. *Science* 307, 1428–1434.

Klein, F., Bach, W., Humphris, S.E., Kahl, W.A., Jöns, N., Moskowitz, B., Berquó, T.S. (2014) Magnetite in seafloor serpentinite-Some like it hot. *Geology* 42, 135–138.

Klein, F., Bach, W., Jöns, N., McCollom, T., Moskowitz, B., Berquó, T. (2009) Iron partitioning and hydrogen generation during serpentinization of abyssal peridotites from 15°N on the Mid-Atlantic Ridge. *Geochimica et Cosmochimica Acta* 73, 6868–6893.

Klein, F., Bach, W., McCollom, T.M. (2013) Compositional controls on hydrogen generation during serpentinization of ultramafic rocks. *Lithos* 178, 55–69.

Klein, F., Le Roux, V. (2020) Quantifying the volume increase and chemical exchange during serpentinization. *Geology* 48, 552–556.

Kodaira, S., Iidaka, T., Kato, A., Park, J.-O., Iwasaki, T., Kaneda, Y. (2004) High Pore Fluid Pressure May Cause Silent Slip in the Nankai Trough. *Science*. Cambridge Univ. Press 304, 1295–1298.

Koepke, J., Garbe-Schönberg, D., Müller, T., Mock, D., Müller, S., Nasir, S. (2022) A Reference Section Through Fast-Spread Lower Oceanic Crust, Wadi Gideah, Samail Ophiolite (Sultanate of Oman): Petrography and Petrology. *Journal of Geophysical Research: Solid Earth* 127.

Konn, C., Charlou, J.L., Holm, N.G., Mousis, O. (2015) The production of methane, hydrogen, and organic compounds in ultramafic-hosted hydrothermal vents of the mid-atlantic ridge. *Astrobiology*. Mary Ann Liebert Inc. 15, 381–399.

Korenaga, J. (2007) Thermal cracking and the deep hydration of oceanic lithosphere: A key to the generation of plate tectonics? *Journal of Geophysical Research: Solid Earth*. John Wiley & Sons, Ltd 112, 5408.

Kostoglodov, V., Singh, S.K., Santiago, J.A., Franco, S.I., Larson, K.M., Lowry, A.R., Bilham, R. (2003) A large silent earthquake in the Guerrero seismic gap, Mexico. *Geophysical Research Letters*. American Geophysical Union 30.

Kourim, F. *et al.* (2022) Geochemical Characterization of the Oman Crust-Mantle Transition Zone, OmanDP Holes CM1A and CM2B. *Journal of Geophysical Research: Solid Earth*. John Wiley & Sons, Ltd 127.

Kranz, R.L. (1983) Microcracks in rocks: A review. *Tectonophysics* 100, 449–480.

Kuleci, H., Ulven, O.I., Rybacki, E., Wunder, B., Abart, R. (2017) Reaction-induced fracturing in a hot pressed calcite-periclase aggregate. *Journal of Structural Geology*. Elsevier Ltd 94, 116–135.

Kuster, G.T., Toksöz, M.N. (1974) Velocity and attenuation of seismic waves in two-phase media; Part I, Theoretical formulations. *GEOPHYSICS* 39, 587–606.

Lafay, R., Montes-Hernandez, G., Janots, E., Chiriac, R., Findling, N., Toche, F. (2012) Mineral replacement rate of olivine by chrysotile and brucite under high alkaline conditions. *Journal of Crystal Growth* 347, 62–72.

Lafay, R., Montes-Hernandez, G., Renard, F., Vonlanthen, P. (2018) Intracrystalline reaction-induced cracking in olivine evidenced by hydration and carbonation experiments. *Minerals* 8, 1–18.

Lefeldt, M., Grevemeyer, I. (2008) Centroid depth and mechanism of trench-outer rise earthquakes. *Geophysical Journal International* 172, 240–251.

Leong, J.A., Nielsen, M., McQueen, N., Karolytė, R., Hillegonds, D.J., Ballentine, C., Darrah, T., McGillis, W., Kelemen, P. (2023) H2 and CH4 outgassing rates in the Samail ophiolite, Oman: Implications for low-temperature, continental serpentinization rates. *Geochimica et Cosmochimica Acta*. Elsevier Ltd 347, 1–15.

Lewis, B.T.R., Snydsman, W.E. (1979) Fine structure of the lower oceanic crust on the Cocos Plate.

Tectonophysics 55, 87–105.

Lichtner, P.C. (1988) The quasi-stationary state approximation to coupled mass transport and fluid-rock interaction in a porous medium. *Geochimica et Cosmochimica Acta* 52, 143–165.

Maekawa, H., Yamamoto, K., Ueno, T., Osada, Y., Nogami, N. (2004) Significance of Serpentinites and Related Rocks in the High-Pressure Metamorphic Terranes, Circum-Pacific Regions. *International Geology Review* 46, 426–444.

Majumdar, A.S., Ray, D., Shukla, A.D. (2020) Serpentinization of olivine–gabbro in Central Indian ridge: Insights into H2 production during alteration in lower oceanic crust and sustenance of life at slow–spreading ridges. *Lithos*. Elsevier B.V. 374–375.

Malthe-Sørenssen, A., Jamtveit, B., Meakin, P. (2006) Fracture patterns generated by diffusion controlled volume changing reactions. *Physical Review Letters* 96, 1–4.

Malvoisin, B., Brantut, N., Kaczmarek, M.A. (2017) Control of serpentinisation rate by reaction-induced cracking. *Earth and Planetary Science Letters*. Elsevier B.V. 476, 143–152.

Malvoisin, B., Brunet, F. (2014) Water diffusion-transport in a synthetic dunite: Consequences for oceanic peridotite serpentinization. *Earth and Planetary Science Letters*. Elsevier B.V. 403, 263–272.

Malvoisin, B., Brunet, F., Carlut, J., Rouméjon, S., Cannat, M. (2012a) Serpentinization of oceanic peridotites: 2. Kinetics and processes of San Carlos olivine hydrothermal alteration. *Journal of Geophysical Research: Solid Earth*. Blackwell Publishing Ltd 117.

Malvoisin, B., Carlut, J., Brunet, F. (2012b) Serpentinization of oceanic peridotites: 1. A high-sensitivity method to monitor magnetite production in hydrothermal experiments. *Journal of Geophysical Research: Solid Earth*. Blackwell Publishing Ltd 117.

Manning, C.E., MacLeod, C.J., Weston, P.E. (2000) Lower-crustal cracking front at fast-spreading ridges: Evidence from the East Pacific Rise and the Oman Ophiolite. *Ophiolites and oceanic crust: new insights from field studies and the Ocean Drilling Program*. Geological Society of America.

Marcaillou, C., Muñoz, M., Vidal, O., Parra, T., Harfouche, M. (2011) Mineralogical evidence for H2 degassing during serpentinization at 300°C/300bar. *Earth and Planetary Science Letters* 303, 281–290.

Mark, H.F., Lizarralde, D., Wiens, D.A. (2023) Constraints on Bend-Faulting and Mantle Hydration at the Marianas Trench From Seismic Anisotropy. *Geophysical Research Letters*. John Wiley and Sons Inc 50.

Martin, B., Fyfe, W.S. (1970) Some experimental and theoretical observations on the kinetics of hydration reactions with particular reference to serpentinization. *Chemical Geology* 6, 185–202.

Martin, W., Baross, J., Kelley, D., Russell, M.J. (2008) Hydrothermal vents and the origin of life. *Nature Reviews Microbiology*, 805–814.

McClain, J.S., Atallah, C.A. (1986) Thickening of the oceanic crust with age. *Geology* 14, 574.

McCollom, T.M., Bach, W. (2009) Thermodynamic constraints on hydrogen generation during serpentinization of ultramafic rocks. *Geochimica et Cosmochimica Acta* 73, 856–875.

McCollom, T.M., Klein, F., Moskowitz, B., Berquó, T.S., Bach, W., Templeton, A.S. (2020) Hydrogen generation and iron partitioning during experimental serpentinization of an olivine–pyroxene mixture. *Geochimica et Cosmochimica Acta*. Elsevier Ltd 282, 55–75.

McCollom, T.M., Klein, F., Ramba, M. (2022) Hydrogen generation from serpentinization of iron-rich olivine on Mars, icy moons, and other planetary bodies. *Icarus*. Academic Press Inc. 372.

McCollom, T.M., Klein, F., Robbins, M., Moskowitz, B., Berquó, T.S., Jöns, N., Bach, W., Templeton, A. (2016) Temperature trends for reaction rates, hydrogen generation, and partitioning of iron during experimental serpentinization of olivine. *Geochimica et Cosmochimica Acta*. Elsevier Ltd 181, 175–200.

McDonough, W.F., Sun, S. s. (1995) The composition of the Earth. *Chemical Geology*. Elsevier 120, 223–253.

Mellini, M., Fuchs, Y., Viti, C., Lemaire, C., Linarè s, J. (2002) Insights into the antigorite structure from Mossbauer and FTIR spectroscopies. *European Journal of Mineralogy*. Schweizerbart 14, 97–104.

Ménez, B., Pisapia, C., Andreani, M., Jamme, F., Vanbellingen, Q.P., Brunelle, A., Richard, L., Dumas, P., Réfrégiers, M. (2018) Abiotic synthesis of amino acids in the recesses of the oceanic lithosphere. *Nature*. Nature Publishing Group 564, 59–63.

Merdith, A.S., Daniel, I., Sverjensky, D., Andreani, M., Mather, B., Williams, S., Vitale Brovarone, A. (2023) Global Hydrogen Production During High-Pressure Serpentinization of Subducting Slabs. *Geochemistry, Geophysics, Geosystems*. John Wiley and Sons Inc 24.

Mével, C. (2003) Serpentinisation des péridotites abysales aux dorsales océaniques. *Comptes Rendus - Geoscience* 335, 825–852.

Michard, A., Boudier, F., Goffé, B. (1991) Obduction Versus Subduction and Collision in the Oman Case and Other Tethyan Settings. *Ophiolite genesis and evolution of the oceanic lithosphere. Proc. conference, Muscat, 1990*, 447–467.

Michibayashi, K., Tominaga, M., Ildefonse, B., Teagle, D. (2019) What Lies Beneath: The Formation and Evolution of Oceanic Lithosphere. *Oceanography*. The Oceanography Society 32, 138–149.

Miller, H.M., Matter, J.M., Kelemen, P., Ellison, E.T., Conrad, M.E., Fierer, N., Ruchala, T., Tominaga, M., Templeton, A.S. (2016) Modern water/rock reactions in Oman hyperalkaline peridotite aquifers and implications for microbial habitability. *Geochimica et Cosmochimica Acta*. Elsevier Ltd 179, 217–241.

Mindaleva, D., Uno, M., Higashino, F., Nagaya, T., Okamoto, A., Tsuchiya, N. (2020) Rapid fluid infiltration and permeability enhancement during middle–lower crustal fracturing: Evidence from amphibolite–granulite-facies fluid–rock reaction zones, Sør Rondane Mountains, East Antarctica. *Lithos*. Elsevier B.V. 372–373.

Miyoshi, A., Kogiso, T., Ishikawa, N., Mibe, K. (2014) Role of silica for the progress of serpentinization reactions: Constraints from successive changes in mineralogical textures of serpentinites from Iwanaidake ultramafic body, Japan. *American Mineralogist*. Walter de Gruyter GmbH 99, 1035–1044.

MORI, Y., SHIGENO, M., MIYAZAKI, K., NISHIYAMA, T. (2019) Peak metamorphic temperature of the Nishisonogi unit of the Nagasaki Metamorphic Rocks, western Kyushu, Japan. *Journal of Mineralogical and Petrological Sciences*. Tohoku University 114, 170–177.

Mügler, C., Jean-Baptiste, P., Perez, F., Charlou, J.L. (2016) Modeling of hydrogen production by serpentinization in ultramafic-hosted hydrothermal systems: application to the Rainbow field. *Geofluids* 16, 476–489.

Murata, K., Maekawa, H., Yokose, H., Yamamoto, K., Fujioka, K., Ishii, T., Chiba, H., Wada, Y. (2009) Significance of serpentinization of wedge mantle peridotites beneath Mariana forearc, western Pacific. *Geosphere* 5, 90–104.

Nakajima, J., Uchida, N. (2018) Repeated drainage from megathrusts during episodic slow slip. *Nature Geoscience*. Nature Publishing Group 11, 351–356.

Nakao, A., Iwamori, H., Nakakuki, T., Suzuki, Y.J., Nakamura, H. (2018) Roles of Hydrous Lithospheric Mantle in Deep Water Transportation and Subduction Dynamics. *Geophysical Research Letters*. Blackwell Publishing Ltd 45, 5336–5343.

Nakatani, T., Nakamura, M. (2016) Experimental constraints on the serpentinization rate of fore-arc peridotites: Implications for the upwelling condition of the slab-derived fluid. *Geochemistry, Geophysics, Geosystems*. Blackwell Publishing Ltd 17, 3393–3419.

Nakatani, T., Nakamura, M. (2019) Preferential Orthopyroxene Serpentinization and Implications for Seismic Velocity Interpretation in the Fore-Arc Mantle. *Journal of Geophysical Research: Solid Earth*. Blackwell Publishing Ltd 124, 3420–3435.

Nicolas, A. (2003) High-temperature seawater circulation throughout crust of oceanic ridges: A model derived from the Oman ophiolites. *Journal of Geophysical Research* 108, 1–20.

Nicolas, A., Boudier, F. (2015) Structural contribution from the Oman ophiolite to processes of crustal accretion at the East Pacific Rise. *Terra Nova* 27, 77–96.

Nicolas, A., Boudier, F., Ildefonse, B. (1996) Variable crustal thickness in the Oman ophiolite: Implication for oceanic crust. *Journal of Geophysical Research: Solid Earth*. American Geophysical Union 101, 17941–17950.

Nicolas, A., Bouldier, F., Ildefonse, B., Ball, E. (2000) Accretion of Oman and United Arab Emirates ophiolite - Discussion of a new structural map. *Marine Geophysical Research*. Springer Netherlands 21, 147–180.

Nicolas, A., Ceuleneer, G., Boudier, F., Misseri, M. (1988) Structural mapping in the Oman ophiolites: Mantle diapirism along an oceanic ridge. *Tectonophysics* 151, 27–56.

Ninkabou, D. *et al.* (2021) Structure of the Offshore Obducted Oman Margin: Emplacement of Semail Ophiolite and Role of Tectonic Inheritance. *Journal of Geophysical Research: Solid Earth*. Blackwell Publishing Ltd 126.

Nippress, S.E.J., Rietbrock, A. (2007) Seismogenic zone high permeability in the Central Andes inferred from relocations of micro-earthquakes. *Earth and Planetary Science Letters* 263, 235–245.

Normand, C., Williams-Jones, A.E., Martin, R.F., Vali, H. (2002) Hydrothermal alteration of olivine in

a flow-through autoclave: Nucleation and growth of serpentine phases. *American Mineralogist* 87, 1699–1709.

Nozaka, T. (2012) Petrological constraints on hydrogen production during serpentinization: a review. *Japanese Magazine of Mineralogical and Petrological Sciences* 41, 174–184.

Nozaka, T., Tateishi, Y. (2023) Incompatibility between serpentinization and epidote formation in the lower oceanic crust: Evidence from the Oman Drilling Project. *Journal of Metamorphic Geology*. John Wiley and Sons Inc 41, 665–684.

Nutman, A.P., Bennett, V.C., Friend, C.R.L., Van Kranendonk, M.J., Chivas, A.R. (2016) Rapid emergence of life shown by discovery of 3,700-million-year-old microbial structures. *Nature*. Nature Publishing Group 537, 535–538.

Obara, K. (2002) Nonvolcanic Deep Tremor Associated with Subduction in Southwest Japan. *Science* 296, 1679–1681.

Oelkers, E.H., Declercq, J., Saldi, G.D., Gislason, S.R., Schott, J. (2018) Olivine dissolution rates: A critical review. *Chemical Geology*. Elsevier B.V. 500, 1–19.

Oelkers, E.H., Helgeson, H.C. (1988) Calculation of the thermodynamic and transport properties of aqueous species at high pressures and temperatures: Aqueous tracer diffusion coefficients of ions to 1000°C and 5 kb. *Geochimica et Cosmochimica Acta* 52, 63–85.

Ogasawara, Y., Okamoto, A., Hirano, N., Tsuchiya, N. (2013) Coupled reactions and silica diffusion during serpentinization. *Geochimica et Cosmochimica Acta* 119, 212–230.

O'Hanley, D.S., Dyar, M.D. (1993) *The composition of lizardite 1T and, the formation of magnetite in serpentinites*. *American Mineralogist*.

O'Hanley, D.S., Dyar, M.D. (1998) THE COMPOSITION OF CHRYSOTILE AND ITS RELATIONSHIP WITH LIZARDITE. *The Canadian Mineralogist* 36, 727–739.

Okamoto, A., Ogasawara, Y., Ogawa, Y., Tsuchiya, N. (2011) Progress of hydration reactions in olivine-H2O and orthopyroxenite-H2O systems at 250C and vapor-saturated pressure. *Chemical Geology* 289, 245–255.

Okamoto, A., Oyanagi, R., Yoshida, K., Uno, M., Shimizu, H., Satish-Kumar, M. (2021) Rupture of wet mantle wedge by self-promoting carbonation. *Communications Earth & Environment*. Springer Science and Business Media LLC 2.

Okamoto, A., Shimizu, H. (2015) Contrasting fracture patterns induced by volume-increasing and -decreasing reactions: Implications for the progress of metamorphic reactions. *Earth and Planetary Science Letters*. Elsevier B.V. 417, 9–18.

Okamoto, A., Tsuchiya, N. (2009) Velocity of vertical fluid ascent within vein-forming fractures. *Geology* 37, 563–566.

Oliver, N.H.S., Rubenach, M.J., Fu, B., Baker, T., Blenkinsop, T.G., Cleverley, J.S., Marshall, L.J., Ridd, P.J. (2006) Granite-related overpressure and volatile release in the mid crust: Fluidized breccias from the Cloncurry District, Australia. *Geofluids* 6, 346–358.

Oufi, O., Cannat, M., Horen, H. (2002) Magnetic properties of variably serpentinized abyssal peridotites.

Journal of Geophysical Research: Solid Earth. American Geophysical Union (AGU) 107.

Oyanagi, R., Okamoto, A., Harigane, Y., Tsuchiya, N. (2018) Al-zoning of serpentine aggregates in mesh texture induced by metasomatic replacement reactions. *Journal of Petrology*. Oxford University Press 59, 613–634.

Oyanagi, R., Okamoto, A., Tsuchiya, N. (2020) Silica controls on hydration kinetics during serpentinization of olivine: Insights from hydrothermal experiments and a reactive transport model. *Geochimica et Cosmochimica Acta*. Elsevier Ltd 270, 21–42.

Ozawa, S., Murakami, M., Kaidzu, M., Tada, T., Sagiya, T., Hatanaka, Y., Yarai, H., Nishimura, T. (2002) Detection and monitoring of ongoing aseismic slip in the Tokai region, central Japan. *Science* 298, 1009–1012.

Padrón-Navarta, J.A., Tommasi, A., Garrido, C.J., López Sánchez-Vizcaíno, V. (2012) Plastic deformation and development of antigorite crystal preferred orientation in high-pressure serpentinites. *Earth and Planetary Science Letters* 349–350, 75–86.

Pallister, J.S., Hopson, C.A. (1981) Samail ophiolite plutonic suite: field relations, phase variation, cryptic variation and layering, and a model of a spreading ridge magma chamber. *Journal of Geophysical Research* 86, 2593–2644.

Parai, R., Mukhopadhyay, S. (2012) How large is the subducted water flux? New constraints on mantle regassing rates. *Earth and Planetary Science Letters* 317–318, 396–406.

Passaglia, E., Rinaldi, R. (1984) Katoite, a new member of the Ca3Al2(SiO4)3-Ca3Al2(OH)12 series and a new nomenclature for the hydrogrossular group of minerals. *Bulletin de Minéralogie* 107, 605–618.

Pearce, J.A., Alabaster, T., Shelton, A.W., Searle, M.P. (1981) The Oman ophiolite as a Cretaceous arc-basin complex: evidence and implications. *Philosophical Transactions of the Royal Society of London. Series A, Mathematical and Physical Sciences* 300, 299–317.

Plank, T., Ludden, J.N. (1992) 8. GEOCHEMISTRY OF SEDIMENTS IN THE ARGO ABYSSAL PLAIN AT SITE 765: A CONTINENTAL MARGIN REFERENCE SECTION FOR SEDIMENT RECYCLING IN SUBDUCTION ZONES. *Proceedings of the Ocean Drilling Program, Scientific Results* 123, 167–189.

Plümper, O., Beinlich, A., Bach, W., Janots, E., Austrheim, H. (2014) Garnets within geode-like serpentinite veins: Implications for element transport, hydrogen production and life-supporting environment formation. *Geochimica et Cosmochimica Acta*. Elsevier Ltd 141, 454–471.

Plümper, O., John, T., Podladchikov, Y.Y., Vrijmoed, J.C., Scambelluri, M. (2017) Fluid escape from subduction zones controlled by channel-forming reactive porosity. *Nature Geoscience*. Nature Publishing Group 10, 150–156.

Plümper, O., Røyne, A., Magrasó, A., Jamtveit, B. (2012) The interface-scale mechanism of reaction-induced fracturing during serpentinization. *Geology* 40, 1103–1106.

Plümper, O., Wallis, D., Teuling, F., Moulas, E., Schmalholz, S.M., Amiri, H., Müller, T. (2022) High-magnitude stresses induced by mineral-hydration reactions. *Geology*. Geological Society of

America 50, 1351–1355.

Pollard, D.D., Fletcher, R.C., Pollard, D.D., Fletcher, R.C. (2006) Fundamentals of structural geology. *Choice Reviews Online* 43, 43-5304-43–5304.

Preiner, M. *et al.* (2020) A hydrogen-dependent geochemical analogue of primordial carbon and energy metabolism. *Nature Ecology and Evolution*. Nature Research 4, 534–542.

Prieto, A.C. (1991) Structure-Composition Relationships in Trioctahedral Chlorites: A Vibrational Spectroscopy Study. *Clays and Clay Minerals*. Clay Minerals Society 39, 531–539.

Proskurowski, G., Lilley, M.D., Seewald, J.S., Früh-Green, G.L., Olson, E.J., Lupton, J.E., Sylva, S.P., Kelley, D.S. (2008) Abiogenic Hydrocarbon Production at Lost City Hydrothermal Field. *Science* 319, 604–607.

Putnis, A. (2002) Mineral replacement reactions: from macroscopic observations to microscopic mechanisms. *Mineralogical Magazine*. Mineralogical Society 66, 689–708.

Ranero, C.R., Phipps Morgan, J., McIntosh, K., Reichert, C. (2003) Bending-related faulting and mantle serpentinization at the Middle America trench. *Nature* 425, 367–373.

Ranero, C.R., Sallarès, V. (2004) Geophysical evidence for hydration of the crust and mantle of the Nazca plate during bending at the north Chile trench. *Geology* 32, 549–552.

Ranero, C.R., Villaseñor, A., Morgan, J.P., Weinrebe, W. (2005) Relationship between bend-faulting at trenches and intermediate-depth seismicity. *Geochemistry, Geophysics, Geosystems* 6.

Reynard, B., Bezacier, L., Caracas, R. (2015) Serpentines, talc, chlorites, and their high-pressure phase transitions: a Raman spectroscopic study. *Physics and Chemistry of Minerals*. Springer Verlag 42, 641–649.

Reynard, B., Fellah, C., McCammon, C. (2022) Iron oxidation state in serpentines and magnesian chlorites of subduction-related rocks. *European Journal of Mineralogy*. Copernicus Publications 34, 645–656.

Ribeiro Da Costa, I., Barriga, F.J.A.S.V., Mellini, M., Wicks, F.J. (2008) Antigorite in deformed serpentinites from the Mid-Atlantic Ridge. *European Journal of Mineralogy*. Schweizerbart 20, 563–572.

Rioux, M., Bowring, S., Kelemen, P., Gordon, S., Dudás, F., Miller, R. (2012) Rapid crustal accretion and magma assimilation in the Oman-U.A.E. ophiolite: High precision U-Pb zircon geochronology of the gabbroic crust. *Journal of Geophysical Research: Solid Earth*. Blackwell Publishing Ltd 117.

Rioux, M., Bowring, S., Kelemen, P., Gordon, S., Miller, R., Dudás, F. (2013) Tectonic development of the Samail ophiolite: High-precision U-Pb zircon geochronology and Sm-Nd isotopic constraints on crustal growth and emplacement. *Journal of Geophysical Research: Solid Earth* 118, 2085–2101.

Rioux, M., Garber, J., Bauer, A., Bowring, S., Searle, M., Kelemen, P., Hacker, B. (2016) Synchronous formation of the metamorphic sole and igneous crust of the Semail ophiolite: New constraints on the tectonic evolution during ophiolite formation from high-precision U–Pb zircon geochronology.

Earth and Planetary Science Letters. Elsevier B.V. 451, 185–195.

Robertson, E.C. (1988) Thermal Properties of Rocks. *US Department of the Interior: Geological Survey* 88–441.

Rouméjon, S., Andreani, M., Früh-Green, G.L. (2019) Antigorite crystallization during oceanic retrograde serpentinization of abyssal peridotites. *Contributions to Mineralogy and Petrology*. Springer Verlag 174.

Rouméjon, S., Cannat, M., Agrinier, P., Godard, M., Andreani, M. (2014) Serpentinization and fluid pathways in tectonically exhumed peridotites from the southwest Indian ridge (62-65°E). *Journal of Petrology* 56, 703–734.

Rowe, C.D., Griffith, W.A. (2015) Do faults preserve a record of seismic slip: A second opinion. *Journal of Structural Geology*. Elsevier Ltd, 1–26.

Røyne, A., Jamtveit, B., Mathiesen, J., Malthe-Sørenssen, A. (2008) Controls on rock weathering rates by reaction-induced hierarchical fracturing. *Earth and Planetary Science Letters*. Elsevier B.V. 275, 364–369.

Rüpke, L.H., Hasenclever, J. (2017) Global rates of mantle serpentinization and H2 production at oceanic transform faults in 3-D geodynamic models. *Geophysical Research Letters*. Blackwell Publishing Ltd 44, 6726–6734.

Rüpke, L.H., Morgan, J.P., Hort, M., Connolly, J.A.D. (2004) Serpentine and the subduction zone water cycle. *Earth and Planetary Science Letters* 223, 17–34.

Russell, M.J. (2007) The alkaline solution to the emergence of life: Energy, entropy and early evolution. *Acta Biotheoretica* 55, 133–179.

Sacerdoti, M., Passaglia, E. (1985) The crystal structure of katoite and implications within the hydrogrossular group of minerals. *Bulletin de Minéralogie* 108, 1–8.

Saffer, D.M., Tobin, H.J. (2011) Hydrogeology and Mechanics of Subduction Zone Forearcs: Fluid Flow and Pore Pressure. *Annual Review of Earth and Planetary Sciences* 39, 157–186.

Salters, V.J.M., Stracke, A. (2004) Composition of the depleted mantle. *Geochemistry, Geophysics, Geosystems* 5.

Sato, H. (1977) Nickel content of basaltic magmas: identification of primary magmas and a measure of the degree of olivine fractionation. *LITHOS* 10, 113–120.

Schlindwein, V., Schmid, F. (2016) Mid-ocean-ridge seismicity reveals extreme types of ocean lithosphere. *Nature*. Nature Publishing Group 535, 276–279.

Schmidt, M.W., Poli, S. (1998) *Experimentally based water budgets for dehydrating slabs and consequences for arc magma generation*. *S. Poli / Earth and Planetary Science Letters*.

Schwartz, S., Guillot, S., Reynard, B., Lafay, R., Debret, B., Nicollet, C., Lanari, P., Auzende, A.L. (2013) Pressure-temperature estimates of the lizardite/antigorite transition in high pressure serpentinites. *Lithos*. Elsevier B.V. 178, 197–210.

Schwarzenbach, E.M., Caddick, M.J., Beard, J.S., Bodnar, R.J. (2016) Serpentinization, element transfer, and the progressive development of zoning in veins: evidence from a partially serpentinized

harzburgite. *Contributions to Mineralogy and Petrology*. Springer Verlag 171, 5.

Scicchitano, M.R., Spicuzza, M.J., Ellison, E.T., Tuschel, D., Templeton, A.S., Valley, J.W. (2021) In Situ Oxygen Isotope Determination in Serpentine Minerals by SIMS: Addressing Matrix Effects and Providing New Insights on Serpentinisation at Hole BA1B (Samail ophiolite, Oman). *Geostandards and Geoanalytical Research*. Blackwell Publishing Ltd 45, 161–187.

Searle, M.P. (2007) Structural geometry, style and timing of deformation in the Hawasina Window, Al Jabal al Akhdar and Saih Hatat culminations, Oman Mountains. *GeoArabia*. GeoScienceWorld 12, 99–130.

Seyfried, W.E., Dibble, W.E. (1980) Seawater-peridotite interaction at 300°C and 500 bars: implications for the origin of oceanic serpentinites. *Geochimica et Cosmochimica Acta* 44, 309–321.

Seyfried, W.E., Foustoukos, D.I., Fu, Q. (2007) Redox evolution and mass transfer during serpentinization: An experimental and theoretical study at 200°C, 500bar with implications for ultramafic-hosted hydrothermal systems at Mid-Ocean Ridges. *Geochimica et Cosmochimica Acta* 71, 3872–3886.

Shimizu, H. (2010) *Distinct element modeling for fundamental rock fracturing and application to hydraulic fracturing*. Kyoto.

Shimizu, H., Okamoto, A. (2016) The roles of fluid transport and surface reaction in reaction-induced fracturing, with implications for the development of mesh textures in serpentinites. *Contributions to Mineralogy and Petrology*. Springer Berlin Heidelberg 171, 1–18.

Sibson, R.H. (1992) Implications of fault-valve behaviour for rupture nucleation and recurrence. *Tectonophysics* 211, 283–293.

Sleep, N.H., Meibom, A., Fridriksson, T., Coleman, R.G., Bird, D.K. (2004) *H 2-rich fluids from serpentinization: Geochemical and biotic implications*. .

Steele, A. *et al.* (2022) Organic synthesis associated with serpentinization and carbonation on early Mars. *Science* 375, 172–177.

Suda, K. *et al.* (2014) Origin of methane in serpentinite-hosted hydrothermal systems: The CH4-H2-H2O hydrogen isotope systematics of the Hakuba Happo hot spring. *Earth and Planetary Science Letters* 386, 112–125.

Suzuki, S., Ishii, S., Hoshino, T., Rietze, A., Tenney, A., Morrill, P.L., Inagaki, F., Kuenen, J.G., Nealson, K.H. (2017) Unusual metabolic diversity of hyperalkaliphilic microbial communities associated with subterranean serpentinization at the Cedars. *ISME Journal*. Nature Publishing Group 11, 2584–2598.

Tamura, Y. *et al.* (2022) The nature of the Moho beneath fast-spreading centers: Evidence from the Pacific plate and Oman ophiolite. *Island Arc*. John Wiley and Sons Inc.

Tao, C. *et al.* (2020) Deep high-temperature hydrothermal circulation in a detachment faulting system on the ultra-slow spreading ridge. *Nature Communications*. Nature Research 11.

Tarling, M.S., Rooney, J.S., Viti, C., Smith, S.A.F., Gordon, K.C. (2018) Distinguishing the Raman spectrum of polygonal serpentine. *Journal of Raman Spectroscopy*. John Wiley and Sons Ltd 49,

1978–1984.

Tarling, M.S., Smith, S.A.F., Rooney, J.S., Viti, C., Gordon, K.C. (2021) A common type of mineralogical banding in serpentine crack-seal veins. *Earth and Planetary Science Letters*. Elsevier B.V. 564.

Tauzin, B., Reynard, B., Perrillat, J.P., Debayle, E., Bodin, T. (2017) Deep crustal fracture zones control fluid escape and the seismic cycle in the Cascadia subduction zone. *Earth and Planetary Science Letters*. Elsevier B.V. 460, 1–11.

Templeton, A.S., Ellison, E.T. (2020) Formation and loss of metastable brucite: does Fe(II)-bearing brucite support microbial activity in serpentinizing ecosystems? *Philosophical Transactions of the Royal Society A: Mathematical, Physical and Engineering Sciences*. Royal Society Publishing 378, 20180423.

Tucholke, B.E., Lin, J. (1994) A geological model for the structure of ridge segments in slow spreading ocean crust. *Journal of Geophysical Research: Solid Earth* 99, 11937–11958.

Tulley, C.J., Fagereng, Å., Ujiie, K., Piazolo, S., Tarling, M.S., Mori, Y. (2022) Rheology of Naturally Deformed Antigorite Serpentinite: Strain and Strain-Rate Dependence at Mantle-Wedge Conditions. *Geophysical Research Letters*. John Wiley and Sons Inc 49.

Tutolo, B.M., Evans, B.W., Kuehner, S.M. (2019) Serpentine–Hisingerite solid solution in altered ferroan peridotite and Olivine Gabbro. *Minerals*. MDPI AG 9.

Tutolo, B.M., Tosca, N.J. (2023) Observational constraints on the process and products of Martian serpentinization. *Science Advances* 9.

Ulrich, M., Muñoz, M., Boulvais, P., Cathelineau, M., Cluzel, D., Guillot, S., Picard, C. (2020) Serpentinization of New Caledonia peridotites: from depth to (sub-)surface. *Contributions to Mineralogy and Petrology*. Springer 175, 1–25.

Ulven, O.I., Jamtveit, B., Malthe-Sørenssen, A. (2014) Reaction-driven fracturing of porous rock. *Journal of Geophysical Research: Solid Earth* 119, 7473–7486.

Uno, M., Koyanagawa, K., Kasahara, H., Okamoto, A., Tsuchiya, N. (2022) Volatile-consuming reactions fracture rocks and self-accelerate fluid flow in the lithosphere. *Proceedings of the National Academy of Sciences* 119.

Van Avendonk, H.J.A., Holbrook, W.S., Lizarralde, D., Denyer, P. (2011) Structure and serpentinization of the subducting Cocos plate offshore Nicaragua and Costa Rica. *Geochemistry, Geophysics, Geosystems*. Blackwell Publishing Ltd 12, n/a-n/a.

Van Keken, P.E., Hacker, B.R., Syracuse, E.M., Abers, G.A. (2011) Subduction factory: 4. Depth-dependent flux of H2O from subducting slabs worldwide. *Journal of Geophysical Research: Solid Earth*. Blackwell Publishing Ltd 116.

VanTongeren, J.A., Kelemen, P.B., Hanghøj, K. (2008) Cooling rates in the lower crust of the Oman ophiolite: Ca in olivine, revisited. *Earth and Planetary Science Letters* 267, 69–82.

Viti, C. (2010) Serpentine minerals discrimination by thermal analysis. *American Mineralogist*. Walter de Gruyter GmbH 95, 631–638.

Viti, C., Mellini, M. (1998) *Mesh textures and bastites in the Elba retrograde serpentinites*. *Eur. J. Mineral*.

Wang, A., Freeman, J.J., Jolliff, B.L. (2015) Understanding the Raman spectral features of phyllosilicates. *Journal of Raman Spectroscopy*. John Wiley and Sons Ltd 46, 829–845.

Wang, J., Watanabe, N., Okamoto, A., Nakamura, K., Komai, T. (2019) Acceleration of hydrogen production during water-olivine-CO2 reactions via high-temperature-facilitated Fe(II) release. *International Journal of Hydrogen Energy*. Elsevier Ltd 44, 11514–11524.

Wang, Q., Guo, Q., Li, N., Cui, L., Liao, L. (2022a) Study of the mechanism of color change of prehnite after heat treatment. *RSC Advances*. Royal Society of Chemistry 12, 3044–3054.

Wang, Z., Singh, S.C., Prigent, C., Gregory, E.P.M., Marjanović, M. (2022b) Deep hydration and lithospheric thinning at oceanic transform plate boundaries. *Nature Geoscience*. Nature Research 15, 741–746.

Wanne, T.S., Young, R.P. (2008) Bonded-particle modeling of thermally fractured granite. *International Journal of Rock Mechanics and Mining Sciences* 45, 789–799.

Wegner, W.W., Ernst, G.W. (1983) EXPERIMENTALLY DETERMINED HYDRATION AND DEHYDRATION REACTION RATES IN THE SYSTEM MgO-SiO2-H2O*. *American Journal of Science* 283, 151–180.

Whitmarsh, R.B. (1978) Seismic refraction studies of the upper igneous crust in the North Atlantic and porosity estimates for Layer 2. *Earth and Planetary Science Letters* 37, 451–464.

Whittaker, B.E.J.W. (1957) *The Structure of Chrysotile. V. Diffuse Reflexions and Fibre Texture*. *Acta Cryst*.

Wilson, D.S. *et al.* (2006) Drilling to Gabbro in Intact Ocean Crust. *Science* 312, 1016–1020.

Wimpenny, J., Gíslason, S.R., James, R.H., Gannoun, A., Pogge Von Strandmann, P.A.E., Burton, K.W. (2010) The behaviour of Li and Mg isotopes during primary phase dissolution and secondary mineral formation in basalt. *Geochimica et Cosmochimica Acta*. Elsevier Ltd 74, 5259–5279.

Wunder, B., Schreyer, W. (1997) *Antigorite: High-pressure stability in the system MgO-SiO,-H,O (MSH)*. *Lithos*.

Wunder, B., Wirth, R., Gottschalk, M. (2001) Antigorite: Pressure and temperature dependence of polysomatism and water content. *European Journal of Mineralogy*. Schweizerbart 13, 485–495.

Yada, K. (1971) Study of microstructure of chrysotile asbestos by high-resolution electron microscopy. *Acta Crystallographica Section A* 27, 659–664.

Yada, K., Iishi, K. (1977) Growth and microstructure of synthetic chrysotile. *American Mineralogist* 62, 958–965.

Yokoyama, T. *et al.* (2023) Samples returned from the asteroid Ryugu are similar to Ivuna-type carbonaceous meteorites. *Science* 379.

Yoshikawa, M., Python, M., Tamura, A., Arai, S., Takazawa, E., Shibata, T., Ueda, A., Sato, T. (2015) Melt extraction and metasomatism recorded in basal peridotites above the metamorphic sole of the northern Fizh massif, Oman ophiolite. *Tectonophysics*. Elsevier B.V. 650, 53–64.

Yoshitake, N., Arau, S., Ishida, Y., Tamura, A. (2009) Geochemical characteristics of chloritization of mafic crust from the northern Oman ophiolite: Implications for estimating the chemical budget of hydrothermal alteration of the oceanic lithosphere. *Journal of Mineralogical and Petrological Sciences* 104, 156–163.

Yoshiya, K., Sato, T., Omori, S., Maruyama, S. (2019) The Birthplace of Proto-Life: Role of Secondary Minerals in Forming Metallo-Proteins through Water-Rock Interaction of Hadean Rocks. *Origins of Life and Evolution of Biospheres*. Springer Netherlands.

Zhang, C., Koepke, J., Wolff, P.E., Horn, I., Garbe-Schönberg, D., Berndt, J. (2021) Multi-Stage Hydrothermal Veins in Layered Gabbro of the Oman Ophiolite: Implications for Focused Fluid Circulation in the Lower Oceanic Crust. *Journal of Geophysical Research: Solid Earth*. John Wiley and Sons Inc 126.

Zheng, X., Cordonnier, B., Zhu, W., Renard, F., Jamtveit, B. (2018) Effects of Confinement on Reaction-Induced Fracturing During Hydration of Periclase. *Geochemistry, Geophysics, Geosystems* 19, 2661–2672.

Zihlmann, B., Müller, S., Coggon, R.M., Koepke, J., Garbe-Schönberg, D., Teagle, D.A.H. (2018) Hydrothermal fault zones in the lower oceanic crust: An example from Wadi Gideah, Samail ophiolite, Oman. *Lithos*. Elsevier B.V. 323, 103–124.

Zolotov, M.Y. (2014) Formation of brucite and cronstedtite-bearing mineral assemblages on Ceres. *Icarus* 228, 13–26.

Acknowledgements

I am deeply indebted to Dr. Atsushi Okamoto at Graduate School of Environmental Studies, Tohoku University, for grateful supervision, discussions, and support for research execution.

I would like to express my deepest appreciation to Dr. Oliver Plümper at Department of Earth Sciences, Faculty of Geosciences, Utrecht University for teaching and promotions on my research.

I would like to express my deepest gratitude to Dr. Noriyoshi Tsuchiya at Graduate School of Environmental Studies, Tohoku University, for valuable discussions and constructive suggestions.

I would like to express my thanks to Dr. Michihiko Nakamura at Graduate School of Science, Tohoku University, for valuable discussions and constructive suggestions.

I would like to thank Dr. Masaoki Uno at Graduate School of Environmental Studies, Tohoku University, for valuable discussions, advice, and lecture about analytical techniques.

I would like to express my thanks to Dr. Christoph Hilgers at Structural Geology and Tectonics, KIT – Karlsruher Institut für Technologie, for valuable discussions and constructive suggestions on more industrial applications.

I would like to thank Dr. Masanobu Kamitakahara at Graduate School of Environmental Studies, Tohoku University, for valuable discussions and helpful comments from a chemist's perspective.

Special thanks to Dr. Hiroyuki Shimizu, who developed the original simulation code used in this study, for his kind support and advice on the simulation methodology.

I would like to thank Masao Kimura, Yasuhiro Niwa, Tomohiro Ishii for helping on XANES and X-ray CT measurement and analysis at the Institute of Material Structure Science (IMSS), High Energy Accelerator Research Organization (KEK), Tsukuba, Japan.

I thank Dr. Katsuyoshi Michibayashi and Natsume Itsuki of Nagoya University for their great cooperation during the field survey at the Oman Ophiolite in January 2023.

I would like to thank Dr. Kenta Yoshida of JAMSTEC for his kind guidance in the use of FIB-SIM.

I am grateful to Dr. Mayuko Fukuyama at Akita University for helping with trace element analysis using LA-ICP-MS.

I would like to thank Dr. Otgonbayar Dandar and Dr. Astin Nurdiana for kind support of my research. Many thanks to Dr. Ryosuke Oyanagi for valuable discussions and kind advice on general research life.

I thank Alireza Chongani for helping TEM sample preparation using FIB-SEM at Utrecht University, Dr. Yuntao Ji and Hannah Vogel for helping measurement and data processing on X-ray microscopy and Dr. Lisa Eberhard, and Austin Arias for valuable discussions. I would like to thank the members of the Structural Geology Group at the Department of Earth Sciences, Faculty of Geosciences, Utrecht University, for the warm welcome and fruitful discussions. I would like to thank Dr. Hanaya Okuda at the JAMSTEC for his kind advice on general research life.

I would like to thank Mr. Shuhei Tanaka, a graduate of Okamoto & Uno Laboratory, for his great help in preparing samples for the XANES measurements.

I would like to thank Dr. Toshio Suga and Ms. Shinobu Okuyama, at the International Joint Graduate Program, Tohoku University for kind support for my overseas travels and research support.

This research used samples and data provided by the Oman Drilling Project (https://doi.org/10.14379/OmanDP.proc.2020). I would like to thanks to all members of the Oman Drilling Project for the sample collection, descriptions, analysis at onboard *Chikyu*.

This study was supported by JSPS KAKENHI Grant Number JP21J20281 to K. Yoshida, and International Joint Graduate Program in Earth and Environmental Sciences (GP-EES), Tohoku University.

I would like to extend my sincere thanks to all members of Geomaterials and Energy Science, Okamoto and Uno laboratory, and Interdisciplinary Lab for International and Environmental Issues of Energy and Resources, Tsuchiya laboratory, Graduate School of Environmental Studies, Tohoku University for the kind support of my research life.

Finally, I would like to express my greatest gratitude to my family for their warm encouragement.

Publications

1. Kazuki Yoshida, Atsushi Okamoto, Hiroyuki Shimizu, Ryosuke Oyanagi, Noriyoshi Tsuchiya, Oman Drilling Project Phase 2 Science Party (2020). Fluid Infiltration Through Oceanic Lower Crust in Response to Reaction‐Induced Fracturing: Insights From Serpentinized Troctolite and Numerical Models. *Journal of Geophysical Research: Solid Earth*, 125, 11. DOI:10.1029/2020JB020268.
2. Atsushi Okamoto, Ryosuke Oyanagi, Kazuki Yoshida, Masaoki Uno, Hiroyuki Shimizu, Madhusoodhan Satish-Kumar (2021). Rupture of wet mantle wedge by self-promoting carbonation, *Communications Earth & Environment*, DOI:10.1038/s43247-021-00224-5.
3. Kazuki Yoshida, Ryosuke Oyanagi, Masao Kimura, Oliver Plümper, Mayuko Fukuyama, and Atsushi Okamoto (2023). Geological records of transient fluid drainage into the shallow mantle wedge, *Science Advances*, 9, 14, DOI:10.1126/sciadv.ade6674.

International conference

1. Kazuki Yoshida, Hiroyuki Shimizu, Noriyoshi Tsuchiya, Atsushi Okamoto: “Numerical simulations of reaction-induced fracturing and permeability enhancement of layered gabbro during serpentinization” 16th International Workshop on WATER DYNAMICS Fluids in the Earth -Mysterious but Valuable Things-, Sendai, March 12-14, 2019（Poster）
2. Kazuki Yoshida, Atsushi Okamoto, Ryosuke Oyanagi, Hiroyuki Shimizu, Noriyoshi Tsuchiya, Oman Drilling Project Phase 2 Science Party: “Formation of fracture network and permeability enhancement during olivine hydration within oceanic lower crust”, International Conference on Ophiolites and the Oceanic Lithosphere: Results of the Oman Drilling Project and Related Research, 12-14th January, 2020, Sultan Qaboos University, Muscat, Sultanate of Oman（Oral）
3. Kazuki Yoshida, Atsushi Okamoto, Hiroyuki Shimizu, Noriyoshi Tsuchiya: “Fluid percolation induced by reaction-induced fracturing during serpentinization of oceanic lithosphere”, 17th‐International Workshop on Water Dynamics, Sendai, 2020/3/27. （Poster）
4. Kazuki Yoshida, Ryosuke Oyanagi, Hiroyuki Shimizu, Atsushi Okamoto, Noriyoshi Tsuchiya: “Fracture patterns during serpentinization in oceanic lower crust: insights from the oman ophiolite and numerical simulations”, GSA 2020 connects online, 26-30 October, online（Poster）.

5. Kazuki Yoshida, "[P-16]Depth profile of serpentinization of the lower crust to upper mantle of the Oman ophiolite: insights from Oman Drilling Project CM1A & CM2B", Earth, Sea and Sky VI: International Joint Graduate Program Workshop in Earth and Environmental Sciences, 2021 年 6 月 7 日-6 月 11 日 （Poster）
6. Kazuki Yoshida, Atsushi Okamoto, Ryosuke Oyanagi, and Masao Kimura, [EGU22-3483] "Rapid fluid infiltration recorded in the brucite-rich reaction zone along the antigorite veins from the Oman ophiolite", EGU General Assembly 2022, Vienna, Austria & Online, 2022 年 5 月 23 日-5 月 27 日 （Poster）
7. Kazuki Yoshida, Ryosuke Oyanagi, Masao Kimura, Plümper Oliver, Mayuko Fukuyama, Atsushi Okamoto, Transient fluid flow in the shallow mantle wedge: insight from the Oman ophiolite, Utrecht University - Tohoku University discussion forum on fluid-rock interactions and deformation within the solid Earth, 10th Novermber 2022（Oral）.
8. Kazuki Yoshida, Ryosuke Oyanagi, Masao Kimura, Oliver Plümper, Mayuko Fukuyama, and Atsushi Okamoto, Transient fluid flow recorded in the Crust-Mantle transition zone of the Oman Ophiolite, EGU General Assembly 2023, 23-28 April 2023 （Poster）.
9. Kazuki Yoshida, Ryosuke Oyanagi,, Masao Kimura, Oliver Plümper, Mayuko Fukuyama, Atsushi Okamoto, Transient fluid flow in the subduction zone setting: Implications from the Oman Ophiolite, Water-Rock Interaction WRI-17, Sendai, 2023/08/18-22 (Oral)
10. Kazuki Yoshida, Atsushi Okamoto, Ryosuke Oyanagi,, Masakazu Fujii, Yasuhiro Niwa, Yasuo Takeichi, Shuhei Tanaka, Masao Kimura, Redox state of iron during serpentinization of the crust-mantle transition zone to the upper mantle section of the Oman Ophiolite, Water-Rock Interaction WRI-17, Sendai, 2023/08/18-22 (Poster)

Table A1. Analytical results of LA-ICP-MS for standards (NIST 612, BIR-1G, and BHVO-2G). ^{29}Si was used as the internal standard.

Sample	NIST 612 (n=8)		BIR-1G (n=22)			BHVO-2G (n=8)		
(ppm)	Average	RSD (%)	Average	RSD (%)	Recom.	Average	RSD (%)	Recom.
Li	40.4	2.5	3.1	3.2	3	4.50	2.4	4.4
B	34.4	3.0	2.2	12.5		4.30	12.6	
Na_2O (%)	13.7	2.4	1.78	4.0	1.85	2.22	2.3	2.4
Al_2O_3 (%)	2.0	1.9	16.4	4.1	15.5	14.3	3.6	13.6
CaO (%)	11.9	2.2	13.3	3.1	13.3	11.2	3.1	11.4
Sc	39.7	3.4	40.6	5.4	43	30.9	5.0	33
Ti	43.9	4.6	5948	4.0	5400	15936	3.0	16300
V	39.1	2.3	332	2.7	326	317	3.0	308
Cr	36.5	4.2	393	2.3	392	292	2.3	293
Mn	38.8	1.9	1345	2.8	1471	1293	2.8	1317
Co	35.5	1.6	53.8	4.1	52	46.2	1.6	44
Ni	38.8	2.2	176	3.2	178	122	5.5	116
Cu	38.0	2.5	120	2.7	119	125	4.3	127
Zn	39.3	3.8	80.3	3.1	78	116	2.8	102
As	35.7	1.9	0.055	54.3		0.759	5.3	
Rb	31.7	4.6	0.199	4.8	0.197	9.54	2.0	9.2
Sr	78.2	2.9	109	2.3	109	383	2.5	396
Y	38.2	3.5	13.4	4.9	14.3	23.0	3.9	26
Zr	37.7	3.6	13.0	4.9	14	158	4.2	170
Nb	38.8	2.1	0.53	5.3	0.52	18.2	3.2	18.3
Sb	34.8	3.5	0.51	4.3	0.56	0.20	26.1	0.3
Cs	43.0	4.4	0.006	22.7	0.007	0.11	3.3	0.1
Ba	39.3	3.0	6.8	1.6	6.5	132	2.4	131
La	36.0	3.4	0.59	4.0	0.609	15.1	3.8	15.2
Ce	38.5	2.6	1.94	1.5	1.89	37.1	2.4	37.6
Pr	37.9	3.5	0.37	2.6	0.37	5.16	2.9	5.35
Nd	35.5	3.9	2.34	3.9	2.37	24.1	3.6	24.5
Sm	37.7	4.1	1.09	3.7	1.09	5.98	4.4	6.1
Eu	35.6	3.9	0.534	3.8	0.517	2.05	3.3	2.07
Gd	37.3	5.0	1.69	4.9	1.85	5.83	5.1	6.16
Tb	37.6	5.1	0.33	3.8	0.35	0.869	4.1	0.92
Dy	35.5	4.9	2.34	6.0	2.55	4.94	5.2	5.28
Ho	38.3	4.5	0.52	4.3	0.56	0.92	5.3	0.98
Er	38.0	4.6	1.6	4.8	1.7	2.38	4.4	2.56
Tm	36.8	4.4	0.22	3.9	0.24	0.30	6.9	0.34
Yb	39.2	4.6	1.58	4.8	1.64	1.93	4.1	2.01
Lu	37.1	4.8	0.226	5.5	0.248	0.256	3.3	0.279
Hf	36.8	5.3	0.52	4.7	0.57	4.16	5.9	4.32
Ta	37.7	4.8	0.035	6.9	0.036	1.11	5.2	1.15
Pb	39.0	6.6	3.5	3.8	3.7	1.91	2.4	1.7
Th	37.8	5.0	0.03	6.7	0.03	1.20	5.1	1.22
U	37.6	4.6	0.019	10.2	0.023	0.448	3.1	0.403

Notes: RSD%: relative standard deviation; Recom.: GEOREM preferred values.

Table A2-1. Bulk-rock major element composition measured by XRF.

			Bulk-rock major element composition and loss on ignition (LOI) in weight percent (wt%)											
Sample name	Depth (m)	Lithology	SiO_2	TiO_2	Al_2O_3	Fe_2O_3*	MnO	MgO	CaO	Na_2O	K_2O	P_2O_5	Total	LOI
C5707A-7Z1-43-45	0	gabbroic	40.5	0.1	5.9	13.9	0.2	32.0	5.8	0.16	0.03	0.01	98.7	7.8
C5707A-7Z2-38-42	1.25	gabbroic	45.5	0.2	3.9	12.5	0.2	27.0	9.6	0.17	0.03	0.01	99.1	7.8
C5707A-8Z2-10-14	11.25	gabbroic	45.1	0.2	8.7	9.5	0.2	22.0	12.6	0.23	0.02	0.01	98.7	6.7
C5707A-28Z1-85-88	65.25	gabbroic	46.7	0.2	15.0	5.2	0.1	12.7	17.7	0.81	0.03	0.01	98.4	4.6
C5707A-32Z1-53-55	74.25	gabbroic	41.8	0.2	8.8	16.4	0.2	22.5	7.9	0.55	0.03	0.00	98.3	5.8
C5707A-39Z1-84-88	95.25	gabbroic	46.8	0.2	21.2	3.8	0.1	6.5	17.2	1.61	0.03	0.01	97.4	1.9
C5707A-46Z1-34-39	113.25	gabbroic	46.0	0.1	23.0	3.3	0.1	6.8	17.4	1.19	0.03	0.01	97.9	2.0
C5707A-47Z2-62-67	117.14	gabbroic	44.4	0.1	14.4	6.4	0.1	18.2	14.1	0.47	0.04	0.00	98.2	4.7
C5707A-48Z3-10-15	120.42	gabbroic	44.7	0.1	14.5	6.7	0.1	18.5	13.3	0.41	0.05	0.00	98.3	7.2
C5707A-51Z2-72-77	125.97	gabbroic	41.7	0.1	17.1	5.8	0.2	19.6	13.9	0.07	0.02	0.01	98.5	8.4
C5707A-51Z4-72-77	127.78	gabbroic	44.7	0.1	15.0	4.5	0.1	15.1	19.3	0.12	0.02	0.00	99.0	5.7
C5707A-55Z1-76-81	137.25	gabbroic	41.1	0.1	9.5	13.8	0.2	25.8	8.0	0.43	0.02	0.01	99.0	5.1
C5707A-57Z3-12-17	142.11	gabbroic	38.6	0.0	4.7	20.2	0.2	32.0	2.2	0.06	0.02	0.00	98.1	9.5
C5707A-57Z3-43-48	142.11	gabbroic	41.1	0.0	15.3	9.2	0.1	20.2	12.4	0.25	0.03	0.01	98.5	7.5
C5707A-58Z1-50-54	143.25	gabbroic	41.0	0.0	15.7	8.3	0.1	20.5	12.0	0.25	0.04	0.01	97.9	7.1
C5707A-70Z2-26-31	169.05	dunite	38.6	0.0	0.4	11.0	0.2	47.8	0.1	n.d.	0.02	0.01	98.1	15.1
C5707A-79Z3-6-9	186.7	dunite	38.4	0.0	0.4	11.1	0.2	48.4	0.1	n.d.	0.02	0.01	98.5	14.8
C5707A-79Z3-40-45	186.7	dunite	37.6	0.0	0.4	12.8	0.2	46.9	0.1	n.d.	0.02	0.01	98.0	14.3
C5707A-80Z1-26-31	188.25	dunite	39.1	0.0	0.4	8.7	0.1	49.3	0.1	n.d.	0.02	0.01	97.7	14.8
C5707A-80Z4-24-29	190.92	dunite	39.0	0.0	0.3	9.0	0.1	49.3	0.1	n.d.	0.02	0.01	97.8	15.0
C5707A-89Z4-12-17	202.52	dunite	37.2	0.0	0.3	11.5	0.2	48.6	0.1	n.d.	0.02	0.01	97.9	15.0
C5707A-90Z2-48-53	206.99	dunite	38.8	0.0	0.3	9.5	0.1	49.6	0.1	n.d.	0.02	0.01	98.4	15.8
C5707A-107Z2-5-10	249.17	dunite	40.8	0.0	0.4	12.0	0.2	45.3	0.1	n.d.	0.02	0.01	98.8	13.4
C5707A-111Z1-87-91	254.25	dunite	40.8	0.1	1.2	11.8	0.2	41.4	0.5	n.d.	0.02	0.01	95.9	12.1
C5707A-111Z1-87-91	254.25	dunite	40.8	0.1	1.2	11.8	0.2	41.4	0.5	n.d.	0.02	0.01	95.9	12.1
C5707A-113Z3-25-30	259.16	gabbroic	45.5	0.1	18.6	3.7	0.1	11.7	17.6	0.68	0.03	0.01	97.8	1.9
C5707A-113Z4-11-16	259.82	gabbroic	39.8	0.1	16.7	3.9	0.1	13.5	24.0	0.09	0.02	0.01	98.2	6.5

Notes: n.d.: not detected. *: Total Fe calculated as Fe_2O_3.

Table A2-2. Continue of the bulk-rock major element composition measured by XRF.

			Bulk-rock major element composition and loss on ignition (LOI) in weight percent (wt%)											
Sample name	Depth (m)	Lithology	SiO_2	TiO_2	Al_2O_3	Fe_2O_3*	MnO	MgO	CaO	Na_2O	K_2O	P_2O_5	Total	LOI
C5707A-124Z1-40-48	278.15	gabbroic	42.8	0.1	10.6	4.3	0.1	17.5	22.7	0.06	0.02	0.01	98.1	4.9
C5707A-137Z3-46-54	298.17	dunite	38.6	0.0	0.9	10.8	0.1	47.0	0.2	n.d.	0.02	0.01	97.7	14.2
C5707A-138Z2-18-26	299.96	dunite	39.2	0.0	0.7	9.4	0.1	48.7	0.4	n.d.	0.02	0.00	98.5	14.0
C5707A-142Z4-3-11	310.66	dunite	38.5	0.0	0.3	10.3	0.1	48.8	0.3	n.d.	0.02	0.01	98.4	15.1
C5707A-144Z2-24-32	314.81	harzburgite	41.3	0.0	0.5	8.1	0.1	47.3	0.6	n.d.	0.02	0.01	97.9	14.7
C5707A-144Z4-60-68	316.38	harzburgite	42.6	0.0	0.6	8.8	0.1	45.0	1.1	n.d.	0.02	0.01	98.3	10.9
C5707A-150Z1-24-32	332.15	dunite	41.3	0.0	0.6	7.9	0.1	47.0	1.4	n.d.	0.02	0.01	98.3	15.5
C5707A-160Z3-47-55	360.75	harzburgite	42.0	0.0	0.8	7.8	0.1	45.9	1.3	0.03	0.02	0.01	97.9	13.8
C5707A-163Z1-12-20	365.15	harzburgite	41.4	0.0	0.5	8.6	0.1	47.4	0.7	n.d.	0.02	0.00	98.7	13.0
C5707A-170Z1-31-39	383.15	dunite	41.4	0.0	0.9	7.9	0.1	45.8	0.9	n.d.	0.02	0.01	97.0	14.7
C5707A-179Z2-30-38	402.03	harzburgite	42.4	0.0	0.8	7.7	0.1	46.4	0.0	n.d.	0.02	0.01	97.5	13.5
C5707A-179Z3-18-26	402.93	harzburgite	42.3	0.0	0.6	8.7	0.1	46.3	0.1	n.d.	0.02	0.00	98.1	13.9
C5708B-13Z3-7-12	17.6	dunite	38.9	0.0	0.4	9.6	0.1	49.4	0.0	0.00	0.02	0.01	98.4	15.6
C5708B-15Z3-7-12	23.6	dunite	38.5	0.0	0.4	10.7	0.2	48.8	0.1	n.d.	0.02	0.01	98.6	14.9
C5708B-15Z3-38-43	23.6	dunite	38.5	0.1	1.0	10.8	0.1	47.6	0.1	n.d.	0.02	0.02	98.2	14.7
C5708B-16Z2-34-35	26.6	dunite	38.7	0.0	0.5	10.7	0.1	47.9	0.1	0.00	0.03	0.01	98.3	14.8
C5708B-24Z1-14-19	50.6	dunite	39.0	0.0	0.5	10.0	0.1	48.9	0.1	n.d.	0.02	0.01	98.7	15.1
C5708B-41Z4-72-77	74.6	gabbroic	43.1	0.1	12.5	5.9	0.1	21.4	15.5	0.09	0.02	0.01	99.2	7.2
C5708B-52Z3-16-21	95.6	dunite	38.5	0.0	0.3	15.0	0.2	44.7	0.1	n.d.	0.02	0.00	98.9	14.4
C5708B-54Z1-29-34	101.6	dunite	39.7	0.0	1.6	10.1	0.1	46.5	0.4	n.d.	0.03	0.01	98.5	14.6
C5708B-56Z3-51-56	107.6	dunite	39.0	0.0	1.3	9.8	0.1	47.5	0.4	0.01	0.02	0.01	98.1	14.9
C5708B-59Z4-11-16	116.6	dunite	38.9	0.0	0.3	10.4	0.1	48.6	0.3	n.d.	0.02	0.01	98.7	16.2
C5708B-63Z3-37-42	125.6	dunite	38.6	0.0	0.3	11.6	0.2	47.8	0.3	n.d.	0.02	0.01	98.8	16.0
C5708B-68Z1-27-31	134.6	harzburgite	42.3	0.0	0.5	8.6	0.1	46.5	0.7	n.d.	0.02	0.00	98.8	14.9
C5708B-73Z3-64-69	149.6	harzburgite	43.0	0.0	0.7	9.6	0.1	41.8	3.6	n.d.	0.02	0.00	98.8	13.5
C5708B-77Z4-70-75	161.6	harzburgite	42.3	0.0	0.7	8.6	0.1	45.3	0.9	n.d.	0.02	0.00	97.9	11.3
C5708B-83Z2-8-13	176.6	harzburgite	42.6	0.0	0.8	8.4	0.1	45.8	0.8	0.01	0.03	0.00	98.6	12.5

Notes: n.d.: not detected. *: Total Fe calculated as Fe_2O_3.

Table A2-3. Continue of the bulk-rock major element composition measured by XRF.

			Bulk-rock major element composition and loss on ignition (LOI) in weight percent (wt%)											
Sample name	Depth (m)	Lithology	SiO_2	TiO_2	Al_2O_3	Fe_2O_3*	MnO	MgO	CaO	Na_2O	K_2O	P_2O_5	Total	LOI
C5708B-86Z3-10-15	185.6	harzburgite	42.0	0.0	0.6	8.6	0.1	47.1	0.6	0.00	0.03	0.01	99.1	14.5
C5708B-90Z3-40-45	194.6	harzburgite	42.7	0.0	0.6	8.7	0.1	46.1	0.9	0.00	0.02	0.00	99.0	12.4
C5708B-90Z4-65-70	194.6	harzburgite	42.0	0.0	0.6	9.0	0.1	46.4	0.8	0.01	0.02	0.01	99.0	11.0
C5708B-92Z4-35-40	200.6	harzburgite	42.1	0.0	0.7	8.9	0.1	46.5	0.8	0.00	0.02	0.01	99.2	11.6
C5708B-92Z4-80-85	200.6	harzburgite	42.0	0.0	0.7	8.9	0.1	46.9	0.8	0.01	0.03	0.01	99.4	11.8
C5708B-99Z2-68-73	218.6	harzburgite	42.2	0.0	0.6	8.9	0.1	46.2	0.7	0.01	0.02	0.00	98.8	11.0
C5708B-100Z2-15-20	221.6	harzburgite	43.0	0.0	0.6	8.7	0.1	45.8	0.9	0.00	0.02	0.00	99.1	10.7
C5708B-100Z2-65-70	221.6	harzburgite	42.8	0.0	0.5	9.0	0.1	45.8	0.8	0.00	0.02	0.00	99.1	11.3
C5708B-100Z2-80-85	221.6	harzburgite	41.6	0.0	0.4	9.4	0.1	46.8	0.7	0.00	0.02	0.00	99.1	12.4
C5708B-100Z2-85-90	221.6	harzburgite	42.2	0.0	0.5	8.2	0.1	46.8	0.7	n.d.	0.03	0.00	98.6	12.9
C5708B-104Z1-33-38	233.6	harzburgite	42.9	0.0	0.9	8.6	0.1	45.3	1.0	0.03	0.03	0.01	98.8	11.2
C5708B-106Z2-16-21	239.6	harzburgite	42.9	0.0	0.7	7.8	0.1	46.5	0.8	n.d.	0.03	0.01	98.7	15.2
C5708B-106Z3-16-21	239.6	harzburgite	43.3	0.0	0.6	8.2	0.1	45.6	1.0	0.02	0.03	0.01	98.8	13.6
C5708B-106Z3-33-38	239.6	harzburgite	42.6	0.0	0.6	8.6	0.1	45.9	0.8	0.01	0.03	0.01	98.8	13.9
C5708B-106Z3-45-50	239.6	harzburgite	42.5	0.0	0.7	8.7	0.1	45.2	0.9	0.02	0.03	0.01	98.2	13.1
C5708B-110Z1-57-62	248.6	harzburgite	42.8	0.1	1.8	8.1	0.1	42.5	3.0	0.02	0.03	0.01	98.6	13.0
C5708B-110Z1-62-67	248.6	harzburgite	43.5	0.0	1.0	8.1	0.1	44.1	1.9	0.02	0.02	0.01	98.8	13.5
C5708B-112Z4-47-52	254.6	harzburgite	43.9	0.0	1.2	7.7	0.1	43.2	2.5	0.06	0.03	0.01	98.8	13.0
C5708B-119Z1-34-39	272.6	harzburgite	42.9	0.0	0.6	8.9	0.1	46.0	0.2	n.d.	0.02	0.01	98.8	13.0
C5708B-119Z2-7-12	272.6	harzburgite	43.0	0.0	0.8	8.5	0.1	45.7	0.6	0.02	0.02	0.01	98.8	9.3
C5708B-119Z3-78-83	272.6	harzburgite	43.1	0.1	1.5	8.4	0.1	44.8	0.6	0.03	0.03	0.05	98.8	13.8
C5708B-120Z3-8-13	275.6	harzburgite	42.8	0.0	0.7	8.2	0.1	44.7	0.6	0.02	0.03	0.01	97.3	13.8
C5708B-120Z4-82-87	275.6	harzburgite	43.4	0.1	1.2	8.4	0.1	44.4	1.1	0.06	0.04	0.03	98.9	11.4
C5708B-121Z4-55-60	278.6	harzburgite	41.7	0.0	0.6	10.7	0.1	45.2	0.1	n.d.	0.02	0.01	98.5	13.7

Notes: n.d.: not detected. *: Total Fe calculated as Fe_2O_3.

Table A3-1. Magnetic properties and mass fraction of magnetite of gabbroic rocks.

Sample	Lithology	Ms (Am^2/kg)	Mr/Ms	Hcr/Hc	Mag (wt.%)
CM1A-7Z1-43-45	Gabbroic rocks	6.0	0.20	1.68	6.5
CM1A-7Z2-38-42	Gabbroic rocks	3.3	0.20	1.95	3.5
CM1A-8Z2-10-14	Gabbroic rocks	0.0	0.17	1.99	0.0
CM1A-28Z1-85-88	Gabbroic rocks	0.0	0.21	1.93	0.0
CM1A-32Z1-53-55	Gabbroic rocks	4.1	0.20	1.98	4.5
CM1A-39Z1-84-88	Gabbroic rocks	0.0	0.21	2.16	0.0
CM1A-46Z1-34-39	Gabbroic rocks	0.0	0.25	1.93	0.0
CM1A-47Z2-62-67	Gabbroic rocks	1.0	0.21	1.75	1.1
CM1A-48Z3-10-15	Gabbroic rocks	0.0	0.23	1.75	0.0
CM1A-51Z2-72-77	Gabbroic rocks	0.2	0.09	2.88	0.2
CM1A-51Z4-72-77	Gabbroic rocks	0.0	0.11	4.17	0.0
CM1A-55Z1-76-81	Gabbroic rocks	1.2	0.25	1.74	1.3
CM1A-57Z3-12-17	Gabbroic rocks	2.2	0.11	1.95	2.4
CM1A-57Z3-43-48	Gabbroic rocks	0.3	0.12	2.39	0.3
CM1A-58Z1-50-54	Gabbroic rocks	2.8	0.08	3.18	3.0
CM1A-113Z3-25-30	Gabbroic rocks	0.0	0.24	2.41	0.0
CM1A-113Z4-11-16	Gabbroic rocks	0.0	0.16	4.76	0.0
CM1A-124Z1-40-48	Gabbroic rocks	0.1	0.12	2.58	0.1

Table A3-2. Magnetic properties and mass fraction of magnetite of dunite.

Sample	Lithology	Ms (Am^2/kg)	Mr/Ms	Hcr/Hc	Mag (wt.%)
CM1A-70Z2-26-31	Dunite	4.3	0.08	2.87	4.7
CM1A-79Z3-6-9	Dunite	4.6	0.06	3.23	5.0
CM1A-79Z3-40-45	Dunite	3.5	0.05	3.59	3.9
CM1A-80Z1-26-31	Dunite	6.2	0.06	5.31	6.8
CM1A-80Z4-24-29	Dunite	3.6	0.05	4.28	3.9
CM1A-89Z4-12-17	Dunite	4.8	0.05	3.49	5.2
CM1A-90Z2-48-53	Dunite	3.7	0.05	3.62	4.0
CM1A-137Z3-46-54	Dunite	5.4	0.08	2.86	5.9
CM1A-138Z2-18-26	Dunite	1.1	0.16	1.97	1.2
CM1A-142Z4-3-11	Dunite	2.8	0.07	3.04	3.0
CM2B-13Z3-7-12	Dunite	1.7	0.08	2.92	1.8
CM2B-15Z3-7-12	Dunite	2.4	0.10	2.19	2.6
CM2B-15Z3-38-43	Dunite	2.4	0.09	2.44	2.6
CM2B-16Z2-34-35	Dunite	2.9	0.10	2.35	3.1
CM2B-24Z1-14-19	Dunite	2.3	0.09	2.73	2.5
CM2B-52Z3-16-21	Dunite	5.5	0.12	2.15	6.0
CM2B-54Z1-29-34	Dunite	2.5	0.11	2.21	2.7
CM2B-56Z3-51-56	Dunite	1.8	0.10	2.42	2.0
CM2B-59Z4-11-16	Dunite	2.0	0.09	2.79	2.2
CM2B-63Z3-37-42	Dunite	2.0	0.10	2.68	2.2

Table A3-3. Magnetic properties and mass fraction of magnetite of harzburgite.

Sample	Lithology	Ms (Am^2/kg)	Mr/Ms	Hcr/Hc	Mag (wt.%)
CM1A-107Z2-5-10	Harzburgite	7.3	0.10	2.23	8.0
CM1A-111Z1-87-91	Harzburgite	6.4	0.09	2.61	6.9
CM1A-144Z2-24-32	Harzburgite	3.8	0.05	4.21	4.1
CM1A-144Z4-60-68	Harzburgite	0.3	0.16	1.92	0.3
CM1A-150Z1-24-32	Harzburgite	0.6	0.09	2.87	0.7
CM1A-160Z3-47-55	Harzburgite	0.5	0.17	1.94	0.5
CM1A-163Z1-12-20	Harzburgite	0.9	0.16	1.91	0.9
CM1A-170Z1-31-39	Harzburgite	0.8	0.12	2.48	0.9
CM1A-179Z2-30-38	Harzburgite	3.6	0.09	2.54	3.9
CM1A-179Z3-18-26	Harzburgite	4.7	0.06	3.24	5.2
CM2B-68Z1-27-31	Harzburgite	0.8	0.11	2.37	0.9
CM2B-73Z3-64-69	Harzburgite	1.7	0.08	3.00	1.8
CM2B-77Z4-70-75	Harzburgite	0.4	0.14	2.08	0.5
CM2B-83Z2-8-13	Harzburgite	0.4	0.15	1.86	0.4
CM2B-86Z3-10-15	Harzburgite	1.3	0.08	2.94	1.4
CM2B-90Z3-40-45	Harzburgite	0.4	0.16	1.77	0.4
CM2B-90Z4-65-70	Harzburgite	0.7	0.11	2.28	0.7
CM2B-92Z4-35-40	Harzburgite	0.5	0.15	1.90	0.5
CM2B-92Z4-80-85	Harzburgite	1.0	0.12	2.21	1.1
CM2B-99Z2-68-73	Harzburgite	1.0	0.09	2.67	1.0
CM2B-100Z2-15-20	Harzburgite	0.9	0.13	2.08	0.9
CM2B-100Z2-65-70	Harzburgite	1.0	0.10	2.41	1.0
CM2B-100Z2-80-85	Harzburgite	1.4	0.11	2.36	1.6
CM2B-100Z2-85-90	Harzburgite	0.5	0.12	2.22	0.5
CM2B-104Z1-33-38	Harzburgite	0.4	0.18	1.67	0.4
CM2B-106Z2-16-21	Harzburgite	0.5	0.11	2.34	0.5
CM2B-106Z3-16-21	Harzburgite	0.5	0.16	1.82	0.5
CM2B-106Z3-33-38	Harzburgite	0.6	0.19	1.71	0.7
CM2B-106Z3-45-50	Harzburgite	0.7	0.19	1.69	0.8
CM2B-110Z1-57-62	Harzburgite	0.7	0.19	1.73	0.8
CM2B-110Z1-62-67	Harzburgite	0.7	0.18	1.75	0.8
CM2B-112Z4-47-52	Harzburgite	0.9	0.15	2.00	0.9
CM2B-119Z1-34-39	Harzburgite	2.2	0.09	2.63	2.4
CM2B-119Z2-7-12	Harzburgite	0.4	0.23	1.58	0.4
CM2B-119Z3-78-83	Harzburgite	0.8	0.18	1.85	0.9
CM2B-120Z3-8-13	Harzburgite	1.5	0.11	2.37	1.6
CM2B-120Z4-82-87	Harzburgite	0.6	0.22	1.64	0.7
CM2B-121Z4-55-60	Harzburgite	6.5	0.06	3.12	7.1